

REPORT DOCUMENTATION PAGE

Form Approved
OMB No. 0704-0188

Public reporting burden for this collection of information is estimated to average 1 hour per response, including the time for reviewing instructions, searching existing data sources, gathering and maintaining the data needed, and completing and reviewing this collection of information. Send comments regarding this burden estimate or any other aspect of this collection of information, including suggestions for reducing this burden to Department of Defense, Washington Headquarters Services, Directorate for Information Operations and Reports (0704-0188), 1215 Jefferson Davis Highway, Suite 1204, Arlington, VA 22202-4302. Respondents should be aware that notwithstanding any other provision of law, no person shall be subject to any penalty for failing to comply with a collection of information if it does not display a currently valid OMB control number. PLEASE DO NOT RETURN YOUR FORM TO THE ABOVE ADDRESS.

1. REPORT DATE (DD-MM-YYYY)	2. REPORT TYPE Technical Paper	3. DATES COVERED (From - To)		
4. TITLE AND SUBTITLE		5a. CONTRACT NUMBER		
		5b. GRANT NUMBER		
		5c. PROGRAM ELEMENT NUMBER		
6. AUTHOR(S)		5d. PROJECT NUMBER 2303		
		5e. TASK NUMBER M1A3		
		5f. WORK UNIT NUMBER 346127		
7. PERFORMING ORGANIZATION NAME(S) AND ADDRESS(ES)		8. PERFORMING ORGANIZATION REPORT		
9. SPONSORING / MONITORING AGENCY NAME(S) AND ADDRESS(ES) Air Force Research Laboratory (AFMC) AFRL/PRS 5 Pollux Drive Edwards AFB CA 93524-7048		10. SPONSOR/MONITOR'S ACRONYM(S)		
		11. SPONSOR/MONITOR'S NUMBER(S)		
12. DISTRIBUTION / AVAILABILITY STATEMENT Approved for public release; distribution unlimited.				
13. SUPPLEMENTARY NOTES				
14. ABSTRACT				
20030123 054				
15. SUBJECT TERMS				
16. SECURITY CLASSIFICATION OF: a. REPORT Unclassified		17. LIMITATION OF ABSTRACT A	18. NUMBER OF PAGES	19a. NAME OF RESPONSIBLE PERSON Leilani Richardson
b. ABSTRACT Unclassified				19b. TELEPHONE NUMBER (include area code) (661) 275-5015
c. THIS PAGE Unclassified				

MEMORANDUM FOR PRS (In-House Publication)

FROM: PROI (STINFO)

22 March 2002

SUBJECT: Authorization for Release of Technical Information, Control Number: **AFRL-PR-ED-TP-2002-064**
Capt. Rene I. Gonzalez, "Synthesis and In-Situ Atomic Oxygen Erosion Studies of Space-Survivable
Hybrid Organic/Inorganic Polyhedral Oligomeric Silsesquioxane Polymers"

Ph.D. Dissertation (Statement A)
(University of Florida, FL, 01 May 2002) (Deadline: 01 May 02)

1. This request has been reviewed by the Foreign Disclosure Office for: a.) appropriateness of distribution statement, b.) military/national critical technology, c.) export controls or distribution restrictions, d.) appropriateness for release to a foreign nation, and e.) technical sensitivity and/or economic sensitivity.

Comments: _____

Signature _____ Date _____

2. This request has been reviewed by the Public Affairs Office for: a.) appropriateness for public release and/or b) possible higher headquarters review.

Comments: _____

Signature _____ Date _____

3. This request has been reviewed by the STINFO for: a.) changes if approved as amended, b) appropriateness of references, if applicable; and c.) format and completion of meeting clearance form if required

Comments: _____

Signature _____ Date _____

4. This request has been reviewed by PR for: a.) technical accuracy, b.) appropriateness for audience, c.) appropriateness of distribution statement, d.) technical sensitivity and economic sensitivity, e.) military/national critical technology, and f.) data rights and patentability

Comments: _____

APPROVED/APPROVED AS AMENDED/DISAPPROVED

PHILIP A. KESSEL
Technical Advisor
Space and Missile Propulsion Division

Date

SYNTHESIS AND IN-SITU ATOMIC OXYGEN EROSION STUDIES OF SPACE-SURVIVABLE HYBRID ORGANIC/INORGANIC POLYHEDRAL OLIGOMERIC SILSESQUIOXANE POLYMERS

By

RENE I. GONZALEZ

DISTRIBUTION STATEMENT A

Approved for Public Release
Distribution Unlimited

A DISSERTATION PRESENTED TO THE GRADUATE SCHOOL
OF THE UNIVERSITY OF FLORIDA IN PARTIAL FULFILLMENT
OF THE REQUIREMENTS FOR THE DEGREE OF
DOCTOR OF PHILOSOPHY

UNIVERSITY OF FLORIDA

2002

Copyright 2002

by

Rene I. Gonzalez

This dissertation is dedicated to my late father, Rene A. Gonzalez Freyre.

ACKNOWLEDGMENTS

I would first like to thank my research advisor, Professor Gar Hoflund, for his unwavering optimism, support and encouragement. He is truly a good friend whose company I enjoy very much. I would also like to thank my research group at the Air Force Research Laboratory at Edwards AFB, CA. In particular, I would like to thank Dr. Shawn Phillips, Dr. Tim Haddad, Dr. Steve Svejda, Dr. Brent Viers, Dr. Rusty Blanski, Justin Leland, Patrick Ruth and Brian Moore for their support, guidance and continual motivation in this endeavor. I would also like to thank my friends and laboratory co-workers at the University of Florida: Dr. Helena Haeglin, Professor Jason Weaver, Alex Gerard, Paulo Morales, Brandy Colwell and Bryan Fitzsimmons. Most importantly, I would like to thank my parents and my beautiful wife, Monica.

I also gratefully acknowledge financial support from Dr. Charles Lee of the Air Force Office of Scientific Research.

TABLE OF CONTENTS

	<u>page</u>
ACKNOWLEDGMENTS	iv
LIST OF TABLES	viii
LIST OF FIGURES	ix
LIST OF ABBREVIATIONS	xvi
ABSTRACT	xix
1 INTRODUCTION	1
1.1 Research Objective	1
1.2 The Space Environment	2
1.2.1 Atomic Oxygen	3
1.2.2 Literature Review on Materials Degradation in Space	4
1.3 Polyhedral Oligomeric Silsesquioxane (POSS) Polymers	14
1.4 Overview of UHV System and X-ray Photoelectron Spectroscopy	20
1.5 X-ray Photoelectron Spectroscopy	22
1.5.1 Sampling depth of Photoelectron	23
1.5.2 Electron Energy Analyzer	25
2 DESCRIPTION OF THE ELECTRON STIMULATED DESORPTION ATOMIC OXYGEN SOURCE	27
2.1 Introduction	27
2.2 ESD Atomic Oxygen Source Design and Recent Improvements	28
2.2.1 Adsorption and Permeation	32
2.2.2 Electron Stimulated Desorption	34
2.2.3 Energy Distribution and Neutral Atom Detection	36
2.2.4 Flux quantification	38
2.3 Comparison of AO Sources Used to Simulate LEO	39
2.3.1 Oxygen Radio Frequency and Microwave Plasma Sources	39
2.3.2 Pulsed Laser Excitation Sources	40
2.4 Summary	43

3 IN-SITU ATOMIC OXYGEN EROSION STUDY OF A POLYHEDRAL OLIGOMERIC SILSESQUIOXANE SILOXANE COPOLYMER.....	44
3.1 Introduction.....	44
3.2 Experimental.....	46
3.2.1 Synthesis of a POSS-PDMS Copolymer	46
3.2.2 Preparation of Thin Films by Solvent Casting.....	47
3.3.3 Surface Characterization.....	48
3.3 Results and Discussion	49
3.4 Summary	57
4 IN-SITU ATOMIC OXYGEN EROSION STUDY OF POLYHEDRAL OLIGOMERIC SILSESQUIOXANE POLYURETHANE COPOLYMERS	59
4.1 Introduction.....	59
4.2 Experimental.....	60
4.2.1 Synthesis of POSS-Polyurethane Copolymers	60
4.2.2 Preparation of Thin Films by Solvent Casting.....	64
4.2.3 Surface Characterization.....	64
4.3 Results and Discussion	65
4.4 Summary	78
5 SYNTHESIS, CHARATERIZATION AND IN-SITU ATOMIC OXYGEN EROSION STUDIES OF POSS-POLYIMIDES	80
5.1 Introduction.....	80
5.2 Development of First POSS-Aniline Monomer For Polyimide Synthesis	89
5.2.1 Synthesis of $(c\text{-C}_6\text{H}_{11})_8\text{Si}_8\text{O}_{11}[p\text{-C}_6\text{H}_4\text{NH}_2]_2$	91
5.2.2 Synthesis of POSS-Polyimides	94
5.3 Mechanical and Thermal Properties of POSS-Polyimides	95
5.4 Experimental	99
5.4.1 Profilometry and Atomic Oxygen Etching Experiments	99
5.4.2 Surface Characterization.....	105
5.5 Results and Discussion	106
5.6 (MISSE) Materials on International Space Station Experiment.....	114
5.7 Summary	117
6 IN-SITU ATOMIC OXYGEN EROSION STUDY OF FLUOROPOLYMER FILMS USING X-RAY PHOTOELECTRON SPECTROSCOPY.....	118
6.1 Introduction.....	118
6.2 Experimental.....	121
6.3 Results and Discussion	122
6.4 Summary	132

7 NEW SYNTHETIC ROUTE AND NMR CHARACTERIZATION OF POSS ANILINES FOR POLYIMIDES	133
7.1 Introduction.....	133
7.2 Experimental	135
7.2.1 General Information.....	135
7.2.2 Synthesis of Cp_7T_8 aniline $\{(c-C_5H_{19})_7Si_8O_{12}[p,m,o-C_6H_4NH_2]\}$	135
7.2.2.1 Preparation of Cp_7T_8 phenyl $\{(c-C_5H_{19})_7Si_8O_{12}C_6H_5\}$	136
7.2.2.2 Nitration: Preparation of Cp_7T_8 nitrobenzene $\{(c-C_5H_{19})_7Si_8O_{12}[p,m,o-C_6H_4NO_2]\}$	137
7.2.2.3 Reduction: Preparation of Cp_7T_8 aniline $\{(c-C_5H_{19})_7Si_8O_{12}[p,m,o-C_6H_4NH_2]\}$	141
7.2.3 Synthesis of $Cp_8T_8D_1$ dianiline $\{(c-C_5H_{19})_7Si_9O_{13}[p,m,o-C_6H_4NH_2]_2\}$	143
7.2.3.1 Preparation of $Cp_8T_8D_1$ diphenyl $\{(c-C_5H_{19})_8Si_9O_{13}[C_6H_4]_2\}$	143
7.2.3.2 Nitration: Preparation of $Cp_8T_8D_1$ dinitrobenzene $\{(c-C_5H_{19})_8Si_9O_{13}[p,m,o-C_6H_4NO_2]_2\}$	145
7.2.3.3 Reduction: Preparation of $Cp_8T_8D_1$ dianiline $\{(c-C_5H_{19})_8Si_9O_{13}[p,m,o-C_6H_4NH_2]_2\}$	147
7.3 Results and Discussion	148
7.4 Summary	156
8 CONCLUSIONS AND SUGGESTIONS FOR FUTURE WORK	157
8.1 Atomic Oxygen Survivability of POSS-Polymers.....	157
8.2 Atomic Oxygen Source Characterization	158
8.2.1 Flux Characterization.....	158
8.2.2 Determination of AO Energy Distribution	159
8.3 Characterization Of Polymer Surfaces.....	159
8.3.1 Mass Spectrometry.....	159
8.3.2 Infrared Spectroscopy (IR)	160
8.3.3 Atomic Force Microscopy/ Secondary Electron Microscopy.....	160
8.3.4 Mechanical and Tribological Experiments	160
8.4 Exploring Synergistic Effects	161
8.4.1 Effects of UV Radiation.....	161
8.4.2 Effect of Temperature	162
8.4.3 Effect of Total AO Fluence.....	162
8.4.4 Exposures to Different Gases.....	163
8.4.5 Influence of Sputter Effects	163
LIST OF REFERENCES	165
BIOGRAPHICAL SKETCH	179

LIST OF TABLES

<u>Table</u>		<u>Page</u>
1-1	Bond dissociation energies for commonly used space polymers and inorganic materials.....	5
1-2	Materials Reactivity Data in LEO.....	6
3-1	Near-surface composition determined from XPS data obtained from the as-entered, solvent cleaned, AO and air-exposed POSS-PDMS sample.....	51
4-1	Polyurethane thermal property enhancements through POSS incorporation.	61
4-2	Polyurethane Modulus enhancements through POSS incorporation.	61
4-3	Molecular weights of TMP-POSS-Polyurethanes.	64
4-4	Near-surface composition determined from XPS data obtained from the as-entered, solvent cleaned, AO and air-exposed 20 wt % POSS-Polyurethane sample.	67
4-5	Near-surface composition determined from XPS data obtained from the as-entered, solvent cleaned, AO and air-exposed 60 wt % POSS-Polyurethane sample.	67
5-1	Kapton Binding Energies.....	85
5-2	POSS-Polyimide AO Reaction efficiencies determined from profilometry data.....	103
5-3	Near-surface composition determined from XPS data obtained from the as-entered, solvent cleaned, AO and air-exposed 10 wt% POSS-Polyimide sample.	107
6-1	Polymer Name, Binding Energies, F/C ratio and Structure.....	121
6-2	Near-surface composition (atomic %) determined from XPS data obtained from the as-entered, solvent cleaned, and 15 min AO exposed HDPE and fluoropolymer samples.....	123

LIST OF FIGURES

<u>Figure</u>	<u>Page</u>
1-1 Atomic oxygen undercutting aluminum-kapton multilayer insulation samples flown on the Long Duration Exposure Facility.	9
1-2 Contribution to atomic oxygen undercutting due to unreacted atomic oxygen scattering.....	10
1-3 Condensation reaction for sysnthesis of POSS cages.	15
1-4 Anatomy of a POSS nanostructure.	16
1-5 Common POSS-polymer Structures.	17
1-6 Illustration of enhanced property space of hybrid polymers containing POSS nanostructures.	17
1-7 POSS miscibility in 2 million Mw polystyrene: (a) 50 wt% Cp_8T_8 reveals formation of immiscible POSS crystallites (20-50k atoms), (b) 50 wt% Vi_8T_8 also immiscible, (c) 50 wt% Cp_7T_8 Styryl, significant decrease in size of crystallites evident, (d) 50 wt % Styrenyl ₈ T ₈ , partial miscibility, and (e) 50 wt % Phenethyl ₈ T ₈ , obtained through catalytic hydrogenation of Styrenyl ₈ T ₈ shows complete miscibility.....	18
1-8 Photograph of UHV system at the University of Florida used to conduct Low Earth Orbit simulation and characterization studies.	21
1-9 Illustration of the photoemission process occurring during XPS.	23
1-10 Percent of photoemitted electrons that escape without suffering inelastic collisions versus sampling depth during XPS.....	24
1-11 Schematic diagram of the double pass cylindrical mirror analyzer used to measure the energy distribution of photoemitted electrons in the UHV system during XPS.....	25
2-1 A shematic diagram of the atomic oxygen source.	28

2-2	The atomic oxygen source	29
2-3	Photograph of a sample being exposed to AO source in the reaction chamber...	29
2-4.	Improved reflector/lens assembly on latest prototype ESD AO source.	31
2-5	Reinforced membrane assembly on latest prototype ESD AO source.	33
2-6	Potential energy diagram showing the processes involved in the electron-stimulated desorption of an adsorbed species as a neutral species with excess kinetic energy, according to the MGR model.....	34
2-7	O neutral flux as a function of primary electron emission current at a membrane temperature of 550 °C.....	36
2-8.	Atomic oxygen signal detected by a quadrupole mass spectrometer taken in the appearance potential mode.....	38
2-9.	Schematic diagram illustrating the operational concept of this pulsed CO ₂ laser AO source.....	40
2-10	Energy distribution of overall beam produced by the pulsed CO ₂ laser AO source	42
2-11	Energy distribution of chopped beam produced by the pulsed CO ₂ laser AO source	42
3-1	SEM of (a) unexposed and (b) exposed POSS-siloxane copolymer surfaces. The simulated LEO exposure “healed” the micro-cracks present initially in the POSS-siloxane sample.....	45
3-2	Scheme for synthesis of the POSS-PDMS copolymer used in this study.....	48
3-3	XPS survey spectra obtained from a solvent-cleaned, POSS-PDMS film (a) after insertion into the vacuum system, (b), after a 2-hr (c) 24.6-hr and (d) 63-hr exposure to the hyperthermal AO flux, and (e) 4.75-hr air exposure following the 63-hr AO exposure	50
3-4	XPS C 1s spectra obtained from a solvent-cleaned, POSS-PDMS film (a) after insertion into the vacuum system, (b) after a 2-hr, (c) 24.6-hr, and 63-hrs exposure to the hyperthermal AO flux, and (e) 4.75-hr air exposure following the 63-hr AO exposure.....	54
3-5	XPS O 1s spectra obtained from a solvent-cleaned, POSS-PDMS film (a) after insertion into the vacuum system , (b) after a 2-hr, (c) 24.6-hr, and (d) 63-hr exposure to the hyperthermal AO flux, and (e) 4.75-hr air exposure following the 63-hr AO exposure.....	55

3-6	XPS Si 2p spectra obtained from a solvent-cleaned, POSS-PDMS film (a) after insertion into the vacuum system, (b) after a 2-hr, (c) 24.6-hr, and (d) 63-hr exposure to the hyperthermal AO flux, and (e) 4.75-hr air exposure following the 63-hr AO exposure.	56
4-1	Primary Structure of Polyurethanes.	60
4-2	Synthesis of POSS mono-hydride monomer.	62
4-3	Syntheis of POSS-TMP diol monomer used in copolymerization reaction.	63
4-4	Scheme for synthesis of POSS-polyurethane.	63
4-5	XPS survey spectra obtained from a 20-wt% POSS-polyurethane film after insertion into the vacuum system (a), after 2 hr (b), 24 hr (c), and 63 hr exposure to the hyperthermal AO flux (d), and 4 hr air exposure following the 63 hr exposure (e).	68
4-6	XPS survey spectra obtained from a 60 wt% POSS-polyurethane film after insertion into the vacuum system (a), after a 2 hr (b), 24 hr (c) and 63 hr exposure to the hyperthermal AO flux (d), and 3.3 hr air exposure following the 63 hr exposure (e).	69
4-7	XPS C 1s spectra obtained from a solvent-cleaned, 20-wt% POSS-polyurethane film after insertion into the vacuum system (a), after 2 hr (b), 24 hr (c), and 63 hr exposure to the hyperthermal O-atom flux (d), and 4.0 hr air exposure following the 63 hr O-atom exposure (e).	71
4-8	XPS C 1s spectra obtained from a solvent-cleaned, 60-wt% POSS-polyurethane film after insertion into the vacuum system (a), after 2 hr (b), 24 hr (c), and 63 hr exposure to the hyperthermal O-atom flux (d), and 3.3 hr air exposure following the 63 hr O-atom exposure (e).	72
4-9	XPS O 1s spectra obtained from a solvent-cleaned, 20-wt% POSS-polyurethane film after insertion into the vacuum system (a), after 2 hr (b), 24 hr (c), and 63 hr exposure to the hyperthermal O-atom flux (d), and 4.0 hr air exposure following the 63 hr O-atom exposure (e).	74
4-10	XPS O 1s spectra obtained from a solvent-cleaned, 60-wt% POSS-polyurethane film after insertion into the vacuum system (a), after 2 hr (b), 24 hr (c), and 63 hr exposure to the hyperthermal O-atom flux (d), and 3.3 hr air exposure following the 63 hr O-atom exposure (e).	75
4-11	XPS Si 2p spectra obtained from a solvent-cleaned, 20-wt% POSS-polyurethane film after insertion into the vacuum system (a), after 2 hr (b), 24 hr (c), and 63 hr exposure to the hyperthermal O-atom flux (d), and 4.0 hr air exposure following the 63 hr O-atom exposure (e).	76

4-12	XPS Si 2p spectra obtained from a solvent-cleaned, 60-wt% POSS-polyurethane film after insertion into the vacuum system (a), after 2 hr (b), 24 hr (c), and 63 hr exposure to the hyperthermal O-atom flux (d), and 3.3 hr air exposure following the 63 hr O-atom exposure (e)	77
5-1	Synthesis of Kapton (PMDA-ODA) polyimide through condensation polymerization of pyromellitic dianhydride and oxydianiline.....	81
5-2	High resolution electron microscopy image of PMDA-ODA crystal lamellae .	82
5-3	Computer simulated high resolution electron microscopy images of crystalline PMDA-ODA showing conformational zigzag of the molecule resulting in observed lamellar structure.....	83
5-4	Molecular structure of Kapton (PMDA-ODA) with numerically labeled atomic sites.....	84
5-5	XPS survey spectra obtained from a solvent-cleaned, Kapton film after (a) insertion into the vacuum system, (b) a 20-min, and (c) a 24-h exposure to the hyperthermal AO flux, and (d) a 3-hr air exposure following the 24-hr exposure	86
5-6	High Resolution C 1s and O 1s spectra obtained from a solvent-cleaned, Kapton film after (a) insertion into the vacuum system, (b) a 20-min, and (c) a 24-h exposure to the hyperthermal AO flux, and (d) a 3-hr air exposure following the 24-hr exposure.....	87
5-7	High Resolution N 1s spectra obtained from a solvent-cleaned, Kapton film after (a) insertion into the vacuum system, (b) a 20-min, and (c) a 24-h exposure to the hyperthermal AO flux, and (d) a 3-hr air exposure following the 24-hr exposure.....	88
5-8	Base mediated selective Si-O-Si cleavage of fully condensed silsesquioxane....	90
5-9	Synthesis of $(c\text{-C}_6\text{H}_{11})_8\text{Si}_8\text{O}_{11}[p\text{-C}_6\text{H}_4\text{NH}_2]_2$ POSS dianiline monomer used in POSS-polyimide synthesis.....	92
5-10	^1H NMR of $(c\text{-C}_6\text{H}_{11})_8\text{Si}_8\text{O}_{11}[p\text{-C}_6\text{H}_4\text{NH}_2]_2$ POSS dianiline monomer in CDCl_3	93
5-11	^{13}C NMR of $(c\text{-C}_6\text{H}_{11})_8\text{Si}_8\text{O}_{11}[p\text{-C}_6\text{H}_4\text{NH}_2]_2$ POSS dianiline monomer in CDCl_3	93
5-12	^{29}Si NMR of $(c\text{-C}_6\text{H}_{11})_8\text{Si}_8\text{O}_{11}[p\text{-C}_6\text{H}_4\text{NH}_2]_2$ POSS dianiline monomer in CDCl_3	94
5-13	Synthesis of POSS- Polyimide.	96

5-14	Plot of storage modulus E'(T) vs. temperature for Kapton and POSS-Kapton Polymers	97
5-15	TGA for Kapton and POSS-Kapton polyimides under N ₂ , 10 °C/min heat ramp.	98
5-16	TGA for Kapton and POSS-Kapton polyimides under air, 10 °C/min heat ramp.	99
5-17	Diagram illustrating AO etching experiment using a protective screen to shield selective areas of the sample for profilometry measurements.	100
5-18	Magnified profilometry photographs of (a) the etched Kapton HN standard and (b) a 10 wt % POSS-Kapton polyimide sample. The dark regions correspond to the unetched areas protected by the screen.	101
5-19	Profilometry measurements a obtained from Kapton HN and a 10 wt% POSS-Kapton polyimide after a total AO fluence of 8.47×10^{20} atoms/cm ²	102
5-20	Multiplot of profilometry measurements obtained from Kapton HN and 0, 10 and 20 wt% POSS-Kapton polyimides exposed to a total AO fluence of 2.62×10^{20} atoms/cm ²	104
5-21	Molecular structure of POSS-Kapton with numerically labeled atomic sites.	106
5-22	XPS survey spectra obtained from a 10-wt% POSS-polyimide film after insertion into the vacuum system (a), after 2 hr (b), 24 hr (c), and 40 hr exposure to the hyperthermal AO flux (d), and air exposure following the 40 hr exposure (e).	108
5-23	XPS C 1s spectra obtained from a 10-wt% POSS-polyimide film after insertion into the vacuum system (a), after 2 hr (b), 24 hr (c), and 40 hr exposure to the hyperthermal AO flux (d), and air exposure following the 40 hr exposure (e).	110
5-24	XPS N 1s spectra obtained from a 10-wt% POSS-polyimide film after insertion into the vacuum system (a), after 2 hr (b), 24 hr (c), and 40 hr exposure to the hyperthermal AO flux (d), and air exposure following the 40 hr exposure (e).	111
5-25	XPS O 1s spectra obtained from a 10-wt% POSS-polyimide film after insertion into the vacuum system (a), after 2 hr (b), 24 hr (c), and 40 hr exposure to the hyperthermal AO flux (d), and air exposure following the 40 hr exposure (e).	112

5-26	XPS C 1s spectra obtained from a 10-wt% POSS-polyimide film after insertion into the vacuum system (a), after 2 hr (b), 24 hr (c), and 40 hr exposure to the hyperthermal AO flux (d), and air exposure following the 40 hr exposure (e)	113
5-27	Astronaut installing one the Passive Experiment Containers containing POSS polymer samples onto the International Space Station during STS-105.	115
5-28	Close up view of tray containing POSS samples on Passive Experiment Container of the MISSE project on the ISS.	116
5-29	Diagram illustrating the location of the MISSE PEC containers in relation to the ISS.	117
6-1	Photographs of astronauts servicing the Hubble Space Telescope and retrieving samples of degraded metalized Teflon multilayer insulation for further analysis.....	119
6-2	Chemical structures of the polymers used in this study.....	120
6-3	XPS survey spectra obtained from a solvent-cleaned, HDPE film after (a) insertion into the vacuum system (a)* 15-min AO exposure; PVF after (b) insertion into vacuum system, (b)*after 15-min AO exposure; PVdF after (c) insertion into vacuum system, (c)*after 15-min AO exposure; PTFE after (d) insertion into vacuum system, (d)*after 15-min AO exposure.....	124
6-4	XPS C 1s spectra obtained from a solvent-cleaned, HDPE film after (a) insertion into the vacuum system (a)* 15-min AO exposure; PVF after (b) insertion into vacuum system, (b)*after 15-min AO exposure; PVdF after (c) insertion into vacuum system, (c)*after 15-min AO exposure; PTFE after (d) insertion into vacuum system, (d)*after 15-min AO exposure.....	125
6-5	XPS F 1s spectra obtained from a solvent-cleaned, PVF film after (a) insertion into vacuum system, (a)*after 15-min AO exposure; PVdF after (b) insertion into vacuum system, (b)*after 15-min AO exposure; PTFE after (c) insertion into vacuum system, (c)*after 15-min AO exposure.....	126
7-1	Synthesis of Cp ₇ T ₈ aniline { (c-C ₅ H ₁₉) ₇ Si ₈ O ₁₂ [p,m,o-C ₆ H ₄ NH ₂] }	134
7-2	Synthesis of Cp ₈ T ₈ D ₁ dianiline { (c-C ₅ H ₁₉) ₈ Si ₉ O ₁₃ [p,m,o-C ₆ H ₄ NH ₂] ₂ }	134
7-3	¹ H NMR of of Cp ₇ T ₈ phenyl { (c-C ₅ H ₁₉) ₇ Si ₈ O ₁₂ C ₆ H ₅ }	137
7-4	¹³ C NMR of of Cp ₇ T ₈ phenyl { (c-C ₅ H ₁₉) ₇ Si ₈ O ₁₂ C ₆ H ₅ }	137
7-5	¹ H NMR of Cp ₇ T ₈ nitrobenzene { (c-C ₅ H ₁₉) ₇ Si ₈ O ₁₂ [p,m,o-C ₆ H ₄ NO ₂] }	139
7-6	¹³ C NMR of Cp ₇ T ₈ nitrobenzene { (c-C ₅ H ₁₉) ₇ Si ₈ O ₁₂ [p,m,o-C ₆ H ₄ NO ₂] }	139

7-7	^{29}Si NMR of Cp_7T_8 nitrobenzene $\{(c\text{-C}_5\text{H}_{19})_7\text{Si}_8\text{O}_{12}[p,m,o\text{-C}_6\text{H}_4\text{NO}_2]\}$	140
7-8	HPLC of Cp_7T_8 nitrobenzene $\{(c\text{-C}_5\text{H}_{19})_7\text{Si}_8\text{O}_{12}[p,m,o\text{-C}_6\text{H}_4\text{NO}_2]\}$	140
7-9	^1H NMR of Cp_7T_8 aniline $\{(c\text{-C}_5\text{H}_{19})_7\text{Si}_8\text{O}_{12}[p,m,o\text{-C}_6\text{H}_4\text{NH}_2]\}$	142
7-10	^{13}C NMR of Cp_7T_8 aniline $\{(c\text{-C}_5\text{H}_{19})_7\text{Si}_8\text{O}_{12}[p,m,o\text{-C}_6\text{H}_4\text{NH}_2]\}$	142
7-11	^{29}Si NMR of Cp_7T_8 aniline $\{(c\text{-C}_5\text{H}_{19})_7\text{Si}_8\text{O}_{12}[p,m,o\text{-C}_6\text{H}_4\text{NH}_2]\}$	143
7-12	^1H NMR of $\text{Cp}_8\text{T}_8\text{D}_1$ diphenyl $\{(c\text{-C}_5\text{H}_{19})_8\text{Si}_9\text{O}_{13}[\text{C}_6\text{H}_4]_2\}$	144
7-13	^{13}C NMR of $\text{Cp}_8\text{T}_8\text{D}_1$ diphenyl $\{(c\text{-C}_5\text{H}_{19})_8\text{Si}_9\text{O}_{13}[\text{C}_6\text{H}_4]_2\}$	145
7-14	^1H NMR of $\text{Cp}_8\text{T}_8\text{D}_1$ dinitrobenzene $\{(c\text{-C}_5\text{H}_{19})_8\text{Si}_9\text{O}_{13}[p,m,o\text{-C}_6\text{H}_4\text{NO}_2]_2\}$	146
7-15	HPLC of $\text{Cp}_8\text{T}_8\text{D}_1$ dinitrobenzene $\{(c\text{-C}_5\text{H}_{19})_8\text{Si}_9\text{O}_{13}[p,m,o\text{-C}_6\text{H}_4\text{NO}_2]_2\}$	147
7-17	1H NMR of the aromatic region of Cp_7T_8 nitrobenzene with peaks assigned to the ortho, meta and para isomer	149
7-18	^1H - ^1H NMR Correlation Spectroscopy (COSY) of the aromatic region of Cp_7T_8 nitrobenzene	149
7-19	1H NMR of the aromatic region of Cp_7T_8 aniline with peaks assigned to the ortho, meta and para isomer	150
7-20	^1H - ^1H NMR COSY of the aromatic region of Cp_7T_8 aniline	150
7-21	Reaction scheme for the synthesis of Cp_7T_8 aniline/HCl salt	151
7-22	Basicity of isomers as affected by electron withdrawing POSS cage	151
7-23	Formation of Cp_7T_8 aniline/HCl salt as monitored by ^1H NMR	152
7-24	Reaction of Cp_7T_8 aniline with phthalic anhydride and subsequent chemical imidization with acetice anhydride	153
7-25	^1H NMR of the reaction of Cp_7T_8 aniline with phthalic anhydride	154
7-26	^1H NMR of the reaction of Cp_7T_8 aniline with phthalic anhydride after chemical imidization with acetic anhydride	154
7-27	Stereoview of space filling model of otrhio- $\text{Cp}_8\text{T}_8\text{D}_1$ dianiline	155
7-27	Stereoview of ball and stick model of otrhio- $\text{Cp}_8\text{T}_8\text{D}_1$ dianiline	155

LIST OF ABBREVIATIONS

at%	Atomic Percent
AFM	Atomic Force Microscopy
AFRL/PRSM	Air Force Research Laboratory, Propulsion Materials Applications Branch
AES	Auger Electron Spectroscopy
AO	Atomic Oxygen
AP	Appearance Potential
BE	Binding Energy
BDO	1,4-butanediol
COSY	Correlation Spectroscopy
DMAc	N,N-dimethylacetamide
DPCMA	Double Pass Cylindrical Mirror Analyzer
EFS	Epoxy Functionalized Siloxanes
EOIM III	Evaluation of Oxygen Interactions with Materials III flight experiment
ESCA	Electron Spectroscopy for Chemical Analysis
ESD	Electron Stimulated Desorption
E'(T)	Storage Modulus
eV	Electron Volt
FABS	Fast Atom Beam Source
FEP	Fluorinated Ethylene Propylene
FTIR	Fourier Transform Infrared Spectroscopy

GEO	Geosynchronous Orbit
HDPE	high-density polyethylene
HST	Hubble Space Telescope
IR	Infrared Spectroscopy
ISS	International Space Station
ISS	Ion Scattering Spectroscopy
LaRC	Langley Research Center
LEO	Low Earth Orbit
LDEF	Long Duration Exposure Facility
MDI	Diphenylmethane-4,4'-diisocyanate
MGR	Menzel, Gomer and Redhead ESD Model
MISSE	Materials on the International Space Station Experiment
mol%	mole percent
Mw	Molecular Weight
NMR	Nuclear Magnetic Resonance Spectroscopy
ODA	4,4'-oxydianiline
PECs	Passive Experiment Containers
PDMS	Polydimethylsiloxane
PISX	Polyimide Siloxane
PMDA	pyromelliticdianhydride
PMMA	Polymethylmethacrylate
POSS	Polyhedral Oligomeric Silsesquioxane
PTFE	poly(tetrafluoroethylene)

PTHF	polytetrahydrofuran
PTMG	Polytetramethylene glycol
PU	polyurethane
PVdF	poly(vinylidene fluoride)
PVF	poly(vinyl fluoride)
PPTS	pyridinium p-toluenesulfonate
R_e	Atomic Oxygen Reaction Efficiency
RF	Radio-Frequency
SEM	Scanning Electron Microscopy
SIMS	Secondary Ion Mass Spectrometry
STM	Scanning Tunneling Microscopy
STS	Space Transportation System
T_d	Decomposition Temperature
T_g	Glass Transition Temperature
TGA	Thermal Gravimetric Analysis
THF	Tetrahydrofuran
UHV	Ultra-High Vacuum
UV	Ultraviolet Radiation
VUV	Vacuum Ultraviolet Radiation
wt%	Weight Percent
XPS	X-ray Photoelectron Spectroscopy

Abstract of Dissertation Presented to the Graduate School
of the University of Florida in Partial Fulfillment of the
Requirements for the Degree of Doctor of Philosophy

SYNTHESIS AND IN-SITU ATOMIC OXYGEN EROSION STUDIES OF SPACE-
SURVIVABLE HYBRID ORGANIC/INORGANIC POLYHEDRAL OLIGOMERIC
SILSESQUIOXANE POLYMERS

By

Rene I. Gonzalez

May 2002

Chairman: Professor Gar B. Hoflund

Major Department: Chemical Engineering

Polymeric materials offer many advantages for low Earth orbit applications including ease of processing and reduced payload-to-orbit costs derived from a reduction in weight. However, over the last two decades it has been well established that polymers used in the construction of space vehicles undergo severe degradation resulting in reduced spacecraft lifetimes. These materials degrade because spacecraft surfaces must endure a high atomic oxygen (AO) flux, bombardment by low and high-energy charged particles, and thermal cycling along with the full spectrum of solar radiation. Many studies have been conducted in an effort to determine the mechanism of degradation primarily caused by surface reactions with oxygen atoms. Unfortunately, these studies have all been carried out *after* exposing these highly reactive surfaces to air prior to analysis, thus introducing artifacts that do not represent the true effect of the space environment. Recent testing of polymers containing the nanostructured Si-O frameworks known as POSS (polyhedral oligomeric silsesquioxanes) has revealed promising AO

XIX

resistant properties. These POSS frameworks are comprised of a three dimensional inorganic core with a 3:2 O-Si ratio, surrounded by tailorable organic groups. Incorporation of POSS nanocomposites into polymers results in increased use and decomposition temperatures, improved mechanical properties, and oxidation resistance. A variety of POSS-polymers were exposed to AO produced by a unique hyperthermal oxygen atom source capable of producing a neutral, steady state flux of oxygen atoms devoid of any contaminating species or background radiation. Analysis reveals that these POSS-polymers rapidly form a ceramic-like, passivating SiO_2 layer that prevents further degradation of the underlying virgin polymer. This dissertation presents several characterization studies of the surfaces of newly synthesized POSS-containing polymers before and after exposure to AO. Various POSS-containing copolymers were examined because they have diverse properties and might perform well in different space-related applications. The exposed surfaces were characterized using X-ray photoelectron spectroscopy, and atomic oxygen reaction efficiencies were calculated using stylus surface profilometry. Experiments were carried out in-situ because air exposure modifies the reactive surfaces formed during exposure to AO; thus, these studies provide insight on how AO induces chemical state changes on these polymer surfaces and will enable future development of other novel space survivable materials.

CHAPTER 1 INTRODUCTION

1.1 Research Objective

The main objective of the research presented in this dissertation was to gain a fundamental understanding of the reaction of atomic oxygen (AO) on polyhedral oligomeric silsesquioxane (POSS)-containing copolymers and traditional polymer surfaces. This knowledge will be used to help develop space-survivable polymeric materials with superior properties. During this research, a variety of POSS-containing polymers were synthesized and subsequently characterized before and after AO exposure in an ultrahigh vacuum system capable of performing over twenty different spectroscopic analysis techniques such as X-ray photoelectron spectroscopy (XPS), Auger electron spectroscopy (AES), ion scattering spectroscopy (ISS) and others. This system is comprised of several adjoining chambers which also house a unique hyperthermal oxygen atom source described in Chapter 2. The chemical state changes occurring on the surfaces of these AO exposed polymers were determined through in-situ XPS, and atomic oxygen reaction efficiencies were calculated using stylus surface profilometry. This chapter provides a brief introduction to the environment encountered in space that is responsible for material degradation. Also provided is a general introduction to POSS and the ultra-high vacuum (UHV) system used to conduct in-situ characterization of POSS containing polymers.

1.2 The Space Environment

Although satellites in orbit have continued to proliferate to meet the changing needs of society, there is an even larger need for affordable access to space. More remote areas of the globe are becoming explored and populated, requiring the extension of telecommunications and weather networks to provide for the needs of the burgeoning population. Scientists are looking more toward missions to explore the outer reaches of the galaxy and monitor the health, weather and resources of our own planet. With the building of the International Space Station, there will also be a need for easy access for resupply and transportation of inhabitants to and from Earth. However, the limiting factor hindering the achievement of these missions is cost. Currently it costs about \$10,000/lb to put a payload into orbit. The main driver of cost for space missions is the cost of materials. Materials are costly not only in terms of weight but also in availability, survivability, processing and manufacturing.

In an effort to resolve these material issues, scientists have increasingly turned to polymers. Polymers are attractive and desirable materials for use in space applications because they are lightweight and are typically much easier to process, using techniques such as extrusion, casting and injection molding at relatively low temperatures, than metals and ceramics. They also tend to be more flexible and offer a wide variety of choices from optically transparent to opaque, rubbery to stiff and conducting to insulating.

Over the last fifteen years, it has been well established through space-based experiments and ground simulations that polymeric materials and films, widely used in the construction of space vehicles, undergo severe degradation as a result of the aggressive environment encountered in low Earth orbits (LEO) (altitudes ranging from

200 to 700 km). In this high vacuum environment, these materials are subjected to the full spectrum of solar radiation and must endure constant thermal cycling and bombardment by low and high-energy charged particles as well as high incident fluxes of AO.

Each type of orbit has its advantages and disadvantages but LEO is generally preferred. In contrast to LEO, geosynchronous (GEO) satellites reside over one spot on the Earth at all times, thus requiring only one satellite for a particular area. Ground antennas need only be locked on that one satellite. The high altitude of GEO allows three evenly spaced satellites to attain near-global coverage and greatly reduces the number of inter-satellite links. However, a key drawback to GEO satellites is the large transmission delay resulting from the greater orbital distances (60,000 km), as well as the large amount of power necessary for transmission. LEO satellites require less power and exhibit much faster voice and data transmission rates. Because of these smaller power requirements, LEO satellites can be much smaller and less complex. Launch costs are also smaller because several LEO satellites can often be launched simultaneously. However, constellations of LEO satellites are required to attain global coverage driving up system costs. Furthermore, the cost continues to grow because most LEO satellites must be replaced every 5-10 years due to the harsh environment these satellites encounter in LEO, resulting in material degradation and subsequent malfunction.

1.2.1 Atomic Oxygen

Atomic oxygen is the predominant species in LEO responsible for material degradation with a concentration of 10^8 atoms/cm³. It is formed by the photo-dissociation of molecular oxygen in the upper atmosphere. The reverse reaction in which two O atoms recombine to form an O₂ molecule does not have a high reaction rate because it requires a

teratomic collision. The third atom is needed to carry away the energy released through formation of O₂. For this reason the molecular oxygen density is less than one-tenth the atomic oxygen density over this altitude range.

The erosive potential of atomic oxygen is substantially increased as a result of the high orbiting speeds of spacecraft of 8 to 12 km/s. At these relative speeds the actual flux of the impingement is $\sim 10^{15}$ atoms/cm² with kinetic energies of ~ 5 eV [1-4]. Atomic oxygen interacts with these spacecraft surfaces resulting in mass loss or gain, and changes in surface morphology, optical, mechanical and thermal properties. These interactions lead to changes in solar absorptivity and heat emissivity degrading system performance through thermal imbalances and reductions in solar array electrical power output. The energetic atomic oxygen can also react with spacecraft surfaces forming volatile oxidation products that can contaminate sensitive satellite optical components. These surfaces may also be populated with excited state fragments and radicals which could lead to crosslinking and embrittlement. Several studies have also shown that atomic oxygen works synergistically with vacuum ultraviolet radiation (VUV) resulting in increased erosion rates of some polymers systems which exhibit low erosion yields when exposed to atomic oxygen alone as discussed below.

1.2.2 Literature Review on Materials Degradation in Space

A review of the literature pertaining to the development and testing of new polymer systems and protective coatings is presented in this section. Table 1-1 lists the bond dissociation energies for bonds found in commonly used space-qualified polymers Kapton and Fluorinated Ethylene Propylene (FEP) Teflon [5]. With the exception of the CF₂-F bond in FEP Teflon the energies to break these bonds are very low, < 4.5 eV. Furthermore, the surfaces which face the direction of travel of spacecraft in LEO

encounter atomic oxygen with collision energies of approximately 5.0 eV. An option to protect polymers from these environments is to deposit an inorganic coating. Commonly used inorganics tend to have bond dissociation energies larger than those of organic polymers (Table 1-1), as well as having an enhanced ability to absorb vacuum ultraviolet radiation. The wavelength of electromagnetic radiation required to break these bonds represents less than 0.001% of the extraterrestrial solar spectrum [6, 7]. However, failure of the coating either by mechanical or thermal cycling or micro-meteor impacts will expose virgin material, resulting in rapid, localized degradation and subsequent system failure.

Table 1-1: Bond dissociation energies for commonly used space polymers and inorganic materials [5].

Bond	Dissociation Energy (eV)	λ ([nm])	Material
-C ₆ H ₄ C(=O)-	3.9	320	Kapton
C-N	3.2	390	Kapton
CF ₃ -CF ₃	4.3	290	FEP Teflon
CF ₂ -F	5.5	230	FEP Teflon
Si-O	8.3	150	Silica
Zr-O	8.1	150	Zirconia
Al-O	5.3	230	Alumina

The degradation of polymer materials in space has been studied for many years on space missions (STS missions and NASA Long Exposure Duration Facility (LDEF) in orbit for 70 months) [3, 8-15] and in simulation facilities [16-23]. Polymeric films have been and are being used extensively on the surfaces of space vehicles mainly as thermal control surfaces. In particular, the polyimide Kapton has been studied at length, since it

is used as a flexible substrate for light weight, high power solar arrays because of its inherent strength, temperature stability, excellent insulation properties, UV stability and IR transparency [24]. These studies have determined that Kapton is highly susceptible to AO attack and has an erosion yield of $3 \times 10^{-24} \text{ cm}^3$ per atom of O. The effects of atomic oxygen on about 300 different materials have been investigated in three Space Shuttle flight experiments and one satellite recovery [3, 8, 25]. Table 1-2 lists the reaction efficiencies of some of the most commonly used spacecraft polymers [22].

Table 1-2: Materials Reactivity Data in LEO [22].

Material	Rel. Rates* LEO	Reaction Efficiency cm^3/atom
Kapton	1	3.0×10^{-24}
Polyethylene	0.9	3.7×10^{-24}
FEP Teflon	<0.03	$<0.05 \times 10^{-24}$
FEP Teflon (Solar Max)	0.6	1.0×10^{-24}
Mylar	1	3.4×10^{-24}
Polybenzimidazole	0.5	1.5×10^{-24}
Polysulfone	0.8	2.4×10^{-24}
Siloxane-imide block copolymers(25% /75%)	0.1	0.3×10^{-24}
Epoxy	0.6	1.7×10^{-24}

*Mass loss rates in LEO normalized to Kapton rate.

In an effort to determine the degradation mechanism of Kapton, Eck and Hoffman [26] exposed Kapton surfaces to low flux, low-energy oxygen ion bombardments

accompanied by modulated ion beam mass spectrometry. This study confirmed the evolution of CO as a result of oxygen ion bombardment.

Arnold, Peplinski and Cascarano [27] exposed Kapton samples to oxygen atoms produced by a microwave discharge atom beam source. The oxygen atoms produced from this source had translational energies of 0.14 eV at a flux in excess of $2 \times 10^{19} \text{ cm}^{-2}$. At these low translational energies, no observable changes to the Kapton samples were observed, suggesting a strong dependence on incident translational energy of the reaction of atomic oxygen with polyimide films.

Golub, Wydeven and Cormia [18] performed comparative XPS studies of Kapton polyimide films exposed to LEO on STS-8 and Kapton films exposed to oxygen atoms produced from a ground-based radio-frequency (RF) O_2 plasma source. Their comparative XPS analysis revealed that in addition to the surface erosion seen on both sets of samples, the Kapton samples exposed to the RF plasma source had a higher uptake of oxygen than the STS-8 samples. This was attributed to the high O_2 concentration in the plasma reactor which would react with radicals being formed on Kapton as etching was taking place. As a result, oxygen would be incorporated into the polymer.

In 1990, Koontz, Albyn and Leger [28] presented a critical evaluation of existing thermal atom testing methods for materials selection in LEO. In their study they compared the reaction efficiencies of various polymers flown in LEO to those exposed to a RF plasma asher and a flowing afterglow environment. A clear distinction between both of these environments and the actual LEO environment was presented in this study. They indicated that the simulated environments employing the aforementioned methods produce atoms with low kinetic energies, have a high concentration of molecular oxygen

and charged particles, and generate unwanted UV radiation which all combined, significantly change the atomic oxygen reactivities of the samples. The reaction efficiencies of various polymer samples exposed to these systems varied by several orders of magnitude compared to those observed in LEO.

Ritchie and Gjerde [29] investigated atomic oxygen resistant coatings on Kapton film. In particular they studied sputtered SiO_2 , SiO_2 -fluoropolymer mixtures and indium-tin oxide. Although the SiO_2 coatings showed promise, many problems were encountered using the magnetron sputtering technique. Shortly after, Rutledge and Mihelcic [30] stipulated that coatings manufactured in this manner would be compromised by defects present as a result of surface anomalies occurring during the deposition process, handling or micrometeoroid and debris bombardment in LEO. Through experimentation using a plasma source, they demonstrated that these defects provided a pathway for atomic oxygen to reach the underlying polymer allowing oxidation and subsequent undercutting to occur. A NASA study by DeGroh, Terlep and Dever [16] also found similar results.

A NASA study by DeGroh and Banks [13] on Aluminum-Kapton multilayer insulation samples flown on the LDEF revealed severe atomic oxygen undercutting of the samples as shown in Figure 1-1. This study analyzed these occurrences and used a Monte Carlo model to simulate them. They determined that upon entering a hole in the protective coating, atomic oxygen has certain probability of reaction on first impact for a particular material (only 14% for Kapton). The unreacted atomic oxygen is scattered and has multiple opportunities to react with the substrate material, thus causing undercutting as depicted in Figure 1-2.

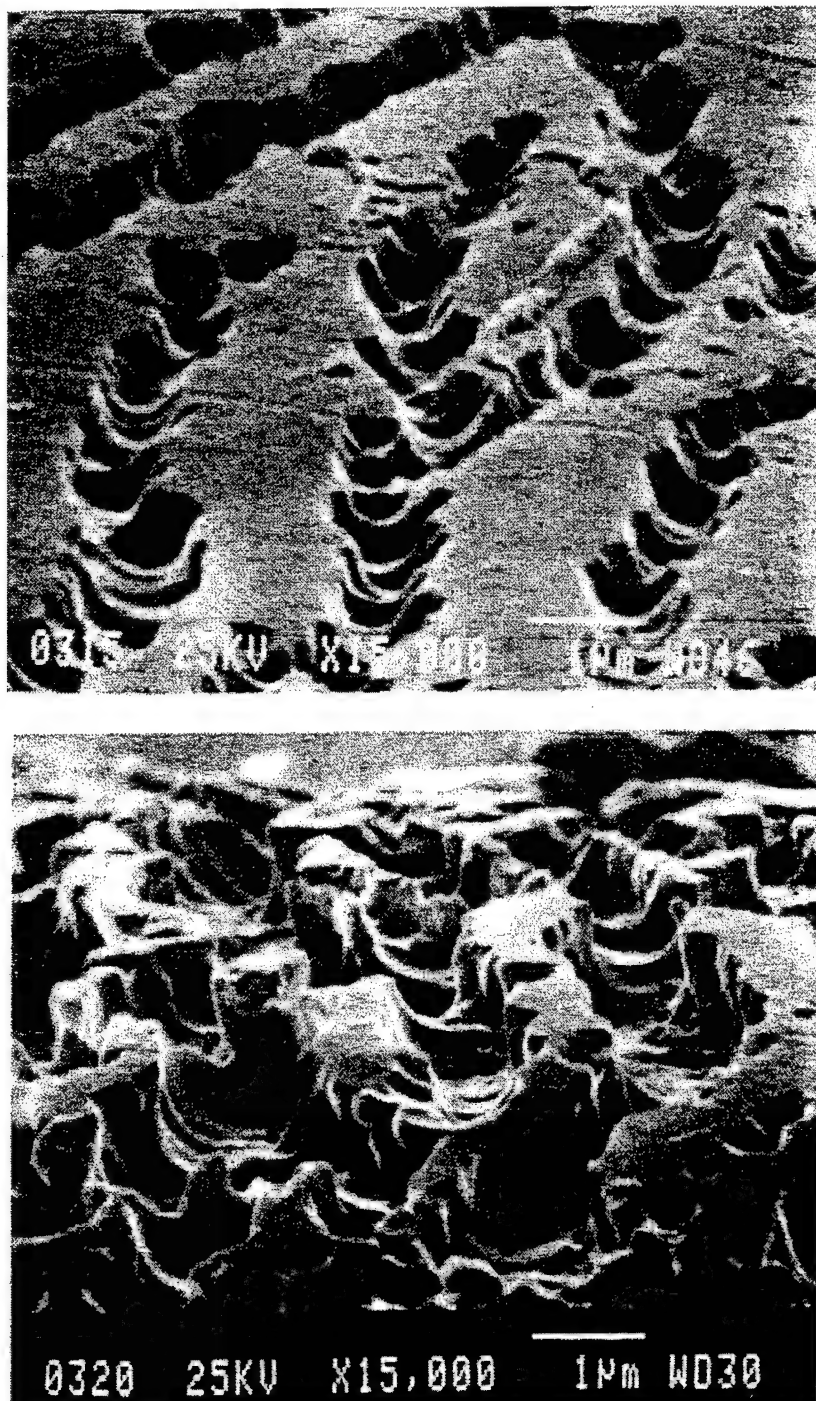


Figure 1-1. Atomic oxygen undercutting aluminum-kapton multilayer insulation samples flown on the Long Duration Exposure Facility, reprinted with permission from AIAA, originally published in reference[13].

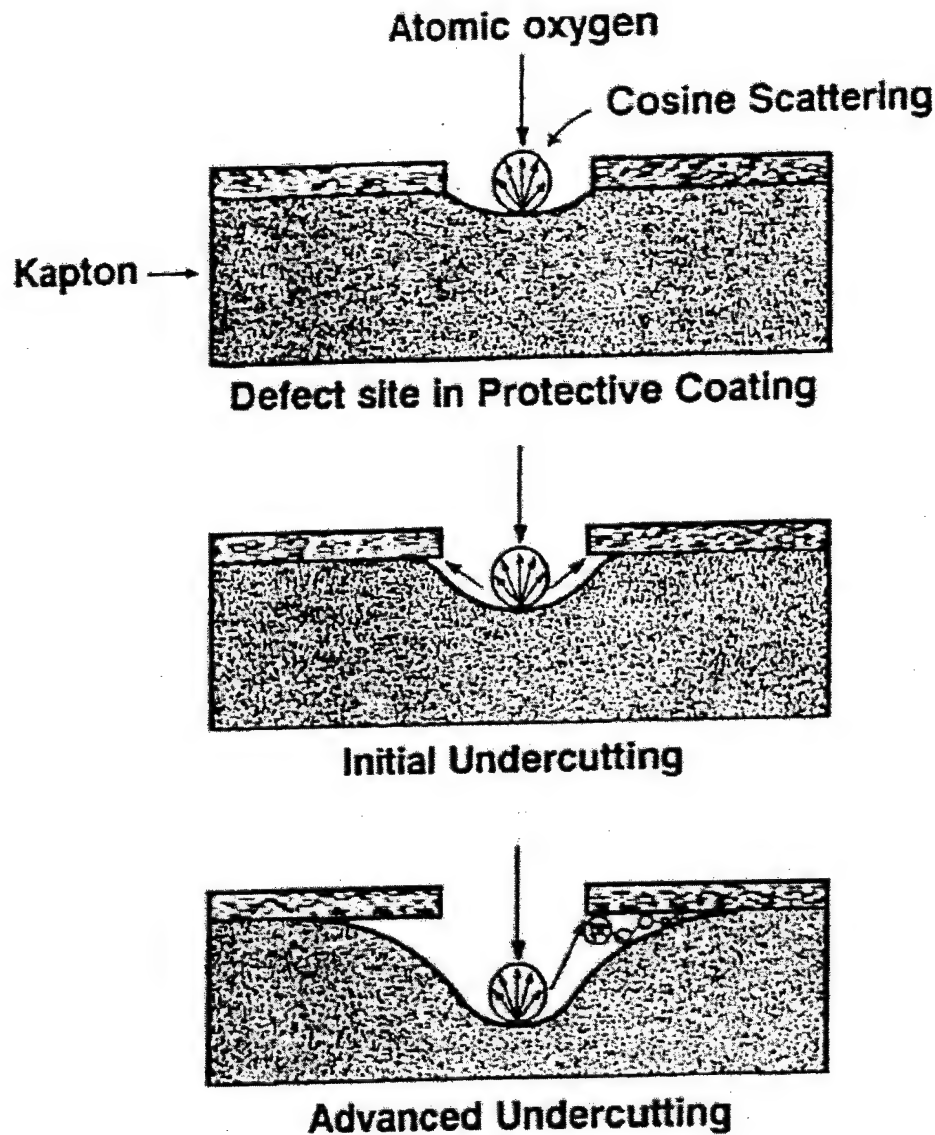


Figure 1-2. Contribution to atomic oxygen undercutting due to unreacted atomic oxygen scattering, reprinted with permission from AIAA, originally published in reference[13].

Silicone coatings have also been studied extensively and display good resistance to atomic oxygen [31, 32], however further ground-based [33] and in flight studies [34] have shown that the use of moderate to high volatility silicones can lead to the release of polymeric scission fragments during combined AO and VUV attack. These fragments

condense on neighboring optical surfaces leading to contamination and reduced power output of solar arrays.

Koontz et al. [35] demonstrated through ground-based experimentation that vacuum ultraviolet radiation significantly increases the atomic oxygen reactivity of fluoro and chlorofluoropolymers.

A NASA study by Golub, Lerner and Wydeven [36] investigated the reactivity of various polybutadienes and EPR rubber with atomic oxygen produced from a plasma source. This study revealed that the erosion rate of these rubbers was highly dependent on their degree of saturation. The more vinyl groups constituting the polymer chain, the less susceptible the polymer was to erosion by atomic oxygen. However, this protective effect of the vinyls in polybutadienes was a result of crosslinking induced through reaction with atomic oxygen. This crosslinking effect would eventually lead to embrittlement.

Dever, et al. [37] conducted atomic oxygen (plasma asher source), UV and thermal cycling studies of SiO_x coated Kapton and a polysiloxane-polyimide AOR Kapton cast from a solution mixture. The SiO_x coated Kapton displayed significantly less fractional mass loss than the AOR Kapton. However, it was observed that the AOR Kapton showed an improvement in durability to atomic oxygen erosion after exposure to VUV radiation and vacuum thermal cycling combined with VUV. Further investigation by Rutledge et al. [38] revealed that the AOR films began to crack and split at a fluence of approximately 7×10^{21} atoms cm^{-2} and fell apart completely at 9.5×10^{21} atoms cm^{-2} . This is about 1/5 of the expected fluence experienced by the space station Freedom solar array.

Vered et al. [23] performed comprehensive (SEM, AFM, XPS) studies of Kapton and Teflon exposed to 30 eV O⁺ and Ne⁺ fluences of 10¹⁵-10¹⁹ ions cm⁻². They were able to determine that chemical processes dominate the degradation of Kapton by 30 eV O⁺ bombardment, while collisional processes dominated for Teflon. However the Teflon erosion under these conditions was three orders of magnitude larger than for 5 eV atomic oxygen erosion in space, indicating that different mechanisms were responsible for Teflon erosion for these two cases.

A multiple layered coating scheme consisting of laminates of 5 to 60 nm Al/AlN separated by thin spacer polyimide layers was studied by Mutikainen [39] after exposures to both a plasma asher and an atomic oxygen beam. The spacing polyimide layers were found to increase the protection efficiency by planarizing the pinhole defects between the coatings and the underlying substrate.

A synergistic effect of VUV radiation in the presence of atomic oxygen was clearly evidenced from XPS studies conducted on fluorinated polyimides by Rasoul et al. [40] using an RF plasma source. Exposure of fluorinated polyimides to VUV radiation alone caused no observable damage to the polymer surfaces, while an atomic oxygen flux resulted in substantial oxidation. However, exposure to VUV radiation and atomic oxygen in combination caused extensive oxidation of the polymer surfaces after a short exposure as compared to AO alone.

In July-August of 1992, STS 46 conducted the Evaluation of Oxygen Interactions with Materials III (EOIM III) flight experiment, during which a well-characterized, short term, high-fluence O-atom exposure was provided for a large number of materials, many of which had never before been exposed to the atomic-oxygen environment [3, 4]. The

experiment consisted of a mass-spectrometer-carousel configuration and produced over 48,000 mass spectra of the gaseous reaction products of various polymers in LEO. XPS studies of several polymer samples flown on this mission show measurable increases in surface oxygen content accompanied by surface depletion of carbon [41].

Connell et al. [42] performed comprehensive scanning electron microscopy (SEM), scanning tunneling microscopy (STM), XPS and weight loss studies on several epoxy functionalized siloxanes (EFS) flown on the EOIM III experiment. EFS are UV curable monomers that can be rapidly photopolymerized to give transparent coatings and composites. Samples of four different EFS exhibited excellent AO resistance both to ambient in-flight conditions as well as exposure to 120°C. SEM, STM and XPS analysis suggest that AO exposure of these materials efficiently produces a thin layer of SiO_x at the surface, providing a barrier toward further AO attack.

Packirisamay, Schwam and Litt published a review of the literature of atomic oxygen resistant coatings in 1995 [43]. The review classifies atomic oxygen resistant coatings into 3 categories: (i) carbon backbone polymers susceptible to AO degradation (e.g., Teflon), (ii) polymers which stabilize by reacting with atomic oxygen (e.g., fluorinated phosphazenes) and (iii) inorganic and semi-inorganic polymers which react with atomic oxygen to form a glassy oxide layer that prevents further reaction of the coatings with atomic oxygen.

In 1996 Gilman, Schlitzer and Lichtenhan [10] evaluated the AO resistance of a polyimide siloxane (PISX) polymer used as the matrix for a composite material flown on the EOIM III experiment, and also conducted preliminary studies on a POSS-siloxane polymer in a simulated LEO environment. XPS analysis showed that the PISX

composites were two orders of magnitude more resistant than homopolyimide-based composites. In addition, erosion rates were slower for PISX when AO was combined with UV radiation. POSS-siloxanes were found to be even more resistant and surprisingly gained weight as a result of exposure and also appeared to heal microcracks that were present originally.

Attempts to use protective coatings have resulted in limited success due to differences in thermal expansion coefficients or substrate undercutting caused by atomic oxygen insertion and scattering through micro-defects on coating surfaces. Silicones have been widely used to protect underlying oxidizable organic materials since they develop a glassy SiO_2 surface on atomic oxygen attack. However the formation of this protective layer is accompanied by density increases and volume shrinkage generating a microporous structure which stresses the coating, causing crack formation. Preceramic polymers such as poly(carborane-siloxane) systems and decaborane-based polymers have shown superior resistance to atomic oxygen; however high cost and availability issues have limited their use [43].

1.3 Polyhedral Oligomeric Silsesquioxane (POSS) Polymers

Recently the Air Force Research Laboratory (AFRL/PRSM) at Edwards AFB has developed a new nanostructured, silicon-based chemical feedstock which can be easily incorporated into most polymeric materials using standard polymerization or processing techniques. This technology utilizes Si-O containing frameworks, known as polyhedral oligomeric silsesquioxanes (POSS). Cooperative efforts by AFRL/PRSM and Hybrid Plastics LLC (limited liability corporation) have led to the optimization of condensation reactions of alkyltrichlorosilanes resulting in an economical synthetic route to obtain the

starting POSS "cages" (Figure 1-3). Traditional silsesquioxane chemistry was focused on the "T-resins" that formed during the condensation. However, in addition to this resin, discrete polyhedra are formed. The polyhedra formed depend on the R group of the starting silane, with open cage systems (those containing unreacted Si-OH groups) being formed only in rare cases (R= cyclohexyl, cyclopentyl) [44-47]. The synthetic methods to form more than fifty monomers, readily useable in conventional polymerization reactions, have been developed to date [48-56].

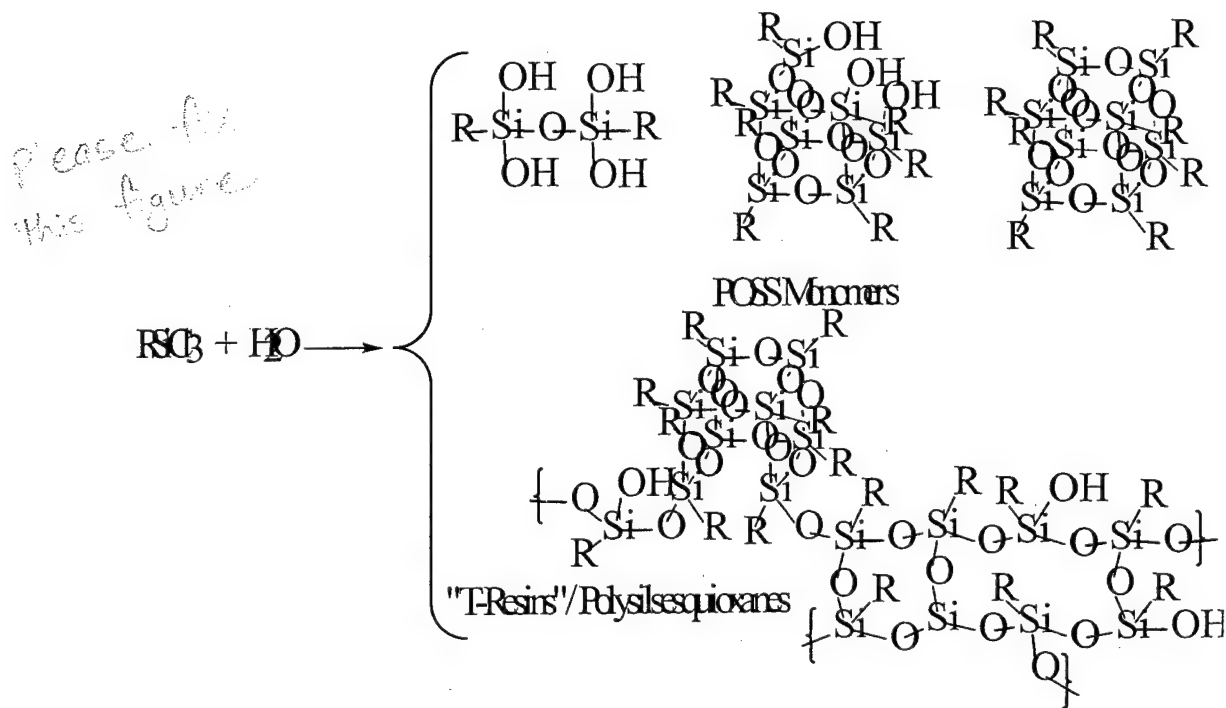


Figure 1-3. Condensation reaction for sysnthesis of POSS cages.

The anatomy of a POSS nanostructure is shown in Figure 1-4 and is defined by the following features. They are single molecules ranging in size from 0.7 nm to 3 nm with an average of 1.5 nm. This diameter renders them approximately two orders of magnitude smaller than conventional inorganic fillers (quartz talc $\sim \mu\text{m}$, fumed Si ~ 100 nm, colloidal $\text{SiO}_2 \sim 10$ nm). They possess a thermally and chemically robust inorganic

framework with well defined three-dimensional polyhedral geometries. They may possess one or more functional groups which enable grafting and copolymerization. They also contain nonreactive R groups (cyclopentyl, cyclohexyl, phenyl, isobutyl, methyl) which aid in the compatibilization with the polymer matrix.

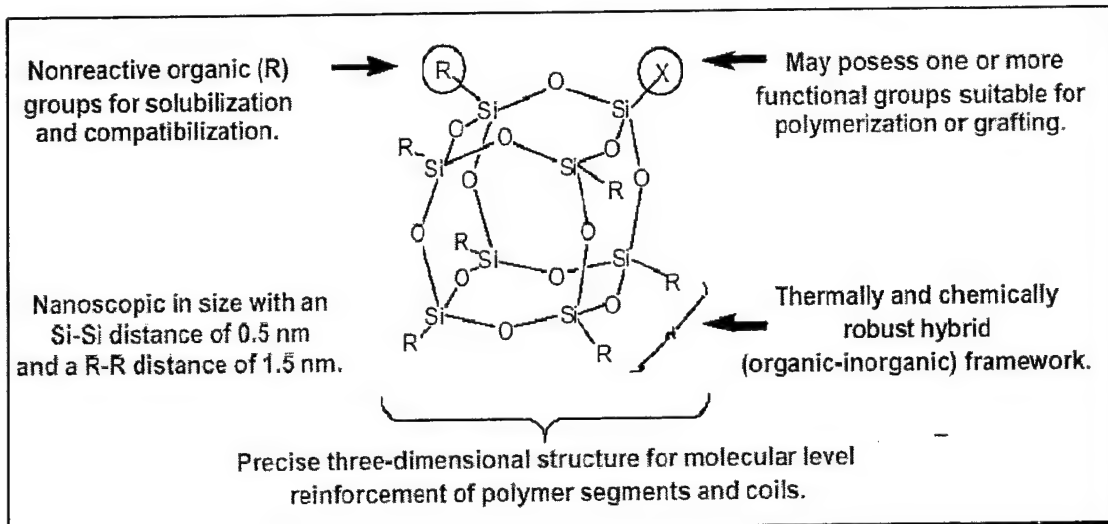


Figure 1-4. Anatomy of a POSS nanostructure.

Three primary POSS-polymer architectures (bead, pendant or crosslinker) are available for use in thermoset systems or in copolymerizations as shown in Figure 1-5.

As shown in Figure 1-6, the hybrid organic/inorganic composition of POSS nanostructures enables them to occupy an enhanced property space relative to traditional hydrocarbons and inorganics, one that marries the beneficial properties of plastics (processability and toughness) with those of ceramics (hardness and stability). Research has shown that addition of POSS monomers via copolymerization, grafting, or blending can result in numerous property enhancements, including increased modulus and temperature stability, oxidation resistance, and ceramic-layer formation. These enhancements are obtained without adversely affecting the density or processibility of the polymer matrix [57-61].

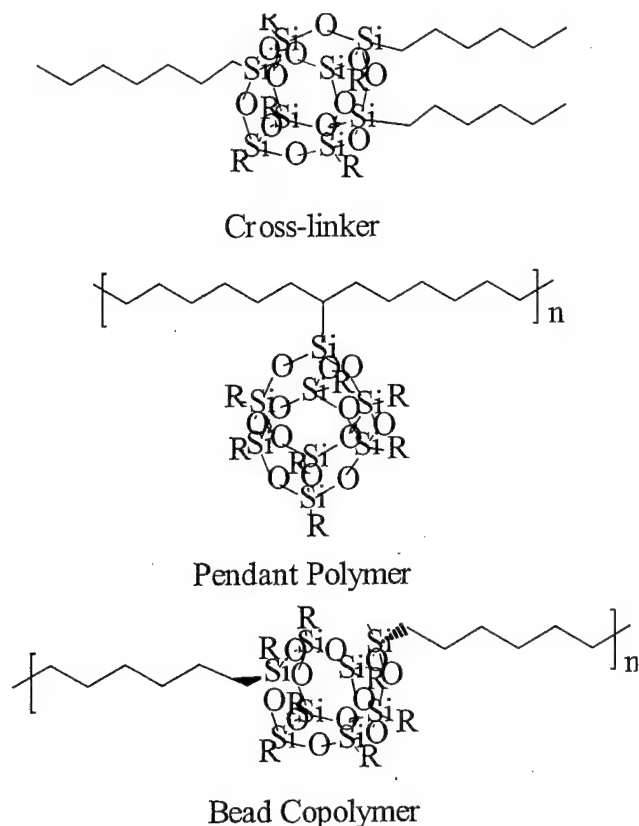


Figure 1-5. Common POSS-polymer Structures.

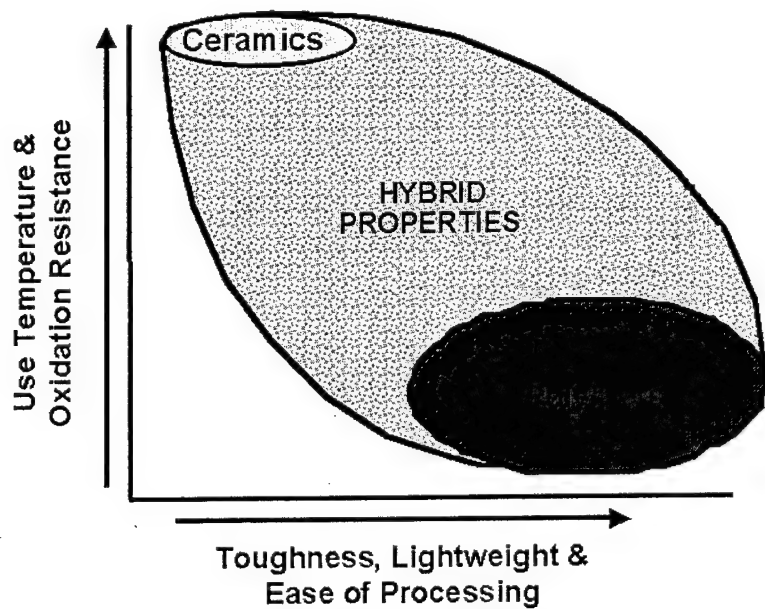


Figure 1-6. Illustration of enhanced property space of hybrid polymers containing POSS nanostructures.

These property enhancements are attributed to the nano-level interaction of the POSS framework with the polymer matrix [62]. Chain entanglement through associated and knotted-rope diffusion, and the size and mass of the POSS cage ($\sim 15 \text{ \AA}$, 1000 amu) are all likely to play roles in determining the physical properties, however this has not been proven. The fundamental cage size and higher length scale association of the cages produce a structural hierarchy that greatly influences physical properties. For example, in the POSS-norbornyl system, changing the compatibilizing R group from cyclopentyl to cyclohexyl results in a 30% higher glass transition temperature (T_g), which was shown by transmission electron microscopy to likely result from POSS entrainment of the polymer network [60]. Modification of the R groups surrounding the POSS cage also affects POSS compatibility in polymer blends as demonstrated by Blanski et al. [63]. Figure 1-7 shows scanning electron micrographs of dissimilar POSS cages blended into 2 million M_w polystyrene illustrating this point.

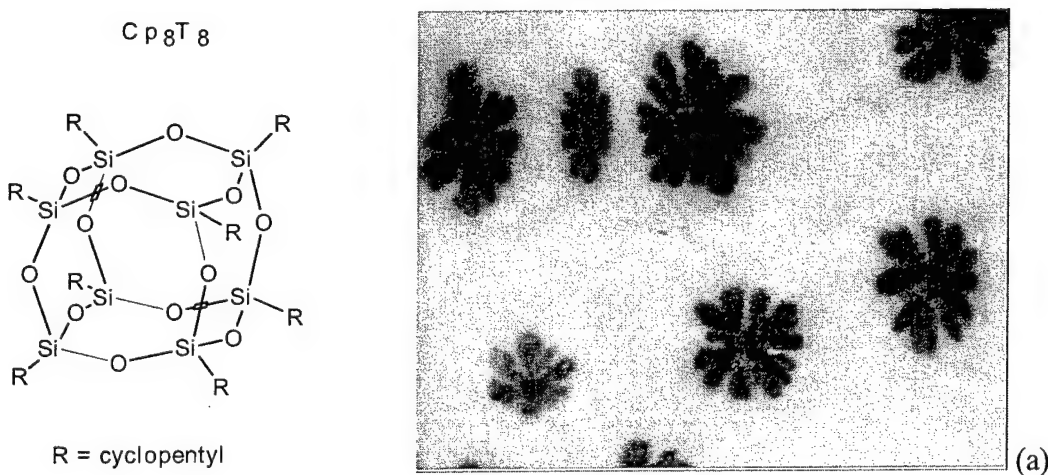
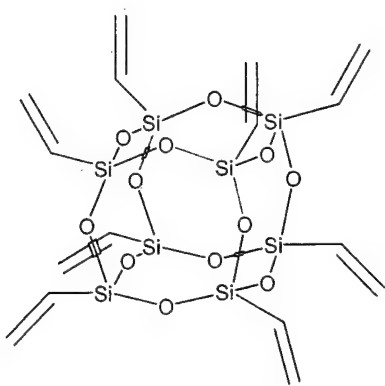
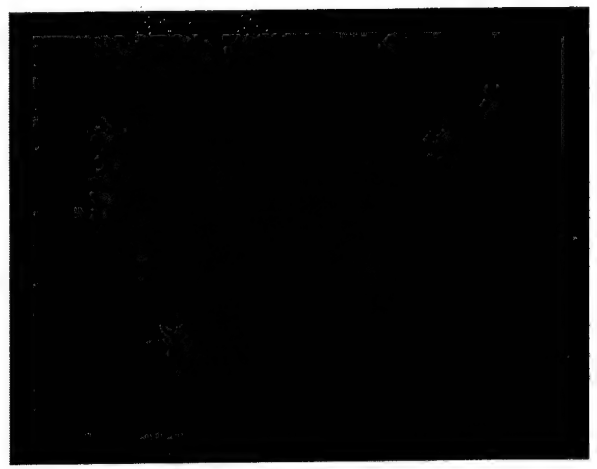
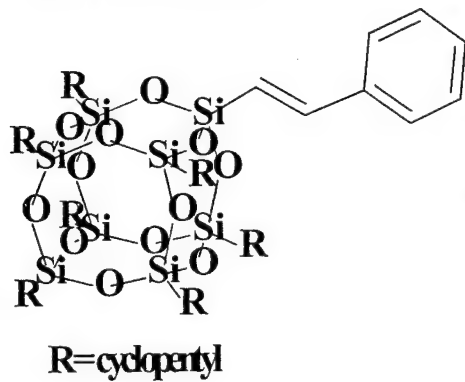


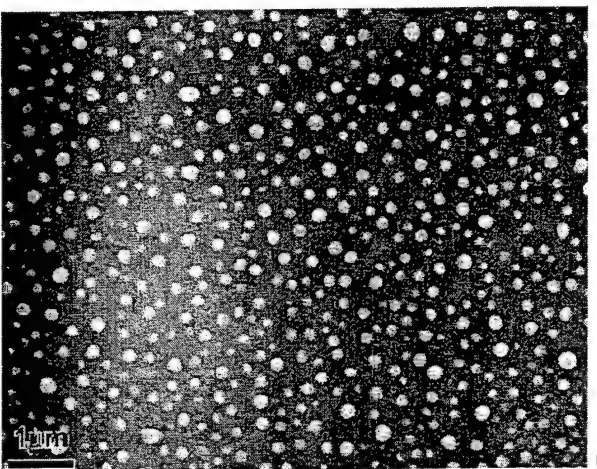
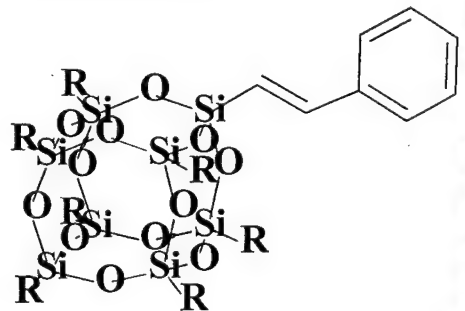
Figure 1-7. POSS compatibility in 2 million M_w polystyrene: (a) 50 wt% Cp_8T_8 reveals formation of immiscible POSS crystallites (20-50k atoms), (b) 50 wt% Vi_8T_8 also immiscible, (c) 50 wt% $\text{Cp}_7\text{T}_8\text{Styryl}$, significant decrease in size of crystallites evident, (d) 50 wt % $\text{Styrenyl}_8\text{T}_8$, partial miscibility, and (e) 50 wt % $\text{Phenethyl}_8\text{T}_8$, obtained through catalytic hydrogenation of $\text{Styrenyl}_8\text{T}_8$ shows complete miscibility; reprinted from reference [63] permission by Dr. Rusty Blanski.

V i₈T₈

(b)

Cp₇T₈Styrenyl

(c)

Styrenyl₈T₈

(d)

Figure 1-7. Continued

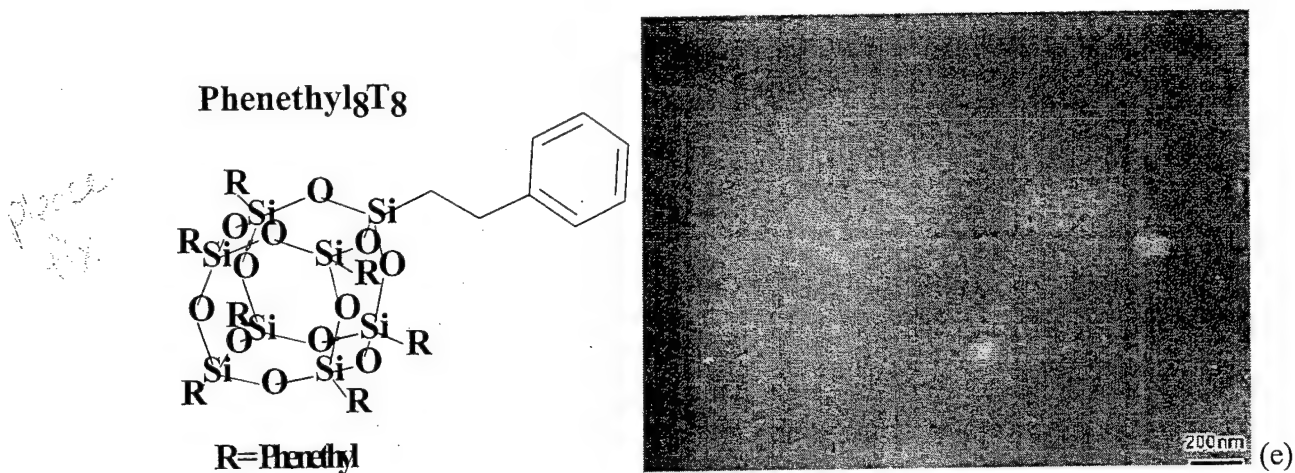


Figure 1-7. Continued

Recent flammability studies and rocket motor insulation testing conducted at AFRL/PRSM, as well as preliminary atomic oxygen results have shown that upon degradation, the hybrid organic/inorganic nanocomposites form a passivating ceramic-like layer. In addition, the property improvements obtained by POSS addition, such as increased oxidation resistance and elevated T_g , suggest their effectiveness for space applications including protective coatings, paints, thermal control components and space inflatables. This dissertation presents several studies wherein a variety of POSS-containing polymers were synthesized and subsequently characterized in an UHV system capable of performing over twenty different spectroscopic analysis techniques such as XPS, AES, ISS and others. The details of this UHV system are described next.

1.4 Overview of UHV System and X-ray Photoelectron Spectroscopy

The Hoflund research group at the University of Florida has the ability of simulating LEO using a UHV system that is capable of performing close to twenty different spectroscopic analysis techniques. This system, shown in Figure 1-8, is comprised of 5 chambers that are joined together in series, one of which contains a

unique hyperthermal oxygen atom source described in Chapter 2. The system also contains a quadrupole mass spectrometer and is currently being modified to accommodate an in-situ, Fourier Transfer Infrared spectrometer. In addition, lamps are also being installed in order to carry out AO erosion studies with and without the presence of VUV and UV light. One lamp will be a deuterium lamp with a magnesium fluoride window. This system provides radiation between 118 and 200 nm. The other lamp will be a mercury-xenon short arc lamp with a quartz window to provide UV radiation between 200 and 400 nm.

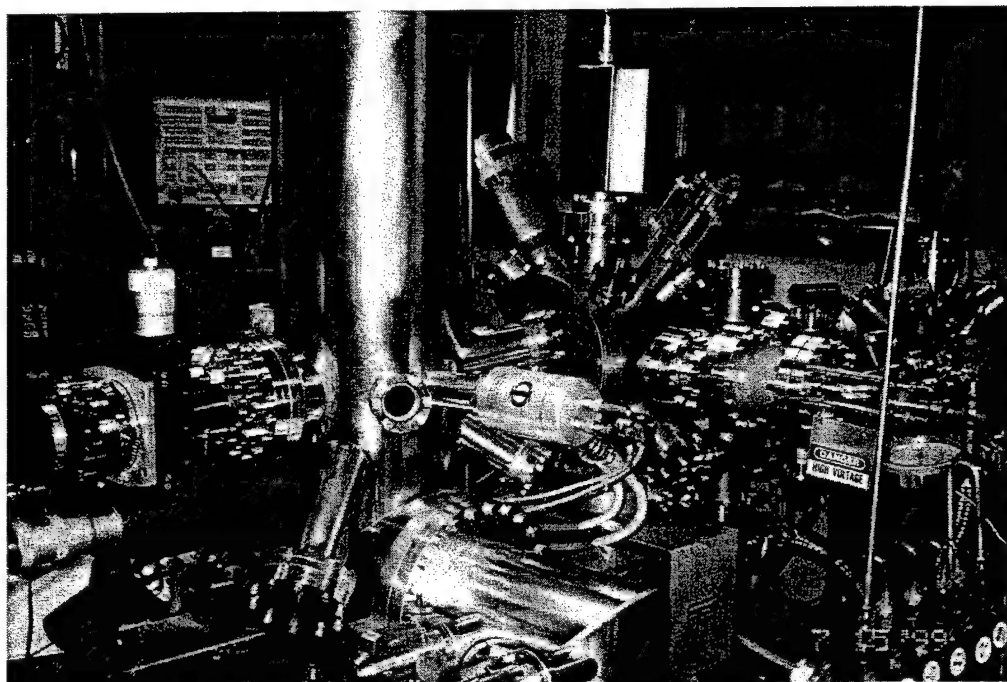


Figure 1-8. Photograph of UHV system at the University of Florida used to conduct Low Earth Orbit simulation and characterization studies.

The main analysis chamber has a base pressure of $<10^{-10}$ Torr and contains the x-ray source, and the ion and electron guns used in the different spectroscopic methods. It also houses a charged particle energy analyzer called a double-pass cylindrical mirror analyzer (DPCMA). Characterization of the POSS-polymers presented in this

dissertation were obtained using a unique surface sensitive technique for chemical analysis known as XPS and briefly described below.

1.5 X-ray Photoelectron Spectroscopy

X-ray photoelectron spectroscopy (XPS), also known as electron spectroscopy for chemical analysis (ESCA), is a photoemission technique, developed by Siegbahn and coworkers [64, 65], which is widely used to examine the composition and chemical state distribution of species at a solid surface. It is performed by irradiating a solid surface with monochromatic X-rays (Mg K α 1253.6 eV) under vacuum and measuring the kinetic energy distribution of the emitted electrons. An electrostatic charged particle energy analyzer is used to obtain the spectral peaks generated from the kinetic energies of the emitted electrons. The corresponding binding energies specific to each individual element are then calculated from the following equation:

$$E_b = h\nu - E_k + \Delta\phi \quad (1-1)$$

where E_b is the electron binding energy (BE) in the solid, E_k is the kinetic energy of the emitted electron and $\Delta\phi$ is the work function difference between the sample and the detector material assuming there is no electrical charging at the sample surface. Because each element has a unique set of binding energies, XPS can be used to provide a semi-quantitative analysis of the elements residing in the near surface region of the sample [66, 67]. Compositions are calculated from the relative areas of the spectral peaks with the assumption that elements are distributed homogeneously in the near surface region.

Figure 1-9 shows a diagram illustrating the photoemission process occurring during XPS. In this process, an incident x-ray photon causes the ejection of a

photoelectron from a core orbital. In addition to these photoelectrons, Auger electrons are also emitted approximately 10^{-14} seconds after the photoelectric event [67]. These electrons are emitted because of the relaxation of the excited ions remaining after photoemission. The competing emission of a fluorescent x-ray photon is negligible in this energy range.

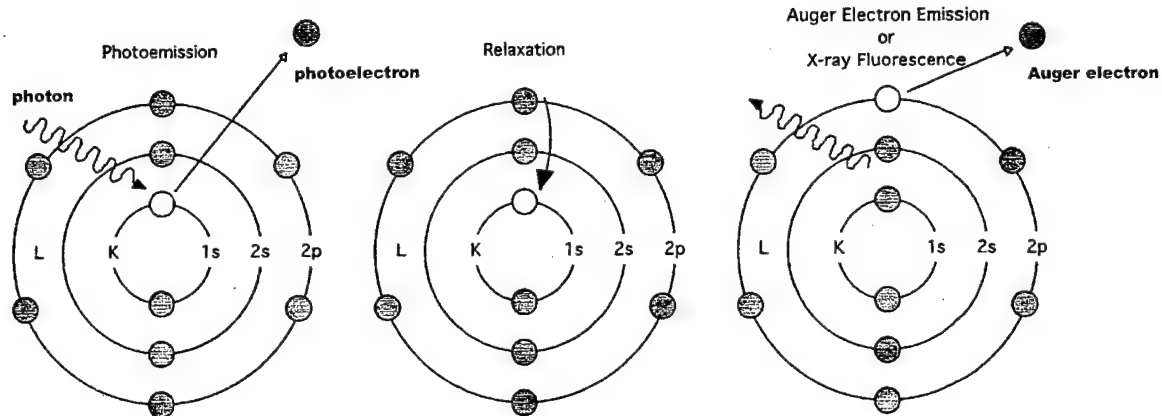
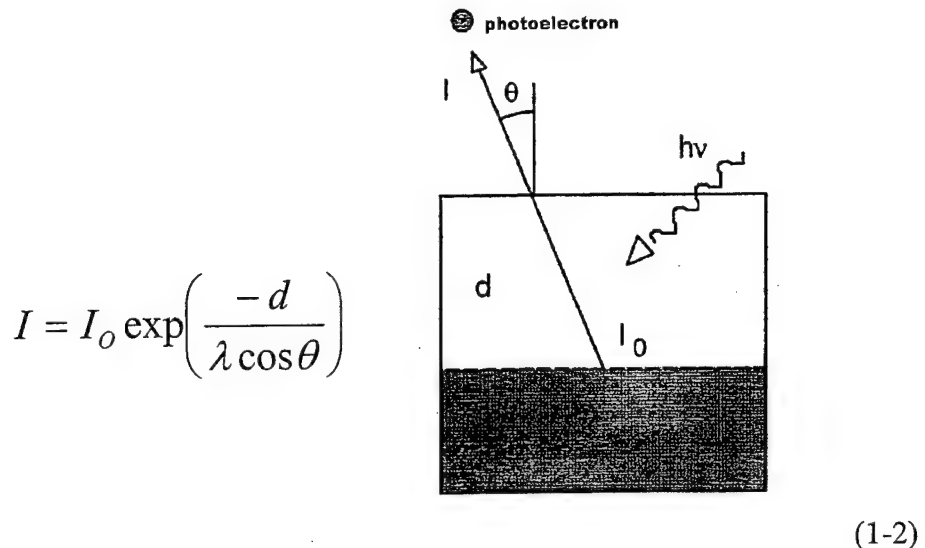


Figure 1-9. Illustration of the photoemission process occurring during XPS.

1.5.1 Sampling depth of Photoelectron

Although the mean free path or penetration depth of photons irradiating a sample during the XPS process is on the order of microns, the slow photoelectrons being emitted during XPS have a higher probability of interacting and scattering inelastically with matter resulting in a mean free path in the order of angstroms [66-68]. This distance that the electrons travel in the solid, depends on their initial kinetic energy and to a much lesser extent the material. Only electrons near the surface can, on average escape without incurring energy loss. The electrons that do suffer inelastic losses before escaping the surface, form the characteristic stepped background of the obtained spectra. The sampling depth of photoelectrons during XPS is expressed by the following equation:



(1-2)

where d is the sample depth, I is the intensity of the emitted photoelectrons which escape from the surface, I_0 is the intensity of the photoelectrons at depth d , λ is the wavelength of the incident x-rays and θ is the take off angle.

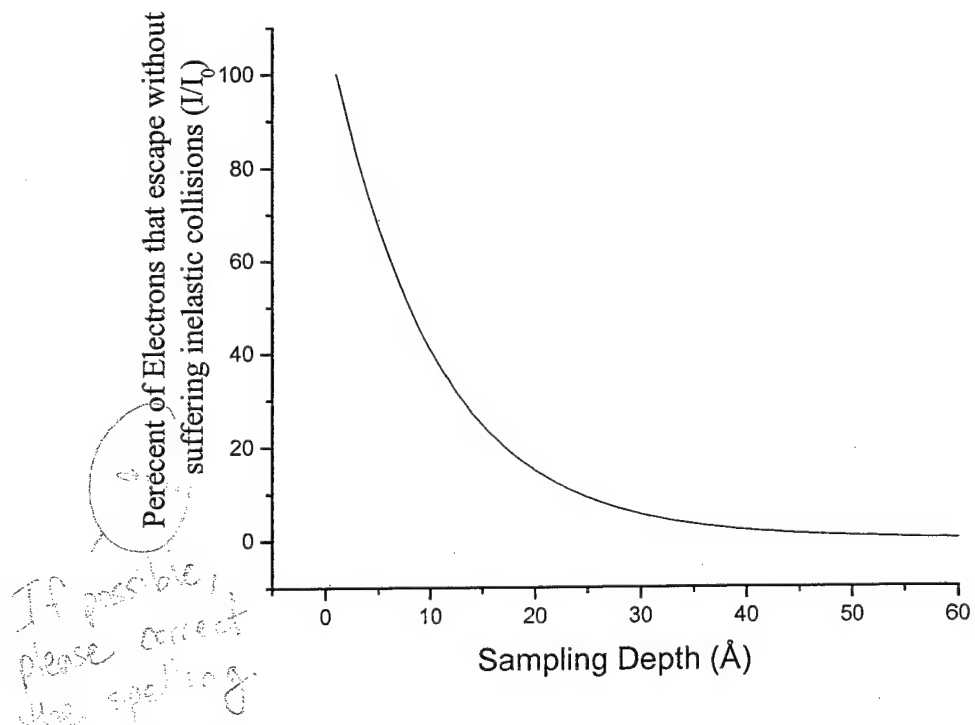


Figure 1-10. Percent of photoemitted electrons that escape without suffering inelastic collisions versus sampling depth during XPS.

Figure 1-10 shows a plot of the percent of electrons that escape without suffering inelastic collisions versus sampling depth during XPS using equation 1-2, assuming a normal takeoff angle ($\cos \theta = 1$) and incident irradiation by Mg K α X-rays (1253.6 eV) with a corresponding $\lambda = 0.9888$ nm. As illustrated by this graph, the sampling depth is about ~4-6 nm (30 atomic layers), and about 10% of the signal originates from the outermost atomic layer. The small escape depth of the emitted photoelectrons makes XPS a highly surface-sensitive technique which yields a weighted average composition placing emphasis on the atomic layers near the surface due to the lower probability of inelastic scattering.

1.5.2 Electron Energy Analyzer

The energy distribution of the emitted photoelectrons during XPS are detected by a charged particle electrostatic analyzer called a double pass cylindrical mirror analyzer (DPCMA) shown schematically in Figure 1-11 and first described by Palmberg [69, 70].

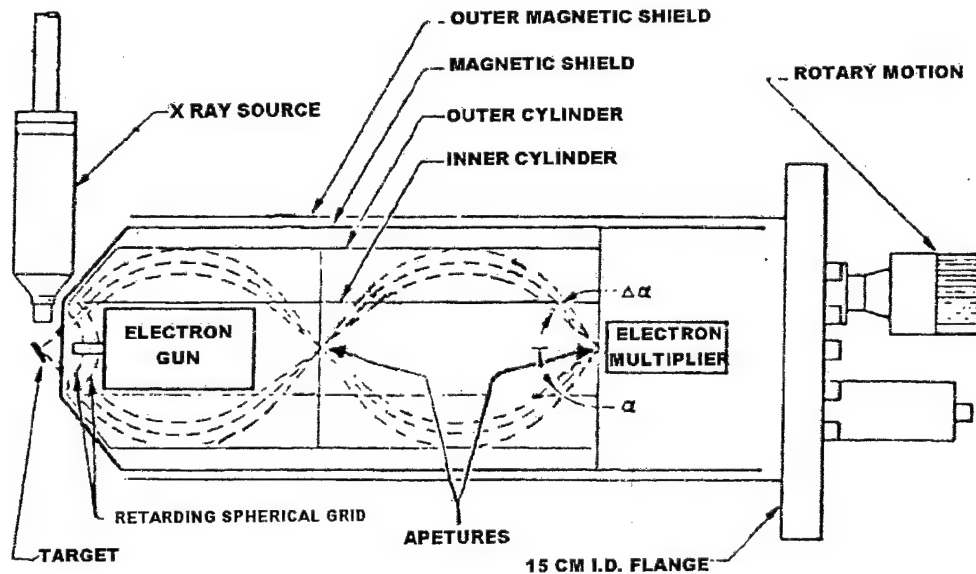


Figure 1-11. Schematic diagram of the double pass cylindrical mirror analyzer used to measure the energy distribution of photoemitted electrons in the UHV system during XPS; reprinted from reference [70] with permission from the American Institute of Physics.

The analyzer is operated as an energy window, referred to as the pass energy, accepting only those electrons having an energy within the range of this window.

The DPCMA consists of two concentric cylindrical electrodes that create an electric field with cylindrical symmetry. The outer cylinder is held at a negative potential with respect to the inner cylinder. Electrons entering the analyzer through the annular entrance are retarded and deflected towards the inner cylinder by an amount depending on their initial kinetic energy. The voltage difference between the inner and outer cylinder is held constant thereby creating a constant pass energy and resolution over the voltage scanned [71]. This is referred to as scanning in the retarding mode. Scanning for different energies is accomplished by varying the electrostatic field before the analyzer. This is accomplished by using spherically shaped preretarding grids which decelerate the incoming electrons thus allowing for increased resolution at higher electron energies [72].

The photoemitted electrons of kinetic energy within the range being accepted by the analyzer strike a spiraltron or channeltron detector which amplifies the electron signal by a factor of 10^8 or 10^9 [66]. Data collection is then accomplished using a computer interfaced, digital pulse-counting circuit [73] followed by smoothing with digital-filtering techniques [74].

CHAPTER 2
DESCRIPTION OF THE ELECTRON STIMULATED DESORPTION ATOMIC
OXYGEN SOURCE

2.1 Introduction

As discussed in Chapter 1, high energy (~ 5 eV) collisions between oxygen atoms and LEO spacecraft cause severe degradation of spacecraft materials. This has provided the motivation to investigate AO induced material degradation mechanisms and the development of materials that are more resistant to AO corrosion. In order to study spacecraft material degradation, our research group has developed over the last 15 years an instrument which produces a high-purity, intense flux of hyperthermal oxygen atoms. The investigations leading to the development, characterization and performance of the AO source have been described previously [75-81]. This AO source is UHV compatible, simple to operate and compact. In addition, this source has been used to conduct studies in other fields and applications. These include the formation of thin insulating oxide and passivating layers on semiconducting materials in molecular beam epitaxy systems, studies of chemically induced alterations on GaAs, InP, Ni/Cr, Ag, Al_2O_3 , and SnO_x surfaces, formation of superconducting oxides, formation of novel oxide compounds, and surface cleaning and modification coupled with surface analytical techniques [82-88]. This chapter reviews the performance characteristics and latest changes to the evolving design of this atomic oxygen source used to expose polyhedral oligomeric silsesquioxane containing polymers discussed in subsequent chapters of this dissertation. This chapter

also briefly describes the operational concept behind a pulsed CO₂ laser excitation AO source used to conduct erosion studies presented in Chapter 5.

2.2 ESD Atomic Oxygen Source Design and Recent Improvements

A schematic diagram illustrating the operational principles of the AO source is shown in Figure 2-1. Figure 2-2 and 2-3 show photographs of the atom source removed from the UHV system and in the UHV system while exposing a sample. Ultrahigh-purity molecular oxygen dissociatively adsorbs on the high-pressure (2 Torr) side of a thin metallic Ag membrane maintained at elevated temperature (340-370°C) and permeates through the membrane to the UHV side. There a continuous flux of neutral oxygen atoms is produced through the electron stimulated desorption (ESD) of the chemisorbed oxygen atoms as they are struck by a directed flux of primary electrons being emitted from a filament.

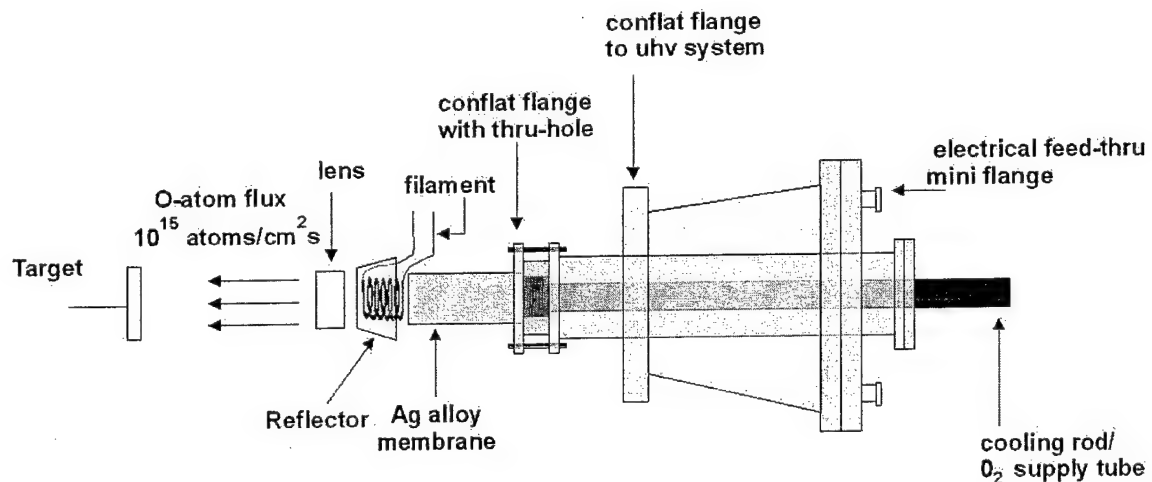


Figure 2-1. A schematic diagram of the atomic oxygen source.

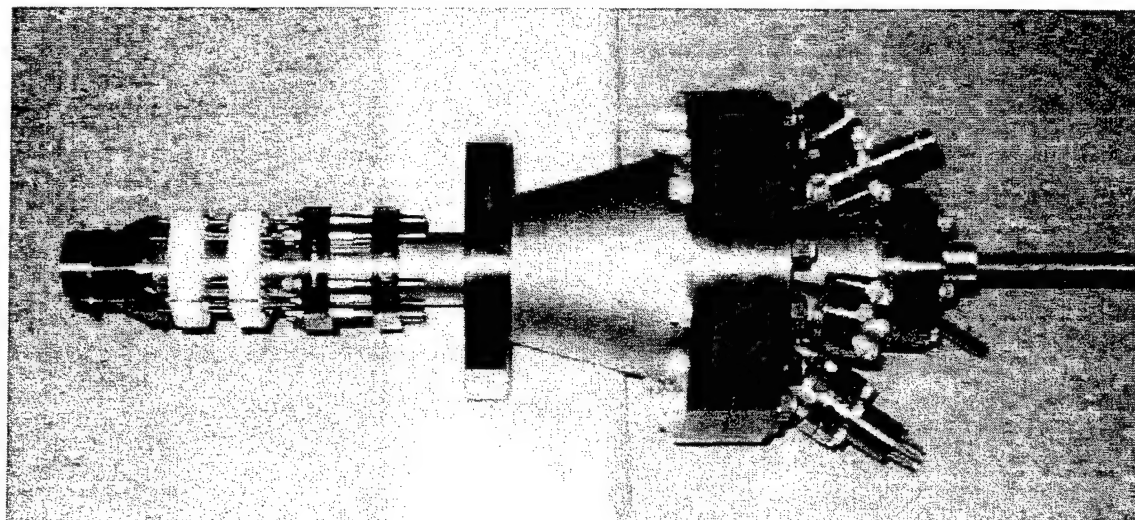


Figure 2-2. The atomic oxygen source.

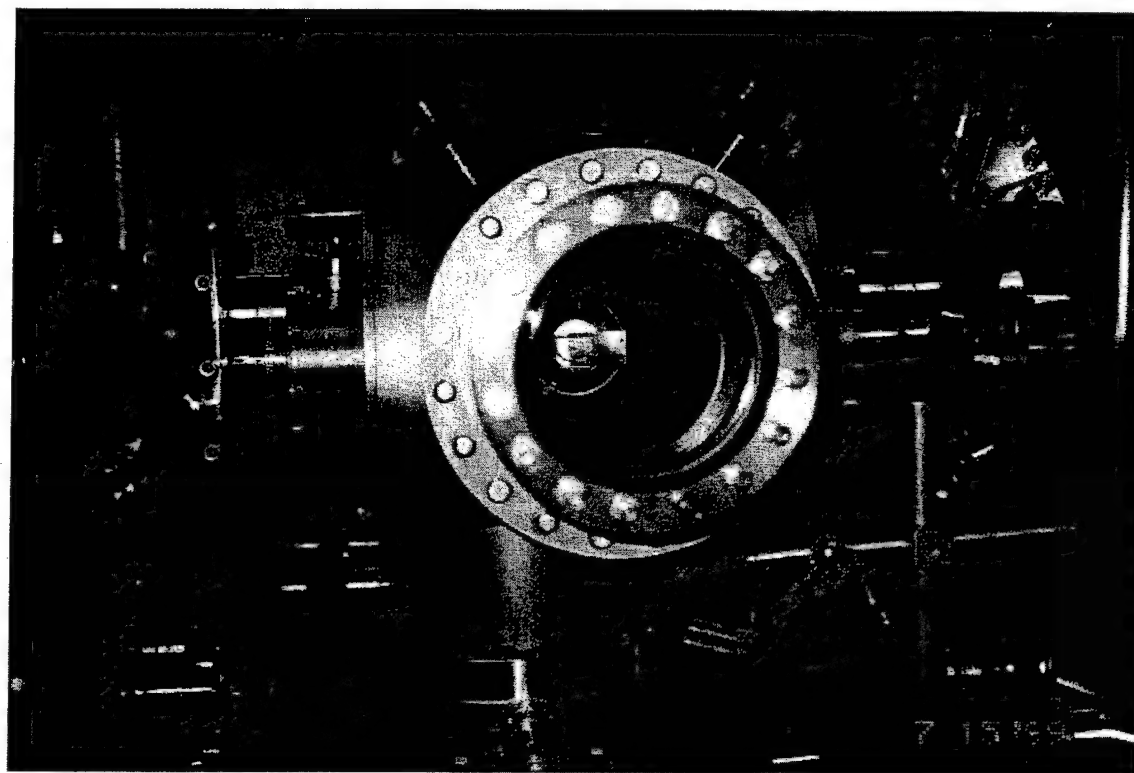


Figure 2-3. Photograph of a sample being exposed to AO source in the reaction chamber.

The primary electrons are produced by thermionic emission from a coiled hot filament support around the perimeter of the Ag alloy membrane. In addition to

providing the 1000 eV primary electron beam flux for ESD, this filament also provides the power input to the source as the accelerated electrons strike the membrane thus increasing its operating temperature. The power input is equal to the primary beam current multiplied by the voltage. The thoriated-tungsten filament in the latest prototype atom source is longer than in previous designs, permitting it to operate at lower temperatures. Previously the filament was shorter and at high power outputs the thorium would sublimate off the filament contaminating samples and increasing the work function. As a result more power would have to be supplied to maintain a level flux. In the new design, the filament is also easier to replace and is permanently fixed in the right position. Before it was free hanging and would change position as temperatures changed resulting in less than optimal performance. It is necessary to design the membrane support assembly to maximize heat transfer away from the membrane so that the filament emission current can be set between 30 and 60 mA. If the membrane temperature is too high then molecular desorption can occur as membrane material can be evaporated.

An electron reflector (lens assembly) surrounds the filament as shown in Figure 2-4. It produces a potential field which creates a uniform flux of electrons over the membrane surface. This is accomplished by establishing a higher negative potential on the reflector which in turn redirects the trajectories of the accelerated electrons from the filament back towards the membrane. The latest prototype atom source contains an improved reflector design which allows for more uniform coverage of the membrane by these electrons thus preventing the formation of hot spots. Another lens is placed between the reflector and the sample for removal of all charged particles including secondary electrons and O^+ and O^- ions produced during the ESD process. The ion

production rate has been shown to be negligible compared to the atom production rate [80]. Furthermore, no molecular oxygen is produced by this source [76, 80, 81]. When high-energy electrons strike a metal surface, a small amount of Bremstrahlung or "braking" radiation is produced which has a broad energy distribution [89]. This radiation is produced when electrons are decelerated as they approach the nucleus of a metal target. This radiation cannot be removed but poses no problem in these studies because photons of these energies do not interact strongly with solids. The sum of the energies of the Bremstrahlung photons produced is less than that of the original incident electron.

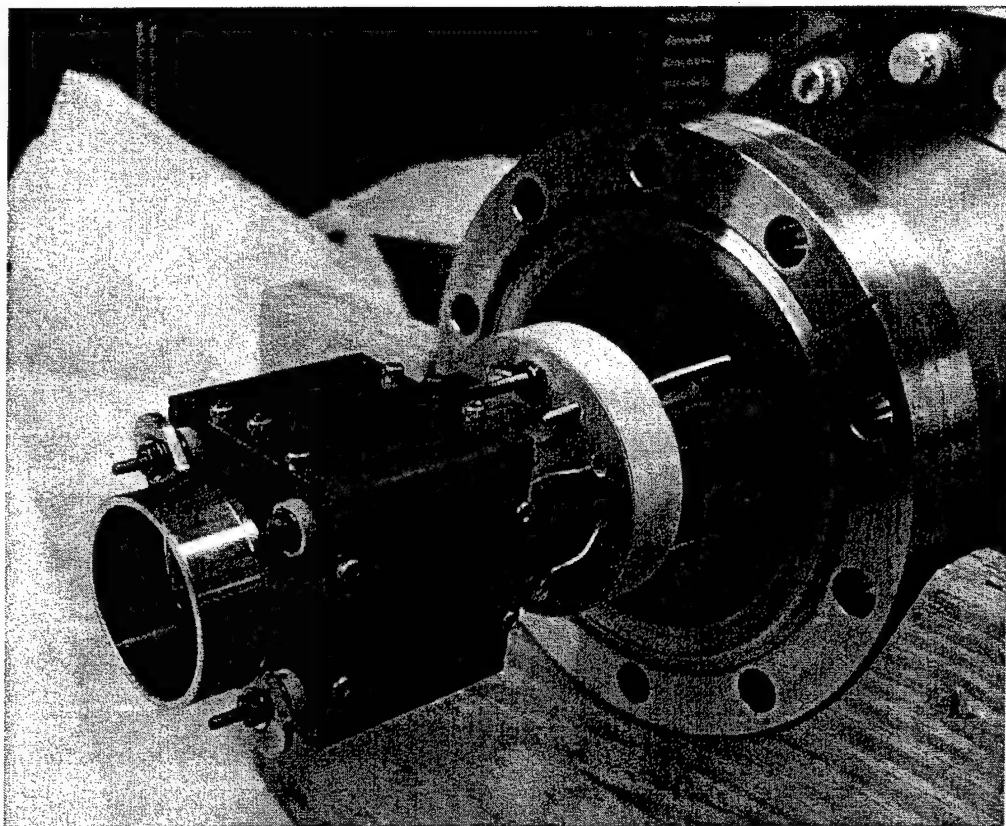


Figure 2-4. Improved reflector/lens assembly on latest prototype ESD AO source.

2.2.1 Adsorption and Permeation

Several processes have to function in series at sufficiently high rates for this system to work, including dissociative adsorption of the molecular gas on the metal surface, permeation of atomic oxygen through the membrane and formation of the neutral flux by ESD. Since these processes occur in series, the slowest one (desorption) will determine the magnitude of the AO flux. Adsorption is the first step in this process. Since the sticking coefficient of O₂ on polycrystalline Ag is fairly small ($s \sim 3 \times 10^{-3}$) [90]. For this reason, it is important to maximize the pressure on the upstream side of the membrane.

Permeation is the second step and the permeation rate through the membrane is proportional to the reciprocal of the membrane thickness. It is therefore desirable to have a high pressure and a thin membrane, but this can lead to membrane failure. This problem has been solved by designing a reinforced membrane assembly as shown in Figure 2-5. Previously the membrane consisted of a silver disk brazed to a copper cylinder which in turn was brazed to the stainless steel body of the AO source. These brazes have been eliminated and the new membrane is made of solid high purity Ag sealed through knife-edge conflat flanges. This new configuration allows for easy replacement of the membrane if needed.

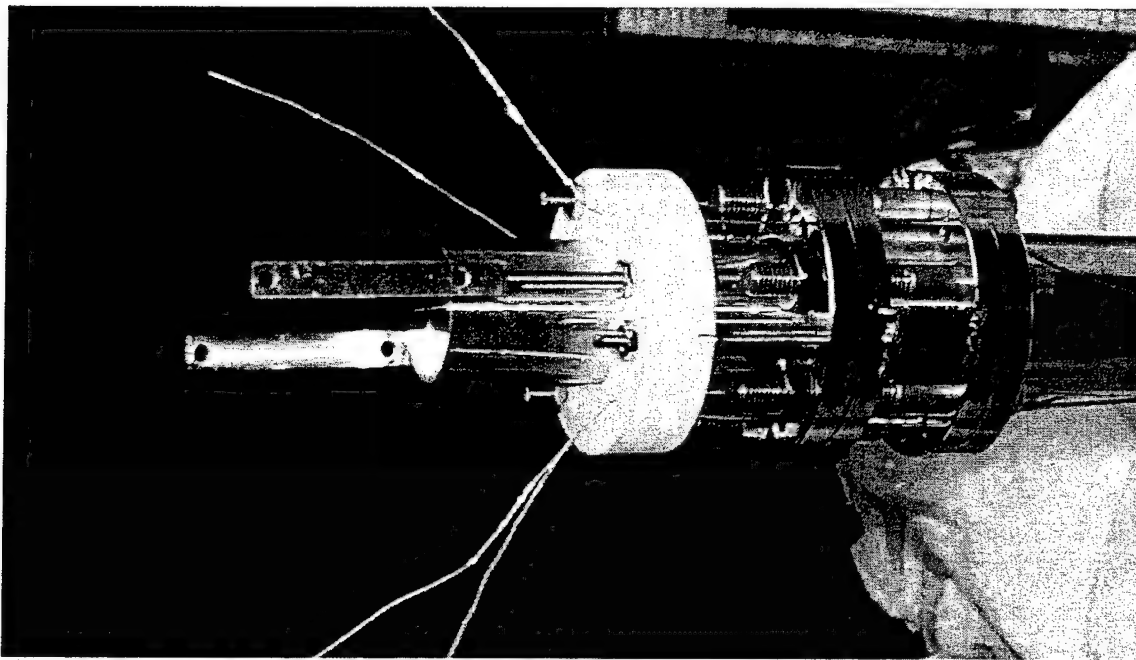


Figure 2-5. Reinforced membrane assembly on latest prototype ESD AO source.

The permeability of the membrane is also a product of solubility and diffusivity, and varies exponentially with temperature. Outlaw et al. have studied the diffusivity of oxygen in silver for a wide temperature range of 400-800 °C [79] [77]. Their data shows that there are substantial deviations from ordinary diffusion-controlled transport. They represented their diffusion data by a piecewise application of the Arrhenius equation,

$$D(T) = A_i \exp(-E_i / k_B T) \quad i = 1, 2, \quad (2-1)$$

where A_i is the amplitude, E_i the local activation energy, k_B is the Boltzmann's constant, and $i = 1$ refers to the range 400 to 630 °C, while $i = 2$ refers to the range 630-800 °C. They reported $A_1 = 2.9 \times 10^{-3} \text{ cm}^2 \text{ s}^{-1}$, $E_1 = 479 \text{ meV}$, $A_2 = 3.2 \times 10^{-2} \text{ cm}^2 \text{ s}^{-1}$, and $E_2 = 665 \text{ meV}$. They suggested that below 630 °C, the activation energy is higher and is attributed to trapping of the atomic oxygen and/or kinetic barriers at the surface and

subsurface of the vacuum interface. Below 400 °C, the evaporation rate of Ag is negligible.

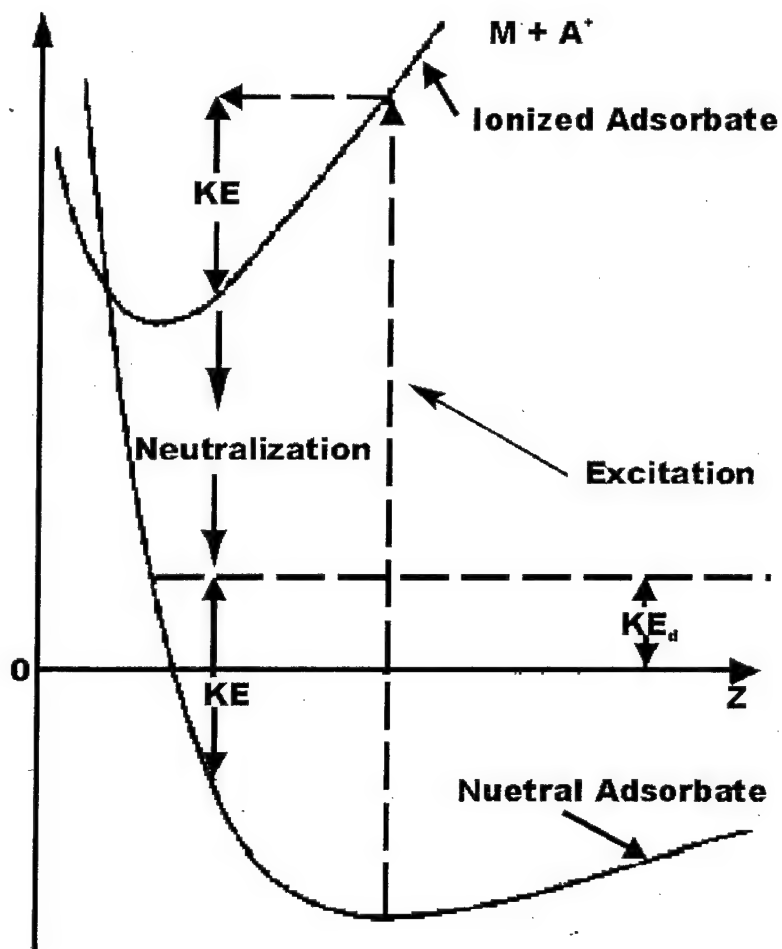


Figure 2-6. Potential energy diagram showing the processes involved in the electron-stimulated desorption of an adsorbed species as a neutral species with excess kinetic energy, according to the MGR model.

2.2.2 Electron Stimulated Desorption

Electron stimulated desorption is a complex process in which particles are emitted from a surface through decay of a localized electronic excitation created by an incident electron. One of the earliest models explaining ESD of ions and neutral species from surfaces was put forward by Menzel, Gomer and Redhead (MGR) in 1964 [91-95]. The mechanism for the MGR model on neutral desorption is shown in Figure 2-6. It

describes the potential energy of an adsorbed species (A) on a surface (M), with the horizontal axis representing the distance between the particle and the surface.

The generation of ground state neutrals through ESD is considered to be a two step process [96]. The first is the excitation of the neutral, adsorbed species on the surface by an incident electron, resulting in the removal of an electron from one of its stable energy levels and in the formation of a positive ion. Direct momentum transfer from the incident electron to the adsorbed atom has been shown to be negligible. The positive ion formed has a smaller radius than the atom (oxygen atom radius is 0.66 Å and the O⁺ radius is 0.22 Å) [97] and a newer equilibrium potential causing it to move closer to surface. In the second step, the ion is neutralized as it moves closer to the surface by means of electron tunneling or from an Auger electron from the substrate [96], thus returning it to the ground state potential energy curve with excess kinetic energy. If this excess kinetic energy is greater than the binding energy, then the neutral atom is released into the gas phase.

Desorption is the rate limiting step and is governed by the number of electrons hitting the membrane per cm²-s. Hoflund reviewed ESD phenomena [98] and stated that the intensity of the desorbing particle flux can be expressed as,

$$\frac{I}{A\varepsilon} = \frac{I_p}{A\varepsilon} Q(N) \quad (2-2)$$

where I_p is the primary electron emission current to the membrane, A is the irradiated area of the membrane, ε is the charge on an electron, Q is the ESD cross section and (N) is the surface concentration of adsorbed neutrals. In order to maximize the ESD flux, it is necessary to maximize both I_p and (N) by optimizing the source operating parameters. The flux has been shown to be linearly dependent on the primary emission current as

shown in Figure 2-7. Increasing the primary electron emission current to the membrane can increase the ESD rate, but this increases the power ($P=IV$) to the membrane, which in turn increases the temperature of the membrane and can result in evaporation of Ag which is unacceptable. This problem has been minimized by designing the membrane to have the optimal heat transfer characteristics. As seen in Figure 2-1 and 2-2, this was accomplished by designing the membrane to accept a threaded copper rod, which supplies the high purity oxygen while simultaneously removing heat away from the membrane. The membrane is also equipped with a closed loop circulatory temperature control unit.

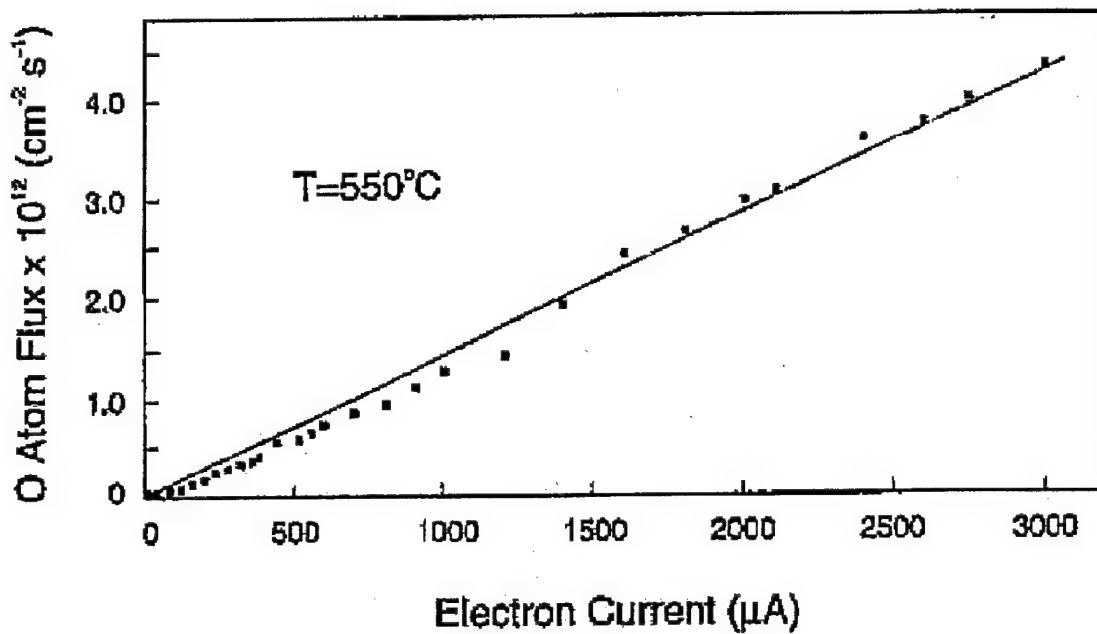


Figure 2-7. O neutral flux as a function of primary electron emission current at a membrane temperature of 550 °C [76].

2.2.3 Energy Distribution and Neutral Atom Detection

The O atoms produced by this source have been shown to be hyperthermal (energies greater than 0.01 or 0.02 eV), but their energy distribution has not been

measured. Corallo et al. [99] have measured the energy distribution of O ions emitted by ESD from a Ag (110) surface and found that this distribution had a maximum of ~ 5 eV and a full-width at half maximum of 3.6 eV. This ion energy distribution would set an upper bound for the neutral energy distribution because ESD neutrals are generally believed to be less energetic than ESD ions. This point has been discussed often in the ESD literature but not actually demonstrated.

Since neutral ESD species are difficult to detect very few ESD studies of neutral species have appeared in the literature. Our research group has detected the neutral atom flux by using a quadrupole mass spectrometer [80, 100] in the appearance potential (AP) mode to allow the atoms to be distinguished from residual gases and background gas products formed by collisions of the neutrals with the walls of the UHV system. In addition, in this configuration, the ion acceleration potential was set at 0.0 V. Since calibration studies demonstrated that the ions entering the quadrupole section had to have a minimum kinetic energy of 2.0 eV to reach the detector, the ESD neutrals have a minimum energy of 2 eV. Therefore, the hyperthermal AO produced by this ESD source have energies greater than 2 eV but possibly less than the ion energy distribution. In addition, these mass spectrometric experiments have shown that the O atom-to-O⁺ ratio is about 10⁸ and that the O⁺-to-O⁻ ratio is about 100. Figure 2-8 shows the atomic oxygen signal from the quadrupole mass spectrometer using this method.

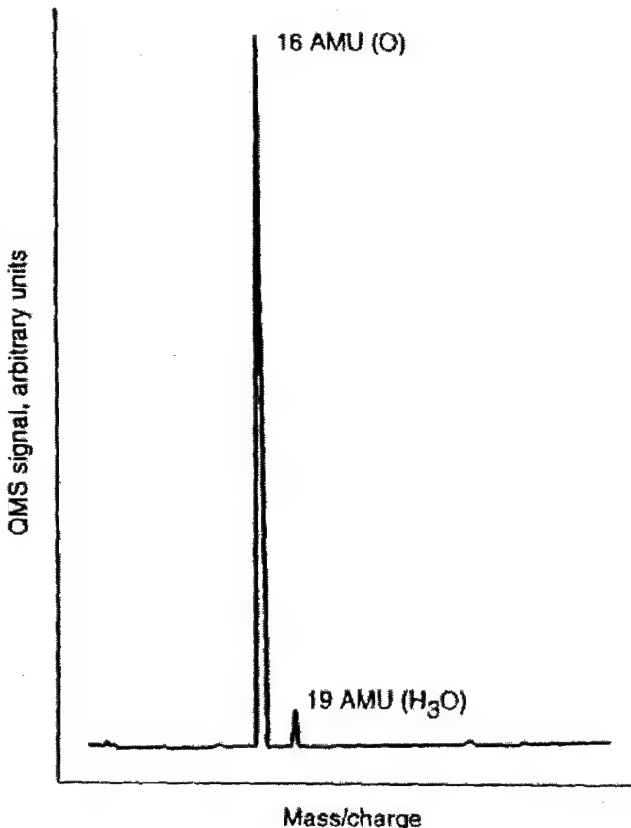


Figure 2-8. Atomic oxygen signal detected by a quadrupole mass spectrometer taken in the appearance potential mode [76].

2.2.4 Flux quantification

Several approaches have been used to measure the magnitude of the hyperthermal AO flux and reasonable agreement was obtained between the various methods. The flux from the ESD source is approximately 2×10^{15} atoms/cm²· s. One of the most reliable methods is the measurement of an oxide film growth rate. This source has been used to epitaxially grow stoichiometric ZrO₂ thin films knowing the Zr flux and the fact that no O₂ is present in the AO flux. Based on the fact that stoichiometric ZrO₂ was formed, we were able to calculate the AO flux for the maximum Zr flux [101]. In addition, it was also shown that when the AO flux was reduced by a factor of 2, stoichiometric ZrO was grown [88]. The AO flux has also been measured by measuring the chemisorption rate of

AO on polycrystalline Au using ion scattering spectroscopy [81]. The maximum flux determined using this method is in excellent agreement with that determined using the oxide growth rate method.

2.3 Comparison of AO Sources Used to Simulate LEO

Since space experiments are costly and require a large effort, a variety of ground simulation techniques have been used to model AO erosion in space. Unfortunately, the AO sources used have had significant drawbacks resulting in both artifacts and inconsistencies in the ground-simulated data [28, 102]. A brief comparison of different sources used to produce atomic oxygen is presented here.

2.3.1 Oxygen Radio Frequency and Microwave Plasma Sources

Oxygen (RF) plasma sources [18, 19, 103, 104] provide a large mixture of thermal species including O , O_2 , O^+ and O_2^+ , as well as UV light. The ambient pressure is high and can contain significant amounts of carbon-containing contaminants. In addition, it was found that these sources produce positive ions with an average energy of 278 eV and electrons with an average energy of 8 eV [104]. Extraction of a downstream flux can eliminate most of the ionic species and the UV radiation, but the pressure is high, contaminating species are contained in the flux and the AO energy is low. All of these problems result in alteration of the highly reactive surfaces produced by AO exposure. Furthermore, high energy species results in surface sputterings and bond breakage. The resulting reactive surface species react further with other surface species or AO. Therefore, the actual process of degradation of spacecraft materials by 5 eV AO cannot be simulated using low-energy AO.

A microwave power source used to generate AO have also been developed [22, 105]. This source generates a microwave plasma in a space between a nozzle and a skimmer to excite a processing O₂-He gas. This source operates at high temperatures, and has low degrees of O₂ dissociation while generating UV light.

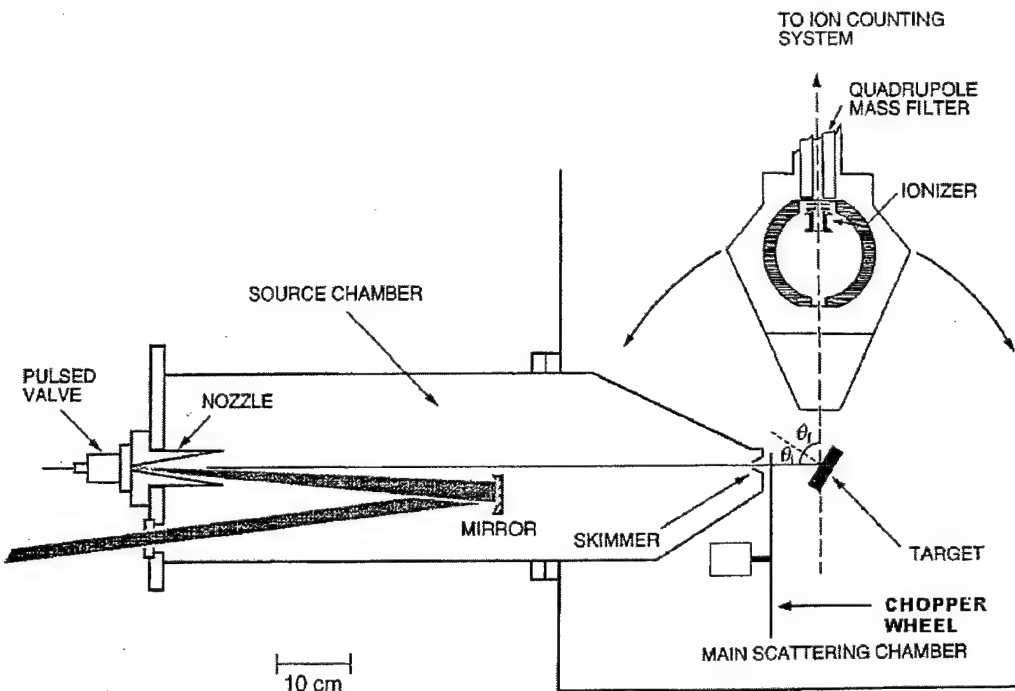


Figure 2-9. Schematic diagram illustrating the operational concept of this pulsed CO₂ laser AO source; reprinted from reference [106] with permission from the American Institute of Physics.

2.3.2 Pulsed Laser Excitation Sources

Another type of system is based on the hypersonic expansion of O₂ (with or without a carrier gas) excited by a laser pulse. These systems have been well characterized and have been shown to provide 2-15 eV AO at high fluxes of 10¹⁶ atoms cm⁻² sec⁻¹, but like other sources they have some drawbacks which introduce artifacts into space-polymer studies. The major drawbacks include the presence of a high flux of UV light, the presence of a large amount of O₂, and the unsteady state nature of these sources.

The UV light has been shown to erode some polymers both by itself and synergistically with AO. This UV light is not present at this energy and flux in space and it precludes understanding the effects of only AO on polymer surfaces. The O₂ can react with the highly reactive surfaces formed by AO exposure, and the unsteady-state AO flux induced by the laser operation is not encountered in space and may result in quite different erosion characteristics.

A source of this design has been used in a collaboration with Prof. Tim Minton at Montana State University to conduct erosion studies on some of the POSS polymers presented in Chapter 5 of this dissertation. Figure 2-9 shows a schematic diagram illustrating the operational concept of this pulsed laser source [106]. Within a vacuum chamber, molecular oxygen flows into a conical nozzle at several atmospheres pressure through a pulsed valve. A laser induced breakdown is then generated at the nozzle throat by a pulsed CO₂ laser focused to an intensity greater than 10⁹ W/cm². The resulting plasma is then heated to 20,000 K. This high-temperature, high-density plasma expands rapidly into the diverging cone following the detonation and engulfs the remaining cold gas. The local densities in the nozzle are sufficient to permit efficient electron-ion recombination. By the time atoms or radicals formed in the beam have cooled enough to recombine, the termolecular collision rate has dropped so low that these reactive species are, in effect, frozen in the emerging beam. The resultant beam from the nozzle consists predominantly of fast neutrals, with a very small ionic fraction (<10⁴). Average kinetic energies of the fast species in the beam can range from 2 to 15 eV. A chopper wheel is used to narrow the distribution of the emitted species. Figure 2-10 and 2-11 show the energy distribution of the overall and chopped beam produced by this source.

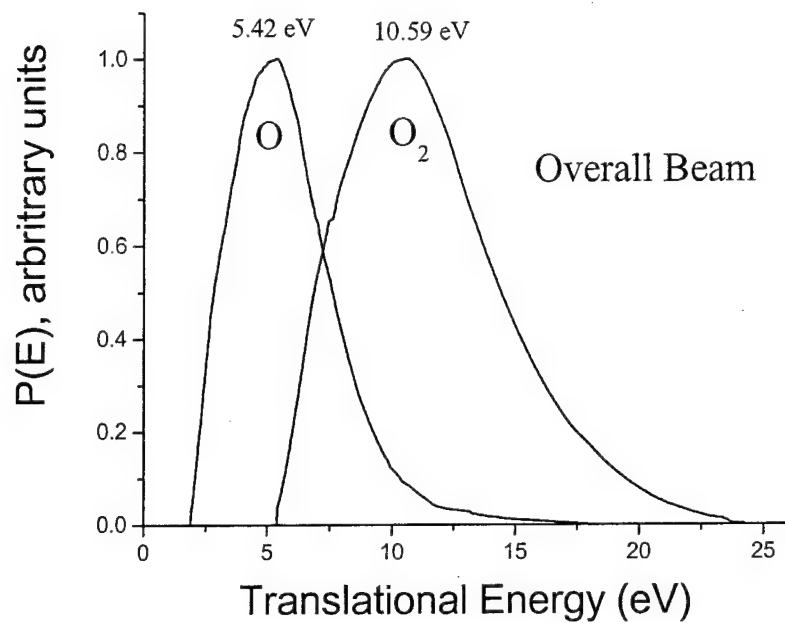


Figure 2-10. Energy distribution of overall beam produced by the pulsed CO₂ laser AO source

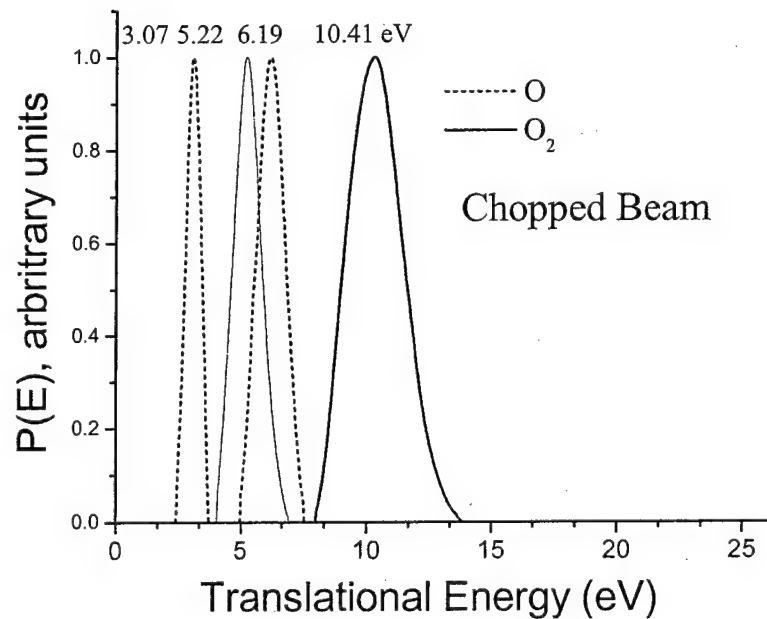


Figure 2-11. Energy distribution of chopped beam produced by the pulsed CO₂ laser AO source

2.4 Summary

In this chapter, the latest modification and theory behind the operation of a compact, UHV-compatible atomic oxygen source based on electron stimulated desorption was described. This source is used to expose polymeric materials in studies presented in subsequent chapters of this dissertation. It is capable of producing a high purity flux $> 10^{15}$ atoms/cm² s of hyperthermal atoms while a pressure of 10⁻⁹ Torr is maintained in the source chamber. The source does not produce contaminants or high energy species which would damage the surface, and the ion flux is negligible compared to the atom flux. The energy distribution has yet to be determined, but preliminary analysis suggests that AO produced by this source is at least 2 eV or greater. In addition, a brief comparison of other sources used to form atomic oxygen was presented in this chapter, including a pulsed CO₂ laser source which was used to conduct erosion studies of POSS polymer presented in Chapter 5.

CHAPTER 3
IN-SITU ATOMIC OXYGEN EROSION STUDY OF A POLYHEDRAL
OLIGOMERIC SILSESQUIOXANE SILOXANE COPOLYMER

3.1 Introduction

In this study a thin film of polyhedral oligomeric silsesquioxane (POSS)-siloxane copolymer has been characterized in-situ using XPS before and after incremental exposures to the flux produced by an electron stimulated desorption (ESD) atomic oxygen source described in Chapter 2. POSS molecules are hybrid inorganic/organic structures synthesized from the self-condensation reactions of alkyl trichlorosilanes. Over the last 10 years, the Air Force Research Laboratory and Hybrid Plastics LLC [107] have focused on incorporating POSS frameworks into traditional polymer systems via copolymerization, grafting and blending processes. Significant property enhancements have been reported for these hybrid polymers including increased use temperature, increased toughness, decreased flammability and increased oxidation resistance as described in Chapter 1. These property enhancements are attributed to the nano-level interaction of the POSS framework with the polymer matrix. Traditionally, silica fillers have been used in polymer applications requiring alterations in physical and mechanical properties such as tensile strength, abrasion and fatigue resistance. In addition to numerous property enhancements, POSS polymers have lower densities (1.2 to 1.5 g/ml) than silica fillers (2.4 to 2.6 g/ml) [44, 108]. Unlike silica fillers, POSS frameworks can be easily functionalized for polymer compatibility without significantly affecting processing conditions. Compared to silica fillers, POSS hybrid polymers are able to

impart similar property enhancements, including many not possible utilizing filler technology. Previous studies have also shown that Si-O systems exhibit a superior resistance to AO degradation due in part to their oxophilicity and high bond strength (~ 8 eV) [42, 109]. However, pure siloxane systems have displayed many disadvantages for space applications including the generation of volatile cyclic species when exposed to AO that can recondense on optical surfaces [34]. This present study details the results obtained from exposing a POSS-polydimethylsiloxane (PDMS) film to a simulated LEO environment. Specifically, it describes the formation of a protective silica layer with exposure to an atomic oxygen flux. This layer serves as a protective barrier preventing further degradation of the underlying virgin polymer with increased AO exposure. Previous exposures of this polymer system [10] to AO and far-UV radiation was shown to result in the healing of surface defects or microcracks initially present as a result of sample preparation as shown in the scanning electron micrographs of Figure 3-1.

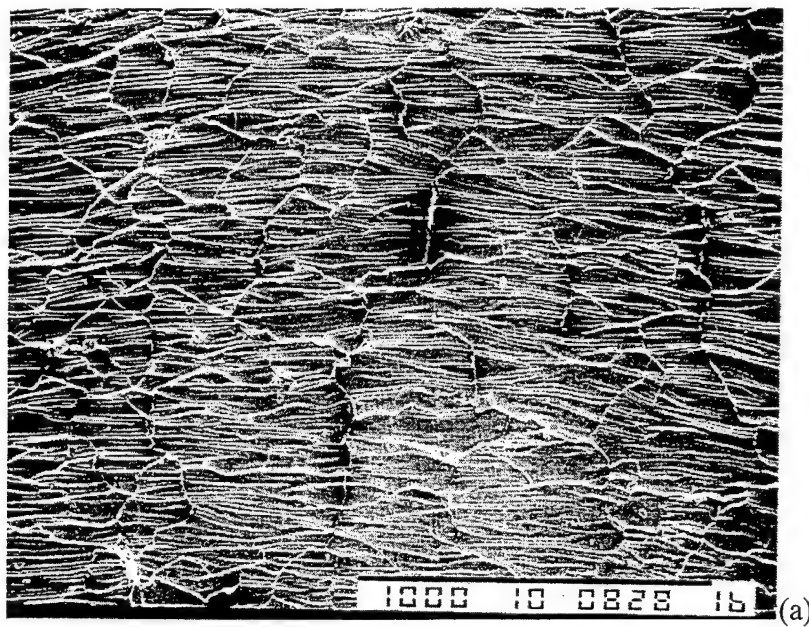


Figure 3-1. SEM of (a) unexposed and (b) exposed POSS-siloxane copolymer surfaces. The simulated LEO exposure “healed” the micro-cracks present initially in the POSS-siloxane sample [10].

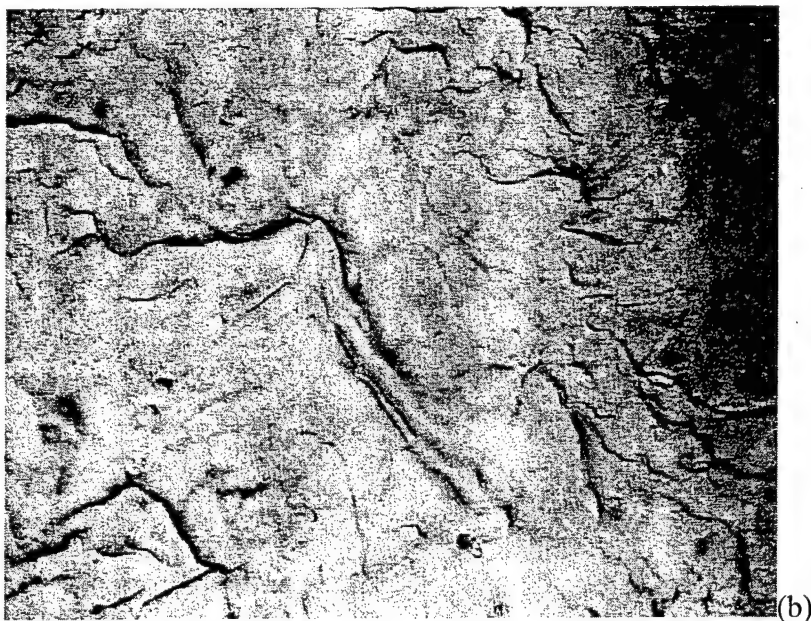


Figure 3-1. Continued.

3.2 Experimental

3.2.1 Synthesis of a POSS-PDMS Copolymer

The POSS siloxane copolymer used in this study and shown in Figure 3-2 was synthesized using a method similar to that described by Lichtenhan et al [10, 49]. The diol-silsesquioxane monomer (5.00 g or 4.54 mmol) was dissolved in 10 ml of tetrahydrofuran (THF) in a 50 ml flask to which 1.98 g (4.54 mmol) of bis(dimethylamino)polydimethylsiloxane (approximately 4.9 silanes per oligomer, $M_w=435.5$ g/mol) was added with an additional 15 ml of THF. The reaction mixture was stirred and heated to 65°C under nitrogen for 48 hrs. The polymer was then precipitated into 350 ml of methanol, stirred for 2 hrs, filtered and air dried for 12 hrs. To end cap the polymer with trimethylsilane, it was dissolved in 25 ml of THF with an excess of *N,N*-(dimethylamino)trimethylsilane and reacted at 65°C under nitrogen for

another 48 hrs. The polymer was again precipitated into 350 ml of methanol. After decanting the solvent, fresh methanol with dilute HCl was added to neutralize any excess amine. The solution was again decanted and the remaining white solid dried under vacuum for 2 hrs, producing a yield of 6.27 g (95% theoretical yield). Molecular weights were determined from multi-angle laser light scattering measurements obtained from a DAWN-F detector (Wyatt Technologies) equipped with a gel-permeation chromatography column. The number average molecular weight, mass average molecular weight and degree of polymerization were found to be 62,000, 118,000 and 43 respectively. Peak area analysis of the ^{29}Si NMR data gives a degree of polymerization of 38 and shows on average 4.8 SiOMe_2 groups per repeat unit. Relevant peaks in the ^{29}Si NMR spectrum are a singlet at 7.2 ppm (Me_3Si endgroups, peak area of 2.0), a multiplet at 21.5 ppm ($\text{Me}_2\text{Si-O}$, peak area of 184) and four singlets at 66.39, 68.13, 68.20 and 69.51 ppm (POSS, peak area of 305.6).

3.2.2 Preparation of Thin Films by Solvent Casting

Thin films of the trimethylsilane-terminated POSS-PDMS were made by dissolving 100 mg of the powder in 15-20 mL of THF, solvent casting onto 1 cm x 1 cm aluminum substrates and drying at room temperature for 24 hrs. The aluminum substrates were prepared and cleaned with Boraxo soap and water, deionized water followed by ultrasonic cleaning in toluene, acetone, trichloroethylene, acetone and ethanol respectively.

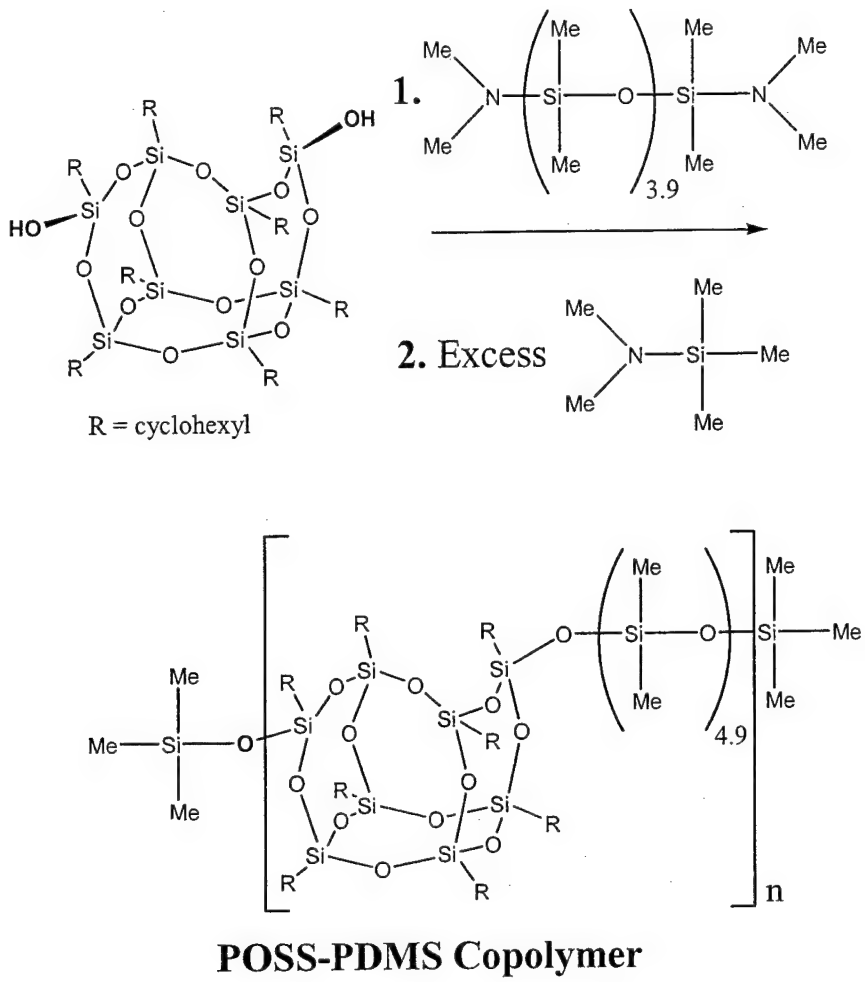


Figure 3-2. Scheme for synthesis of the POSS-PDMS copolymer used in this study.

3.3.3 Surface Characterization

A solvent casted POSS-PDMS film was wiped with isopropanol and inserted into the UHV chamber (base pressure $<10^{-10}$ torr). XPS was performed using a double-pass cylindrical mirror analyzer (DPCMA) (PHI Model 25-270AR). XPS survey spectra were taken in the retarding mode with a pass energy of 50 eV, and high-resolution XPS spectra were taken with a pass energy of 25 eV using Mg K α X-rays (PHI Model 04-151 X-ray source). Data collection was accomplished using a computer interfaced, digital pulse-counting circuit [73] followed by smoothing with digital-filtering techniques [74]. The

sample was tilted 30 deg off the axis of the DPCM, and the DPCM accepted electrons emitted into a cone 42.6 ± 6 deg off the DPCM axis.

XPS spectra were first obtained from the as-entered, solvent-cleaned sample. The sample was then transferred via a magnetically coupled rotary/linear manipulator into an adjoining UHV chamber that houses the ESD AO source. There the surface was exposed to the hyperthermal AO flux and re-examined without air exposure after total exposure times of 2, 24.6, and 63 hrs. The approximate normal distance between the sample face and source in this study was 15 cm, at which distance the flux was about 2×10^{13} atoms/cm²-s for the instrument settings used. The substrate temperature was determined using a chrome-alumel thermocouple attached to the Al substrate. At this distance the sample remained at room temperature during the AO exposures. The sample temperature did increase to 50°C during XPS data collection. After the 63-hr AO exposure, the sample was exposed to air (room temperature ~22°C and relative humidity ~60%) for 4.75 hrs and again examined using XPS.

3.3 Results and Discussion

XPS survey spectra obtained from a solvent-wiped POSS-PDMS surface before and after the 2, 24.6 and 63 hr AO exposures are shown in Figure 3-3 (a) to (d), respectively. Spectrum (e) in Figure 3-3 was taken after the 4.75-hr air exposure following the 63-hr AO treatment. The peak assignments shown in Figure 3-3 pertain to all five spectra. The predominant peaks apparent in these spectra include the C 1s, O 1s, Si 2p, Si 2s, O 2s and O Auger peaks. Significant changes in relative peak heights are observed for the C, O, and Si features following the O-atom exposures. An estimate of the near-surface compositions has been calculated from the peak areas in the survey

spectra by assuming that this region is homogeneous and using published atomic sensitivity factors [67]. The compositions determined in this manner are presented in Table 3-1 for the as-entered, AO-exposed and air-exposed surfaces.

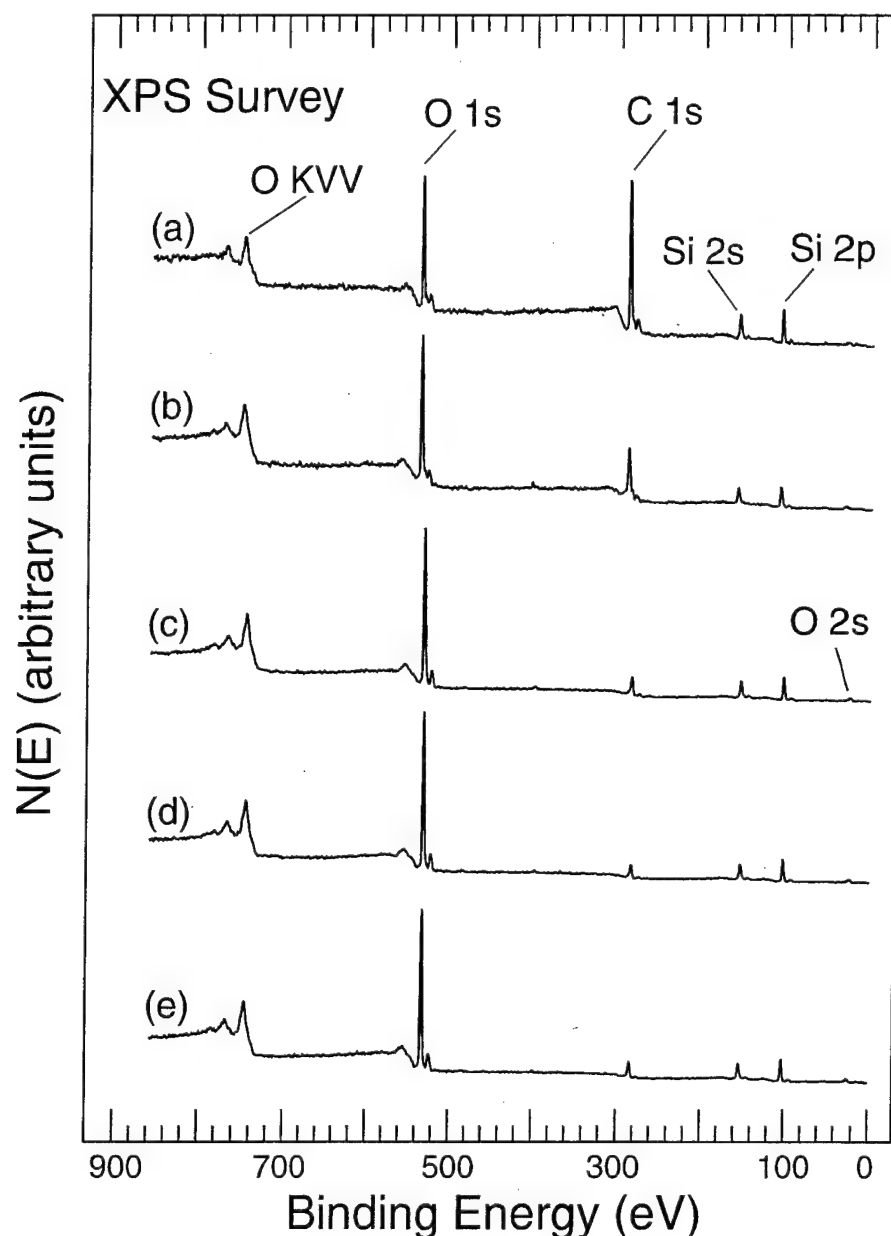


Figure 3-3. XPS survey spectra obtained from a solvent-cleaned, POSS-PDMS film (a) after insertion into the vacuum system, (b), after a 2-hr (c) 24.6-hr and (d) 63-hr exposure to the hyperthermal AO flux, and (e) 4.75-hr air exposure following the 63-hr AO exposure

Table 3-1: Near-surface composition determined from XPS data obtained from the as-entered, solvent cleaned, AO and air-exposed POSS-PDMS sample

Surface	AO Fluence	Composition, at%			atom ratio
Sample Treatment	O/cm ²	O	C	Si	O/Si
As entered, solvent cleaned	---	18.5	65.0	16.6	1.11
2-hr AO exposure	1.44 x 10 ¹⁷	33.8	48.4	17.8	1.90
24.6-hr AO exposure	1.77 x 10 ¹⁸	49.1	22.1	28.8	1.70
63-hr AO exposure	4.53 x 10 ¹⁸	55.7	16.3	28.0	1.99
4.75-hr air exposure following the 63-hr AO exposure	4.53 x 10 ¹⁸	52.8	19.5	27.7	1.91

As described in Chapter 1, XPS probes the near-surface region of the sample and yields a weighted average composition with the atomic layers near the surface being weighted more heavily because these photoemitted electrons have a lower probability of scattering inelastically. The sampling depth is about 30 atomic layers, and about 10% of the signal originates from the outermost atomic layer [66]. This near-surface region is nonhomogeneous because the AO reacts with the outermost few atomic layers. Therefore, the region which is affected to the greatest extent due to reaction with AO also makes the largest contribution to the XPS signal. This fact implies that XPS is an excellent technique for studying AO erosion of spacecraft materials. Even though the distribution functions involving the depth of chemical reactions in the near-surface region and the XPS determination of the weighted average composition of the near-surface region are complex, the compositional values, determined using the homogeneous assumption and shown in Table 3-1 as a function of AO fluence, provide a trend which is indicative of the chemical alterations occurring during AO exposure. This trend is supported by the chemical state alterations determined by XPS, which are discussed

below. The O-to-Si atomic ratio is 1.11 for the as-entered sample, and it is increased to 1.90 after the 2-hr exposure, and then reduced to 1.70 after 24.6 hrs and increased again to 1.99 after the 63-hr O-atom exposures. This behavior indicates that complex chemical reactions occur during AO exposure. After the 4.75-hr air exposure, the O-to-Si atomic ratio is 1.91. These changes in the O-to-Si atomic ratio resulting from exposure to the AO flux indicate the formation of SiO_2 and are consistent with the high-resolution spectra that follow. A large reduction in the C 1s peak is observed as a result of the incremental exposures to the AO flux. The near-surface C concentration decreases from 65.0 at% for the as-entered sample to 16.3 at% after the 63-hr exposure. This decrease is due to reaction of C in the near-surface region with O to form CO_2 . A small increase in the carbon content to 19.5 at% is observed after exposure to air for 4.75 hrs probably due to the adsorption of C-containing molecules such as hydrocarbons from the air. Hydrogen in the POSS-PDMS would also react with the AO to form water which would desorb.

High-resolution XPS C 1s, O 1s and Si 2p obtained from the as-received, solvent-wiped surface before and after the 2-, 24.6- and 63-hr AO exposures are shown in spectra a-d of Figures 3-4, 3-5 and 3-6 respectively. Spectrum (e) was obtained after the 4.75-hr air exposure following the 63-hr O-atom exposure. Variations in peak shapes and positions are observed between the nonexposed, AO-exposed, and air-exposed surfaces indicating that the chemical species distribution is altered by exposure to the AO flux and then to air.

The C 1s peak shown in Fig. 3-4(a) is centered at 285.2 eV indicating that the predominant form of carbon present for the as-entered sample is in the form of a fully

substituted hydrocarbon, i.e. the cyclohexyl groups on the POSS cage [110]. In spectra (b), (c) and (d), the C 1s peak becomes broader and the peak center shifts to lower binding energy (BE) with increasing exposure to the AO flux. After the 63-hr exposure, the C 1s has a BE of 284.4 eV. This value is characteristic of methyl groups on the PDMS chain [110]. The fact that these changes coincide with a decrease in the total carbon concentration in the near-surface region from 64.1 to 13.5 at% implies that the cyclohexyl groups are being removed selectively leaving the methyl groups. This selective removal could be due to the larger size of the POSS cage (1.5 nm) compared to the PDMS chain as shown in Fig. 2. Small shoulders are visible on the high-BE side of the C 1s peak in spectra b, c and d. These probably are due to species such as alcohols, formaldahydes (BE ~286.0 to 287.7 eV) and organic acids (BE ~287.5) which form by reaction with the AO flux. Exposure to air (spectrum e) produces an increase in the shoulder near 285.0 eV indicating adsorption of hydrocarbons from the air at reactive surface sites produced during the AO exposure. This observation is consistent with the increase in the C concentration after the air exposure as shown in Table 3-1.

Did you mean
Fig. 3-2?

The O 1s spectra obtained from the sample before and after the various treatments are shown in Figure 3-5. These peaks are broad indicating that various chemical states of oxygen are present. After the 2-hr exposure to the AO flux, the contribution from oxygen is significantly increased from 18.5 to 33.8 at%, and then it increases further to 49.1 and 55.7 at% after the 24.6-hr and 63-hr exposures respectively. However, the peak shapes and positions do not change much with treatment indicating that the O-containing species have closely spaced O 1s BEs. A previous XPS study of PDMS has shown that the

oxygen in the PDMS chain has a BE of 532.0 eV [110] while SiO_2 has a BE of about 532.5 eV [110].

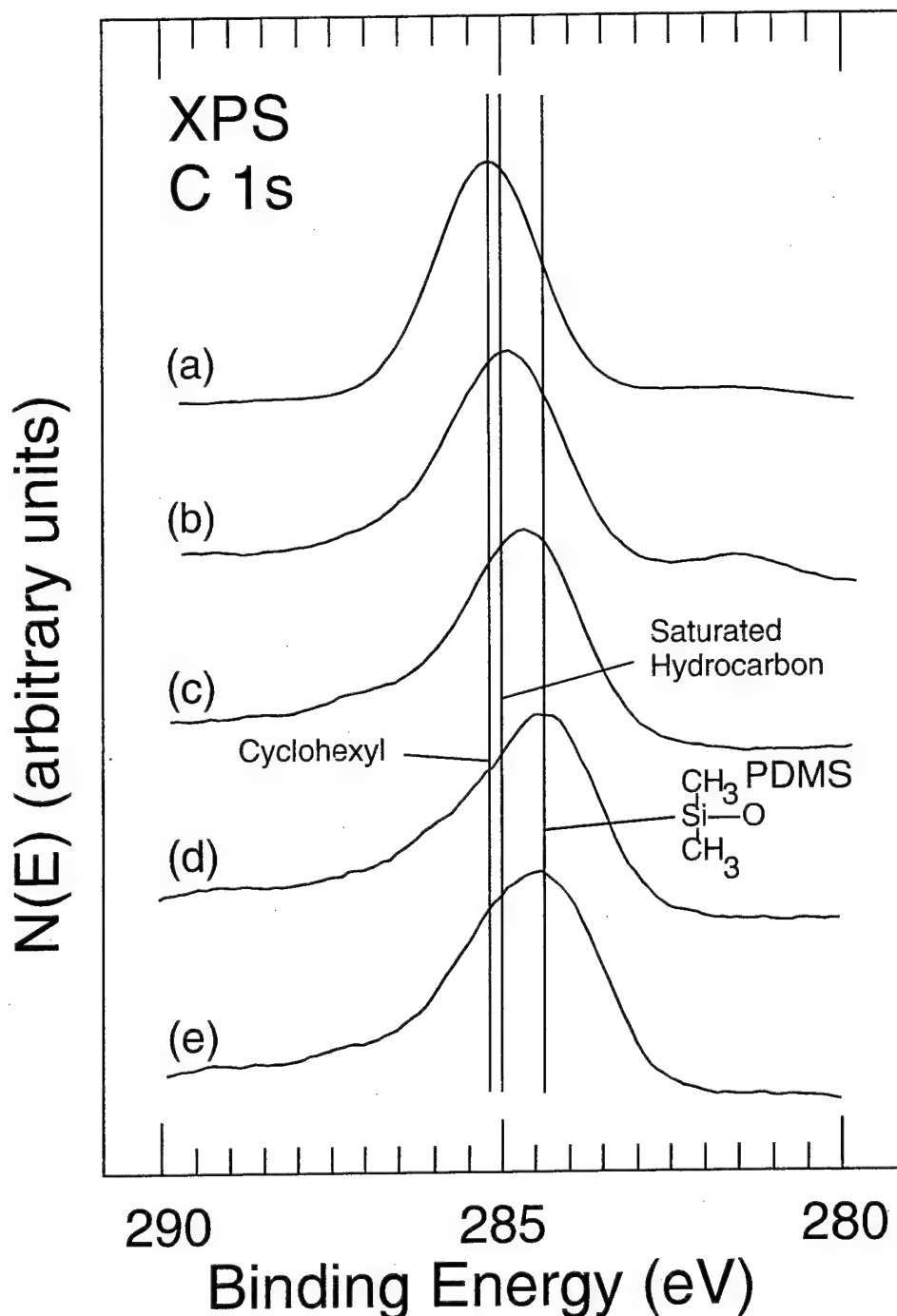


Figure 3-4. XPS C 1s spectra obtained from a solvent-cleaned, POSS-PDMS film (a) after insertion into the vacuum system, (b) after a 2-hr, (c) 24.6-hr, and 63-hrs exposure to the hyperthermal AO flux, and (e) 4.75-hr air exposure following the 63-hr AO exposure

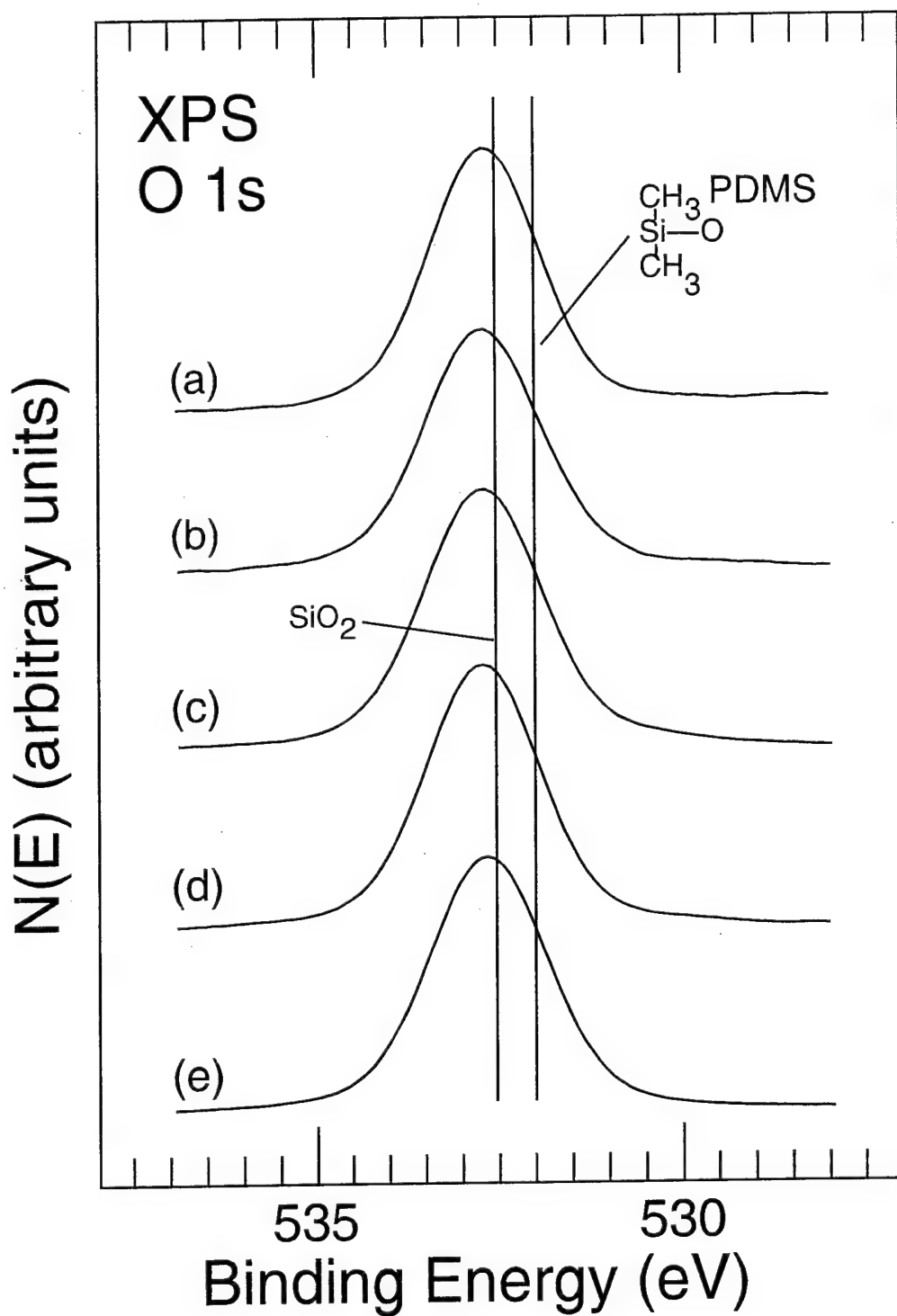


Figure 3-5. XPS O 1s spectra obtained from a solvent-cleaned, POSS-PDMS film (a) after insertion into the vacuum system, (b) after a 2-hr, (c) 24.6-hr, and (d) 63-hr exposure to the hyperthermal AO flux, and (e) 4.75-hr air exposure following the 63-hr AO exposure

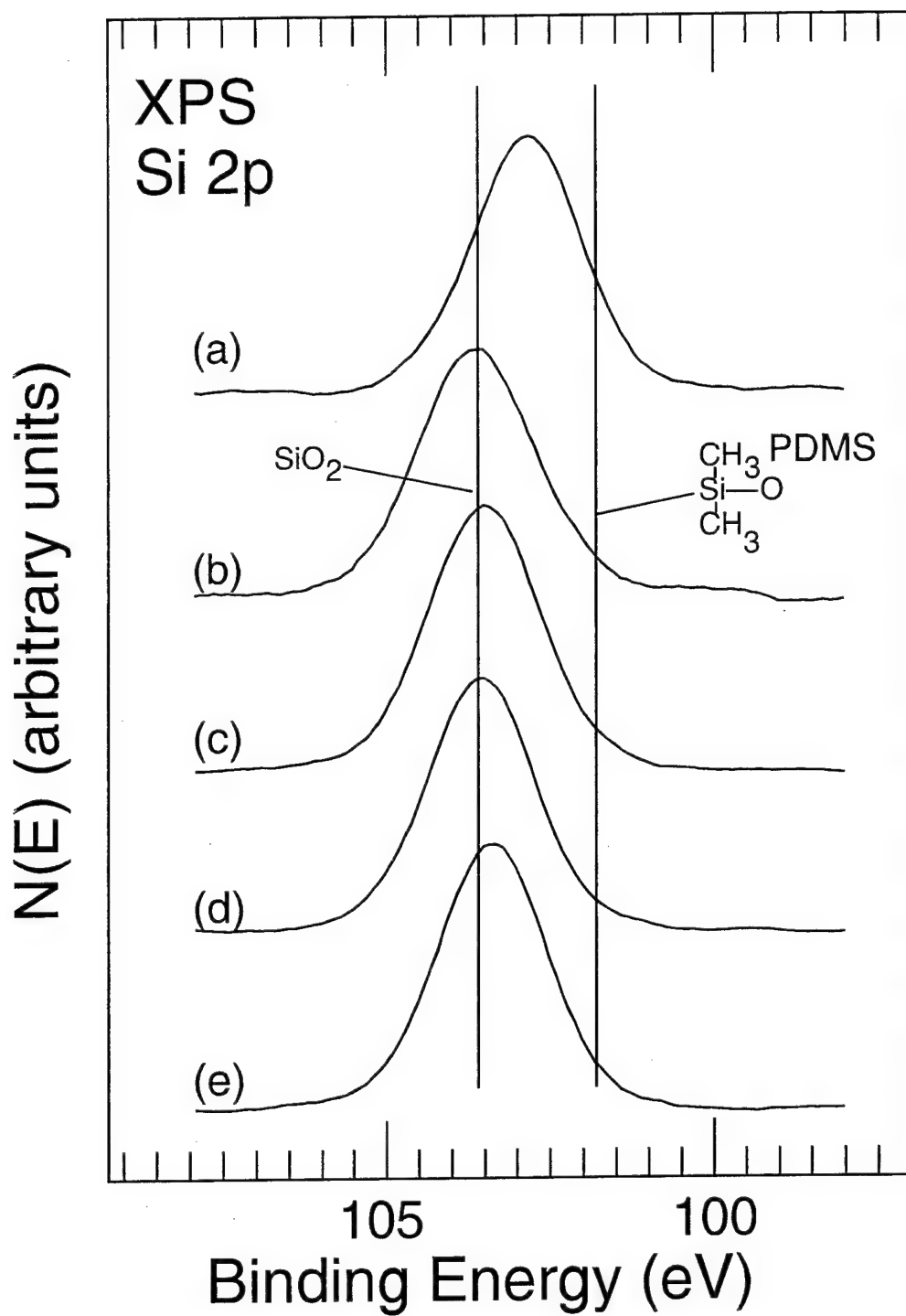


Figure 3-6. XPS Si 2p spectra obtained from a solvent-cleaned, POSS-PDMS film (a) after insertion into the vacuum system, (b) after a 2-hr, (c) 24.6-hr, and (d) 63-hr exposure to the hyperthermal AO flux, and (e) 4.75-hr air exposure following the 63-hr AO exposure.

The Si 2p peaks obtained from the sample before and after the various treatments are shown in Figure 3-6. Similar to the O 1s peak, the Si 2p peak for the as-entered sample (spectrum a) is broad indicating the presence of several chemical states of silicon. This peak is centered at a BE of 102.7 eV which corresponds to $\text{RSiO}_{1.5}$ in the POSS cage. However, spectra b, c and d reveal the formation of a SiO_2 layer with incremental exposures to the AO flux. The fact that little difference is observed in the spectra obtained after the 24.6- and 63-hr exposures indicates that this silica layer forms a protective barrier on the surface which prevents further degradation of the polymer with longer exposure to the AO flux. The significant compositional changes observed indicate that most of the near-surface region examined by XPS is altered by the AO exposure. The chemical reactions which form CO_2 and H_2O are exothermic so the local surface temperature may be relatively high. This fact and the fact that the AO provides a chemically induced driving force at the surface result in diffusion of subsurface C and H to the surface where they react with the AO. This mechanism is responsible for the subsurface compositional alterations observed using XPS and the formation of a relatively thick SiO_2 layer.

3.4 Summary

The surface of a POSS-PDMS copolymer film has been characterized in-situ using XPS before and after exposure to different fluences of AO produced by an ESD hyperthermal oxygen atom source. The XPS data indicate that the carbon content of the near-surface region is decreased from 65.0 to 16.3 at% after a 63-hr exposure to an AO flux of 2×10^{13} atoms/cm² s. The oxygen and silicon concentrations in the near-surface region increase with increasing exposure to the AO flux with the oxygen-to-silicon atom

ratio increasing from 1.11 for the as-entered sample to 1.99 after a 63-hr AO exposure. High resolution XPS data suggest that the AO initially attacks the cyclohexyl groups on the POSS cage forming CO₂ and H₂O which desorb. Increased exposure to the AO flux results in the formation of a silica layer on the surface which acts a protective barrier ^{as} preventing further degradation of the underlying polymer.

CHAPTER 4
IN-SITU ATOMIC OXYGEN EROSION STUDY OF POLYHEDRAL OLIGOMERIC
SILSESQUIOXANE POLYURETHANE COPOLYMERS

4.1 Introduction

In Chapter 3, a polyhedral oligomeric silsesquioxane-siloxane copolymer containing a completely inorganic Si-O polymer backbone was shown to form a passivating ceramic layer upon exposure to hyperthermal oxygen atoms. This silica (SiO_2) layer protects the virgin polymer from undergoing further erosion and resulted in the healing of surface defects initially present due to sample preparation as shown in Figure 3-1. This healing effect caused by POSS incorporation within the polymer matrix would prevent the AO induced undercutting previously reported to occur on materials with protective coating schemes used in space [13, 24, 30]. In order to investigate if this healing phenomenon would also occur if POSS was copolymerized into a conventional C-C backbone organic polymer, similar AO erosion studies were conducted on varying weight fractions of POSS copolymerized into polyurethane and are reported in this chapter and have also recently been published [111, 112]. Polyurethanes have been extensively used on spacecraft as the primary constituents of thermal control paints [8, 11, 113]. In this study, 20 and 60 wt% POSS-Polyurethane (PU) copolymers have been characterized in-situ using XPS before and after incremental exposures to the flux produced by the ESD AO source described in Chapter 2.

4.2 Experimental

4.2.1 Synthesis of POSS-Polyurethane Copolymers

A typical polyurethane is synthesized by reacting short and long chain diols and diisocyanates as shown in Figure 4-1. The polymer formed is comprised of hard segments and soft segments which undergo microphase separation due to thermodynamic incompatibilities that result in the properties of a thermoplastic elastomer [114].

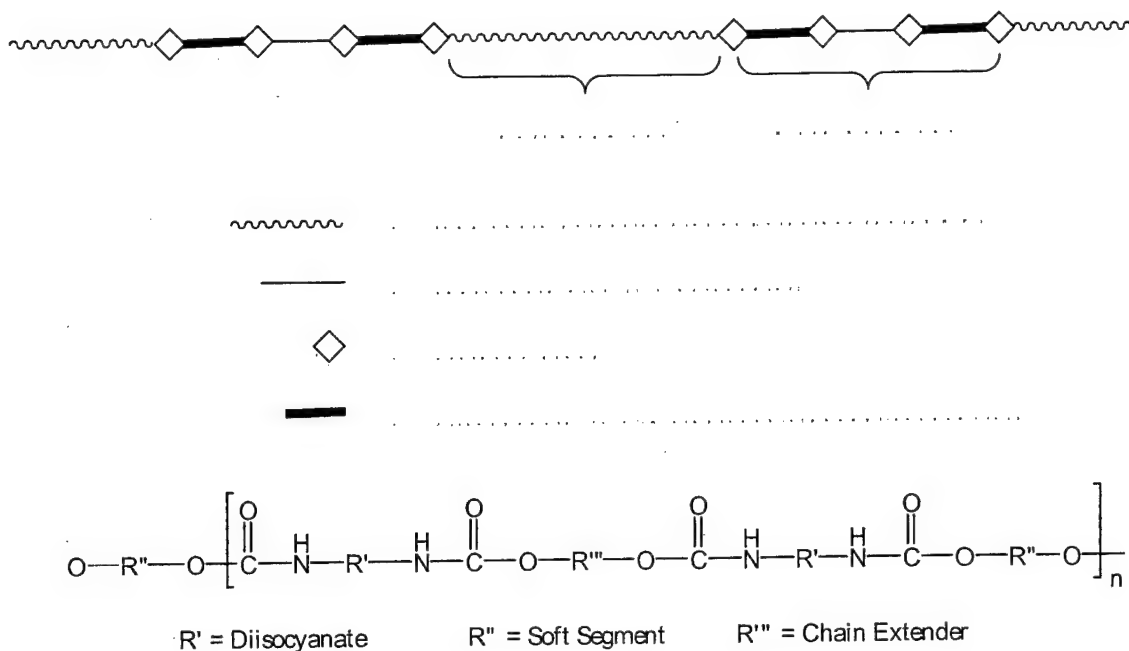


Figure 4-1. Primary Structure of Polyurethanes.

The macroscopic properties of the polyurethanes are influenced by the interchain interactions of the hard segments through van der Waals forces and hydrogen bonding. Polyurethanes with inorganic POSS molecules incorporated into the hard segments were first synthesized by Fu et al. [115, 116]. POSS incorporation into polyurethanes results in significant increase in modulus, glass transition temperature and decomposition temperature as shown in Tables 4-1 and 4-2.

For this study, polyurethane samples were synthesized in a series of reactions similar to that described by Fu et al. [115, 116]. The synthetic schemes illustrating the synthesis of the POSS monomer used for the copolymerization are shown in Figures 4-2 and 4-3. Vacuum distilled tetrachlorosilane is added dropwise, under nitrogen and in the presence of excess triethylamine to cyclopentyl POSS trisilanol **1** in THF. The resulting POSS chloride monomer **2** undergoes hydrolysis upon the addition of acidic water to form the POSS monosilanol **3**. After workup and isolation, chlorodimethylsilane is added to monomer **3** under similar conditions to form the POSS mono-hydride monomer **4** [117].

Table 4-1: Polyurethane thermal property enhancements through POSS incorporation.

Polymer	Melt Transition °C	T_{dec} °	Char Yield%	Appearance
0% POSS	-49, 22	274 °C	1.4	Viscous Fluid
29% POSS	201	372 °C	16.0	Solid Rubber
43% POSS	260, 320	344 °C	20.0	Solid Rubber

Table 4-2: Polyurethane Modulus enhancements through POSS incorporation.

POSS Bisphenol A urethanes		POSS TMP urethanes	
0 wt.% POSS	0.04 Mpa	0 wt.% POSS	0.01 Mpa
17 wt.% POSS	0.42 Mpa	17 wt.% POSS	0.14 Mpa
34 wt.% POSS	1.06 Mpa	34 wt.% POSS	0.39 Mpa

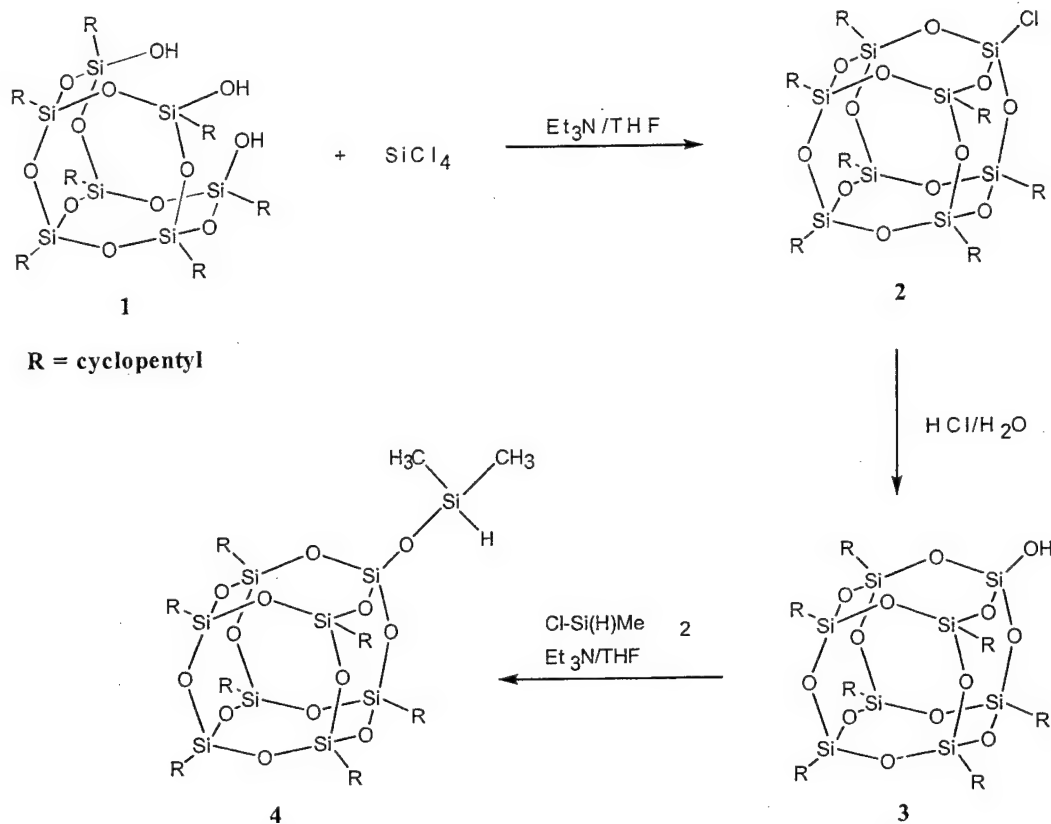


Figure 4-2. Synthesis of POSS mono-hydride monomer.

As shown in Figure 4-3, the POSS monohydride monomer undergoes a platinum catalyzed hydrosilation with methylopropane allyl ether **5** to form the POSS-TMP diol monomer **6** used in the copolymerization reaction. Figure 4-4 shows the synthetic scheme illustrating the polymerization reaction to form the POSS-PU polymers. Diphenylmethane-4,4'-diisocyanate (MDI) and polytetramethylene glycol (PTMG) ($M_w=2000$) were mixed in a molar ratio of 2:1 and prepolymerized at 80°C for 2 hrs. The prepolymer was dissolved into anhydrous polytetrahydrofuran (PTHF). The prepolymer was then chain extended by addition of POSS-TMP diol at room temperature over 6 hours. The mixture was cooled to 5°C and 1,4-butanediol (BDO) added drop-wise. The system was warmed to room temperature and after 1 hour the products were precipitated

in a 1:1 methanol-water solution, separated by filtration and dried in *vacuo*. All the reactions were carried out under nitrogen. Molecular weights determined using gel permeation chromatography are presented in Table 4-3.

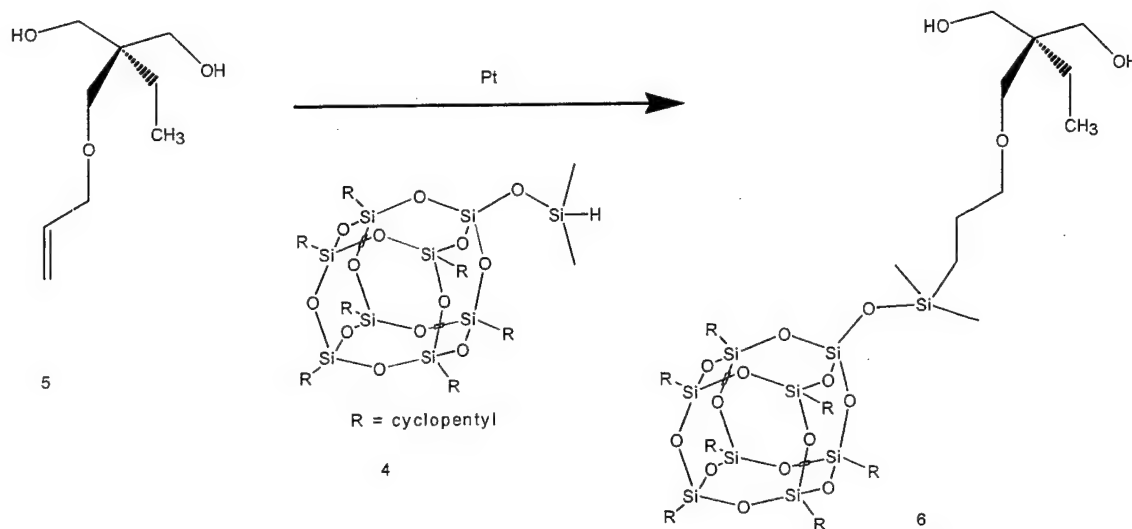


Figure 4-3. Synthesis of POSS-TMP diol monomer used in copolymerization reaction.

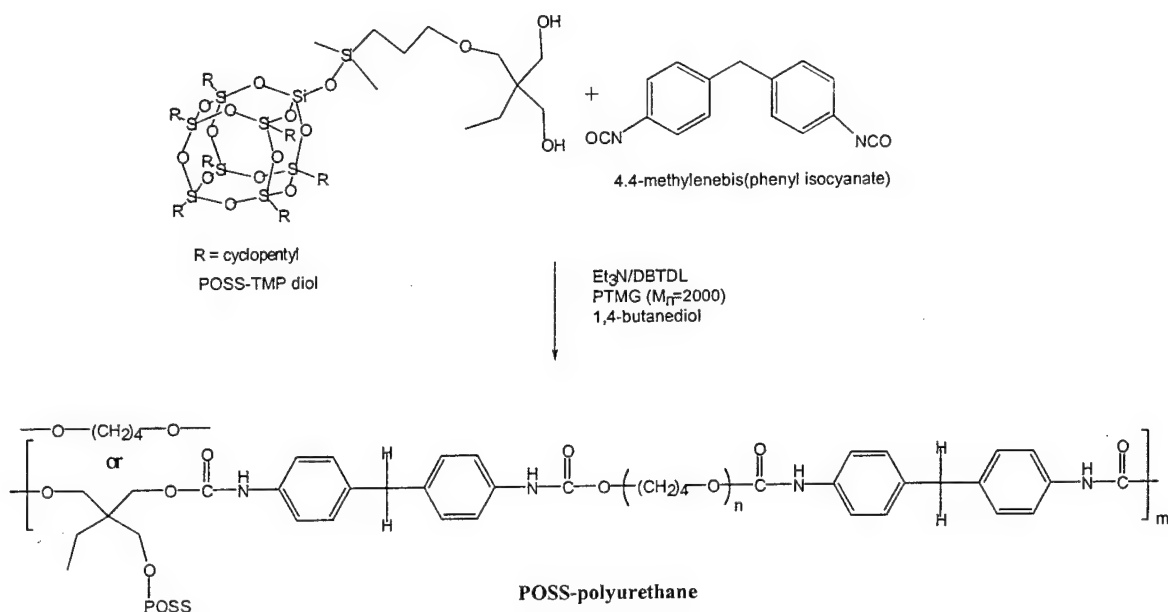


Figure 4-4. Scheme for synthesis of POSS-polyurethane.

Table 4-3: Molecular weights of TMP-POSS-Polyurethanes.

Sample	POSS (mol%)	Molecular weight (Mw)	Polydispersity
POSSPU	0	1.5×10^5	2.42
POSSPU20	0.9	1.2×10^5	2.20
POSSPU40	2.3	2.0×10^5	1.97
POSSPU60	4.8	1.1×10^5	1.78
POSSPU80	10.4	1.5×10^5	2.13

4.2.2 Preparation of Thin Films by Solvent Casting

Thin films of the 20 and 60 wt % POSS-PU were made by solvent casting THF solutions of 5mg/mL concentration of each polymer onto 1 cm x 1 cm aluminum substrates. The films were dried at room temperature for 24 hr. Prior to use, the aluminum substrates were cleaned with BoraxoTM soap and water, rinsed with deionized water, followed by ultrasonic cleaning in toluene, acetone, trichloroethylene, acetone and ethanol successively.

4.2.3 Surface Characterization

Solvent-cast 20 and 60 wt% POSS-PU film were wiped with isopropanol and inserted into the UHV chamber (base pressure $<1.33 \times 10^{-7}$ Pa). XPS measurements were performed using a double-pass cylindrical mirror analyzer (DPCMA) (PHI Model 25-270AR). XPS survey spectra were taken in the retarding mode with a pass energy of 50 eV, and high-resolution XPS spectra were taken with a pass energy of 25 eV using Mg $K\alpha$ X-rays (PHI Model 04-151 x-ray source). Data collection was accomplished using a computer interfaced, digital pulse-counting circuit [73] followed by smoothing with digital-filtering techniques [74]. The sample was tilted 30 degrees off the axis of the

DPCMA, and the DPCMA accepted electrons emitted into a cone 42.6 ± 6 degrees off the DPCMA axis.

XPS spectra were first obtained from the as-entered, solvent-cleaned samples. The samples were then transferred into an adjoining UHV chamber that houses the ESD O-atom source via a magnetically coupled rotary/linear manipulator. There the surfaces were exposed to a hyperthermal O flux and re-examined without air exposure after total exposure times of 2, 24, and 63 hr. The approximate normal distance between the sample faces and source in this study was 15 cm, at which distance the flux was about 2.0×10^{13} atoms/cm²-s for the instrument settings used. The samples were maintained at room temperature during the AO exposures with a slight temperature increase to 50°C due to exposure to the X-ray source during XPS data collection. The substrate temperature was determined using a chromel-alumel thermocouple. After the 63-hr AO exposure, the samples were exposed to air (room temperature, ~22°C, relative humidity ~60%) and again examined using XPS.

4.3 Results and Discussion

XPS survey spectra obtained from an as received, solvent-wiped 20 and 60 wt% POSS-polyurethane surfaces before and after the 2, 24 and 63 hr O-atom exposures are shown in Figures 4-5(a)–4-5(d) and 4-6(a)–4-6(d), respectively. Spectra e in both Figures 4-5 and 4-6 were taken after the samples were exposed to air following the 63 hr AO treatment. The peak assignments shown in Figure 4-5 and 4-6 pertain to all five spectra. The predominant peaks apparent in these spectra include the C 1s, O 1s, Si 2p, Si 2s, O 2s, N 1s, Sn 3d and the Na and O Auger peaks. The presence of Sn is due to the catalyst system (dibutyltindilaurate) used during polymer synthesis. Na is present in parts per

million levels in the reactants used to make the catalyst system and migrates to the surface as a result of AO exposure and affinity for silica. Significant changes in relative peak heights are observed for the C, O, and Si features following the O-atom exposures. Estimates of the near-surface compositions were calculated from the peak areas in the high-resolution spectra using published atomic sensitivity factors [67] with the assumption of a homogeneous surface region. The compositions determined in this manner are presented in Table 4-4 and 4-5 for the as-entered, O-exposed and air exposed 20 wt% and 60 wt% POSS-PU surfaces. It is important to understand when looking at the data that, the ~~he~~ 5-eV AO is not energetic enough to penetrate more than one or two atomic layers into the polymer while, XPS probes as deeply as 30 or more atomic layers beneath the surface. The significant compositional changes observed indicate that most of the near-surface region examined by XPS is altered by the AO exposure.

Atomic oxygen exposure results in an increase in the O/Si atomic ratio for both samples. The 20 wt% POSS-PU sample O/Si ratio increases from an initial 2.28 to 2.93 after the 63.0 hr AO exposure. A similar increase from an initial 1.61 to 1.73 is observed in Figure 4-5 for the 60 wt % POSS-PU sample. This behavior indicates that complex chemical reactions occur during AO exposure. The decrease in the O/Si ratio for both samples after the 24 hr AO exposures could be attributed to the relative increase of Na and Sn on the surface. However, the overall increase in the O/Si atomic ratio resulting from exposure to the AO flux is a trend that has been previously observed in similar study of POSS-PDMS mentioned in Chapter 3. It is attributed to the formation of SiO_2 and is consistent with the high-resolution spectra that follow. A large reduction in the C 1s peak is observed as a result of the incremental exposures to the AO flux in both

samples. The near-surface C concentration decreases from 72.5 at% for the as-entered 20 wt% POSS-PU sample to 37.8 at% after the 63.0 h exposure. The 60 wt% POSS-PU carbon content decreases from 70.1 to 37.3 at%. This decrease is due to reaction of C in the near-surface region with O to form CO and CO₂. In both cases, an increase in the carbon content is observed after exposure to air and is probably due to the adsorption of C-containing molecules (e.g., hydrocarbons) from the air.

Table 4-4: Near-surface composition determined from XPS data obtained from the as-entered, solvent cleaned, AO and air-exposed 20 wt % POSS-Polyurethane sample.

Surface Sample Treatment	AO Fluence O/cm ²	Composition, at.%						Atom ratio O/Si
		O	Si	C	Sn	Na	N	
As entered, solvent cleaned	—	18.5	8.1	72.5	0.9	-	-	2.28
2-hr AO exposure	1.44×10^{17}	20.4	7.9	70.7	1.0	-	-	2.58
24-hr AO exposure	1.77×10^{18}	21.8	9.5	61.7	1.0	3.0	3.0	2.29
63-hr AO exposure	4.53×10^{18}	32.6	11.1	37.8	1.8	13.6	3.1	2.93
4-hr air exposure following 63-hr AO exposure	4.53×10^{18}	38.9	13.7	43.4	2.0	2.0	-	2.83

Table 4-5: Near-surface composition determined from XPS data obtained from the as-entered, solvent cleaned, AO and air-exposed 60 wt % POSS-Polyurethane sample.

Surface Sample Treatment	AO Fluence O/cm ²	Composition, at.%						Atom ratio O/Si
		O	Si	C	Sn	Na	N	
As entered, solvent cleaned	—	18.2	11.3	70.1	0.4	-	-	1.61
2-hr AO exposure	1.44×10^{17}	17.5	11.2	70.2	0.7	0.4	-	1.56
24-hr AO exposure	1.77×10^{18}	23.7	13.2	58.2	0.9	1.4	2.6	1.79
63-hr AO exposure	4.53×10^{18}	35.3	20.4	37.3	1.3	3.0	2.7	1.73
4-hr air exposure following 63-hr AO exposure	4.53×10^{18}	31.6	14.6	48.5	1.0	2.7	1.6	2.16

High-resolution XPS C 1s, O 1s and Si 2p spectra obtained from the as-received, solvent-wiped surface before and after the 2, 24 and 63 hr O-atom exposures are shown

in (a)-(d) of Figures 4-7 through 4-12 for both samples. Spectra (e) of these figures were obtained after the exposure to air following the 63 hr O-atom exposure.

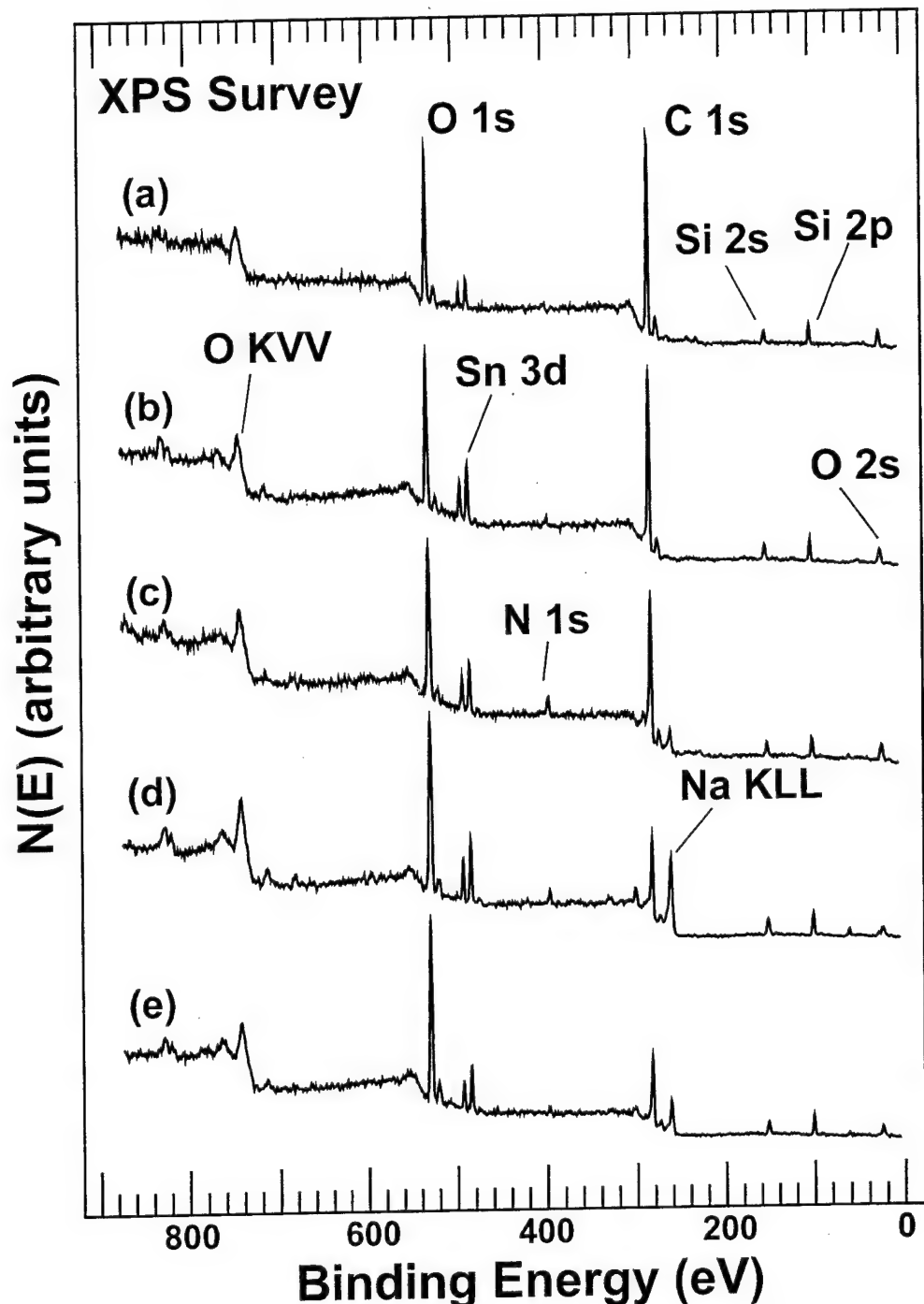


Figure 4-5. XPS survey spectra obtained from a 20-wt% POSS-polyurethane film after insertion into the vacuum system (a), after 2 hr (b), 24 hr (c), and 63 hr exposure to the hyperthermal AO flux (d), and 4 hr air exposure following the 63 hr exposure (e).

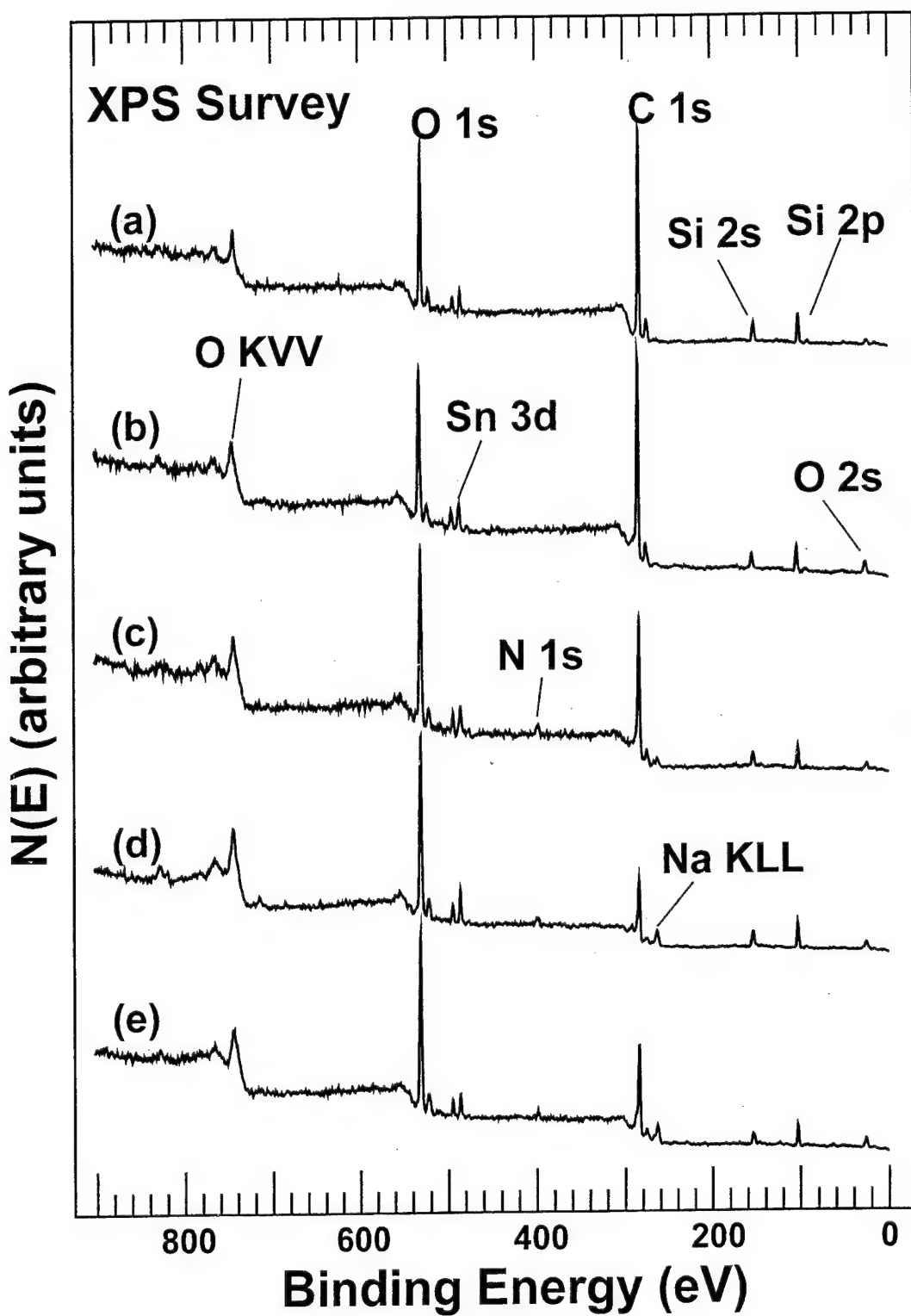


Figure 4-6. XPS survey spectra obtained from a 60 wt% POSS-polyurethane film after insertion into the vacuum system (a), after a 2 hr (b), 24 hr (c) and 63 hr exposure to the hyperthermal AO flux (d), and 3.3 hr air exposure following the 63 hr exposure (e).

Variations in peak shapes and positions are observed between the nonexposed, AO-exposed, and air-exposed surfaces, indicating that the chemical species distribution is altered by exposure to the AO flux and then to air. In addition, no surface charging of the sample was evident during the experiment as this would have altered the spectra resulting in a significant binding energy (BE) shift. Differential charging also results in peak broadening or peak multiplicity. This was not observed in this study.

The C 1s peaks, shown in Figures 4-7(a) and 4-8(a), are broad and centered at 285 eV, indicating that the predominant form of carbon present for both as entered samples is aliphatic, located on the hard and soft segments of the polymer chain and the cyclopentyl groups on the POSS cages [110]. In spectra b-d of both figures, the C 1s peaks becomes broader, displaying visible shoulders with increasing exposure to the O-atom flux. A shoulder due to aromatic carbon is present in these spectra at 284.7 eV. Shoulders are also visible on the high BE side of the C 1s peak in spectra b, c and d of both figures. These are probably due to species such as alcohols, formaldehydes (BE ~286.0 to 287.7 eV) and organic acids (BE ~287.5) which form by reaction with the AO flux. These changes coincide with a decrease in the total carbon concentration in the near surface-region from 72.5 to 37.8 at.% for the 20 wt% POSS-PU sample and a decrease from 70.1 to 37.3 at% for the 60 wt% POSS-PU sample. Large reductions in the carbon concentrations after AO exposure were also seen in the POSS-PDMS study of Chapter 3 suggesting the selective removal of the cyclopentyl groups surrounding the POSS cages. Exposure to air (spectrum e) results in a 5.6 at.% increase and an 11.0 at% increase in C for the 20 wt% and 60 wt% sample respectively. The AO exposure generates reactive surface sites which most likely adsorb hydrocarbons from the air.

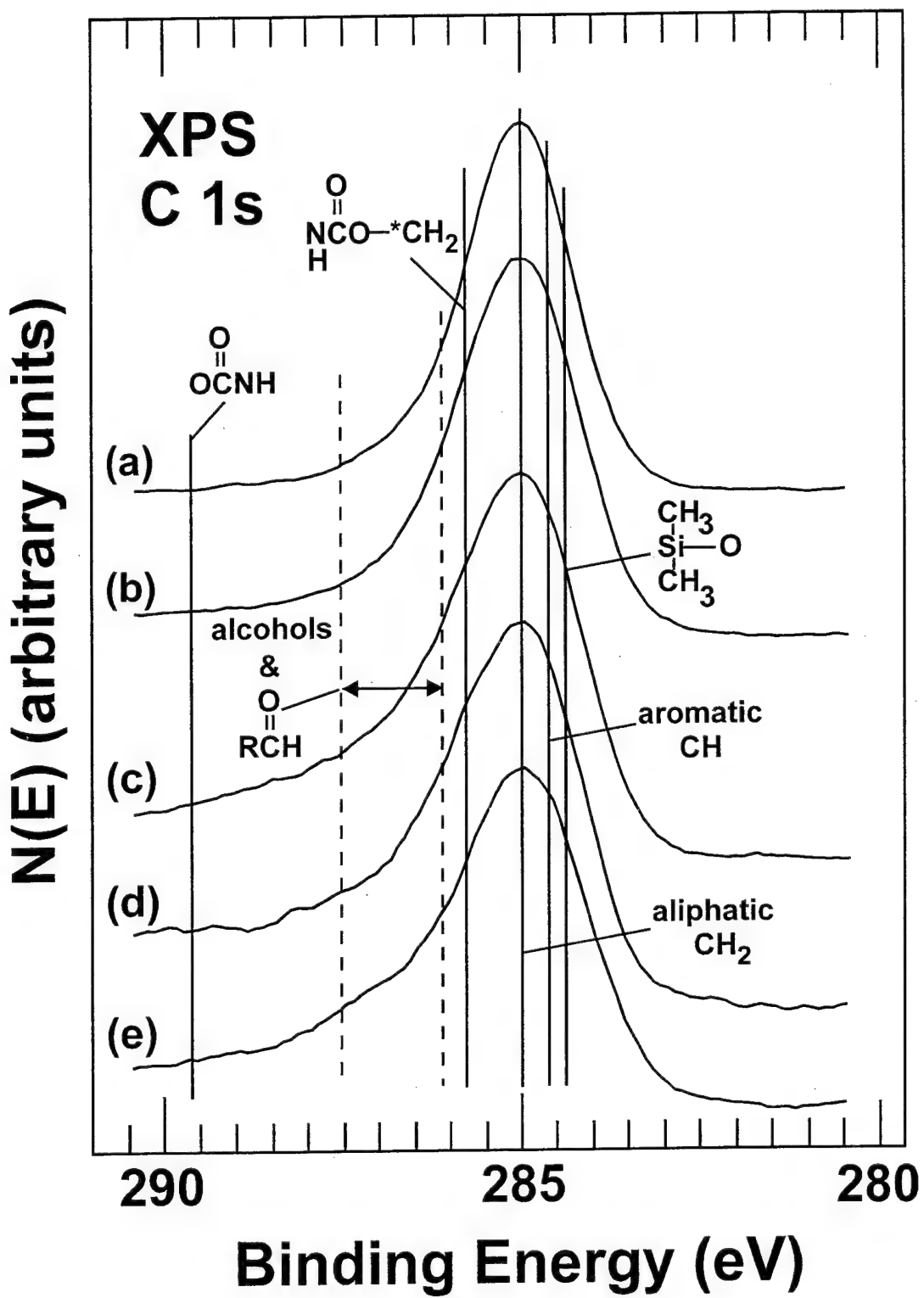


Figure 4-7. XPS C 1s spectra obtained from a solvent-cleaned, 20-wt% POSS-polyurethane film after insertion into the vacuum system (a), after 2 hr (b), 24 hr (c), and 63 hr exposure to the hyperthermal O-atom flux (d), and 4.0 hr air exposure following the 63 hr O-atom exposure (e).

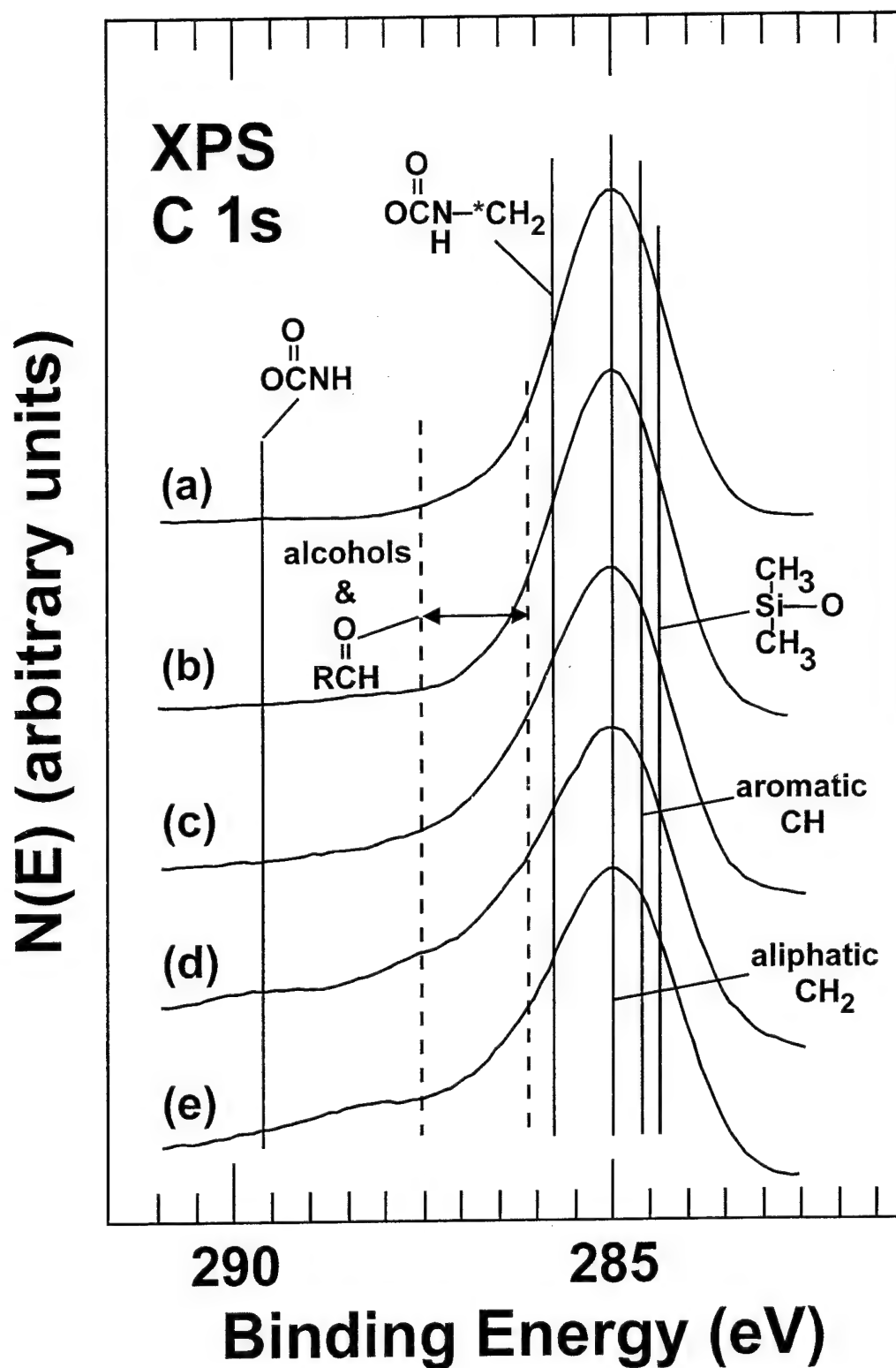


Figure 4-8. XPS C 1s spectra obtained from a solvent-cleaned, 60-wt% POSS-polyurethane film after insertion into the vacuum system (a), after 2 hr (b), 24 hr (c), and 63 hr exposure to the hyperthermal O-atom flux (d), and 3.3 hr air exposure following the 63 hr O-atom exposure (e).

The O 1s spectra obtained from the as-entered samples are shown in spectra (a) of Figures 4-9 and 4-10. Boths peaks are broad and centered at 532.1 eV and 531.9 eV for the 20 wt% and 60 wt% sample respectively. The predominant form of oxygen present for the as-entered samples corresponds to the carbonyl in the urethane segment (531.9 eV) of the polymer and the oxygen present in the POSS cages (532.0 eV). The oxygen content on the surface of both samples gradually increases with increasing exposures to the oxygen-atom source. After 63-h total exposure the oxygen content in the 20 wt% POSS-PU sample increases from an initial 18.5 to 32.6 at.%. This increase coincides with the O 1s spectra in (b)-(d) shifting to a higher binding energy corresponding to the formation of silica on the surface. This trend is also observed for the 60 wt% POSS-PU sample in Figure 4-10 as well as the POSS-PDMS sample in Chapter 3. Na also migrates to the surface from the bulk of the polymer as the silica layer is being formed. After 63-h the Na concentration is 13.6 at.% for the 20 wt% sample and 3.0 at% fo the 60 wt% sample. Exposure to air results in an increase in the surface O content as the reactive surface adsorbs hydrocarbons from the air, changing the relative composition on the surface of the polymer. However, the peak remains centered at the binding energy corresponding to SiO_2 , thus indicating that the silica layer formed is chemically stable. This conclusion is corroborated by the Si 2p spectra discussed next.

The Si 2p peaks obtained for both POSS-PU samples after the various treatments are shown in Figures 4-11 and 4-12. The Si 2p peaks for both as-entered sample (spectra a) are broad, indicating the presence of several chemical states of silicon. These peaks are centered at a BE of 102.7 eV, which corresponds to $\text{RSiO}_{1.5}$ in the POSS cage.

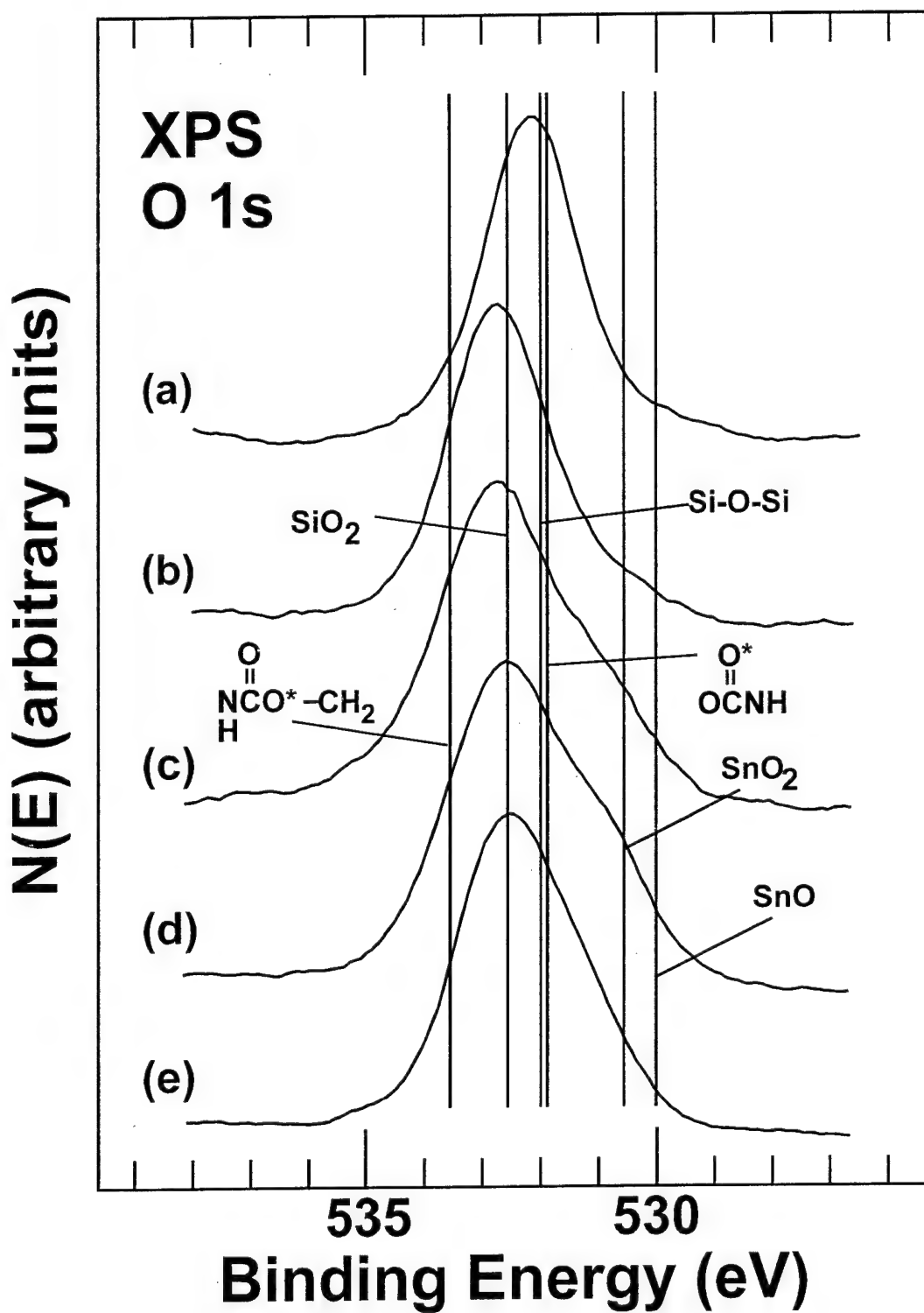


Figure 4-9. XPS O 1s spectra obtained from a solvent-cleaned, 20-wt% POSS-polyurethane film after insertion into the vacuum system (a), after 2 hr (b), 24 hr (c), and 63 hr exposure to the hyperthermal O-atom flux (d), and 4.0 hr air exposure following the 63 hr O-atom exposure (e).

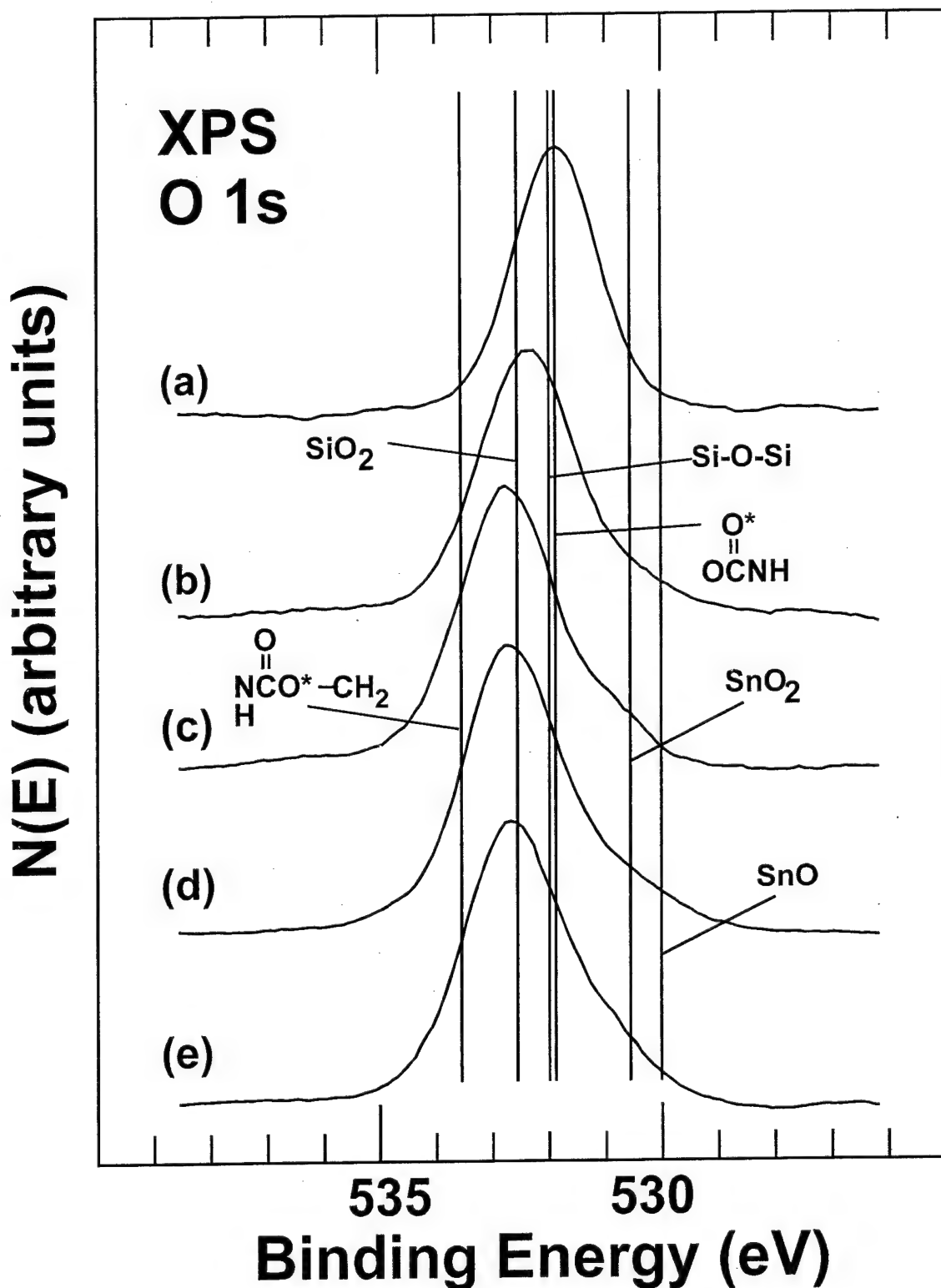


Figure 4-10. XPS O 1s spectra obtained from a solvent-cleaned, 60-wt% POSS-polyurethane film after insertion into the vacuum system (a), after 2 hr (b), 24 hr (c), and 63 hr exposure to the hyperthermal O-atom flux (d), and 3.3 hr air exposure following the 63 hr O-atom exposure (e).

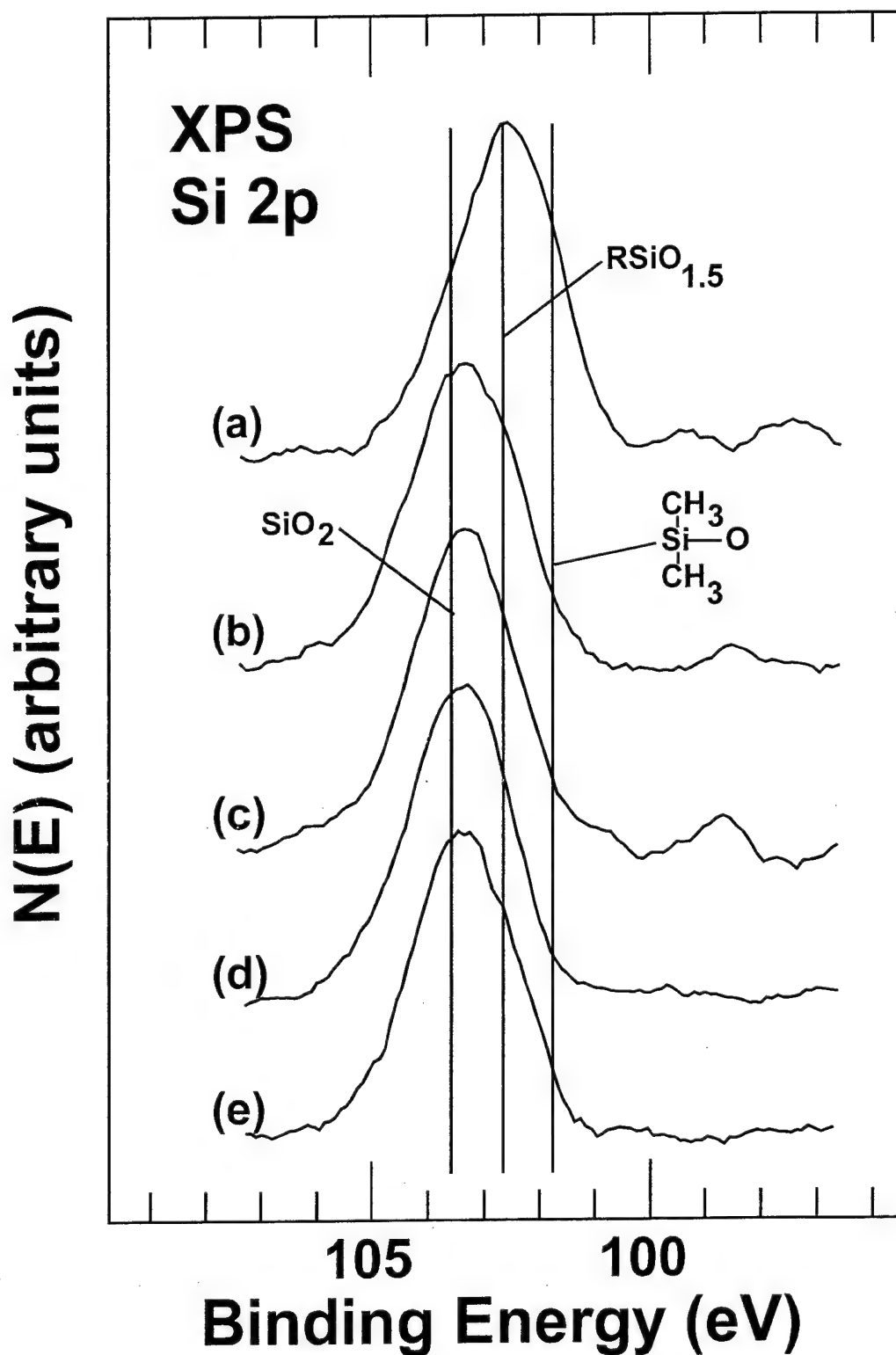


Figure 4-11. XPS Si 2p spectra obtained from a solvent-cleaned, 20-wt% POSS-polyurethane film after insertion into the vacuum system (a), after 2 hr (b), 24 hr (c), and 63 hr exposure to the hyperthermal O-atom flux (d), and 4.0 hr air exposure following the 63 hr O-atom exposure (e).

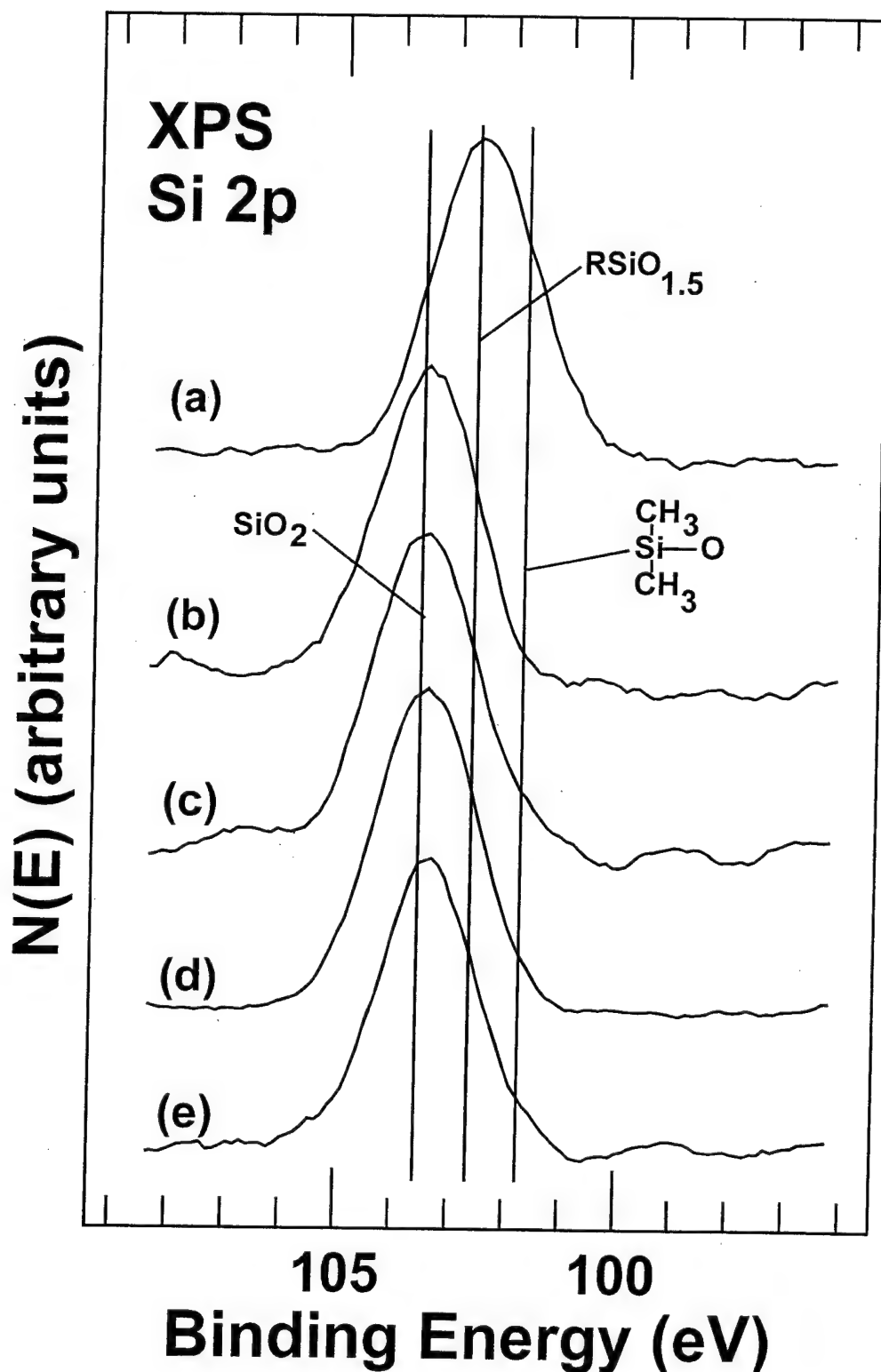


Figure 4-12. XPS Si 2p spectra obtained from a solvent-cleaned, 60-wt% POSS-polyurethane film after insertion into the vacuum system (a), after 2 hr (b), 24 hr (c), and 63 hr exposure to the hyperthermal O-atom flux (d), and 3.3 hr air exposure following the 63 hr O-atom exposure (e).

However, spectra (b)-(d) in both figures reveal the formation of a SiO₂ layer with incremental exposures to the O-atom flux. The fact that for both POSS-PU samples little difference is observed in the spectra obtained after the 24-hr and 63-hr exposures indicates that this silica layer forms a protective barrier on the surface which prevents further degradation of the polymer with longer exposure to the O-atom flux. The 5-eV AO is not energetic enough to penetrate more than one or two atomic layers into the polymer while, XPS probes as deeply as 30 or more atomic layers beneath the surface. The significant compositional changes observed indicate that most of the near-surface region examined by XPS is altered by the AO exposure. The chemical reactions which form CO₂ and H₂O are exothermic, so the local surface temperature may be relatively high. This and the fact that the AO causes a chemically induced driving force result in diffusion of subsurface C and H to the surface where they react with the AO. This mechanism is responsible for the subsurface compositional alterations observed using XPS.

4.4 Summary

The surfaces of two films of a polyhedral oligomeric silsesquioxane-polyurethane copolymer containing 20 wt% and 60 wt% POSS were characterized in-situ using XPS before and after exposure to different fluences of oxygen atoms produced by an ESD hyperthermal oxygen atom source. The XPS data indicate that exposure to AO reduces the carbon content on the surface by approximately 35 at% after a 63 hr exposure to an AO flux of 2.0×10^{13} atoms/cm²-s. High resolution XPS data suggest that the atomic oxygen initially attacks the cyclopentyl groups on the POSS cage forming CO₂ and water which desorb. Increased exposure to the O-atom flux results in the formation of a silica

layer on the surface which acts as a protective barrier preventing further degradation of the underlying polymer. Exposure to air also results in the adsorption of hydrocarbon species on the reactive surface formed by exposure to AO₂

CHAPTER 5
SYNTHESIS, CHARATERIZATION AND IN-SITU ATOMIC OXYGEN EROSION
STUDIES OF POSS-POLYIMIDES

5.1 Introduction

During the course of this research and development of the ESD atomic oxygen source, our research group has carried out several erosion studies of polymeric surfaces used in space. We have also carried out studies of ion-irradiated polymer surfaces, noting similarities between these studies, as highly reactive surfaces are formed in both cases. In particular, we have studied the high performance polyimide Kapton, a widely used spacecraft material which has previously been examined in numerous other AO studies using plasma sources, laser excitation sources and actual space flight data. The general conclusion from these studies is that the oxygen concentration in the near-surface region is increased somewhat by AO exposure. In addition, Kapton has been reported to erode significantly with a reported atomic oxygen reaction efficiency (R_e) of 3.0×10^{-24} cm³/atom of AO [15, 25]. Early degradation studies of these class of polyimides revealed the evolution of CO, CO₂ and hydrogen during decomposition [118].

The polyimide Kapton is synthesized in a condensation polymerization of the monomers 4,4'-oxydianiline (ODA) and pyromellitic dianhydride (PMDA) in the presence of a polar aprotic solvent such as N,N-dimethylacetamide (DMAc) as shown in Figure 5-1. The resulting polyamic acid, a soluble, tractable precursor, is then usually cast as a film by removing the solvent under vacuum followed by imidization through curing under nitrogen at elevated temperatures of around 300°C.

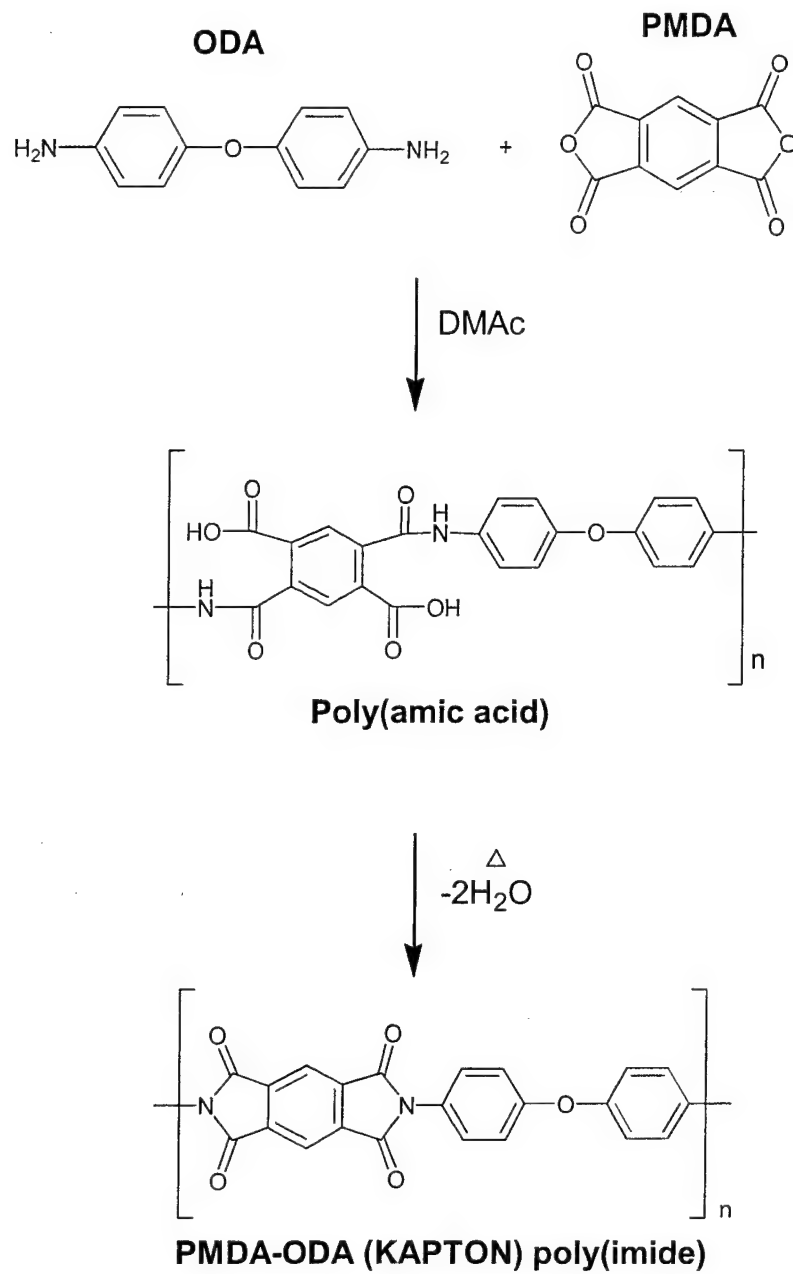


Figure 5-1. Synthesis of Kapton (PMDA-ODA) polyimide through condensation polymerization of pyromellitic dianhydride and oxydianiline.

The resulting polyimides are semi rigid-rod, ladder like polymers, which are insoluble, have excellent thermal stability and mechanical properties as well as low dielectric constants. Morphological studies of this polymer have revealed that these macroscopic properties are dependent on the microstructural organization of the PMDA-ODA polymer

chains [119]. This organization is strongly dependent on the processing method employed. Ojeda and Martin [119] imaged PMDA-ODA crystals using high resolution electron microscopy revealing highly ordered lamellar structures oriented perpendicular to the molecular chain direction as shown in Figure 5-2 and 5-3. Their analysis concluded that not only could these polymer ⁵_A fold about the biphenyl-ether linkages in the ODA segment, but that bending is also possible at the covalent imide nitrogen bond as well.



Figure 5-2. High resolution electron microscopy image of PMDA-ODA crystal lamellae; reprinted from reference [119] with permission from the American Chemical Society.

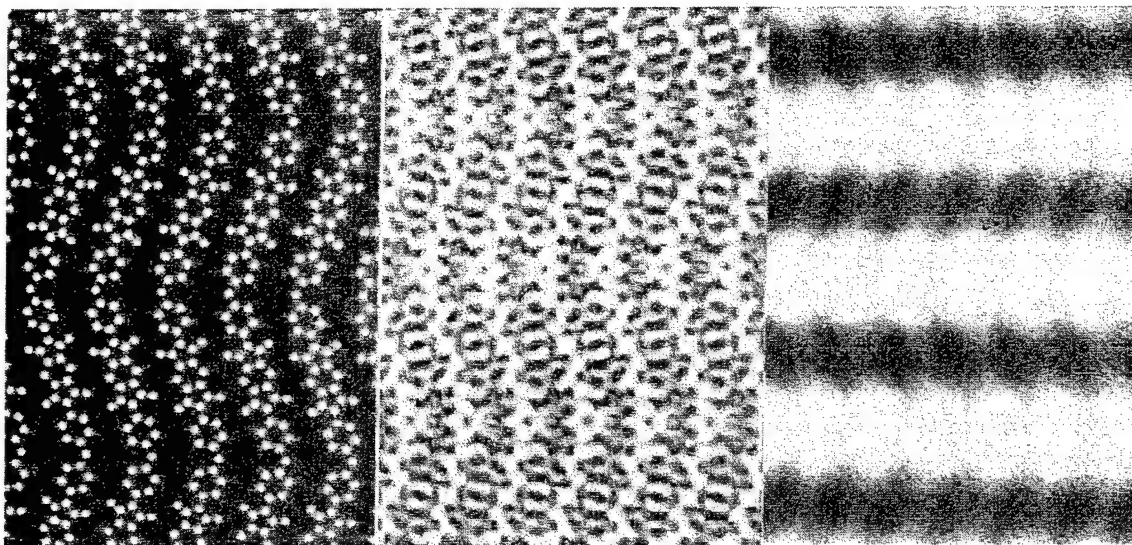


Figure 5-3. Computer simulated high resolution electron microscopy images of crystalline PMDA-ODA showing conformational zigzag of the molecule resulting in observed lamellar structure; reprinted from reference [119] with permission from the American Chemical Society.

In order to understand the AO erosion mechanism of polyimides, our research group carried out studies of a Kapton 300 HN film [120, 121] using the ESD AO source described in Chapter 2. In these investigations, Kapton films were exposed to an AO flux for increasing time periods and the surfaces intermittently characterized using X-ray photoelectron spectroscopy (XPS). Since the ESD AO source and XPS analysis chamber are contained in the same ultrahigh vacuum system the sample was not exposed to air after the AO exposure and before analysis. In order to lay the foundation and set a basis for comparison for POSS-polyimides later in this chapter, the results of these studies are briefly summarized below.

The PMDA-ODA Kapton molecular structure with labeled atomic sites and their corresponding electron binding energies are shown in Figure 5-4 and Table 5-1 respectively. Figure 5-5 shows the XPS survey spectra obtained from the Kapton film (a) after insertion into the UHV system, (b) after a 20-min AO exposure, (c) after a 24-hr

AO exposure and then (d) a 3-hr air exposure. With increasing AO fluence the O1s peak height is decreased relative to the heights of the C 1s and N 1s peaks. After a 24 hr AO exposure the O concentration on the surface decreased from an initial 18.1 at% to 9.2 at%. This is in contrast to reports from other studies from space and ground simulations indicating that there is a significant increase in the oxygen concentration of Kapton surfaces after AO exposure.

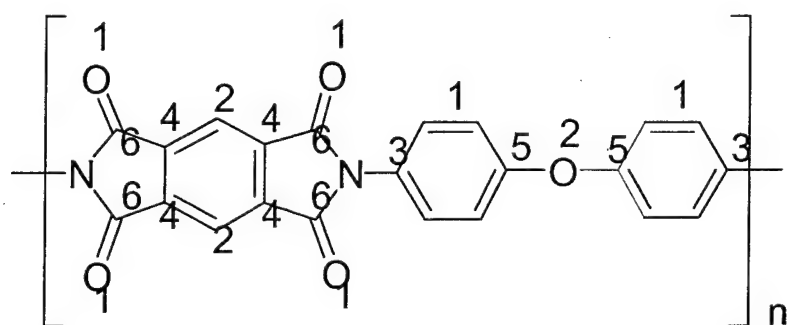


Figure 5-4. Molecular structure of Kapton (PMDA-ODA) with numerically labeled atomic sites.

After exposure of the AO-exposed surface to air, the O 1s peak height is significantly increased relative to the C 1s and N 1s peak heights. The O concentration increases to a calculated 17.9 at%. This result indicates that a highly reactive surface forms during AO exposure and that this surface reacts with components in air to increase the near-surface oxygen concentration. This result explains why all other studies have found an increase in the near-surface oxygen concentration. In those other studies the samples either were exposed to air before characterization or contaminants including O₂, H₂O, etc. were contained in the AO flux.

Table 5-1: Kapton Binding Energies [110].

Parameter	C 1s						O 1s		
	1	2	3	4	5	6	1	2	N 1s
BE, eV	284.7	285.6	285.7	285.8	286.3	288.6	532.0	533.2	400.6
%	36	10	10	17	10	17	77	23	100

Further insight into the erosion mechanism can be gained by examining the high-resolution C 1s and N 1s features shown in Figures 5-6 and 5-7 and relating this information to the PMDA-ODA Kapton structure shown in figure 5-4. An obvious change in the C 1s spectrum with increasing AO exposure is the loss of the C (6) feature which is due to reaction of the carbonyl groups with AO to form CO₂. If these carbonyl groups are chemically eroded out of the polymer matrix, then a change in the chemical state of the nitrogen should be the case. This is clearly observed in the N 1s spectra. As the C (6) feature is lost, a new C-N feature becomes apparent. As surface species are removed from the Kapton surface by AO, chemical bonds are broken leaving reactive radical species behind which do not crosslink due to geometrical bonding constraints [120]. These experiments demonstrate that AO erosion studies of polymers must be carried out without air exposure and using a source which produces a high purity AO flux. Furthermore, the initial Kapton surface is quite smooth, and it becomes quite rough with AO exposure according to AFM data.

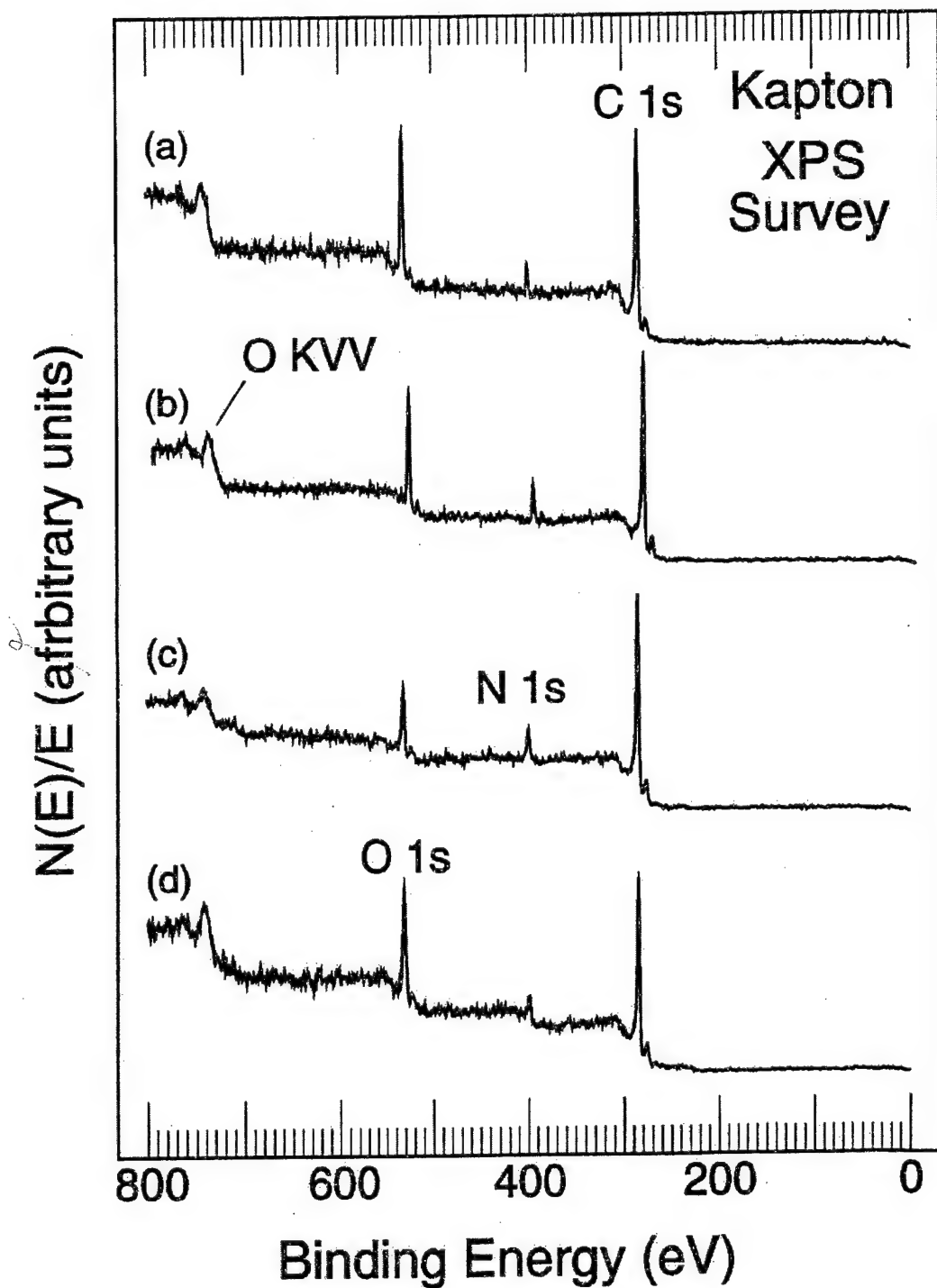


Figure 5-5. XPS survey spectra obtained from a solvent-cleaned, Kapton film after (a) insertion into the vacuum system, (b) a 20-min, and (c) a 24-h exposure to the hyperthermal AO flux, and (d) a 3-hr air exposure following the 24-hr exposure [120].

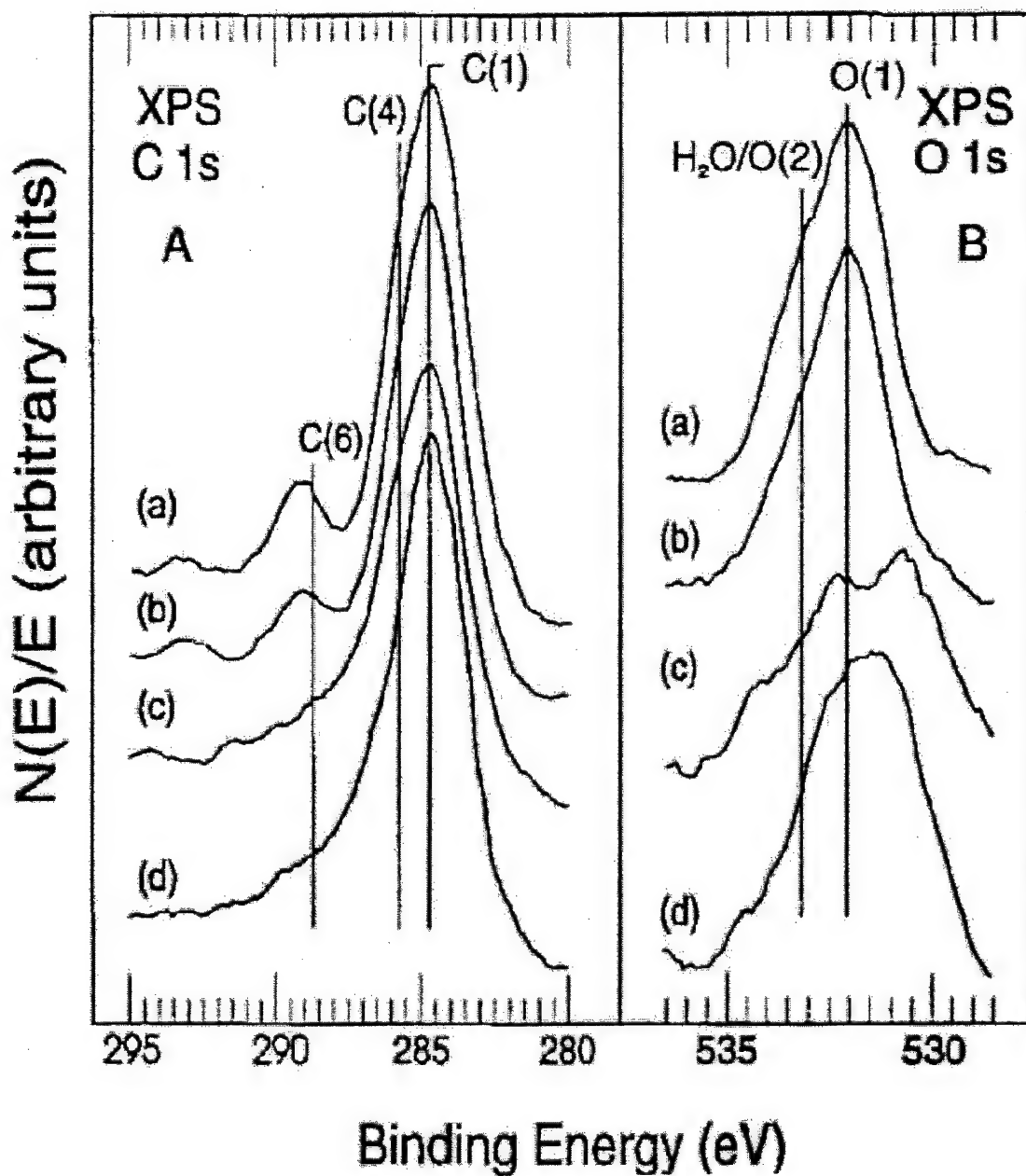


Figure 5-6. High Resolution C 1s and O 1s spectra obtained from a solvent-cleaned, Kapton film after (a) insertion into the vacuum system, (b) a 20-min, and (c) a 24-h exposure to the hyperthermal AO flux, and (d) a 3-hr air exposure following the 24-h exposure [120].

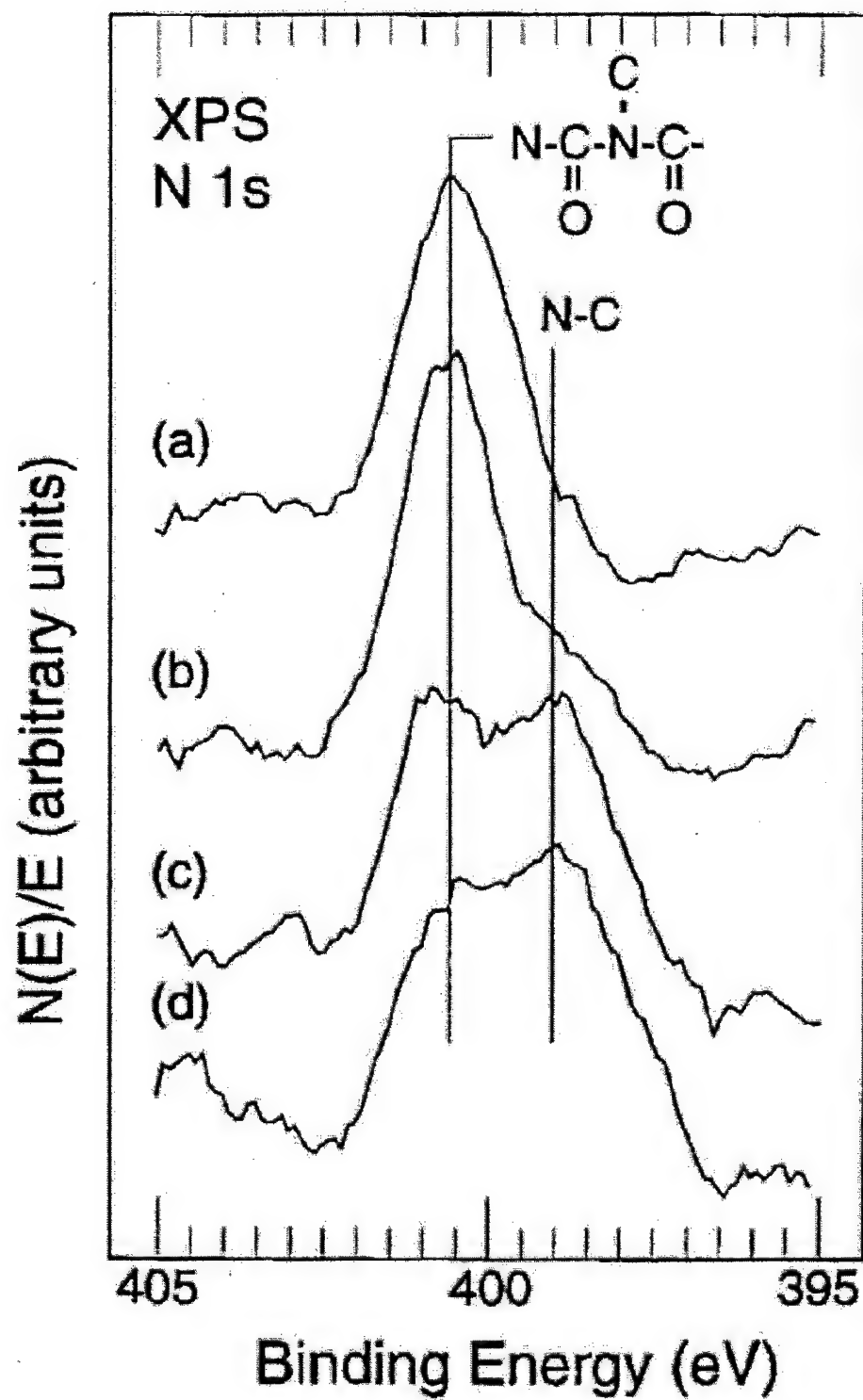


Figure 5-7. High Resolution N 1s spectra obtained from a solvent-cleaned, Kapton film after (a) insertion into the vacuum system, (b) a 20-min, and (c) a 24-h exposure to the hyperthermal AO flux, and (d) a 3-hr air exposure following the 24-hr exposure [120].

Our research group has collaborated with researchers at Gesellschaft fur Schwerionen Forschung (GSI) in Darmstadt on ion irradiation of polymer surfaces. The goal is to use a focused, high-energy beam of ions to alter the refractive index of polymers such as polymethylmethacrylate (PMMA) to produce optical waveguides for computer chip applications. In these studies similar results to those obtained in the AO-exposed Kapton study were obtained. Highly reactive surfaces are produced by ion irradiation and these surfaces react with air. Again, cross-linking is not dominant mechanism leaving reactive unsaturated bonds at the surface. The masses of the species emitted during ion irradiation were monitored, and the distribution was observed to move toward lighter species as the polymer chains were broken by the high-energy ions. These experimental results contradict previous studies in which only low-mass species were detected and in which cross-linking was proposed. However, these results are consistent with a molecular dynamic simulation by Beardmore and Smith [122]. Based on these results our research group carried out a comparison study of ion-irradiated Kapton versus AO-irradiated Kapton [121]. In this study we found that there are many similarities between Kapton surfaces irradiated with AO and 1-keV Ar^+ . One explanation is that the sputtering effect of 5 eV AO is as significant as its chemical reactivity. This will be examined more thoroughly in future studies.

5.2 Development of First POSS-Aniline Monomer For Polyimide Synthesis

Polyhedral oligomeric silsesquioxanes are an interesting class of three dimensional-caged Si-O clusters derived from the hydrolytic condensation of trifunctional organosilicon monomers as discussed in Chapter 1. Feher et al. have focused on developing new routes for synthesizing incompletely condensed

silsesquioxane frameworks which serve as versatile precursors to hybrid organic-inorganic polymers. Recently, Feher's group reported acid and base mediated methods of selectively cleaving fully condensed silsesquioxanes [45, 46, 123, 124]. Particularly, they reported that cleavage of a single Si–O–Si linkage in $R_8Si_8O_{12}$ can be achieved directly with complete retention of stereochemistry at Si to afford endo disilanols with structure **2** as shown in Figure 5-8. These disilanols can then be reacted with strong acids HBF_4/BF_3 under controlled conditions to substitute the two hydroxyl groups with F atoms with inversion of stereochemistry. Details of this synthesis and characterization of **3** has been reported in reference [47].

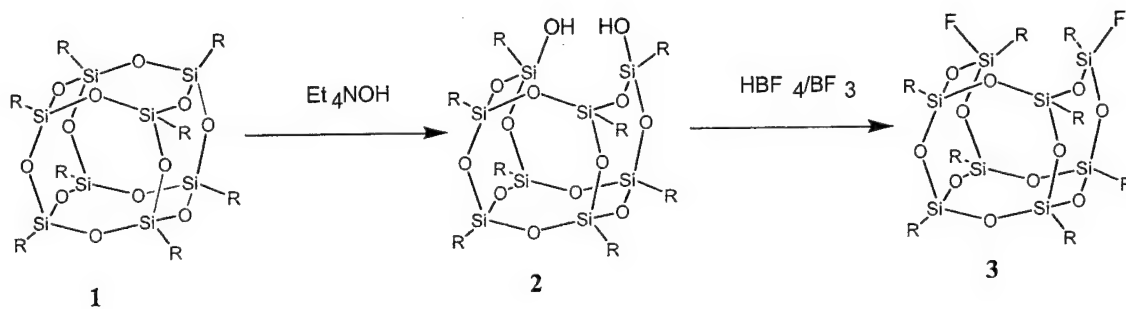


Figure 5-8. Base mediated selective Si–O–Si cleavage of fully condensed silsesquioxane.

The resulting POSS exodifluoride **3** has since then been used as a precursor for a difunctional POSS aniline monomer $R_8Si_8O_{11}(PhNH_2)_2$ which can be copolymerized to form POSS-polyimides. The synthetic scheme for this difunctional POSS aniline monomer shown in Figure 5-9 was also first developed by Feher et al. and relayed to our research group at AFRL/PRSM through personal communication. The reaction is moisture and air sensitive, must be carried out under inert atmosphere and involves an amine protecting step as described below.

5.2.1 Synthesis of $(c\text{-C}_6\text{H}_{11})_8\text{Si}_8\text{O}_{11}[p\text{-C}_6\text{H}_4\text{NH}_2]_2$

Under a nitrogen atmosphere, 4-bromoaniline (1 g, 5.81 mmol) was added to a 15 ml diethylether solution of triethylamine (1.29 mg, 12.78 mmol). In a separate flask, vacuum distilled 1,2-bis(chlorodimethylsilyl)ethane (1.25 g, 5.81 mmol) was dissolved in 15 ml of diethylether and the solution was transferred to an addition funnel and added dropwise to the bromoaniline triethylamine solution. A white precipitate of triethylamine HCl salt formed immediately and the solution is let to stir overnight. The solution was filtered and solvent removed under vacuum. The compound **5** is then redissolved in diethylether at which 1 equivalent of a 1.6 M butyllithium solution is added dropwise under nitrogen atmosphere in order to undergo halogen-metal exchange at 0 °C. The resulting product **6** is reacted in diethylether with 2 equivalents of POSS exodifluoride **3** resulting in precipitation of LiF salts which are subsequently filtered. The dried product is then dissolved in a 3:1:3 diethylether:methanol:THF solution to which is added a 5 mol% solution of pyridinium p-toluenesulfonate (PPTS) while stirring at room temperature for 30 min. The resulting light yellow solution is extracted with diethylether and washed with brine. The extract is dried over Na_2SO_4 , filtered and solvent removed under reduced pressure to afford a white solid which is recrystallized from hexane. The final POSS dianiline product **8** is moisture, air and light sensitive and is stored under nitrogen in a dry box. The ^1H , ^{13}C and ^{29}Si NMR 400MHz spectra for this compound in CDCl_3 are shown in Figures 5-10, 5-11 and 5-12 respectively. ^1H NMR (CDCl_3) δ 0.56-0.74 (m, 8H), 0.90-1.36 (m, 40H), 1.46-1.90 (m, 40H), 3.80 (s, 4H), 6.69 (d, $^3J = 8.2$ Hz, 4H), 7.41 (d, $^3J = 8.2$ Hz, 4H). ^{13}C NMR (CDCl_3) δ 22.95, 24.46, 26.44, 26.51, 26.78,

26.84, 26.89, 26.93, 27.44, 27.65, 27.70, 27.77, 114.22, 124.14, 135.57, 147.47. ^{29}Si NMR (CDCl_3) δ -68.59, -66.93, -33.95. Anal. Calcd for $\text{C}_{60}\text{H}_{100}\text{N}_2\text{O}_{11}\text{Si}_8$: C, 57.65; H, 8.06; N, 2.24. Found: C, 57.72; H 8.18; N, 2.26.

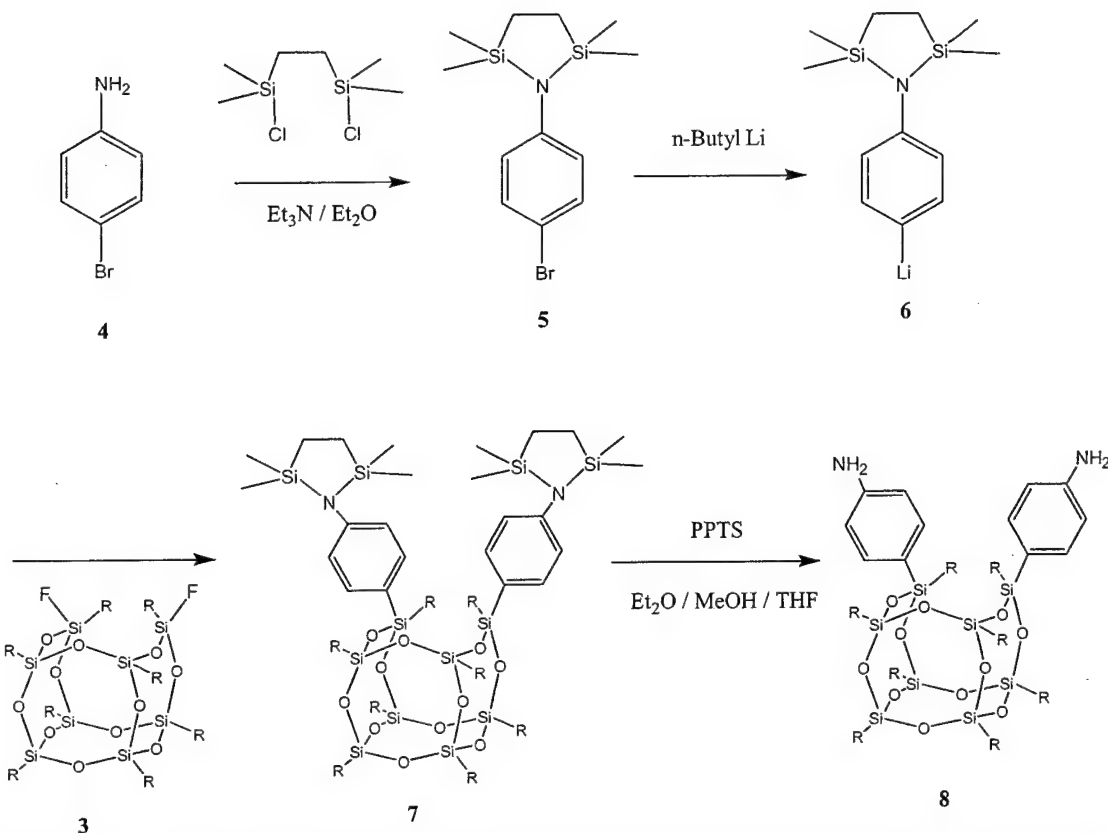


Figure 5-9. Synthesis of $(\text{c-C}_6\text{H}_{11})_8\text{Si}_8\text{O}_{11}[\text{p-C}_6\text{H}_4\text{NH}_2]_2$ POSS dianiline monomer used in POSS-polyimide synthesis.

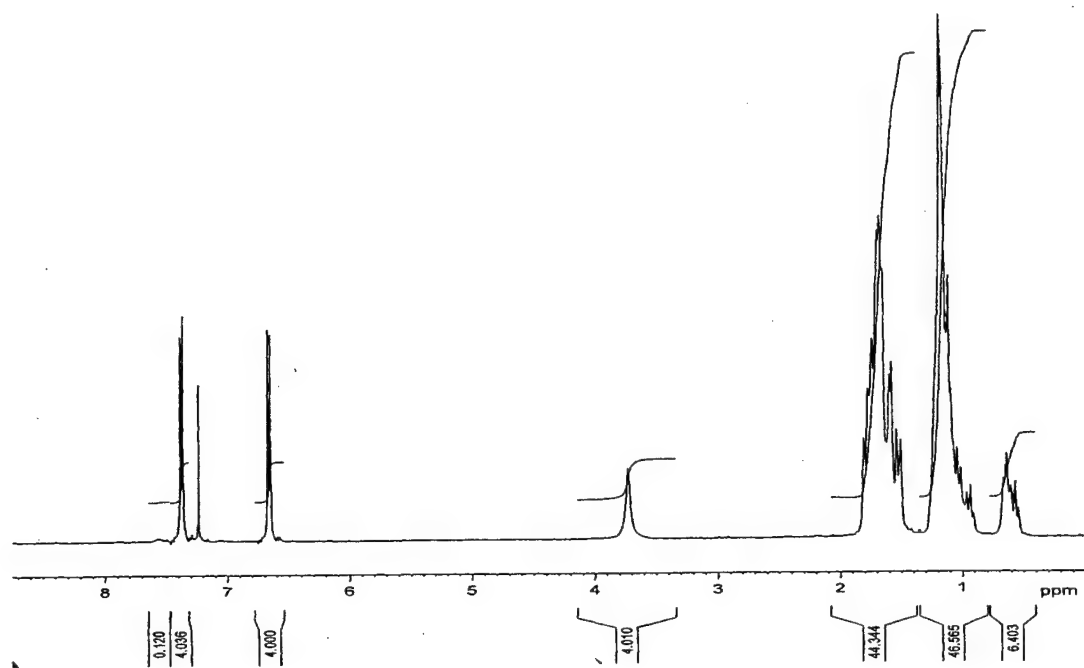


Figure 5-10. ^1H NMR of $(\text{c-C}_6\text{H}_{11})_8\text{Si}_8\text{O}_{11}[\text{p-C}_6\text{H}_4\text{NH}_2]_2$ POSS dianiline monomer in CDCl_3 .

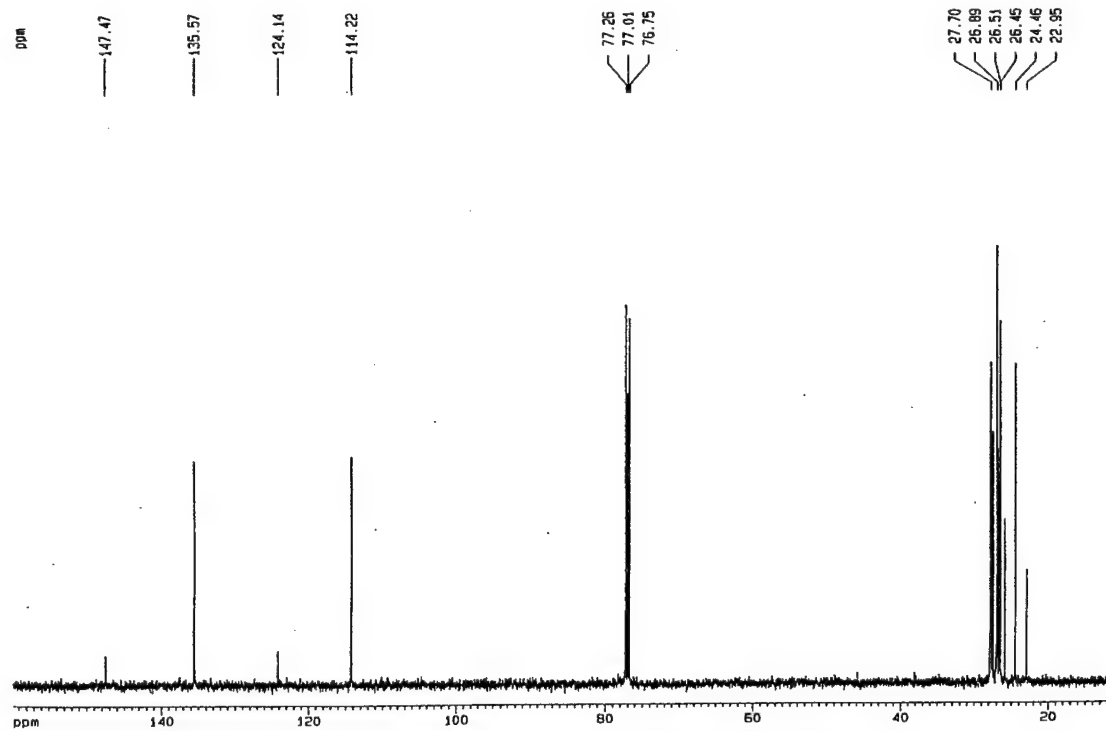


Figure 5-11. ^{13}C NMR of $(\text{c-C}_6\text{H}_{11})_8\text{Si}_8\text{O}_{11}[\text{p-C}_6\text{H}_4\text{NH}_2]_2$ POSS dianiline monomer in CDCl_3 .

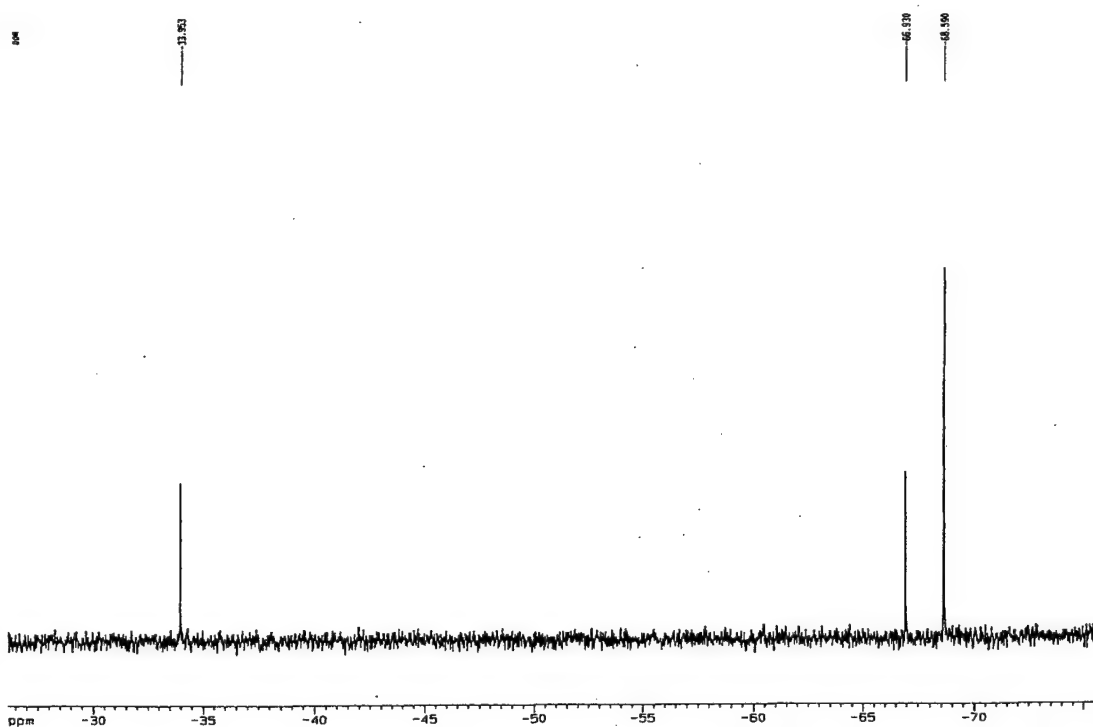


Figure 5-12. ^{29}Si NMR of $(\text{c-C}_6\text{H}_{11})_8\text{Si}_8\text{O}_{11}[\text{p-C}_6\text{H}_4\text{NH}_2]_2$ POSS dianiline monomer in CDCl_3 .

5.2.2 Synthesis of POSS-Polyimides.

Representative procedure for the preparation of 5 weight % POSS polyimide: A small 3-neck round bottom flask was dried in an oven, then equipped with a mechanical stirring apparatus. The system was purged with dry nitrogen for 30 min. 4,4'-oxydianiline (450 mg, 2.25 mmol) and POSS-dianiline **8** (49 mg, 0.040 mmol) were added to a flame-dried 25 mL round bottom flask in a drybox. Pyromellitic dianhydride (500 mg, 2.29 mmol) was added to a separate, flame-dried 25 mL round bottom flask in a drybox. The flasks were sealed with rubber septa, and DMAc (previously purified via ^{from?} distillation from BaO at reduced pressure) (3 mL) was added to each flask via syringe. The anilines readily dissolved, while the dianhydride only partially dissolved. DMAc (5 mL) was added to the 3-necked flask via syringe. The solution of anilines was transferred to the 3-neck flask via syringe, and the 25 mL flask was washed with 2 X 1

mL of DMAc. The washes were transferred to the 3-neck flask. The dianhydride slurry was added to the reaction mixture via syringe and the 25 mL flask was washed with 2 X 1 mL DMAc. Upon addition of the dianhydride, the solution immediately became viscous, homogeneous, and yellow in color. The poly(amic acid) solution was stirred for 4 h at room temperature. A film is then cast from the resulting poly(amic acid) on a clean glass plate and placed in a clean oven with flowing nitrogen at 80 degrees Celsius for 4 hours. The temperature of the oven is then slowly raised to 300 °C at which point the film is ^{left} ~~left~~ ^{to} cure for approximately 1 hour. The synthetic scheme for this synthesis is illustrated in Figure 5-13.

5.3 Mechanical and Thermal Properties of POSS-Polyimides

The linear viscoelastic properties of polyimides with differing amounts of POSS incorporation were determined using a dynamical mechanical analyzer in tensile mode over a wide range of temperatures [125]. Figure 5-14 presents a comparison of storage modulus, $E'(T)$, as a function of temperature for polyimides with 0 %, 5 wt%, and 10 wt% POSS segments, respectively. All polymers exhibited a mechanical relaxation transition at temperature near 400 °C indicating the onset of large scale thermally induced motions. It is well known that this type of polyimide, Kapton, does not flow at elevated temperature. This was confirmed by the change in the magnitude of $E'(T)$ at the transition temperature, i.e., from around 1 GPa to 100 MPa. Normal (flexible) polymers would have dropped down to about 1 MPa. As shown in Figure 5-14, at temperatures below this relaxation, the magnitude of $E'(T)$ was not significantly affected by the addition of POSS segment in the polymer chain. However, at temperatures above this relaxation, the

magnitude of $E'(T)$ increases as Δ amount of POSS segments in the polymer chain increases.

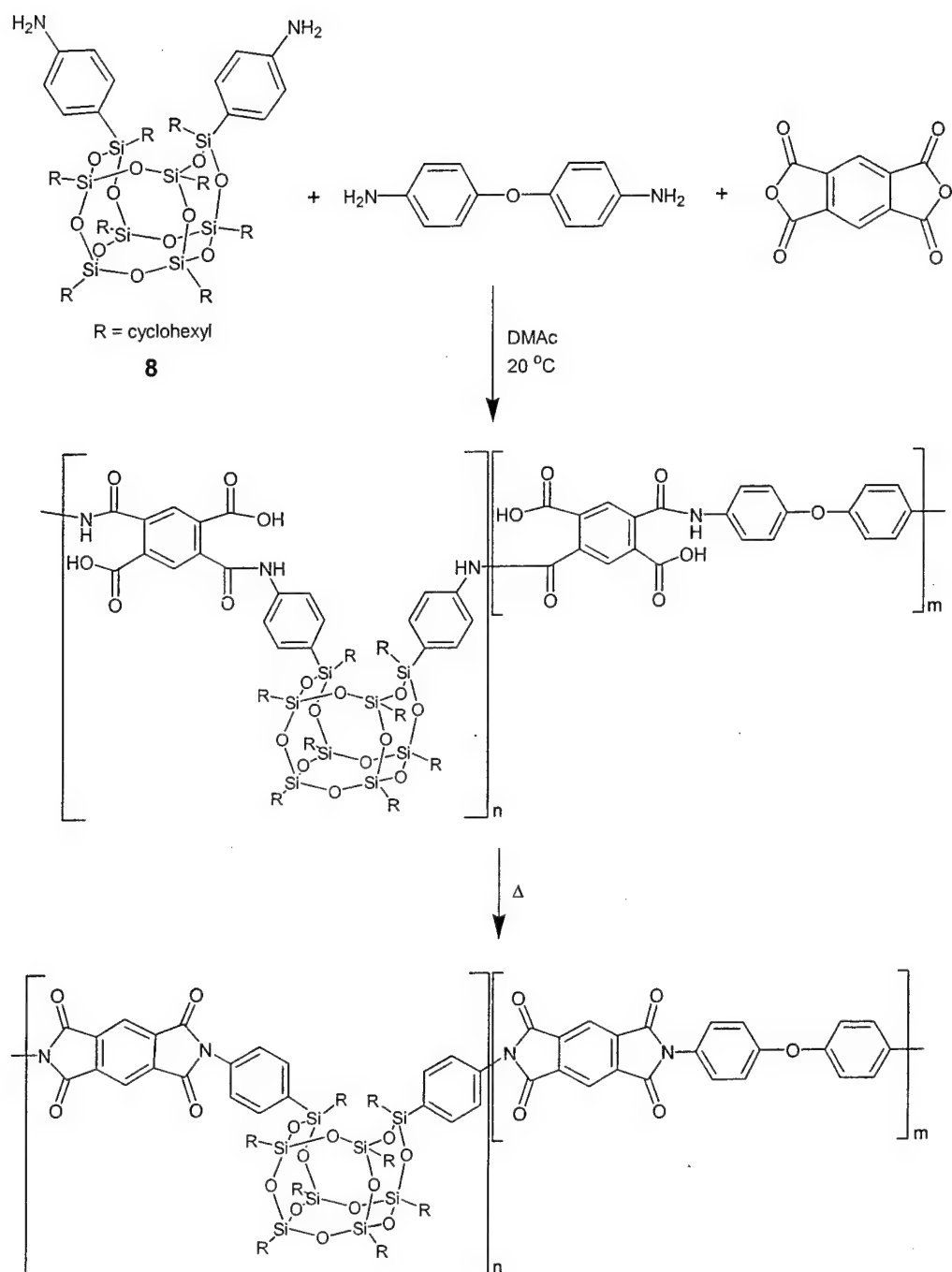


Figure 5-13. Synthesis of POSS- Polyimide.

The corresponding value of the plateau moduli depends on the amount of POSS incorporation in the polymer. The appearance of these plateau at temperatures above the mechanical relaxation transition, indicate a very strong POSS-POSS interaction where the modulus of polymer was not affected by the change in temperature. These observations suggest that the presence of POSS reduces the motion of ^{the} polymer chain, reinforcing it through these POSS-POSS interactions in a manner that could be analogous to entanglements.

Figures 5-15 and 5-16 shows thermal gravimetric analysis (TGA) charts of Kapton control and 5, 10 and 30 wt% POSS-polyimides under nitrogen and air purge respectively.

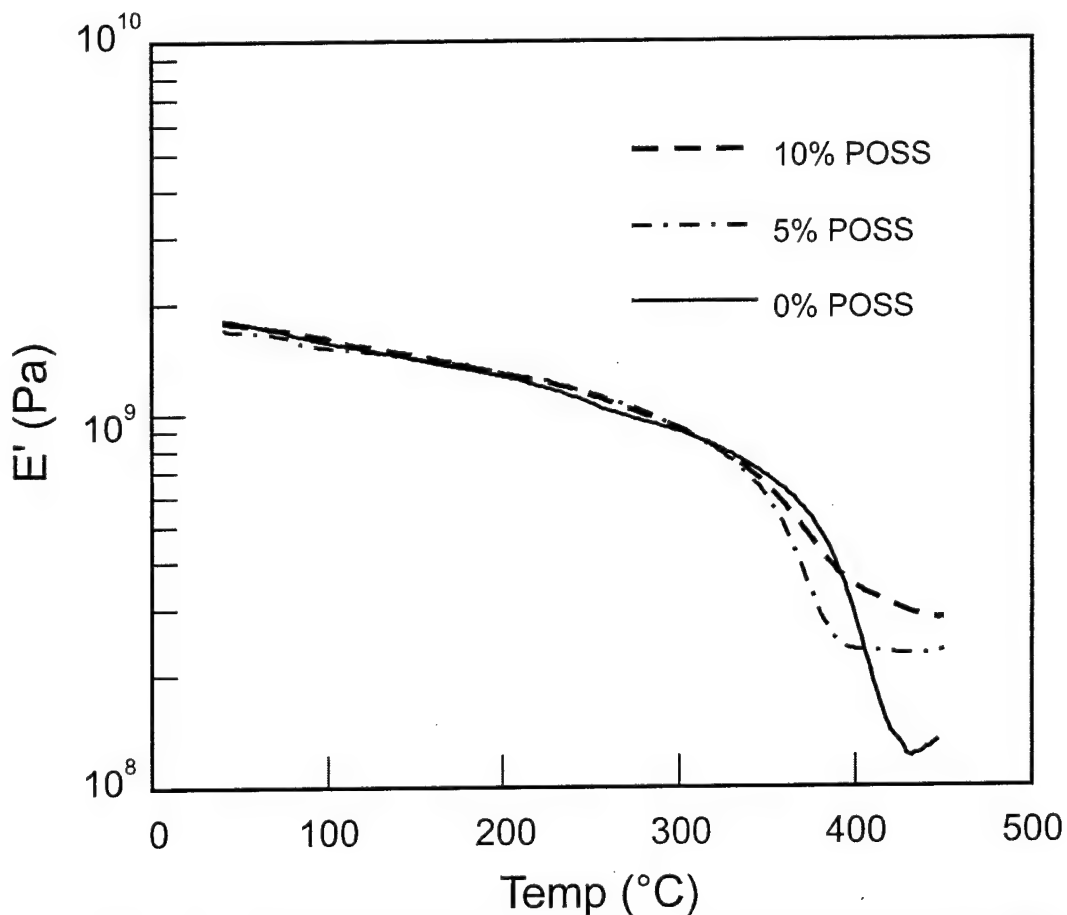


Figure 5-14. Plot of storage modulus $E'(T)$ vs. temperature for Kapton and POSS-Kapton Polymers

As can be seen from Figure 5-15, the onset of thermal degradation under a nitrogen atmosphere for the POSS containing polyimides begins sooner with higher POSS content. This could be attributed to the pyrolyzation of the weak Si-C bonds corresponding to the cyclohexyl groups surrounding the POSS cages. However, this degradation levels off sooner for polyimides with higher POSS content resulting in a higher char yields than for the Kapton control sample. A similar trend is observed for the same experiment conducted in air as shown in Figure 5-16. In this case however, there is a higher magnitude drop in the resulting char yields for each polymer since they pyrolyzed in air.

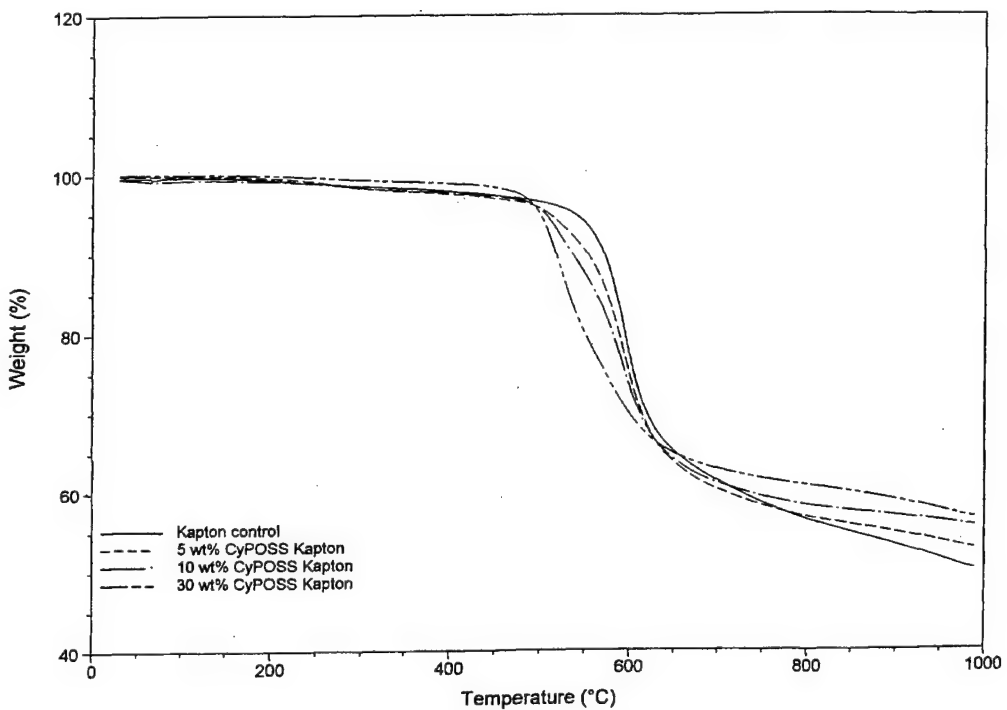


Figure 5-15. TGA for Kapton and POSS-Kapton polyimides under N_2 , $10\text{ }^{\circ}\text{C/min}$ heat ramp.

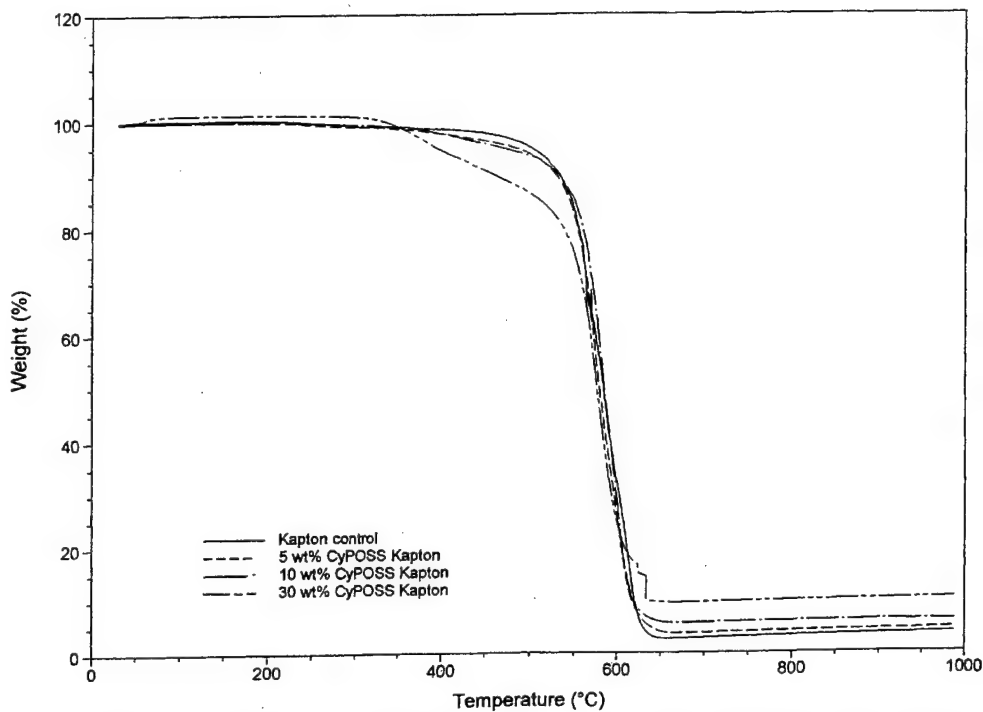


Figure 5-16. TGA for Kapton and POSS-Kapton polyimides under air, 10 °C/min heat ramp.

5.4 Experimental

5.4.1 Profilometry and Atomic Oxygen Etching Experiments

Samples of several POSS polymers, including POSS-Polyimides underwent a series of AO etching experiments conducted through a collaboration established with Prof. Timothy K. Minton from the chemistry department of Montana State University at Bozman. During these experiments, these samples were exposed to an oxygen plasma beam produced by a 5 Joule-pulsed CO₂ laser source described in Chapter 2 containing oxygen atoms with average kinetic energies of 2-15 eV.

Hyperthermal AO Beam

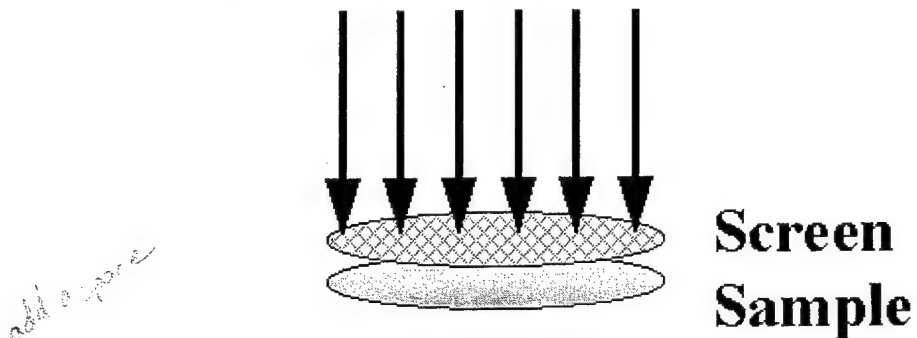


Figure 5-17. Diagram illustrating AO etching experiment using a protective screen to shield selective areas of the sample for profilometry measurements.

As depicted in Figure 5-17, a protective screen was placed in-between the sample and beam path in order to selectively erode only certain portions of the samples. The difference in etch depth between the eroded and protected part of the samples were then measured using stylus surface profilometry. Surface profilometry is a technique in which a diamond stylus, in contact with a sample, can measure minute physical surface variations as a function of position. It is commonly used to measure film thickness in thin film deposition and processing. Another important application is the measurement of crater depths for those surface analysis methods such as secondary ion mass spectrometry (SIMS) that use ion sputtering for depth profiling. Figure 5-18 (a) and (b) show magnified profilometry photographs of an etched, commercially available Kapton HN standard and a 10 wt% POSS-Kapton polyimide sample after being exposed to a total fluence of 8.47×10^{20} atoms/cm². By measuring the difference in height between the etched and unetched portions of the polymer sample, it is possible to calculate an AO reaction efficiency (R_e) or erosion rate for the material for a given flux. Profilometry measurements for the Kapton HN standard and a 10 wt% POSS-Kapton polyimide

sample of Figure 5-18 after a total fluence of 8.47×10^{20} atoms/cm² are shown in Figure 5-19.

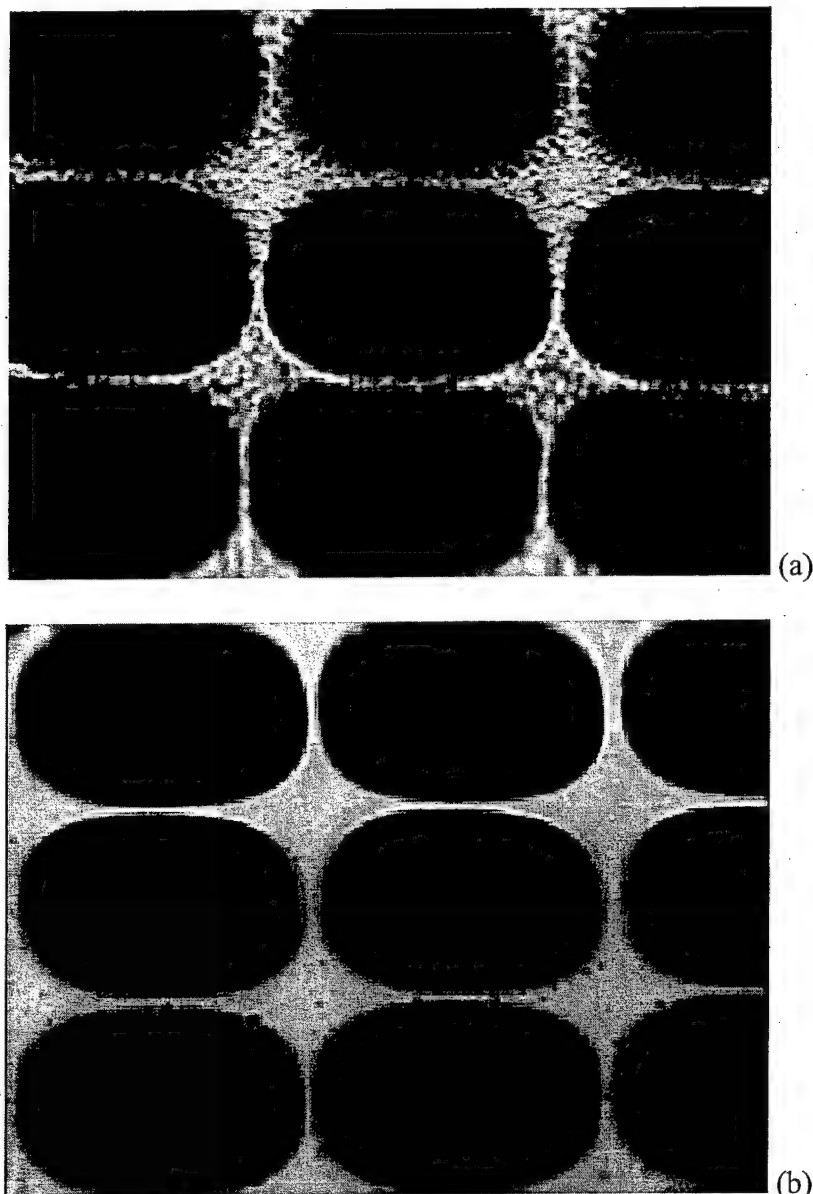


Figure 5-18. Magnified profilometry photographs of (a) the etched Kapton HN standard and (b) a 10 wt % POSS-Kapton polyimide sample. The dark regions correspond to the unetched areas protected by the screen.

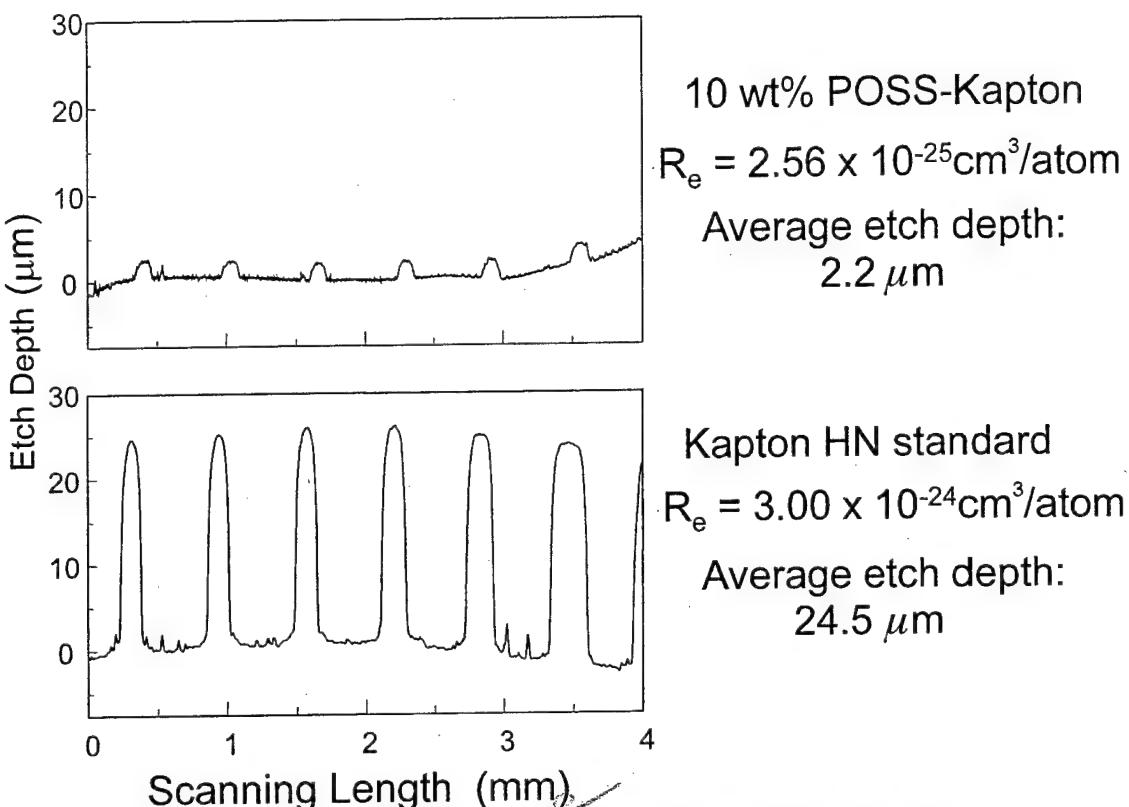


Figure 5-19. Profilometry measurements obtained from Kapton HN and a 10 wt% POSS-Kapton polyimide after a total AO fluence of $8.47 \times 10^{20} \text{ atoms/cm}^2$.

These measurements reveal that the average etch depth for the Kapton HN standard was 24.5 microns which corresponds to a calculated R_e of $3.00 \times 10^{-24} \text{ cm}^3/\text{atom}$. This value agrees with previously reported erosion rates based on space flown and ground tested Kapton samples [22]. However, under the same conditions, the 10 wt% POSS-Kapton polyimide etched on average only 2.2 microns corresponding to an R_e of $2.56 \times 10^{-25} \text{ cm}^3/\text{atom}$. It is interesting to note that this full order of magnitude improvement in atomic oxygen reaction efficiency is brought about by only a 10 wt % (approximately 1 mole%) addition of POSS copolymerized in the polymer matrix.

The experiment was repeated for a total AO fluence of $2.62 \times 10^{20} \text{ atoms/cm}^2$ exposing a commercially available Kapton HN standard, a Kapton control sample with no POSS and a 10 and 20 wt% POSS-Kapton sample. Figure 5-20 shows a multiplot of

the profilometry measurements of these samples. The data for these plots, summarized in Table 5-2, reveal a decreasing average etch depth and corresponding atomic oxygen reaction efficiency as the POSS content in the polymer increases. Again, a full order magnitude improvement in the atomic oxygen reaction efficiency is obtained from addition of 10 wt% POSS. While addition of 20 wt% POSS improves the reaction efficiency by 22.5 times. As discussed in Chapters 3 and 4, this superior resistance to AO induced erosion can be attributed to the silsesquioxane reacting and forming a protective silica layer on the surface of the polymer preventing it from eroding even further. In order to confirm that indeed this is the case for these POSS polyimides as well, the surfaces were characterized using in-situ XPS before and after exposure to the AO flux produced by the ESD source described in Chapter 2. These results are presented below.

Table 5-2: POSS-Polyimide AO Reaction efficiencies determined from profilometry data.

	Kapton HN	0% POSS-Kapton	10% POSS-Kapton	20% POSS-Kapton
Avg Etch Depth (μm)	7.85	9.14	1.17	0.41
Std Deviation	0.05	0.18	0.07	0.07
$\text{Re cm}^3/\text{atom}$	3.00×10^{-24}	3.49×10^{-24}	4.39×10^{-25}	1.55×10^{-25}

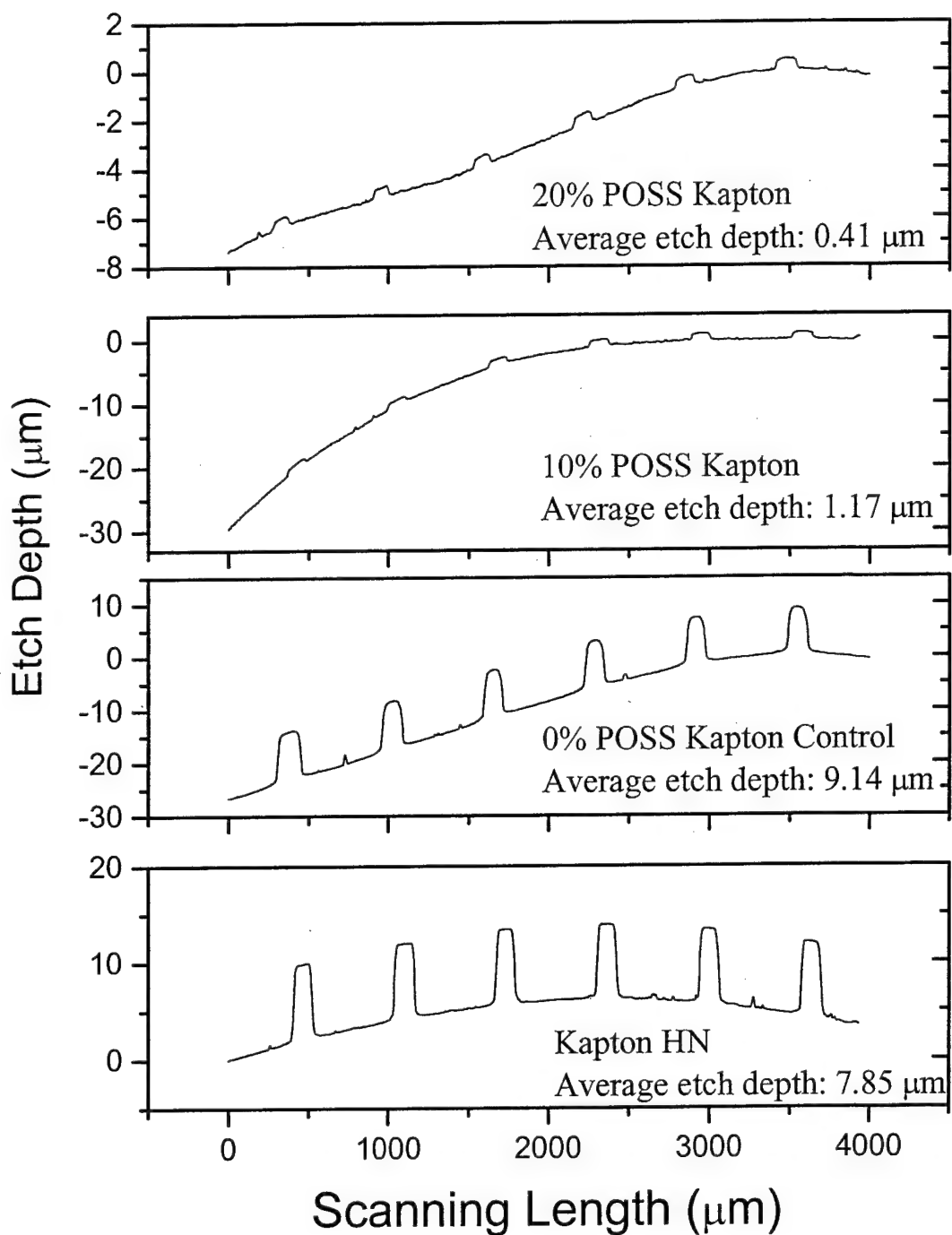


Figure 5-20. Multiplot of profilometry measurements obtained from Kapton HN and 0, 10 and 20 wt% POSS-Kapton polyimides exposed to a total AO fluence of 2.62×10^{20} atoms/ cm^2 .

5.4.2 Surface Characterization

A 10 wt% POSS-Polyimide film was wiped with isopropanol and inserted into the UHV chamber (base pressure $<1.33 \times 10^{-7}$ Pa). XPS measurements were performed using a double-pass cylindrical mirror analyzer (DPCMA) (PHI Model 25-270AR). XPS survey spectra were taken in the retarding mode with a pass energy of 50 eV, and high-resolution XPS spectra were taken with a pass energy of 25 eV using Mg $K\alpha$ X-rays (PHI Model 04-151 x-ray source). Data collection was accomplished using a computer interfaced, digital pulse-counting circuit [73] followed by smoothing with digital-filtering techniques [74]. The sample was tilted 30 degrees off the axis of the DPCMA, and the DPCMA accepted electrons emitted into a cone 42.6 ± 6 degrees off the DPCMA axis.

XPS spectra were first obtained from the as-entered, solvent-cleaned sample. The sample was then transferred into an adjoining UHV chamber that houses the ESD O-atom source via a magnetically coupled rotary/linear manipulator. There the surface was exposed to a hyperthermal O flux and re-examined without air exposure after total exposure times of 2, 24, and 40 hrs. The approximate normal distance between the sample faces and source in this study was 15 cm, at which distance the flux was about 2.0×10^{15} atoms/cm²-s for the instrument settings used. The sample was maintained at room temperature during the AO exposures with a slight temperature increase to 50°C due to exposure to the X-ray source during XPS data collection. The substrate temperature was determined using a chromel-alumel thermocouple. After the 40 hr AO exposure, the sample was exposed to air (room temperature, ~22°C, relative humidity ~60%) and again examined using XPS.

5.5 Results and Discussion

The POSS-Kapton molecular structure with labeled atomic sites is shown in Figure 5-21. XPS survey spectra obtained from a solvent-wiped 10 wt% POSS-polyimide surface before and after the 2, 24 and 40 hr AO exposures and final air exposure are shown in Figure 5-22. The peak assignments shown in Figure 5-22 pertain to all five spectra. The predominant peaks apparent in these spectra include the C 1s, N 1s, O 1s, Si 2p, Si 2s, O 2s and O Auger peaks. Significant changes in relative peak heights are observed for the C, O, and Si features following the O-atom exposures. An estimate of the near-surface compositions has been calculated from the peak areas in the high resolution spectra by assuming that this region is homogeneous and using published atomic sensitivity factors⁶⁷. The compositions determined in this manner are presented in Table 5-3 for the as-entered, AO-exposed and air-exposed surfaces.

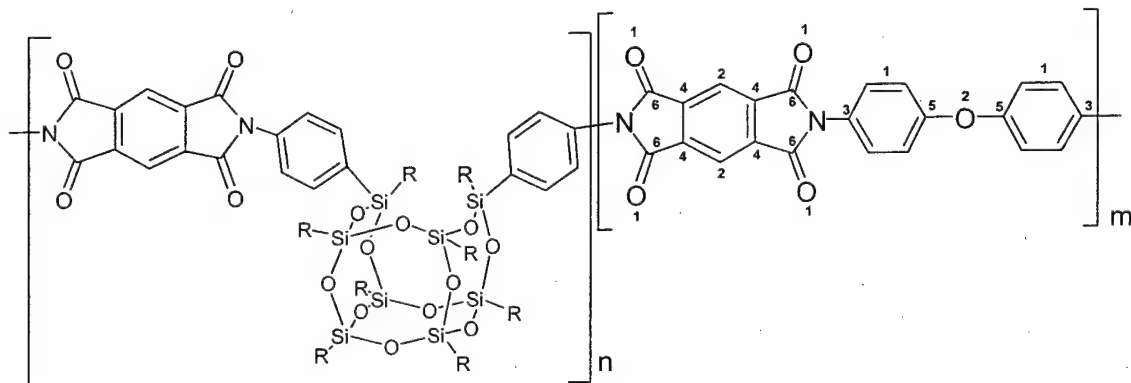


Figure 5-21. Molecular structure of POSS-Kapton with numerically labeled atomic sites.

Table 5-3: Near-surface composition determined from XPS data obtained from the as-entered, solvent cleaned, AO and air-exposed 10 wt% POSS-Polyimide sample.

Surface Sample Treatment	AO Fluence O/cm ²	Composition, at.%				Atom ratio O/Si
		O	Si	C	N	
As entered, solvent cleaned	—	15.9	4.6	74.5	4.9	3.4
2-hr AO exposure	1.44×10^{17}	14.3	4.9	72.6	8.2	2.9
24-hr AO exposure	1.77×10^{18}	11.1	4.4	79.6	4.9	2.5
40-hr AO exposure	4.53×10^{18}	9.1	3.7	81.5	5.6	2.4
Air exposed	4.53×10^{18}	13.9	3.5	76.8	5.8	3.9

As previously explained, XPS is a surface sensitive technique ideally suited for studying AO erosion of spacecraft materials. The outermost surface region which is affected to the greatest extent due to reaction with AO also makes the largest contribution to the XPS signal. The weighted average compositional values of the near-surface region determined using the homogeneous assumption are shown in Table 5-3 as a function of AO fluence. They provide a trend which is indicative of the chemical alterations occurring during AO exposure. This trend is supported by the chemical state alterations determined by XPS, which are discussed below.

As can be seen in Figure 5-22, the O 1s peak decreases significantly upon exposure to AO beam. As a result, the O-to-Si atomic ratio of 3.4 for the as-entered sample, decreases gradually to 2.4 after the 40 hr AO exposure. This reduction of the O/Si ratio is due to AO induced surface compositional changes resulting in the removal of carbonyl groups from the polymer chain and formation of a surface silica layer as shall be explained in the high resolution spectra that follow. After exposure to air, the O-to-Si atomic ratio increases to 3.9 corresponding to adsorption of species present in air. An overall increase is observed in the C concentration on the surface during increased exposure. Since the surface compositions presented in Table 5-3 are relative, it is expected that as the O concentration decreases the C and Si would increase.

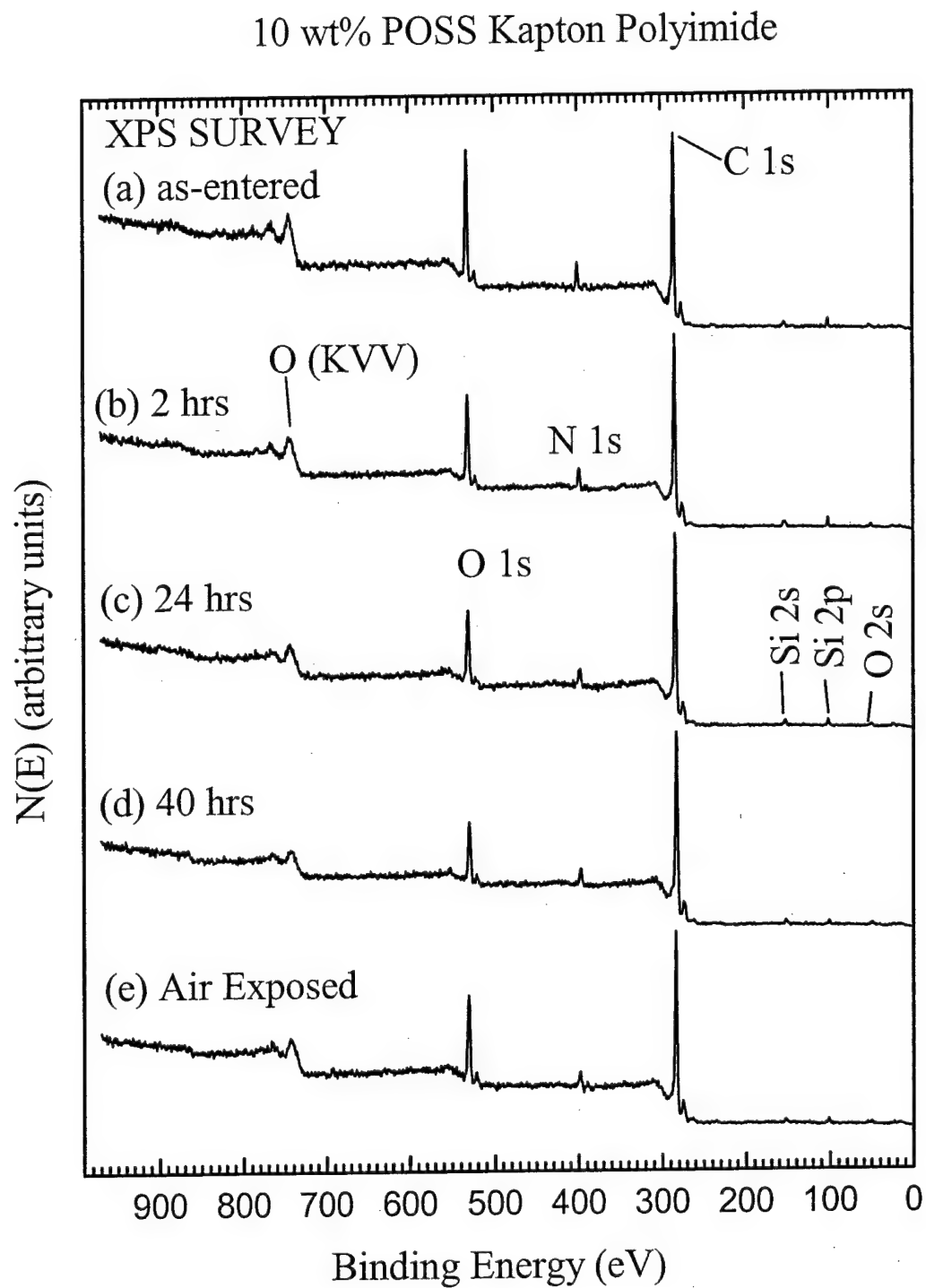


Figure 5-22. XPS survey spectra obtained from a 10-wt% POSS-polyimide film after insertion into the vacuum system (a), after 2 hr (b), 24 hr (c), and 40 hr exposure to the hyperthermal AO flux (d), and air exposure following the 40 hr exposure (e).

High-resolution XPS C 1s, O 1s, N 1s and Si 2p spectra obtained from the as-received, solvent-wiped surface before and after the 2, 24 and 40 hr O-atom exposures are shown in (a)-(d) of Figures 5-23 through 5-26. Spectra (e) of these figures were obtained after the exposure to air following the 40 hr AO exposure. Variations in peak shapes and positions are observed between the nonexposed, AO-exposed, and air-exposed surfaces, indicating that the chemical species distribution is altered by exposure to the AO flux and then to air. In addition, no surface charging of the sample was evident during the experiment as this would have altered the spectra resulting in a significant binding energy (BE) shift. Differential charging would have resulted in peak broadening or peak multiplicity, however, this was not observed in this study.

The C 1s peak for the as entered sample in Figure 5-23 is broad and centered at 284.7 indicating the predominant form of carbon present is aromatic. A high binding energy shoulder is present at 288.6 eV corresponding to the carbonyl carbon (6) in Figure 5-21. However, as was also observed in Figure 5-6 for Kapton, this shoulder diminishes upon exposure to AO. This is due to erosion of the carbonyl groups from the polymer backbone. This also results in a chemical state change of nitrogen on the surface as observed in the N 1s spectra in Figure 5-24.

The N 1s spectra for the as entered sample is centered at 400.6 eV which, as indicated in Table 5-1, corresponds to nitrogen bonded as an imide functional group. However, as with regular Kapton, as the N-C=O bonds are broken upon removal of the carbonyl groups to form CO and CO₂, a lower binding energy shoulder begins to emerge in the N 1s spectra.

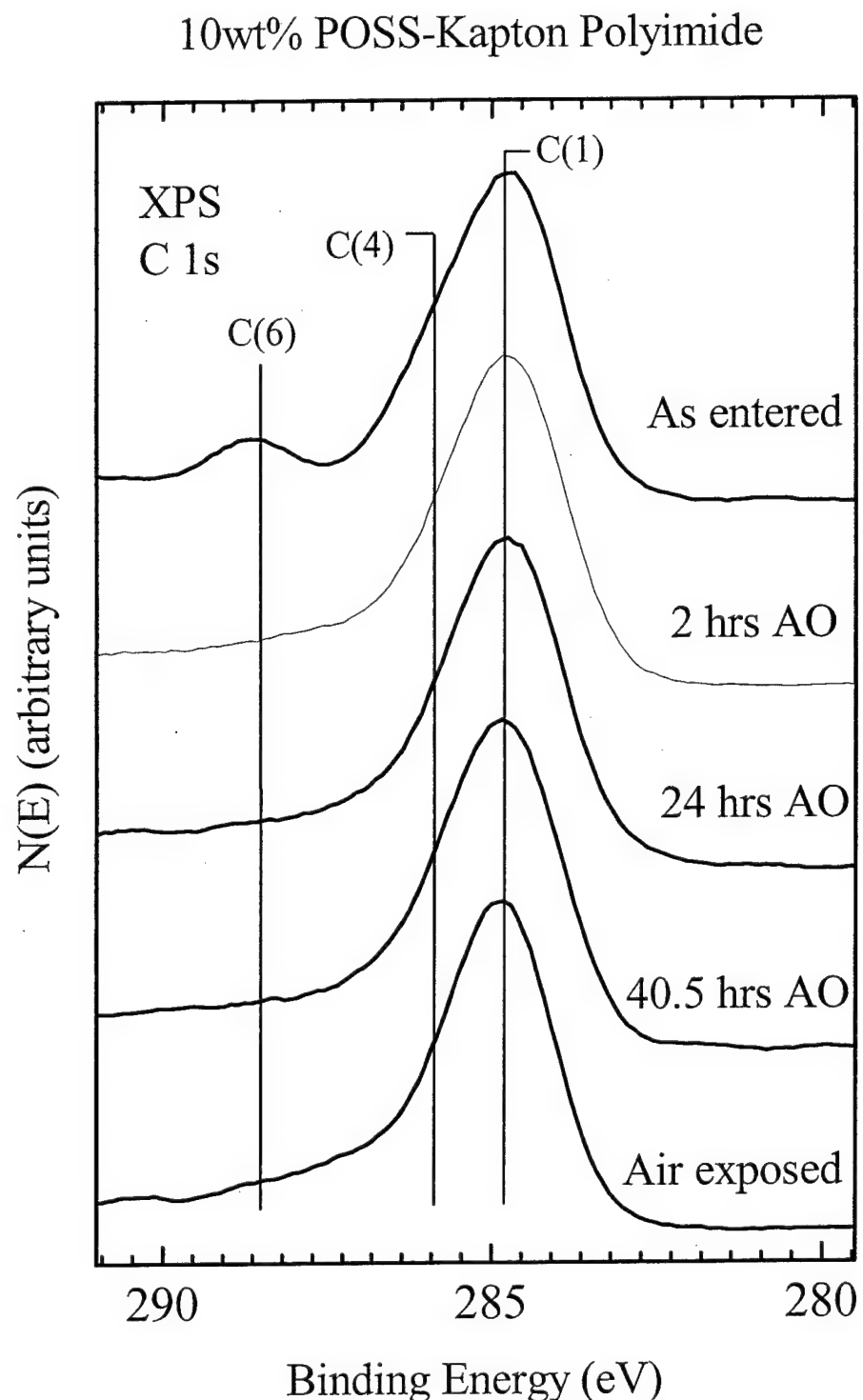


Figure 5-23. XPS C 1s spectra obtained from a 10-wt% POSS-polyimide film after insertion into the vacuum system (a), after 2 hr (b), 24 hr (c), and 40 hr exposure to the hyperthermal AO flux (d), and air exposure following the 40 hr exposure (e).

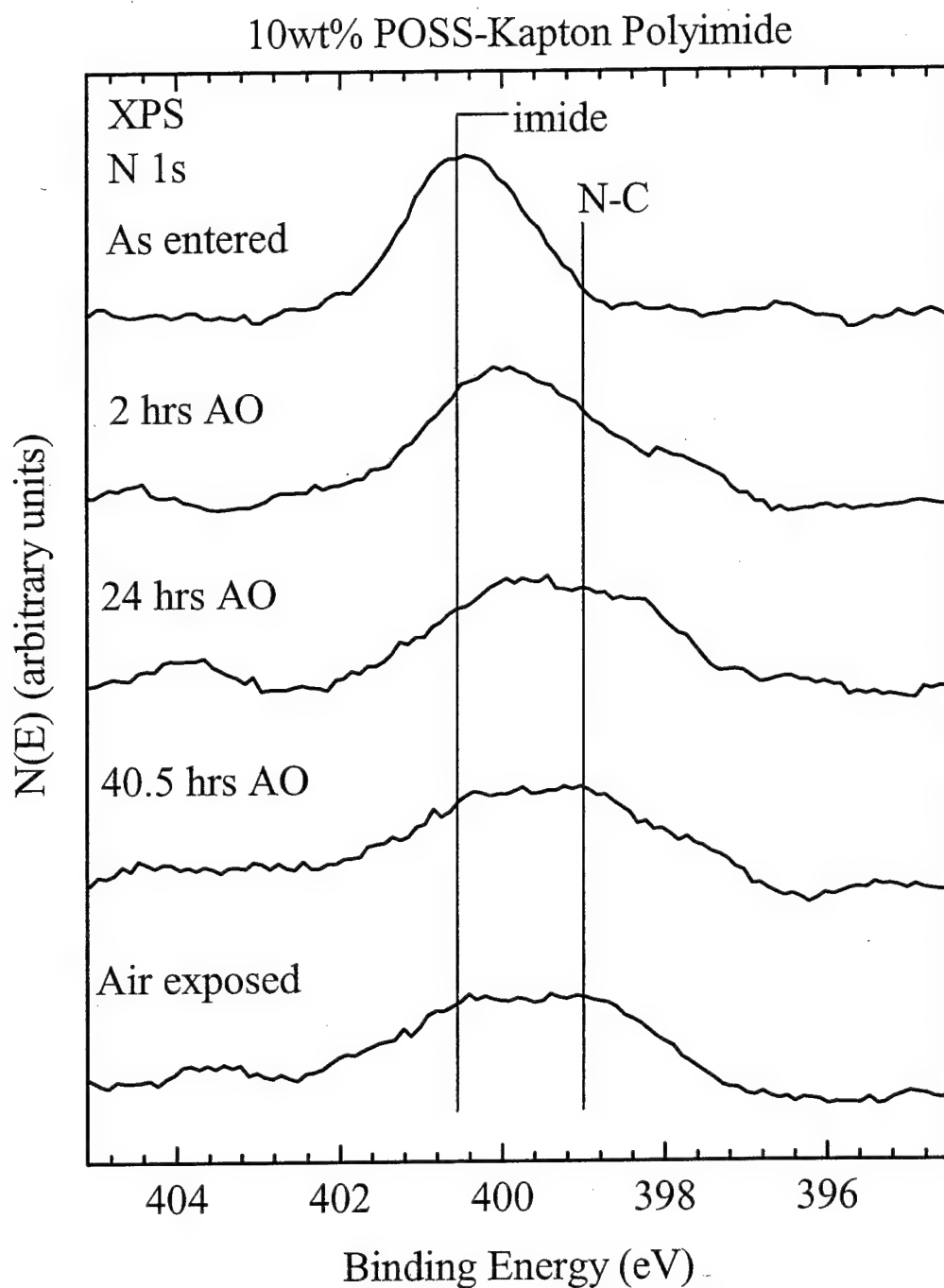


Figure 5-24. XPS N 1s spectra obtained from a 10-wt% POSS-polyimide film after insertion into the vacuum system (a), after 2 hr (b), 24 hr (c), and 40 hr exposure to the hyperthermal AO flux (d), and air exposure following the 40 hr exposure (e).

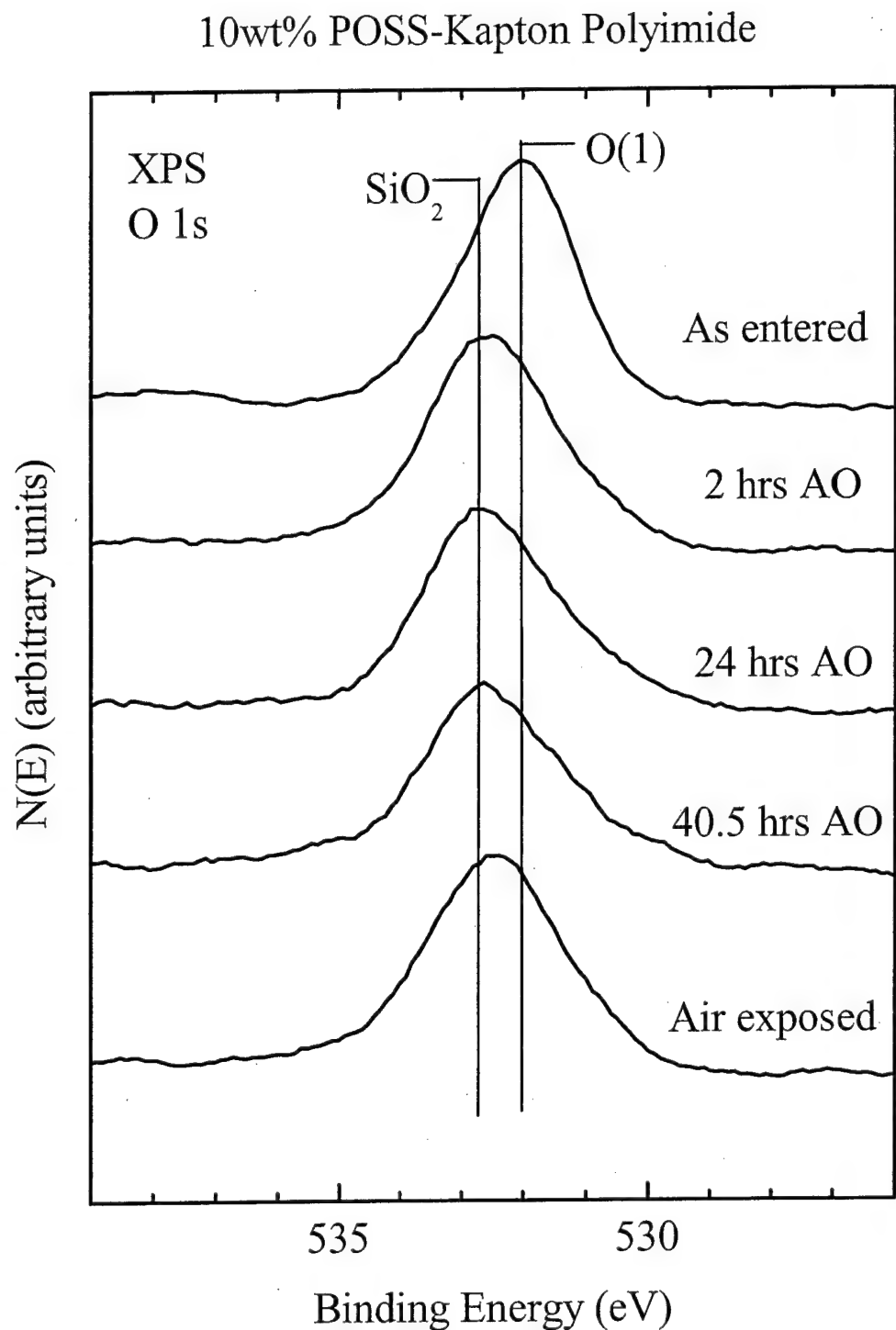


Figure 5-25. XPS O 1s spectra obtained from a 10-wt% POSS-polyimide film after insertion into the vacuum system (a), after 2 hr (b), 24 hr (c), and 40 hr exposure to the hyperthermal AO flux (d), and air exposure following the 40 hr exposure (e).

10wt% POSS-Kapton Polyimide

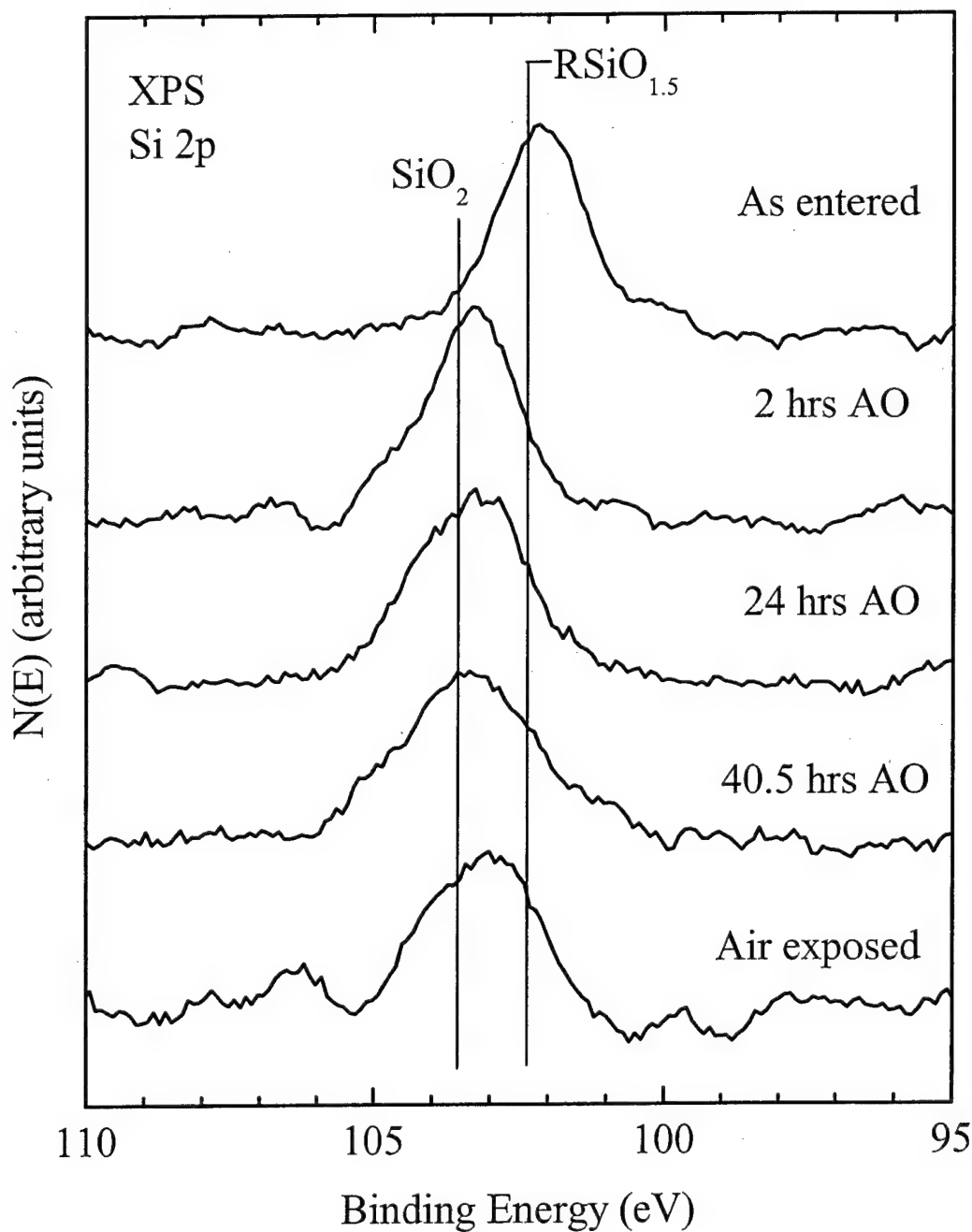


Figure 5-26. XPS Si^{2p} spectra obtained from a 10-wt% POSS-polyimide film after insertion into the vacuum system (a), after 2 hr (b), 24 hr (c), and 40 hr exposure to the hyperthermal AO flux (d), and air exposure following the 40 hr exposure (e).

The chemical state changes in carbon and nitrogen associated with erosion also coincide with chemical state changes in the O 1s and Si 2p spectra in Figures 5-25 and 5-26, which as with other POSS-polymers, reveal the formation of a silica layer on the outer surface. Upon inspection, it is evident from these spectra that a transition occurs for oxygen and silicon from a lower binding energy corresponding to the silsesquioxane to a higher binding energy and oxidation state associated with the formation of SiO_2 on the surface. These changes are presumably responsible for the reduced erosion rates and improved AO reaction efficiencies discussed earlier. In addition, it has been shown that POSS can be nano-dispersed throughout the polymer matrix which would provide the added benefit of forming a truly self healing polymer free from the undercutting phenomenon observed in protective coating schemes mentioned in Chapter 1 and illustrated in Figure 1-2.

5.6 (MISSE) Materials on International Space Station Experiment

Recently, ^{the POSS} our research group at the Air Force Research Laboratory at Edwards AFB, CA, was able to secure a space flight opportunity for the POSS-Polyimides presented in this chapter on the International Space Station (ISS) through a collaboration with NASA and Boeing. Nine POSS-polymer samples were submitted to participate in the Materials on International Space Station Experiment (MISSE). MISSE is a cooperative experiment involving Principle Investigators from Boeing Phantom Works, the Air Force Research Laboratory, and NASA's Langley Research Center and Marshall Space Flight Center and Glenn Research Center.

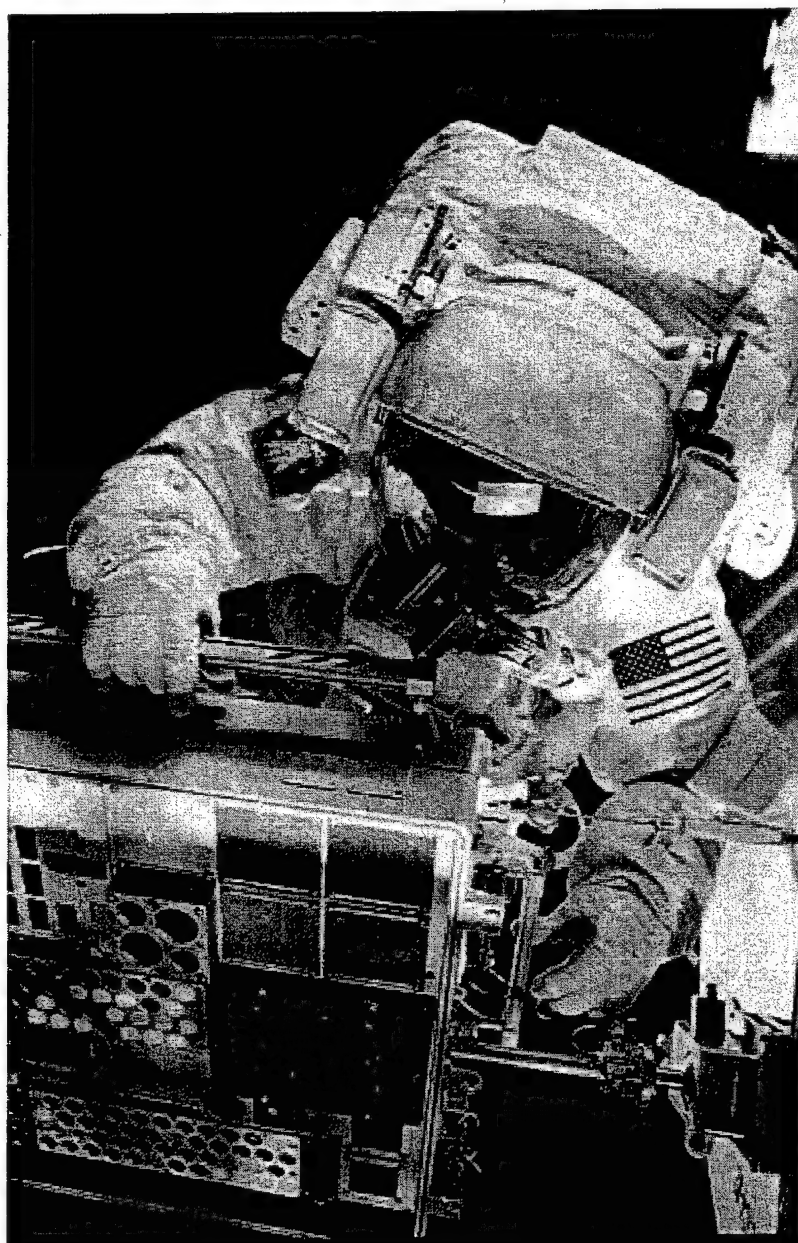


Figure 5-27. Astronaut installing one of the Passive Experiment Containers containing POSS polymer samples onto the International Space Station during STS-105 [NASA photo]. ref?

The MISSE was transported to the ISS and attached to the exterior of the ISS during the STS 105 mission (August 10, 2001). The MISSE will be exposed to the space environments for 18 months while on the ISS. The experiment utilizes Passive Experiment Containers (PECs) developed by Langley Research Center (LaRC) and first

used for ISS Phase I Risk Mitigation Experiments on Mir. Figure 5-27 shows an astronaut installing one of the PEC trays containing samples onto the exterior of one of the airlocks on the ISS. A close up of PEC tray 1 containing the POSS samples is shown in Figure 5-28. Figure 5-29 shows where the PEC containers are located in relation to the ISS. The nine POSS samples are arranged vertically, one after another, on the far left edge of the first vertical tray. The first POSS sample is the third disc from the top. The MISSE will characterize the performance of candidate new space materials over the course of one and three year exposure periods on-orbit. Upon retrieval, the samples will be returned to the principal investigators for analysis.

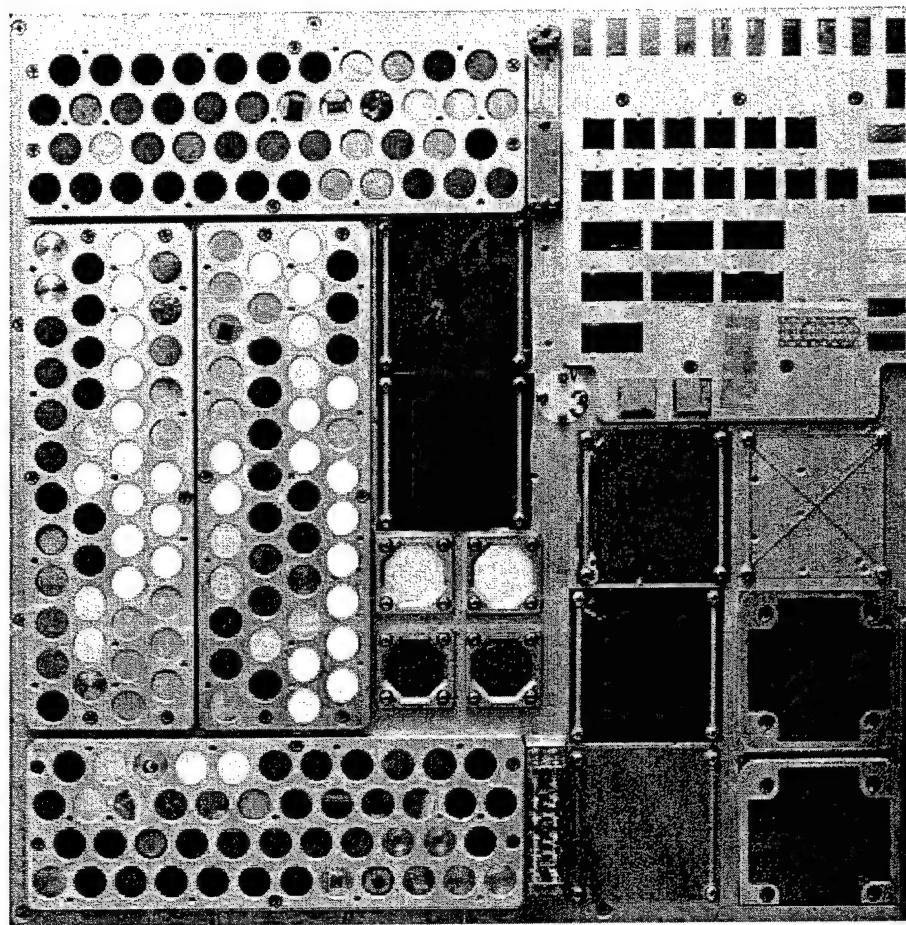


Figure 5-28. Close up view of tray containing POSS samples on Passive Experiment Container of the MISSE project on the ISS.

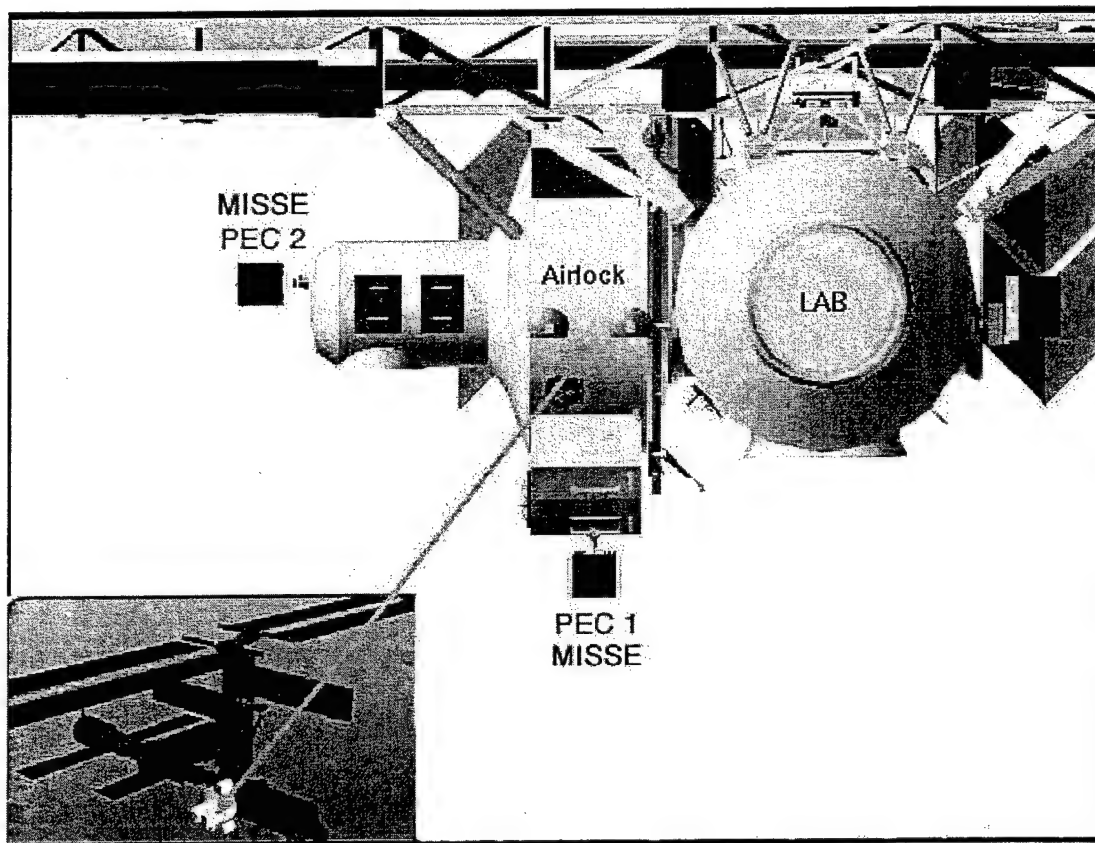


Figure 5-29. Diagram illustrating the location of the MISSE PEC containers in relation to the ISS.

5.7 Summary

Polyimides containing varying weight percent POSS have been synthesized and characterized with XPS before and after exposure to AO. XPS analysis reveals the rapid formation of a silica surface layer preventing further degradation of the underlying virgin polymer. In addition, surface profilometry measurements show that the addition of POSS to the polyimide structure imparts an order of magnitude improvement in the erosion yield.

CHAPTER 6
IN-SITU ATOMIC OXYGEN EROSION STUDY OF FLUOROPOLYMER FILMS
AND POLYETHYLENE USING X-RAY PHOTOELECTRON SPECTROSCOPY

6.1 Introduction

Several studies have been conducted on the deterioration of fluorinated polymers retrieved from spacecraft subjected to the LEO environment. In particular, it has been reported that the outer layer of Teflon fluorinated ethylene propylene multi-layer insulation on the Hubble Space Telescope (HST) was observed to be significantly cracked at the time of the Second HST Servicing Mission, 6.8 years after it was launched into low Earth orbit [14, 126]. Comparatively minor embrittlement and cracking were also observed in the FEP materials retrieved from solar-facing surfaces on the HST at the time of the First Servicing Mission (3.6 years of exposure). It has also been reported that an increased deterioration of fluorinated polymers results from the synergistic effect of VUV radiation in the presence of atomic oxygen [40]. Thin films of fluorinated polymers such as Teflon FEP are used as the outer layer of multi-layer thermal control insulation because of their superior optical properties, including low solar absorptance and high thermal reflectance. A metalized layer is applied to the backside in order to reflect incident sunlight [14]. Figure 6-1 (a) and (b) show astronauts assessing the damage done to the multi-layer insulation of the HST and removing samples for further analysis during the second HST servicing mission in February 1997.

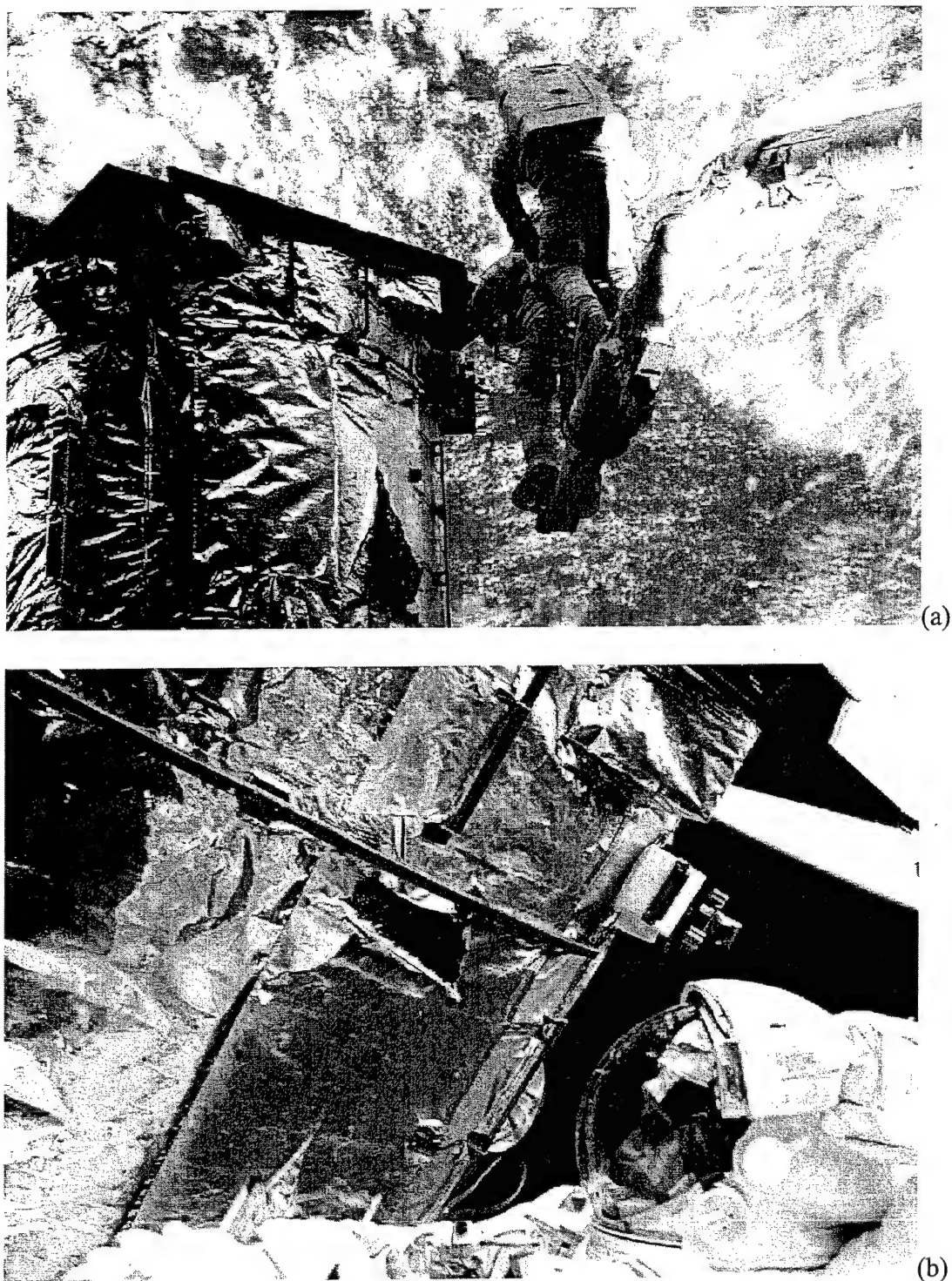


Figure 6-1. Photographs of astronauts servicing the Hubble Space Telescope and retrieving samples of degraded metalized Teflon multilayer insulation for further analysis; NASA photo [14].

In this study, a series of fluoropolymer films was exposed to AO (produced by the ESD source described in Chapter 2) in an effort to further understand AO induced degradation mechanisms and to also establish a basis of comparison with future POSS-fluorinated-polymers. The three polymers chosen for this study (Figure 6-2) were Tedlar, poly(vinyl fluoride) (PVF), poly(vinylidene fluoride) (PVdF), and Teflon, poly(tetrafluoroethylene) (PTFE) having fluorine-to-carbon ratios of 1:2, 1:1, and 2:1 respectively.

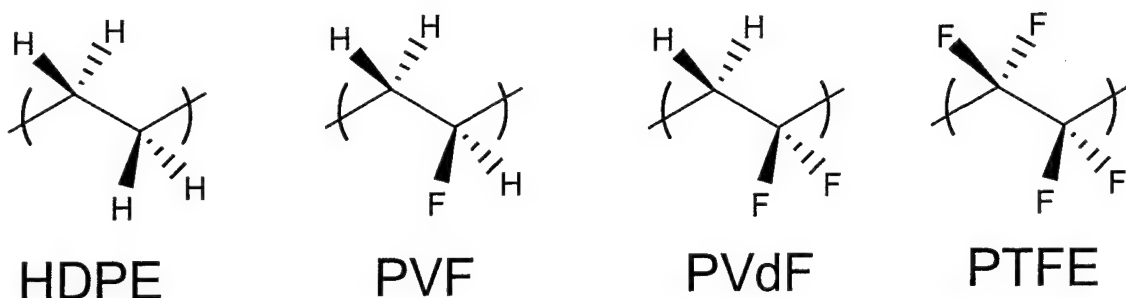


Figure 6-2. Chemical structures of the polymers used in this study.

These polymers were compared with high-density polyethylene (HDPE) which does not contain fluorine. The study of these polymers having similar structure but increasing fluorine content shows a correlation between chemical composition and induced chemical and structural alterations by AO exposure. The data indicates that AO initially attacks the fluorine portion of the polymers resulting in substantial decrease in the near-surface fluorine concentration as observed through lower binding energy shifts in both the high resolution C 1s and F 1s spectra. The near surface fluorine formed volatile species upon reaction with AO as evidenced by outgassing a resulting pressure increase in the reaction chamber during exposure.

6.2 Experimental

As received (E.I. du Pont Nemours & Co., Inc.) Teflon, Tedlar, Tefzel and HDPE films were wiped with isopropanol and inserted into the UHV chamber (base pressure $<1.33 \times 10^{-7}$ Pa). XPS measurements were performed using a double-pass cylindrical mirror analyzer (DPCMA) (PHI Model 25-270AR). XPS survey spectra were taken in the retarding mode with a pass energy of 50 eV, and high-resolution XPS spectra were taken with a pass energy of 25 eV using Mg $K\alpha$ X-rays (PHI Model 04-151 x-ray source). Data collection was accomplished using a computer interfaced, digital pulse-counting circuit [73] followed by smoothing with digital-filtering techniques [74]. The sample was tilted 30 degrees off the axis of the DPCMA, and the DPCMA accepted electrons emitted into a cone 42.6 ± 6 degrees off the DPCMA axis.

Table 6-1: Polymer Name, Binding Energies, F/C ratio and Structure

Polymer	Binding Energy (eV)			F:C
	C 1s 1	2	F 1s	
(a) Poly(ethylene), high density (HDPE) [-CH ₂ -CH ₂ -] _n	285.00	N/A	N/A	0
(b) Tedlar, Poly(vinyl fluoride) (PVF) [-CH ₂ -CHF-] _n	285.74	287.91	686.94	1:2
(c) Tefzel, Poly(vinyl fluoride) (PVdF) [-CH ₂ -CF ₂ -] _n	286.44	290.90	688.15	1:1
(d) Teflon, Poly(tetrafluoroethylene) (PTFE) [-CF ₂ -CF ₂ -] _n	292.48	N/A	689.67	2:1

XPS spectra were first obtained from the as-entered, solvent-cleaned sample. The sample was then transferred into an adjoining UHV chamber that houses the ESD AO source via a magnetically coupled rotary/linear manipulator. There the surface was

exposed to a hyperthermal O flux and re-examined without air exposure after a total exposure time of 15 minutes. The samples were exposed for only 15 because the pressure in the reaction chamber rapidly increased when the fluorinated samples were exposed to AO. This outgassing was a cause of concern because it is very difficult to remove fluorine contamination from the chamber. Therefore a short exposure time was used. At no time were the samples exposed to air after the initial insertion into the UHV chamber. The approximate normal distance between the sample face and source in this study was 15 cm, at which distance the flux was about 2.0×10^{15} atoms/cm²-s for the instrument settings used. The sample was maintained at room temperature during the AO exposures with a slight temperature increase to 50°C due to exposure to the X-ray source during XPS data collection. The substrate temperature was determined using a chromel-alumel thermocouple. Polymer structural repeat units, F-to-C ratios and reference binding energies (BE) used in this study are given in Table 6-1.

6.3 Results and Discussion

6.3.1 Short 15 minute Exposure of Fluoropolymers and Polyethylene

XPS survey spectra obtained from the as-received, solvent-wiped polymer films before and after the 15 min AO exposure are shown in Figure 6-3. The peak assignments shown in Figure 6-3 pertain to all eight spectra. The predominant peaks apparent in these spectra include the C 1s for all the samples in addition to the F 1s, F Auger (KLL) and F 2s for the fluoropolymers. Significant changes in relative peak shapes and heights are observed for the C and F features in the fluoropolymers following the AO exposures. However, little to no change was observed in the spectra corresponding to polyethylene as a result of the 15 min exposure to AO. Estimates of the near-surface compositions

have been made from the peak areas in the high-resolution spectra using published atomic sensitivity factors [67] with the assumption of a homogeneous surface region.

Table 6-2: Near-surface composition (atomic %) determined from XPS data obtained from the as-entered, solvent cleaned, and 15 min AO exposed HDPE and fluoropolymer samples.

Polymer Surface	Composition, at.%						F:C ratio Theoretical	
	As-entered		15 min AO		Experimental			
	C	F	C	F	As-entered	15 min AO		
HDPE $[-\text{CH}_2-\text{CH}_2-]_n$	100	0	100	0	0	0	0	
PVF $[-\text{CH}_2-\text{CHF}-]_n$	69.2	30.8	86.2	13.8	0.89:2	0.32:2	1:2	
PVdF $[-\text{CH}_2-\text{CF}_2-]_n$	52.1	47.9	62.1	37.9	0.92:1	0.61:1	1:1	
PTFE $[-\text{CF}_2-\text{CF}_2-]_n$	34.2	65.8	38.0	62.0	1.92:2	1.63:2	2:1	

The compositions determined using the homogeneous assumption are shown in Table 6-2 before and after the 15 min exposure to AO. It is interesting to note that no oxygen is detected in either the survey or high-resolution spectra before and after exposure to AO.

High-resolution XPS C 1s, and F 1s spectra obtained from the as-received, solvent-wiped polymers before and after the 15 minute AO exposures are shown in a-d and a-c of Figures 6-4 and 6-5, respectively. Variations in peak shapes and positions are observed between the non-exposed and AO-exposed fluoropolymer surfaces, indicating that the chemical species distribution is altered by exposure to the AO flux. No surface charging of the sample was evident during the experiment as this would have resulted in a significant binding energy (BE) shift. Differential charging would have manifested itself through peak broadening or peak multiplicity. However, this was not observed.

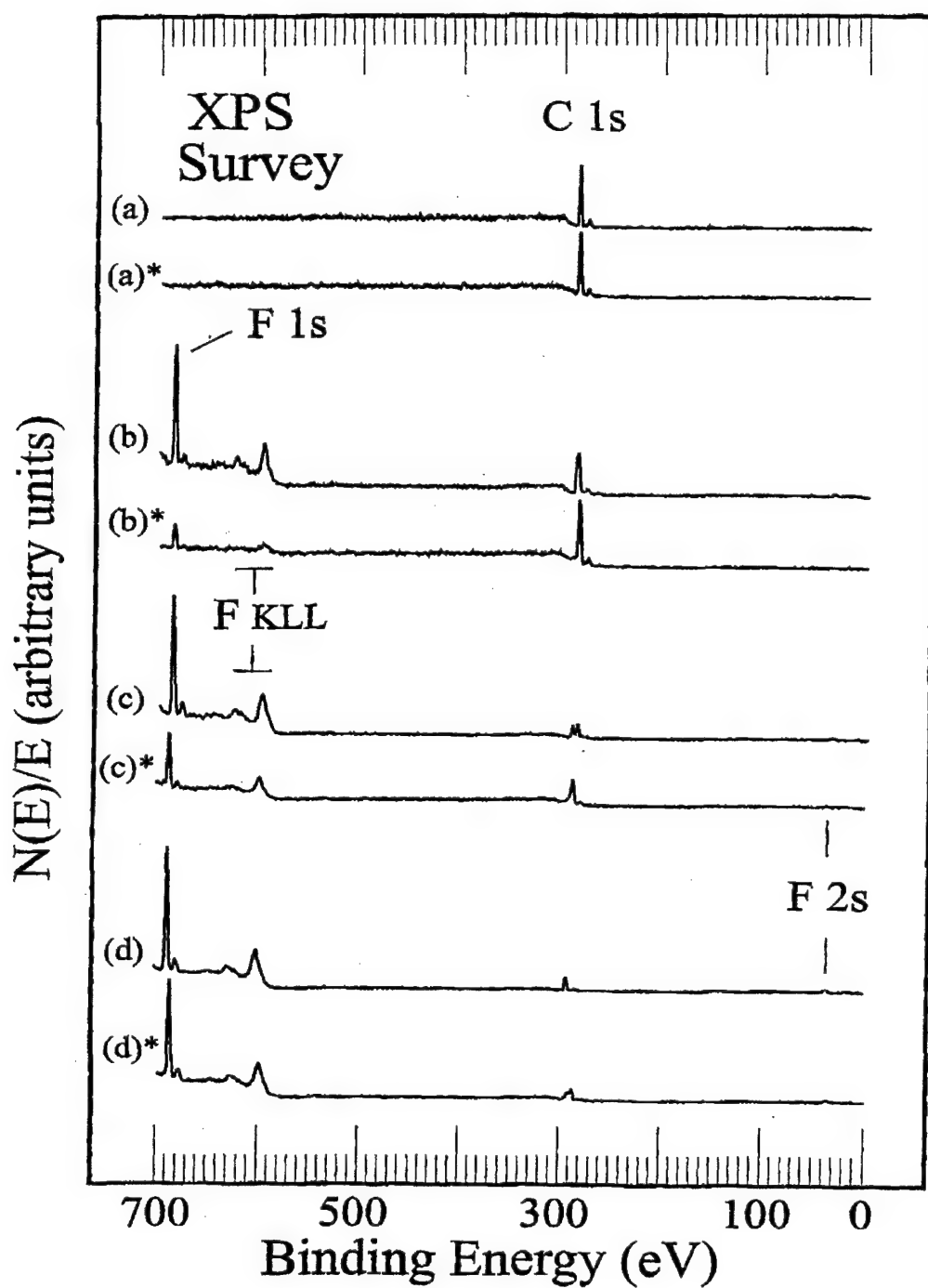


Figure 6-3. XPS survey spectra obtained from a solvent-cleaned, HDPE film after (a) insertion into the vacuum system (a)* 15-min AO exposure; PVF after (b) insertion into vacuum system, (b)*after 15-min AO exposure; PVdF after (c) insertion into vacuum system, (c)*after 15-min AO exposure; PTFE after (d) insertion into vacuum system, (d)*after 15-min AO exposure.

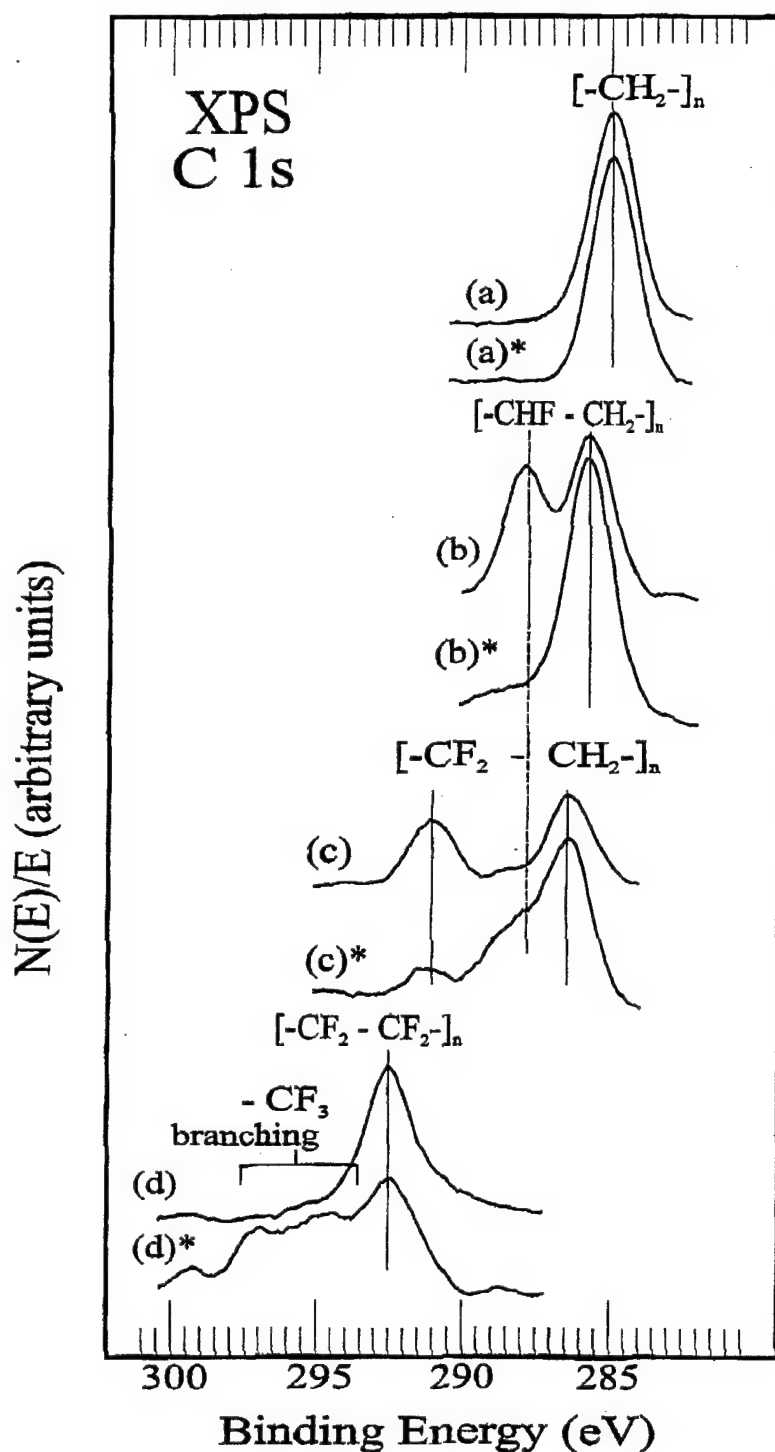


Figure 6-4. XPS C 1s spectra obtained from a solvent-cleaned, HDPE film after (a) insertion into the vacuum system (a)* 15-min AO exposure; PVF after (b) insertion into vacuum system, (b)*after 15-min AO exposure; PVdF after (c) insertion into vacuum system, (c)*after 15-min AO exposure; PTFE after (d) insertion into vacuum system, (d)*after 15-min AO exposure.

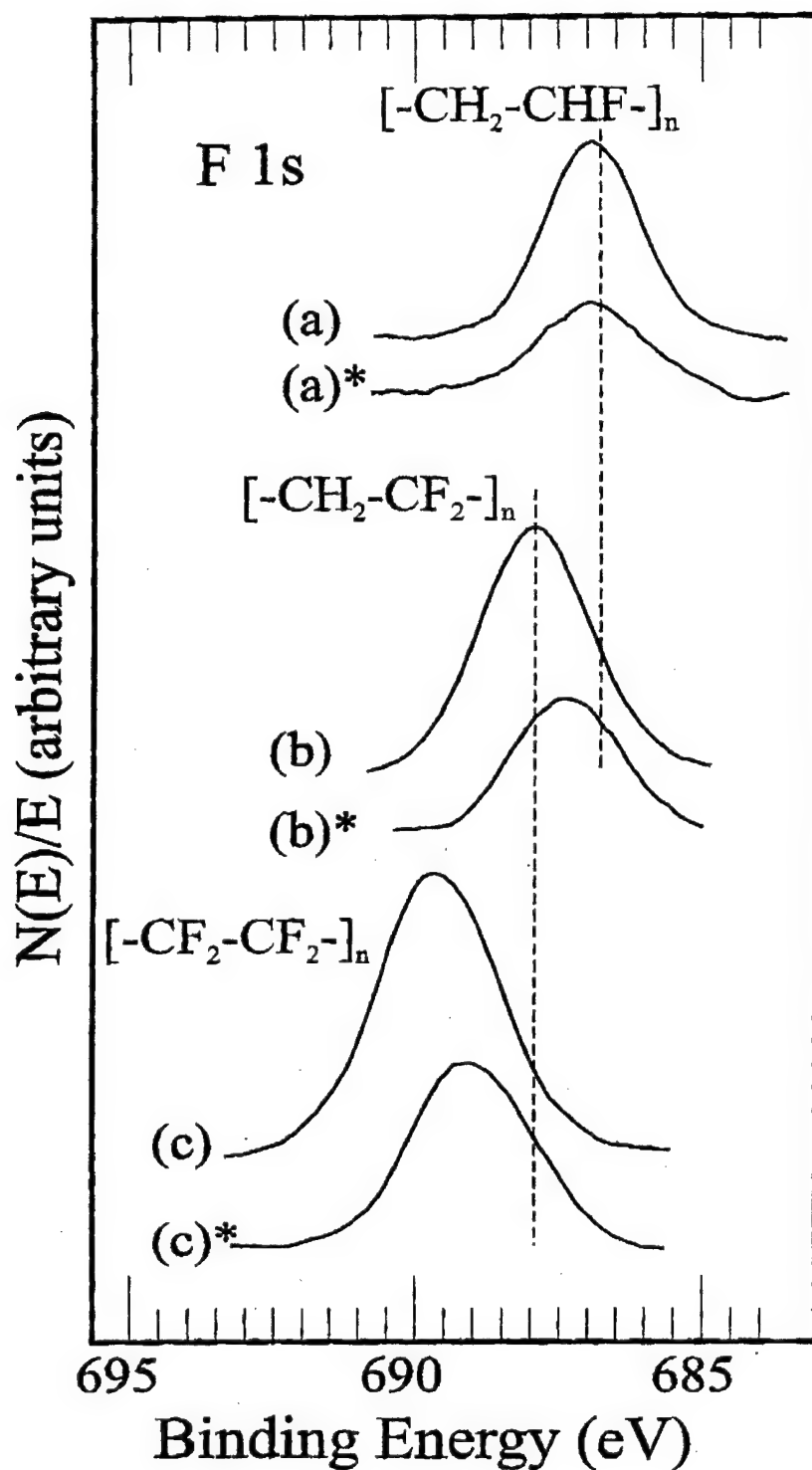


Figure 6-5. XPS F 1s spectra obtained from a solvent-cleaned, PVF film after (a) insertion into vacuum system, (a)*after 15-min AO exposure; PVdF after (b) insertion into vacuum system, (b)*after 15-min AO exposure; PTFE after (c) insertion into vacuum system, (c)*after 15-min AO exposure.

The C 1s features shown in Figure 6-4 indicate that the predominant forms of carbon in the as-entered samples agree well with referenced BE values [110]. Each of these carbons is in a different electrostatic environment and therefore exhibits a different chemical shift, producing C 1s peaks in different positions in the spectrum. The C 1s peak for aliphatic, hydrogen-saturated carbon of HDPE is broad and centered at 285.0 eV [110]. Carbon in the most electronegative environment (PTFE) (Teflon) in Figure 6-4d appears at the highest binding energy. This is because the electronegative fluorine atoms withdraw electron density from the valence and bonding orbitals of the carbon atom, thereby reducing the screening of the core electrons from the nuclear charge and increasing their binding energy. No changes in the C chemical-state are observed for the HDPE sample after the 15 min exposure to AO. However, significant reductions in the fluorinated carbon species are observed for the fluoropolymer films. As seen in C 1s spectra for PVF (Tedlar) in Figure 6-4b*, the peak corresponding to the monofluoro-substituted carbon (-CHF-) is almost drastically reduced. This change coincides with a decrease in the total fluorine concentration in the near surface-region of 17 at.%. Figure 6-4c* also reveals a substantial decrease in the peak corresponding to the difluorinated carbon species (-CF₂-) of PVdF (Tefzel) upon exposure to AO. This change coincides with a decrease in the total fluorine concentration in the near surface-region of 10 at.%. However, a large shoulder develops at an approximate BE of 288 eV corresponding to the formation of the monofluoro-substituted carbon. Essentially, AO attacks Tedlar and Tefzel by cleaving off a fluorine from the polymer backbone. Atomic oxygen reacts differently with PTFE (Teflon) resulting in -CF₃ branching as seen in Figure 6-5d*. This probably results from scission of the polymer chain and subsequent loss of molecular

weight and mechanical properties of the polymer. This is consistent with the results obtained from post density, NMR and DSC analysis of the Teflon FEP samples retrieved from the HST [14].

All the observations made of the C 1s spectra after AO exposure are consistent with the F 1s spectra shown in Figure 6-5. After AO exposure, the F 1s peak for PVF (Tedlar) shown in Figure 4a is significantly reduced. Also, both the F 1s spectra for PVdF (Tefzel) and PTFE (Teflon) shift to lower binding energy values and broaden with newly developed low BE shoulders as seen in Figure 4b and c. These low BE shoulders formed after AO exposure correspond well with the chemical-state of the fluorine found in the preceding polymer of this homologous series when arranged by increasing F:C ratio (Tedlar < Tefzel < Teflon). No specific F 1s feature is seen for the $-CF_3$ formation in the PTFE or have reference BE values for this chemical state been found in the literature. The $-CF_3$ is found in various polymer films such as Viton, Fomblin Y and poly(vinyl trifluoroacetate), however, no specific feature or BE is assigned to this F chemical-state [110].

6.3.2 Prolonged AO exposure of Polyethelyene

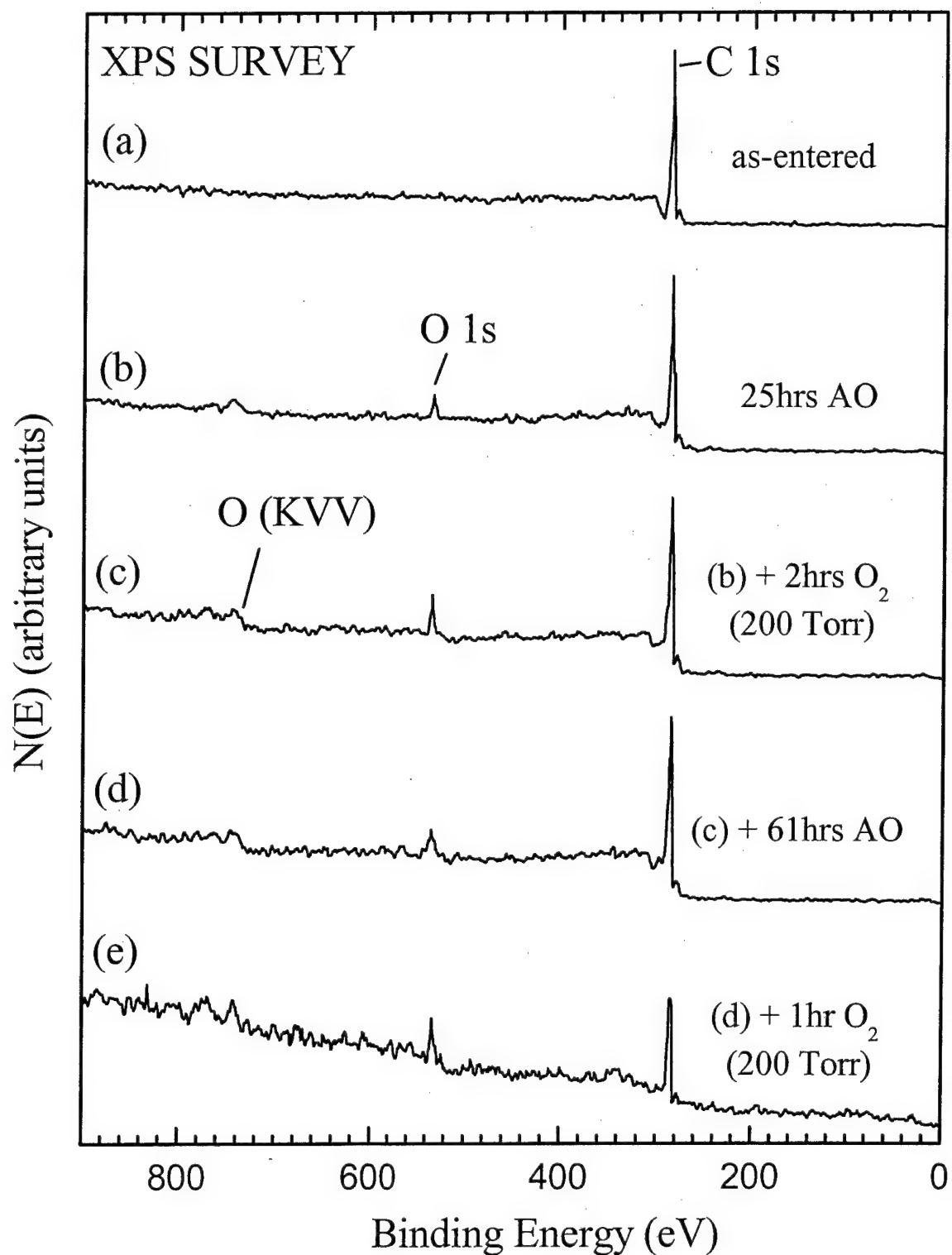
Longer exposures of polyethylene to AO were also conducted and characterized by XPS. Previous experiments on polyethylene have revealed the evolution of volatile CO and CO_2 as a result of AO exposure [127-128]. In this section of experiments, the HDPE sample was exposed for 25 hrs followed by a 2 hr exposure to 200 Torr O_2 . The sample was then exposed to AO for 61 hrs followed by a 1 hr exposure to 200 Torr O_2 .

XPS survey spectra for the HDPE sample under these conditions are shown in Figure 6-6. An O 1s peak is apparent in spectra (b) after 25 hrs of exposure to AO.

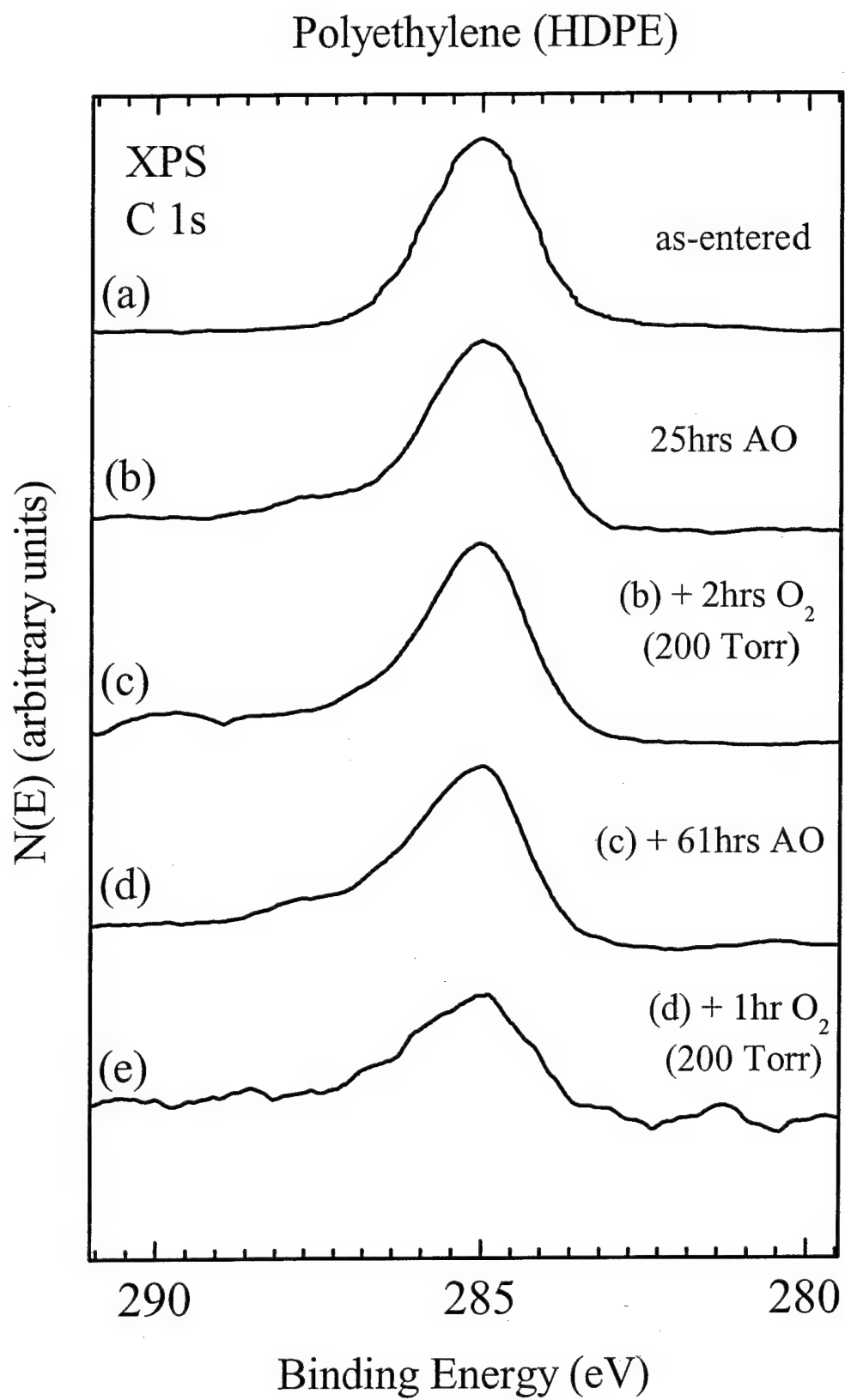
apparent by looking at these spectra that an

Please explain the
following 3 figures

Polyethylene (HDPE)



need Fig. caption



Polyethylene (HDPE)

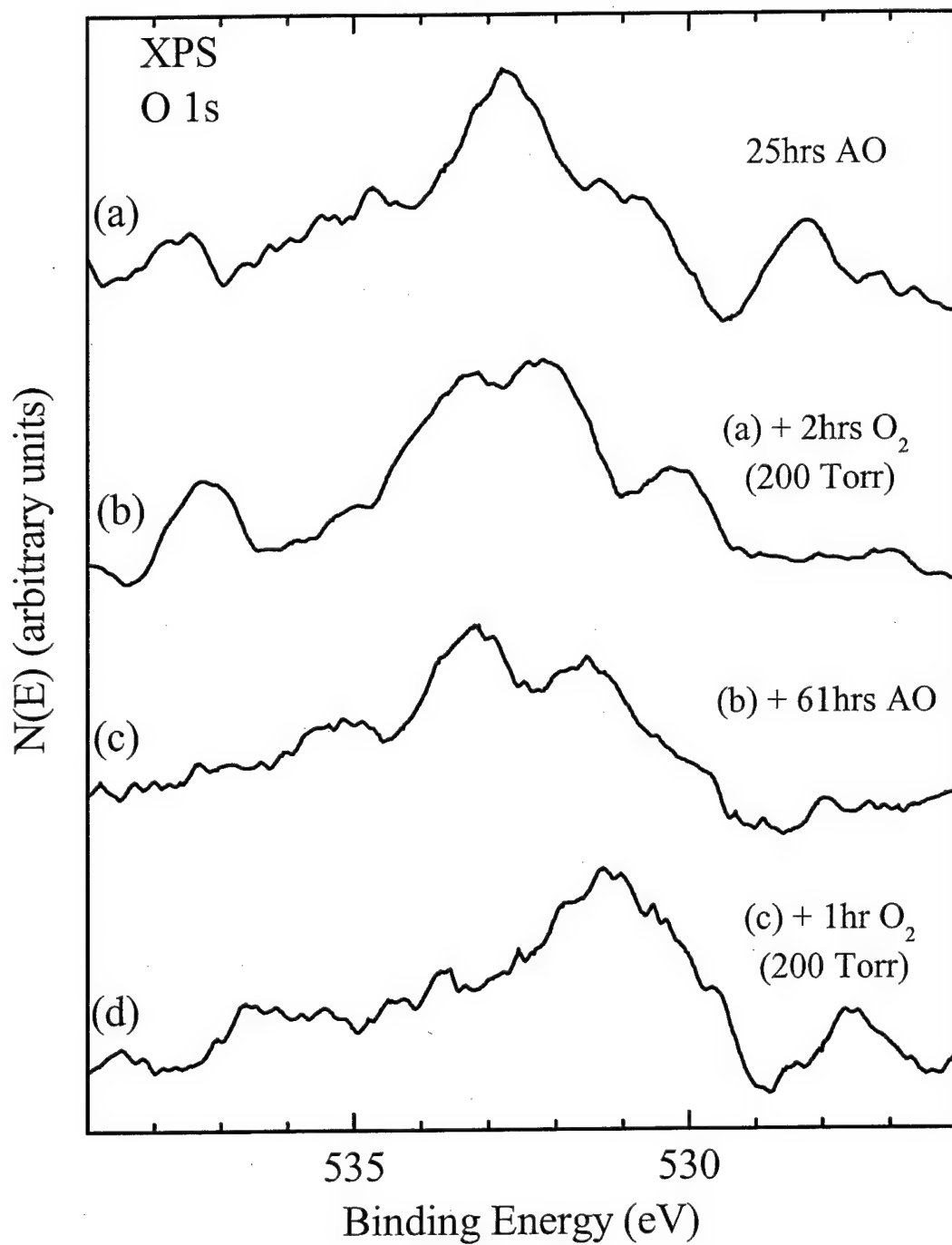


Fig. caption

6.4 Summary

In this study, a homologous series of fluoropolymers, commonly used in space applications, was characterized with XPS before and after a 15-minute exposure to the flux produced by a unique hyperthermal atomic oxygen source of 10^{15} atoms/cm²-s. The linear polymers investigated in this study (HDPE, Tedlar (PVF), Tefzel (PVdF), Teflon(PTFE)) possess a similar base structure with increasing fluorine-to-carbon ratios of 0, 1:2, 1:1 and 2:1 respectively. No interaction of the AO with the non-fluorine containing linear polymer HDPE was detected for the length of time exposed. However, a correlation exists between the chemical composition of the fluorinated polymers and the induced chemical and structural alterations occurring in the near-surface region as a result of exposure to AO. The XPS data indicates that AO initially attacks the fluorine portion of the polymers resulting in substantial decrease in the near-surface fluorine concentration as observed through lower binding energy shifts in both high resolution C 1s and F 1s spectra. The near-surface fluorine-to-carbon ratios of Tedlar, Tefzel and Teflon decreased during AO exposure by 68%, 39% and 18.5% respectively.

CHAPTER 7
NEW SYNTHETIC ROUTE AND NMR CHARACTERIZATION OF POSS ANILINES
FOR POLYIMIDES

7.1 Introduction

As discussed in Chapter 5, several POSS-polyimides were synthesized and characterized before and after exposure to atomic oxygen. The Air Force anticipates that POSS-polyimide polymers may have potential uses in spacecraft applications as thermal control surfaces and solar array substrates. Recent studies have demonstrated that POSS-polyimides show superior resistance to atomic oxygen attack over conventional polyimides. The Air Force is also conducting research on using POSS-polyimides as low dielectric materials for electronic applications. Unfortunately, the polymers originally synthesized are based on POSS-monomers (Section 5.2.1) that are tedious, expensive and have little chance for scale-up. The synthetic reactions involved are moisture and air sensitive, must be carried out under inert atmosphere and include an amine protecting step. This chapter describes a new air and moisture stable, efficient, synthetic route for obtaining POSS aniline monomers which can be subsequently used for polyimide synthesis. The aniline monomers developed (**4** and **8**) are also less expensive to make and can be scaled up easily. Their synthetic schemes are depicted in Figure 7-1 and 7-2. As described below, nuclear magnetic resonance (NMR) characterization and reactivity studies have shown that these new POSS-aniline monomers are in fact a mixture of the ortho, meta and para isomers. Preliminary reactivity studies have also shown that these monomers react with anhydrides similar to those used in polyimide synthesis.

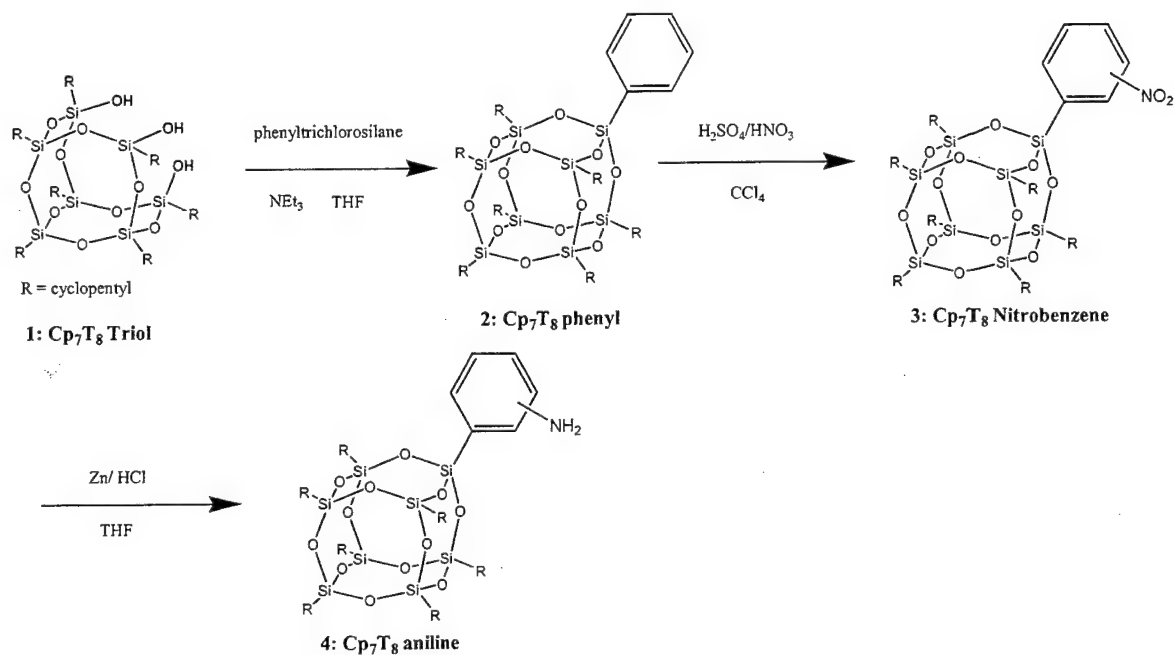


Figure 7-1. Synthesis of Cp_7T_8 aniline $\{(c\text{-C}_5\text{H}_{19})_7\text{Si}_8\text{O}_{12}[p,m,o\text{-C}_6\text{H}_4\text{NH}_2]\}$

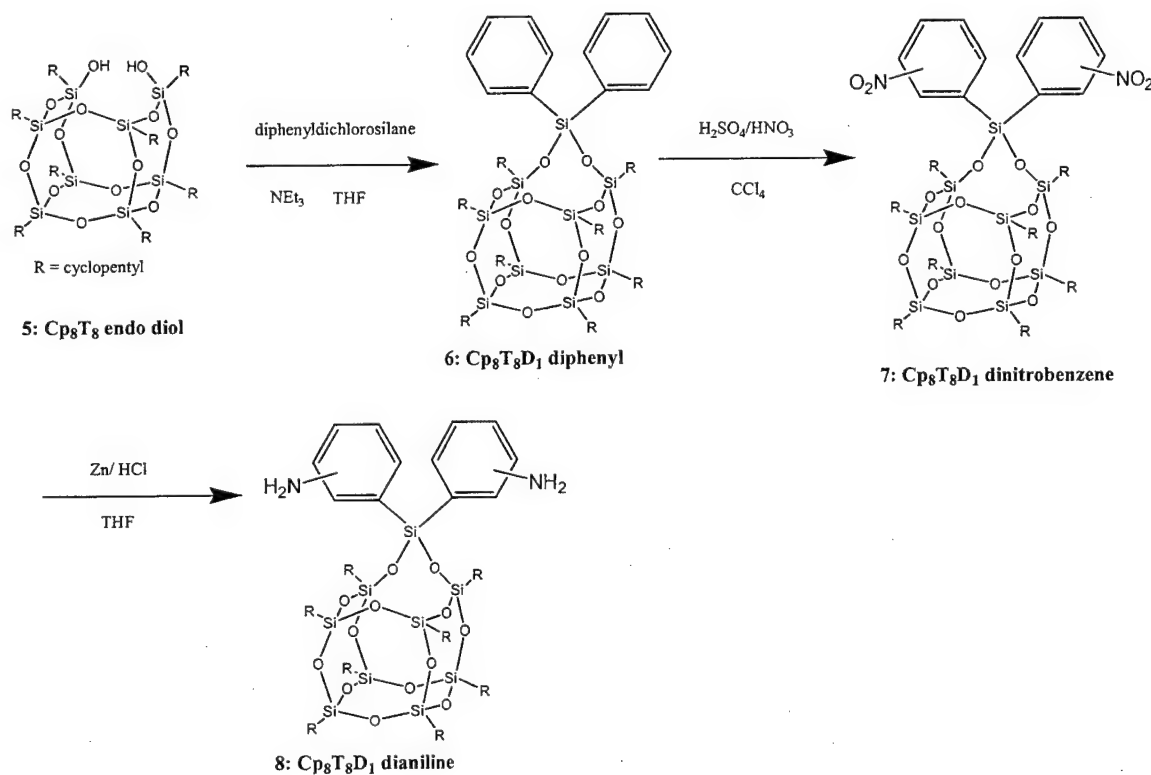


Figure 7-2. Synthesis of $\text{Cp}_8\text{T}_8\text{D}_1$ dianiline $\{(c\text{-C}_5\text{H}_{19})_8\text{Si}_9\text{O}_{13}[p,m,o\text{-C}_6\text{H}_4\text{NH}_2]_2\}$

7.2 Experimental

7.2.1 General Information

Solvents such as THF, ether and hexane were dried by passage through activated alumina columns [129]. Triethylamine was dried by refluxing over sodium metal and distilled prior to use. The POSS-silanols, **1** and **5**, were either synthesized according to the literature methods [130-134] or obtained from Hybrid Plastics Inc. [107]. All NMR spectra were collected on either a Bruker 300 or 400 MHz instrument and obtained from CDCl_3 solutions. ^1H , ^{13}C and ^{29}Si NMR spectra (reported in ppm using the δ scale) were referenced to residual CHCl_3 at 7.26 ppm, to CDCl_3 at 77.0 ppm, and to external SiMe_4 at 0 ppm, respectively. HPLC were obtained on a HP 1090 Liquid Chromatograph by injecting 10 μL of a 5 ppt sample onto a polyvinylalcohol-silicagel column and eluting at 1 mL / minute using a 5 vol % THF / 95 vol % cyclohexane mobile phase and a Varex MKIII evaporative light scattering detector.

7.2.2 Synthesis of Cp_7T_8 aniline $\{(c\text{-C}_5\text{H}_{19})_7\text{Si}_8\text{O}_{12}[p, m, o\text{-C}_6\text{H}_4\text{NH}_2]\}$

The synthetic scheme for Cp_7T_8 aniline is depicted in Figure 7-1. It involves 3 synthetic steps, corner capping a POSS trisilanol **1** with phenyltrichlorosilane, nitration in fuming nitric acid, and reduction using Zn/HCl. Other methods for reduction were attempted including reaction with formic acid and Pd/C, as well as catalytic hydrogenation with H_2 and Pd/C. However, these were not successful or the reactions took ~~to~~ long to go to completion.

7.2.2.1 Preparation of Cp_7T_8 phenyl $\{(\text{c-C}_5\text{H}_{19})_7\text{Si}_8\text{O}_{12}\text{C}_6\text{H}_5\}$

The reaction was conducted under nitrogen using oven-dried glassware, and dry solvents. 100 grams (1 equivalent) of POSS trisilanol **1** was added along with 3.3 equivalents of triethylamine dissolved in 500 mL THF while stirring to a 1 L round bottom flask. To this, a pressure equalizing addition funnel containing 1 equivalent of phenyltrichlorosilane and 200 mL of THF was attached. The silane was added over a couple of hours to maintain good stirring. The solution will get warm and the triethylamine HCl salt will make stirring difficult, especially if the addition rate is too fast. ^{TC} *(see below)* The reaction was allowed to proceed while stirring overnight. The remainder of the procedure was conducted in air. The solution was filtered to remove most of the NEt_3HCl , washed with diethylether and transferred to separatory funnel. The combined organic filtrate was washed with water (100 mL), 1M HCl (100 mL), and brine (100 mL) dried over MgSO_4 , [↓] filtered and most of the organic solvent removed under vacuum. The resulting thick slurry poured into about 400 mL of methanol to fully precipitate the product **2**, which was collected on a glass frit and air-dried to give a 90% yield. ^1H and ^{13}C NMR spectra are shown in Figures 7-3 and 7-4 respectively. ^1H NMR: 7.66(m, aromatic CH, 2H), 7.41(m, aromatic CH, 3H), 1.76 (m, CH_2 , 14H), 1.56(m, CH_2 , 42H), 1.02(m, CH, 7H). ^{13}C NMR: 134.03, 132.18, 130.16, 127.60 (aromatic), 27.32, 27.02, 26.96 (CH_2), 22.26 (CH). ^{29}Si NMR: -66.0, -66.4, -79.7 (3:4:1).

"If the addition rate is too fast, this ... difficult."

(This way, the change in tense will not jar the reader.)

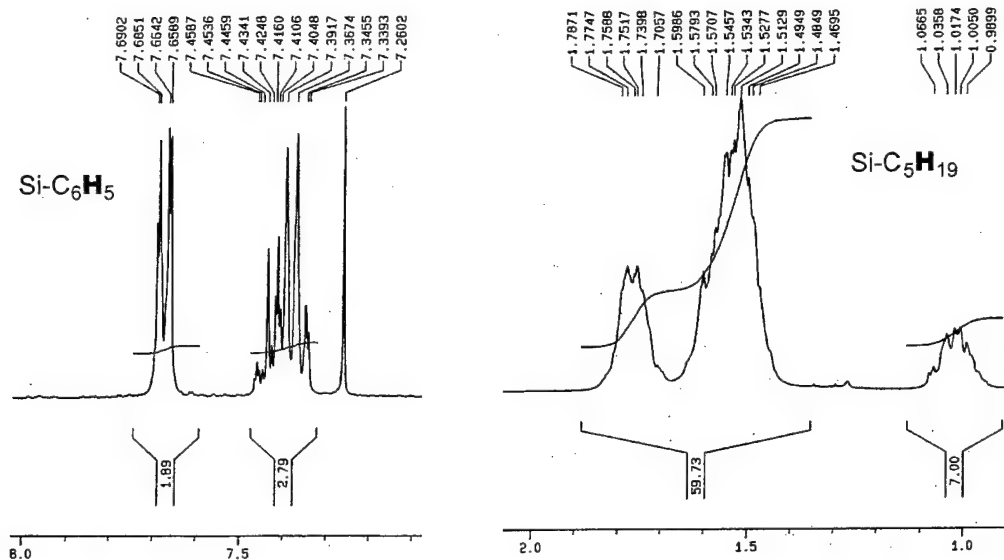


Figure 7-3. ^1H NMR of of Cp_7T_8 phenyl $\{(c\text{-C}_5\text{H}_{19})_7\text{Si}_8\text{O}_{12}\text{C}_6\text{H}_5\}$.

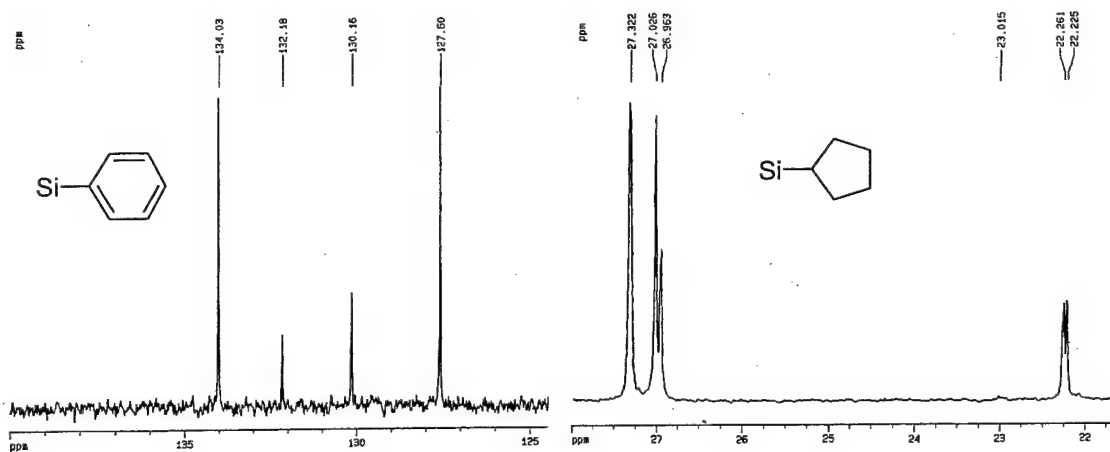


Figure 7-4. ^{13}C NMR of of Cp_7T_8 phenyl $\{(c\text{-C}_5\text{H}_{19})_7\text{Si}_8\text{O}_{12}\text{C}_6\text{H}_5\}$.

7.2.2.2 Nitration: Preparation of Cp_7T_8 nitrobenzene $\{(c\text{-C}_5\text{H}_{19})_7\text{Si}_8\text{O}_{12}[p,m,o\text{-C}_6\text{H}_4\text{NO}_2]\}$

10 grams of Cp_7T_8 phenyl (**2**) was dissolved in approximately 150 mL of carbon tetrachloride. In a 500 mL round bottom flask, 50 mL of concentrated H_2SO_4 followed by 50 mL of concentrated HNO_3 were added slowly while stirring. The Cp_7T_8 phenyl/ CCl_4 solution was then slowly transferred via a pipette to the acid solution

not stirred

— while stirring and ~~let~~ stir for about 1hr. 500mL DI water was placed in a 1 L round bottom flask and chilled in an ice bath. The acid/ $Cp_7T_8phenyl/CCl_4$ solution was then slowly added to the chilled DI water. Everything was then transferred to a separatory funnel and extracted three times with 25 mL of CCl_4 . The CCl_4 organic layer is the bottom layer in the separatory funnel. Some floating white/yellowish compound was present between the aqueous and organic layer, however, this was recovered by gently swirling the sep funnel and adding more CCl_4 . This was followed by an extraction with *brine*. After recovering the organic layer in an erlenmeyer flask, sodium bicarbonate was used to neutralize the solution. The solution was then filtered and the organic solvent removed under vacuum. The resulting material was redissolved in THF (75 mL), precipitated in methanol (300 mL), collected in a glass frit and air dried resulting in a fine white powder giving a 90% yield. The product **3**, is a mixture of the para (8%), meta (37%) and ortho (55%) isomers as confirmed through proton homodecoupling and 2 dimensional $^1H, ^1H$ correlation spectroscopy (COSY) [135] shown later. 1H , ^{13}C , and ^{29}Si NMR spectra are shown in Figures 7-5 through 7-7 respectively. Figure 7-8 shows the HPLC. 1H NMR: 8.52(d, $J_{H-H} = 2.0$ Hz, aromatic CH, meta), 8.26(m, aromatic CH, meta), 8.20(m, aromatic CH, ortho, para), 8.03(m, aromatic CH, ortho,) 7.96(m, aromatic CH, meta), 7.83 (d, aromatic CH, para), 7.67(m, aromatic CH, ortho), 7.62(m, aromatic CH, ortho), 7.55(t, aromatic CH, meta), 1.76 (m, CH_2 , 14H), 1.56(m, CH_2 , 42H), 1.02(m, CH, 7H). ^{13}C NMR: 153.30, 149.27, 147.64, 140.56, 139.92, 137.7, 135.01, 134.82, 133.09, 131.24, 128.88, 128.73, 127.99, 124.95, 123.73, 122.28, (aromatic), 27.29, 27.20, 27.02, 27.00, 26.99, 26.80 (CH_2), 22.26, 22.20, 22.15, 22.06 (CH). ^{29}Si NMR: -66.15, -66.18, -66.27, -66.34, -66.46, -78.25 (meta), -78.76 (para), 79.90 (ortho).

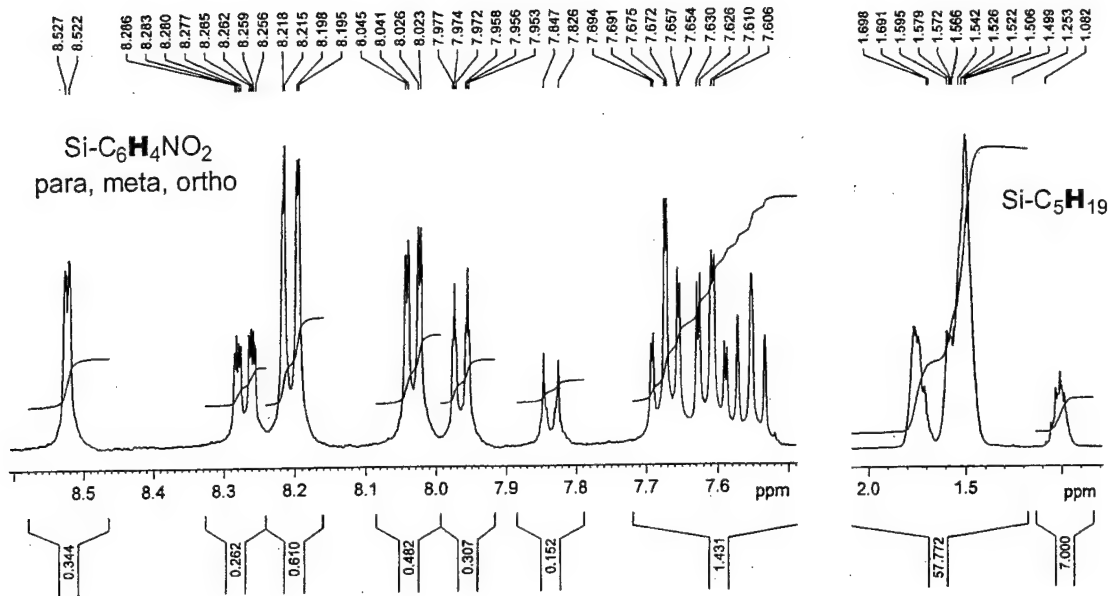


Figure 7-5. ^1H NMR of Cp_7T_8 nitrobenzene $\{(c\text{-C}_5\text{H}_{19})_7\text{Si}_8\text{O}_{12}[p,m,o\text{-C}_6\text{H}_4\text{NO}_2]\}$.

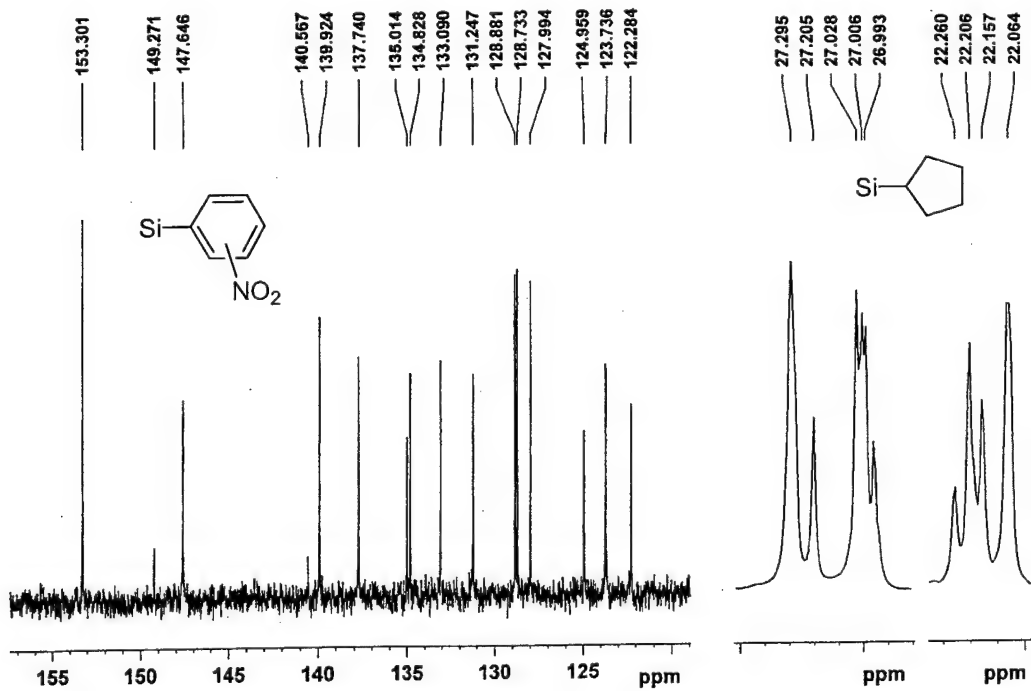


Figure 7-6. ^{13}C NMR of Cp_7T_8 nitrobenzene $\{(c\text{-C}_5\text{H}_{19})_7\text{Si}_8\text{O}_{12}[p,m,o\text{-C}_6\text{H}_4\text{NO}_2]\}$.

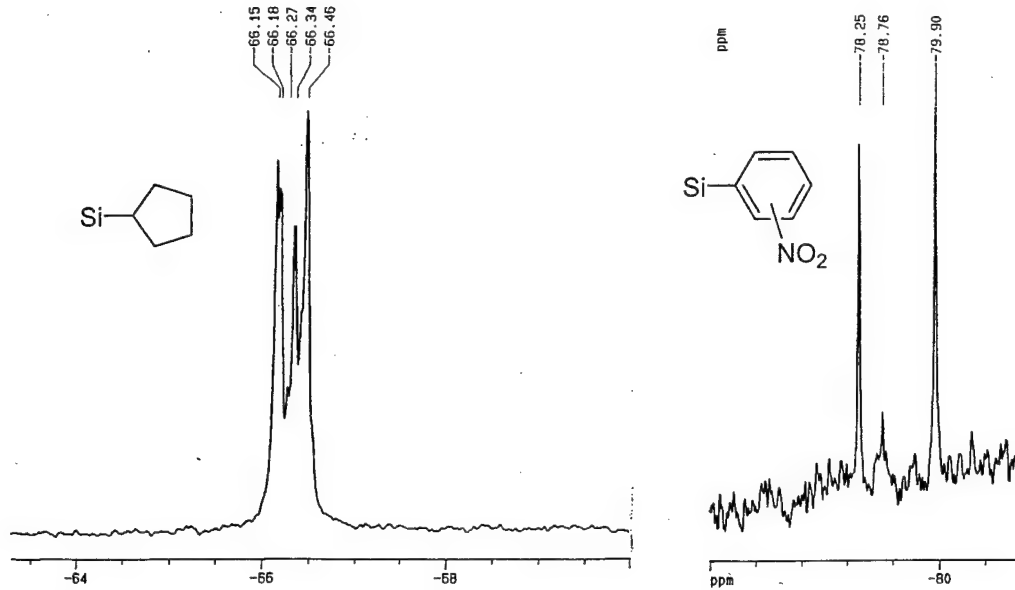


Figure 7-7. ^{29}Si NMR of Cp_7T_8 nitrobenzene $\{(c\text{-C}_5\text{H}_{19})_7\text{Si}_8\text{O}_{12}[p,m,o\text{-C}_6\text{H}_4\text{NO}_2]\}$.

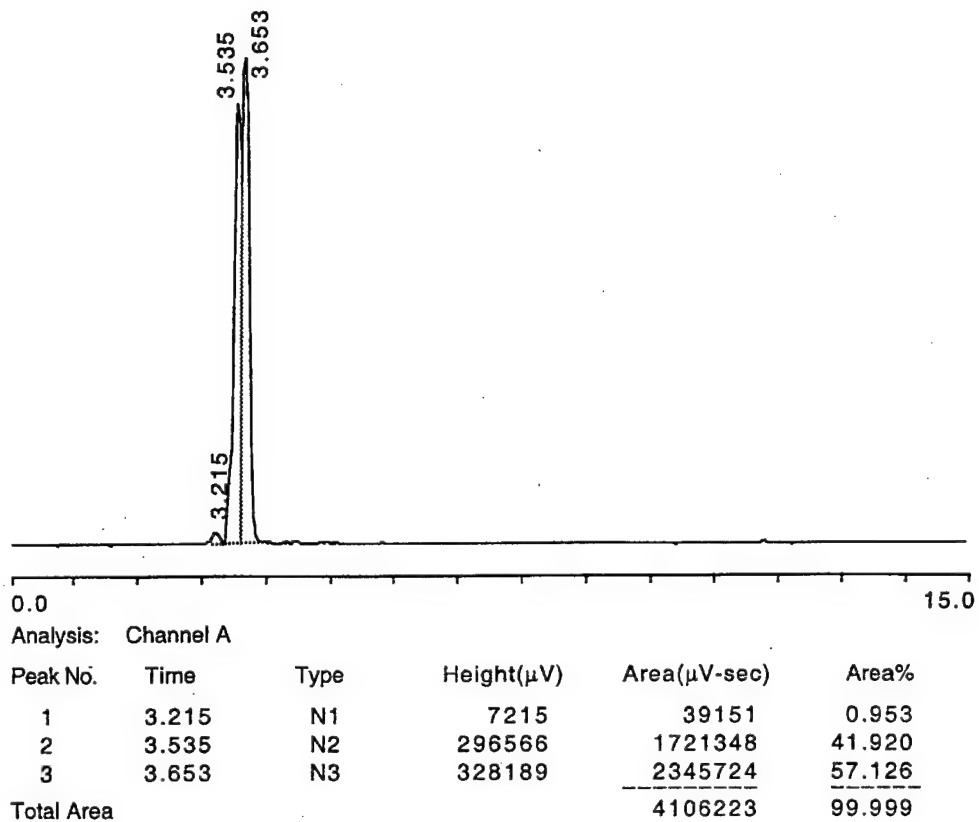


Figure 7-8. HPLC of Cp_7T_8 nitrobenzene $\{(c\text{-C}_5\text{H}_{19})_7\text{Si}_8\text{O}_{12}[p,m,o\text{-C}_6\text{H}_4\text{NO}_2]\}$.

7.2.2.3 Reduction: Preparation of Cp₇T₈ aniline {(c-C₅H₁₉)₇Si₈O₁₂[p,m,o-C₆H₄NH₂]}

5 grams of Cp₇T₈ nitrobenzene (3) and 6 equivalents of zinc were dissolved in THF in a 500 mL round bottom flask while stirring. To the resulting dark grey stirring slurry, approximately 7 equivalents of concentrated (12M) HCl was added slowly via syringe. The reaction bubbled slightly as hydrogen gas was produced in a competing reaction. As the reaction proceeded, the solution began to clear as the remaining zinc agglomerated and sank to the bottom of the stirring flask. The resulting ZnCl₂ that formed was soluble in THF. The reaction was ~~let~~ stir for about 1 hour after which it was filtered using a glass frit to remove any excess zinc. The filtrate was dried under vacuum and redissolved in a minimal amount of diethylether (10 mL). This was then precipitated in methanol (50 mL), filtered and dried in air resulting in an off-white fine powder giving an 87% yield. The product 4 is a mixture of the para (5%), meta (38%) and ortho (57%) isomers as confirmed through proton homodecoupling and 2 dimensional ¹H,¹H COSY shown later. ¹H, ¹³C, and ²⁹Si NMR spectra are shown in Figures 7-9 through 7-11 respectively. ¹H NMR: 7.46(m, aromatic CH, ortho), 7.23(m, aromatic CH, para), 7.21(m, aromatic CH, meta), 7.20(m, aromatic CH, ortho), 7.06(m, aromatic CH, meta), 6.82 (m, aromatic CH, ortho), 6.74(m, aromatic CH, ortho), 6.63(d, J_{H-H} = 8.0 Hz, aromatic CH, ortho), 4.10(s, NH₂, 2H), 1.76 (m, CH₂, 14H), 1.53(m, CH₂, 42H), 1.02(m, CH, 7H). ¹³C NMR: 151.91, 144.12, 135.89, 135.47, 133.28, 131.69, 128.65, 128.65, 125.20, 121.25, 117.69, 117.30, 114.98, 114.56, 114.4 (aromatic), 27.33, 27.28, 27.00, 26.96 (CH₂), 22.24, 22.20, 22.16 (CH). ²⁹Si NMR: -65.86, -65.92, -66.00, -66.09, -66.16, -78., -66.21, -66.30, -78.05, -79.01, -79.82.

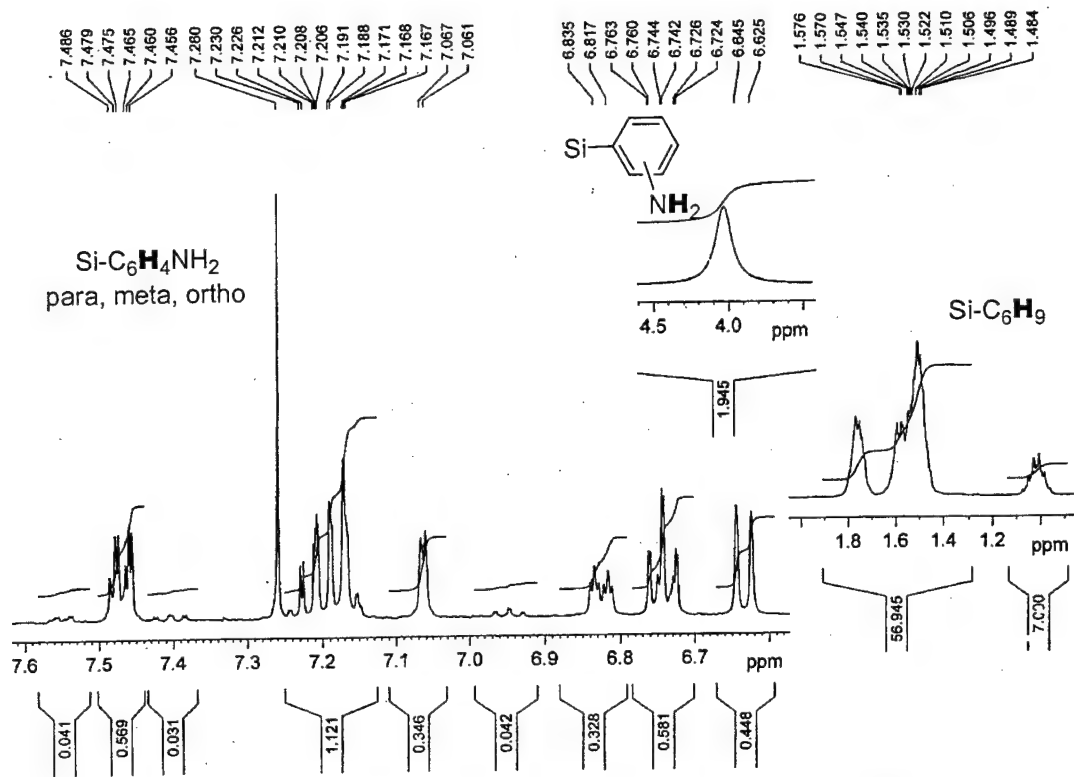


Figure 7-9. ^1H NMR of Cp_7T_8 aniline $\{(\text{c-C}_5\text{H}_{19})_7\text{Si}_8\text{O}_{12}[p,m,o-\text{C}_6\text{H}_4\text{NH}_2]\}$.

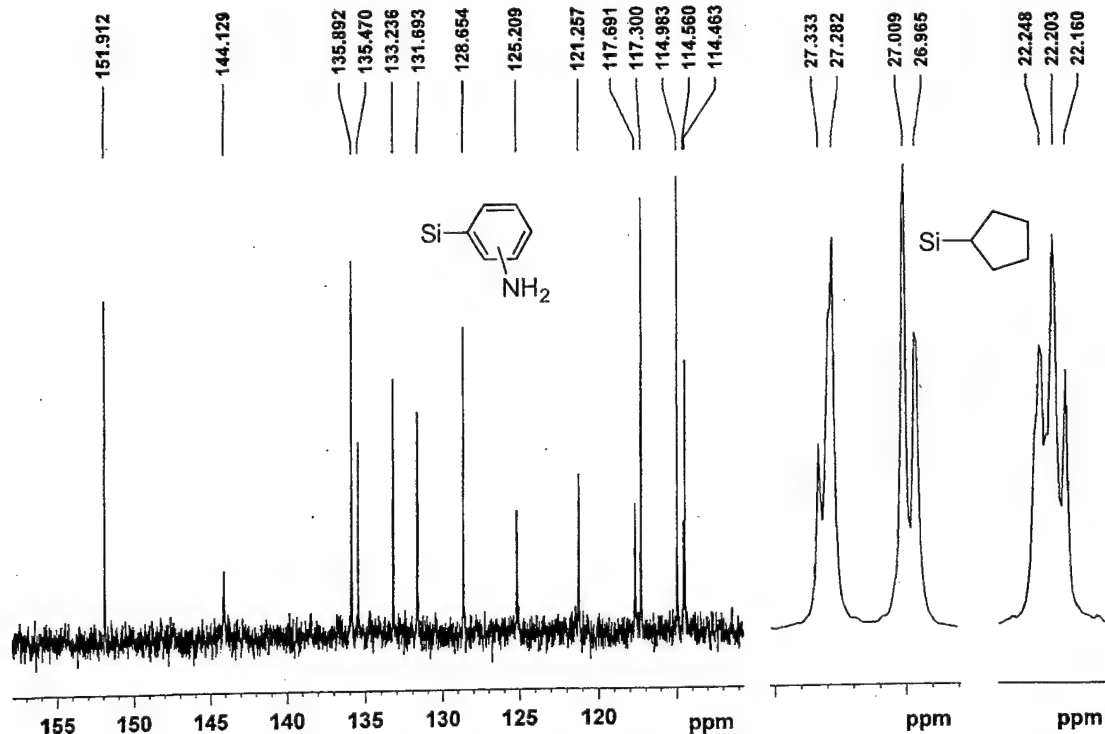


Figure 7-10. ^{13}C NMR of Cp_7T_8 aniline $\{(\text{c-C}_5\text{H}_{19})_7\text{Si}_8\text{O}_{12}[p,m,o-\text{C}_6\text{H}_4\text{NH}_2]\}$

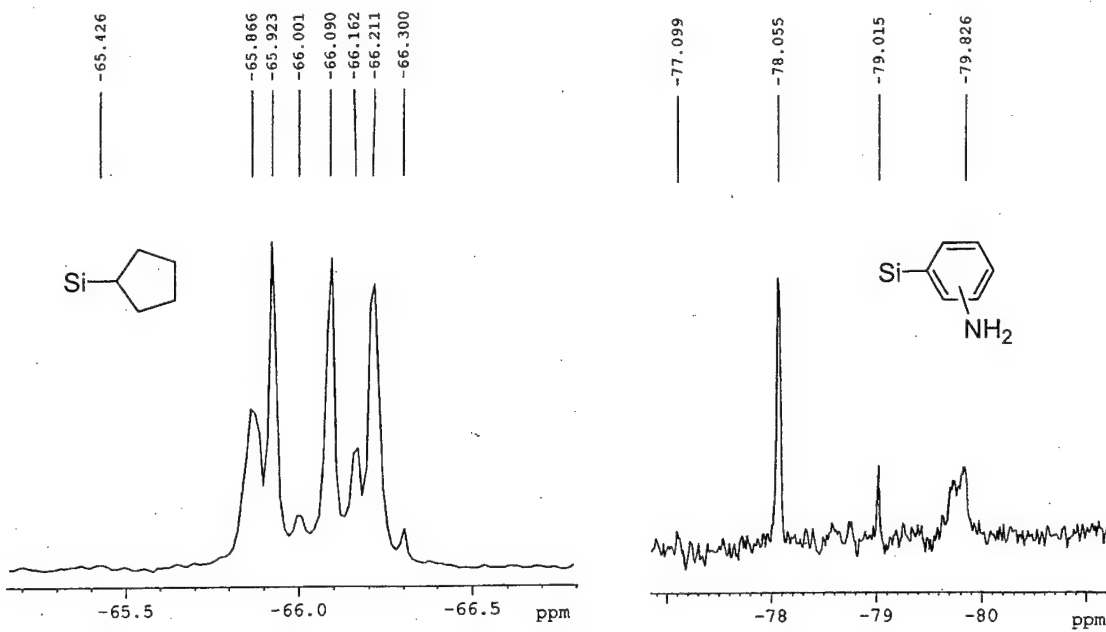


Figure 7-11. ^{29}Si NMR of Cp_7T_8 aniline $\{(\text{c-C}_5\text{H}_{19})_7\text{Si}_8\text{O}_{12}[p,m,o\text{-C}_6\text{H}_4\text{NH}_2]\}$

7.2.3 Synthesis of $\text{Cp}_8\text{T}_8\text{D}_1$ dianiline $\{(\text{c-C}_5\text{H}_{19})_7\text{Si}_9\text{O}_{13}[p,m,o\text{-C}_6\text{H}_4\text{NH}_2]_2\}$

The synthetic scheme for $\text{Cp}_8\text{T}_8\text{D}_1$ dianiline **8** is depicted in Figure 7-2. It involves 3 synthetic steps, capping a POSS endodiol **5** with diphenyldichlorosilane, nitration in fuming nitric acid, and reduction using Zn/HCl. At the time of this writing, the end product **8**, had not been fully characterized due to difficulty in isolating and purification of the final product.

7.2.3.1 Preparation of $\text{Cp}_8\text{T}_8\text{D}_1$ diphenyl $\{(\text{c-C}_5\text{H}_{19})_8\text{Si}_9\text{O}_{13}[\text{C}_6\text{H}_4]_2\}$

The reaction was conducted in a glove box under nitrogen using oven-dried glassware, and dry solvents. To a 100 mL round bottom flask, 10 grams (1 equivalent) of POSS endodiol **5** was added along with 4.4 equivalents of triethylamine dissolved in 50 mls THF while stirring. 1.25 equivalents of vacuum distilled diphenyldichlorosilane was added to the reaction flask via pipette. The solution will get warm and the

If the addition is too fast, the solution will boil.

*no spots
should be
before the
addition*

triethylamine HCl salt will make stirring difficult, especially if the addition rate is too fast.

The reaction was let stir overnight. The remainder of the procedure was conducted in air.

The solution was filtered in a glass frit to remove most of the NEt_3HCl , washed with

diethylether and the filtrate transferred to separatory funnel. The combined organic

filtrate was washed with water, 1M HCl and brine, dried over MgSO_4 , filtered and most

of the organic solvent removed under vacuum. The resulting thick slurry of POSS-

phenyl in $\text{THF}/\text{Et}_2\text{O}$ was precipitated in methanol and let stir several hours after which it

was the product **6** was collected on a glass frit and air-dried to give an 84% yield. ^1H and

^{13}C NMR spectra are shown in Figures 7-12 and 7-13 respectively. ^1H NMR: 7.68(m,

aromatic CH , 4H), 7.37(m, aromatic CH , 6H), 1.76 (m, CH_2 , 16H), 1.56(m, CH_2 , 48H),

0.97(m, CH , 8H). ^{13}C NMR: 135.88, 134.21, 129.62, 127.49 (aromatic), 27.33, 27.31,

27.26, 27.12, 27.09, 27.04, 27.02 (CH_2), 23.24, 22.62, 22.27 (CH).

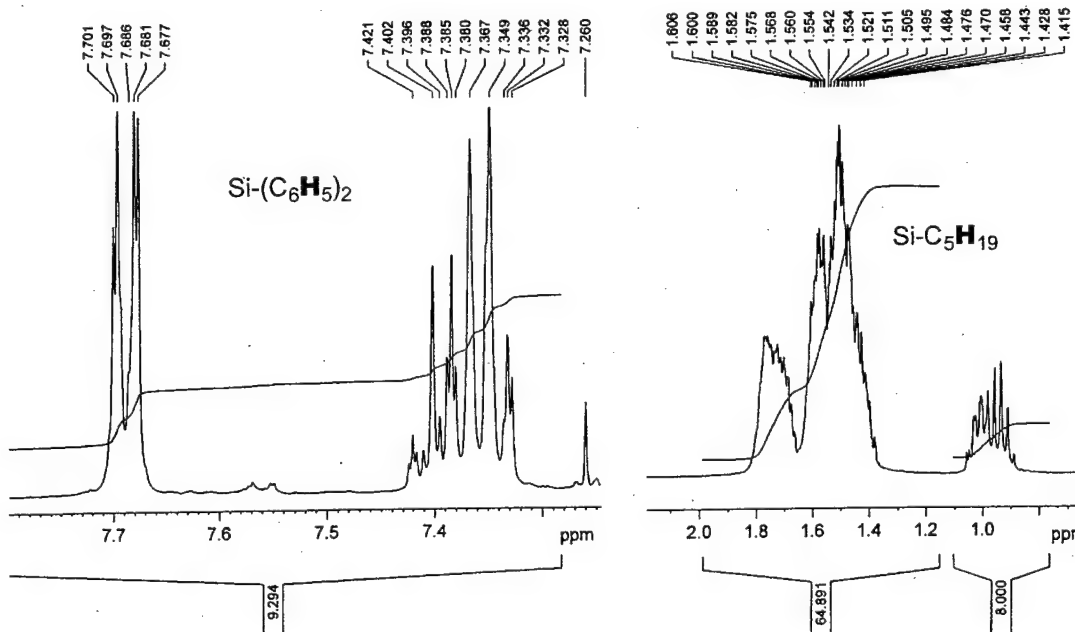


Figure 7-12. ^1H NMR of $\text{Cp}_8\text{T}_8\text{D}_1$ diphenyl $\{(c\text{-C}_5\text{H}_{19})_8\text{Si}_9\text{O}_{13}[\text{C}_6\text{H}_4]_2\}$

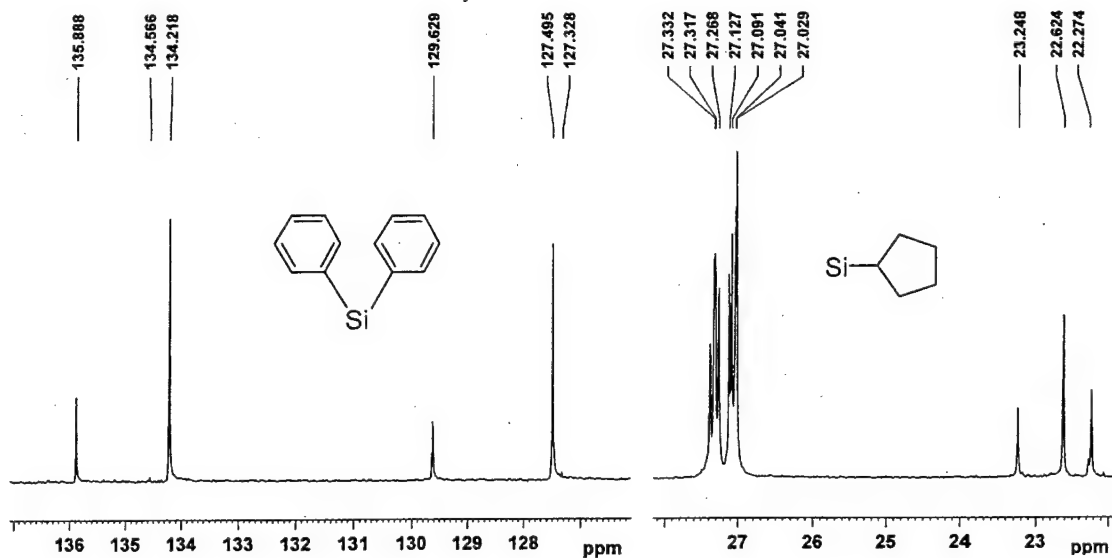


Figure 7-13. ^{13}C NMR of $\text{Cp}_8\text{T}_8\text{D}_1$ diphenyl $\{(c\text{-C}_5\text{H}_{19})_8\text{Si}_9\text{O}_{13}[\text{C}_6\text{H}_4]_2\}$

7.2.3.2 Nitration: Preparation of $\text{Cp}_8\text{T}_8\text{D}_1$ dinitrobenzene $\{(c\text{-C}_5\text{H}_{19})_8\text{Si}_9\text{O}_{13}[\text{p,m,o-}\text{C}_6\text{H}_4\text{NO}_2]_2\}$

10 grams of $\text{Cp}_8\text{T}_8\text{D}_1$ diphenyl (6) was dissolved in approximately 150 mL of carbon tetrachloride. In a 500 mL round bottom flask 50 mL of H_2SO_4 by 50 mL of concentrated HNO_3 were added slowly while stirring. The $\text{Cp}_8\text{T}_8\text{D}_1$ diphenyl / CCl_4 solution was then slowly transferred via a pipette to the acid solution while stirring and ~~left~~ ^{left} stir for about 1hr. 500mL DI water was placed in a 1 L round bottom flask and chilled in an ice bath. The acid/ $\text{Cp}_8\text{T}_8\text{D}_1$ diphenyl / CCl_4 solution was then slowly added to the chilled DI water. Everything was then transferred to a separatory funnel and extracted three times with 25 mL of CCl_4 . The CCl_4 organic layer ~~is~~ ^{made} the bottom layer in the separatory funnel. Some floating white/yellowish compound was present between the aqueous and organic layer, however, this was recovered by gently swirling the sep funnel and adding more CCl_4 . This was followed by an extraction with brine. After recovering the orgainc layer in an erlenmeyer flask, sodium bicarbonate was used to neutralize the

use a clean
sep. funnel

watch
for

solution. The solution was then filtered and the organic solvent removed under vacuum. The resulting material was redissolved in THF (75 mL), precipitated in methanol (300 mL), collected in a glass frit and air dried resulting in a fine white powder giving a 90% yield. The resulting product is a mixture of the ortho-ortho, ortho-meta, ortho-para, meta-meta, meta-para, and para-para isomers. ^1H NMR and HPLC are shown in Figures 7-14 and 7-15 respectively. HPLC clearly shows five of the isomers. The para-para isomer has the lowest probability of occurring and does not appear in the plot.

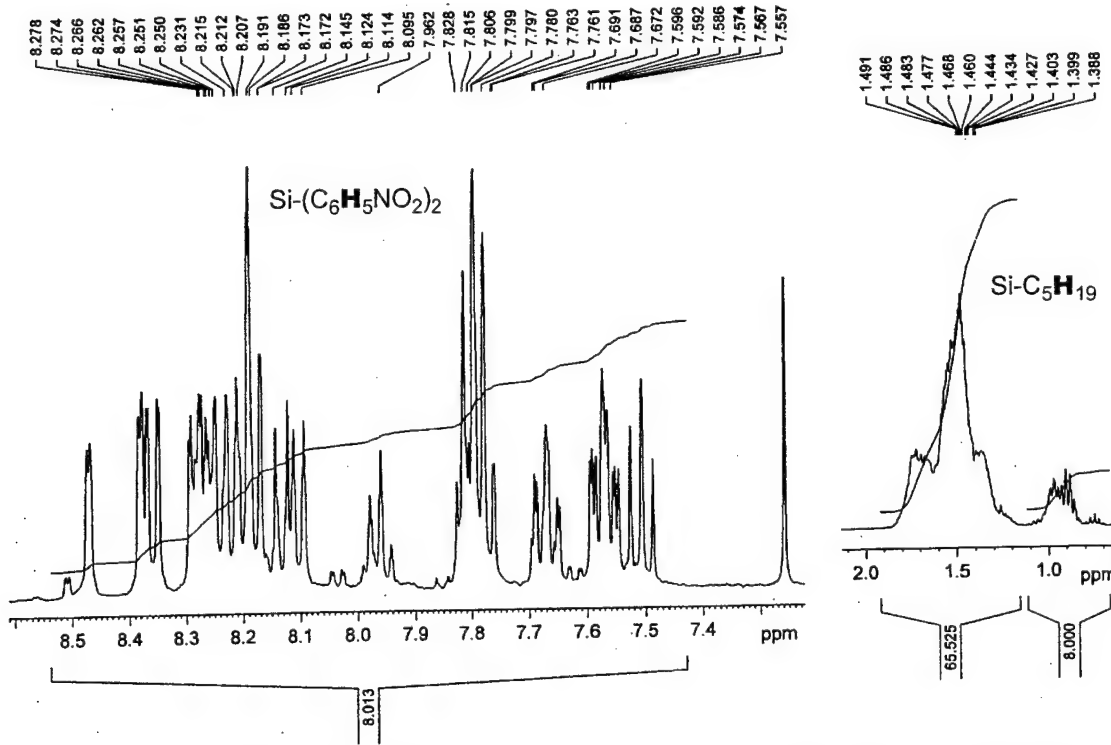


Figure 7-14. ^1H NMR of $\text{Cp}_8\text{T}_8\text{D}_1$ dinitrobenzene $\{(c\text{-C}_5\text{H}_{19})_8\text{Si}_9\text{O}_{13}[\text{p},\text{m},\text{o-C}_6\text{H}_4\text{NO}_2]_2\}$.

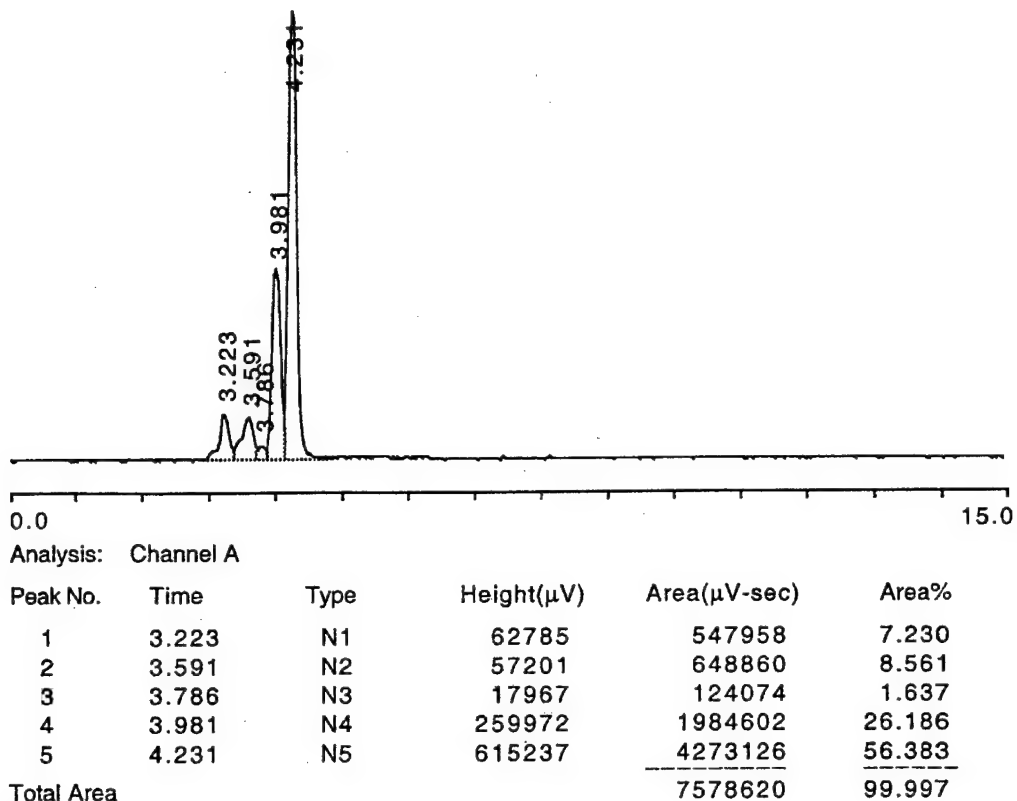


Figure 7-15. HPLC of $\text{Cp}_8\text{T}_8\text{D}_1$ dinitrobenzene $\{(\text{c-C}_5\text{H}_{19})_8\text{Si}_9\text{O}_{13}[\text{p,m,o-C}_6\text{H}_4\text{NO}_2]_2\}$.

7.2.3.3 Reduction: Preparation of $\text{Cp}_8\text{T}_8\text{D}_1$ dianiline $\{(\text{c-C}_5\text{H}_{19})_8\text{Si}_9\text{O}_{13}[\text{p,m,o-C}_6\text{H}_4\text{NH}_2]_2\}$

5 grams of $\text{Cp}_8\text{T}_8\text{D}_1$ dinitrobenzene and 12 equivalents of Zinc were dissolved in THF in a 500 mL round bottom flask while stirring. To the resulting dark grey stirring slurry, approximately 14 equivalents of concentrated (12M) HCl was added slowly via syringe. The reaction bubbled slightly as hydrogen gas was produced in a competing reaction. As the reaction proceededs, the solution began to clear up as the remaining zinc agglomerated and sank to the bottom of the stirring flask. The resulting ZnCl_2 that formed was soluble in THF. The reaction was let to stir for about 1 hour after which was then filtered to remove any excess zinc. The filtrate was dried under vacuum and the solids were redissolved in a minimal amount of diethylether. This was then precipitated

in methanol (50 mL), filtered and dried in air, resulting in an off-white fine powder giving an 89% yield.

7.3 Results and Discussion

Cp_7T_8 aniline was synthesized first as a model compound because it was easier to characterize through NMR than the dianiline monomer **8**. Two dimensional ^1H - ^1H COSY NMR experiments of the nitration product **3**, Cp_7T_8 nitrobenzene, and the reduction product **4**, Cp_7T_8 aniline, revealed that these monomers are a mixture of the meta, para and ortho isomers. Figures 7-16 shows the aromatic region of the ^1H NMR spectra of **3** with the peaks assigned to the corresponding isomers. Figure 7-17 shows the two dimensional ^1H - ^1H COSY NMR of this region. This experiment, along with proton homonuclear decoupling experiments provided sufficient information to adequately assign peaks corresponding to the meta, ortho or para isomer of Cp_7T_7 nitrobenzene **3**. Analysis of this data and calculations based on the integral values of the ^1H NMR of the aromatic region reveal that **3** is a mixture of the para (8%), meta (37%) and ortho (55%). This agrees well with calculations based on ^{13}C NMR which result in the ratio of ortho, meta and para to be 50%, 43% and 7% respectively. These results are interesting because the POSS cage has been shown to be electron withdrawing, and electron-withdrawing groups are considered to be meta directors. However, in this case a significant amount of the ortho isomer is present. Even more surprising is the fact that if in this case the POSS cage is also directing ortho and para, that the sterically-hindered ortho would be the more predominant isomer. Figure 7-19 shows the aromatic region of the ^1H NMR spectra of **4** with the peaks assigned to the corresponding isomers.

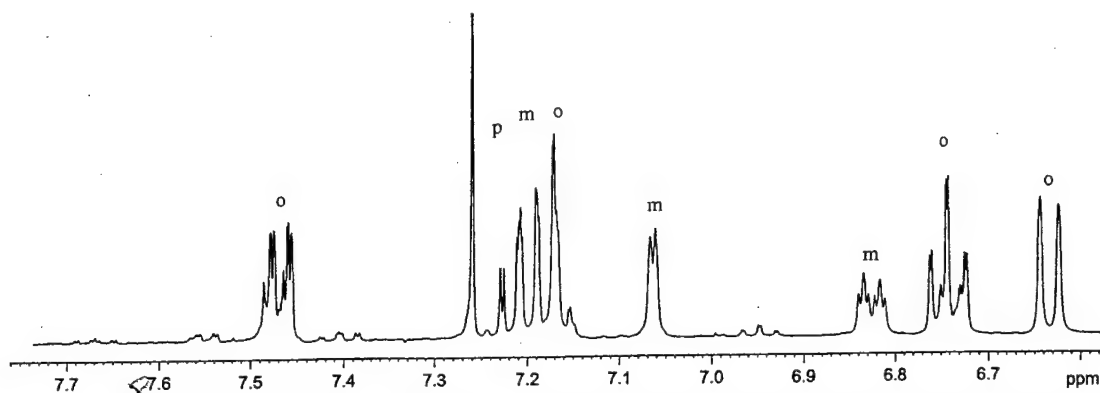


Figure 7-19. ^1H NMR of the aromatic region of Cp_7T_8 aniline with peaks assigned to the ortho, meta and para isomer.

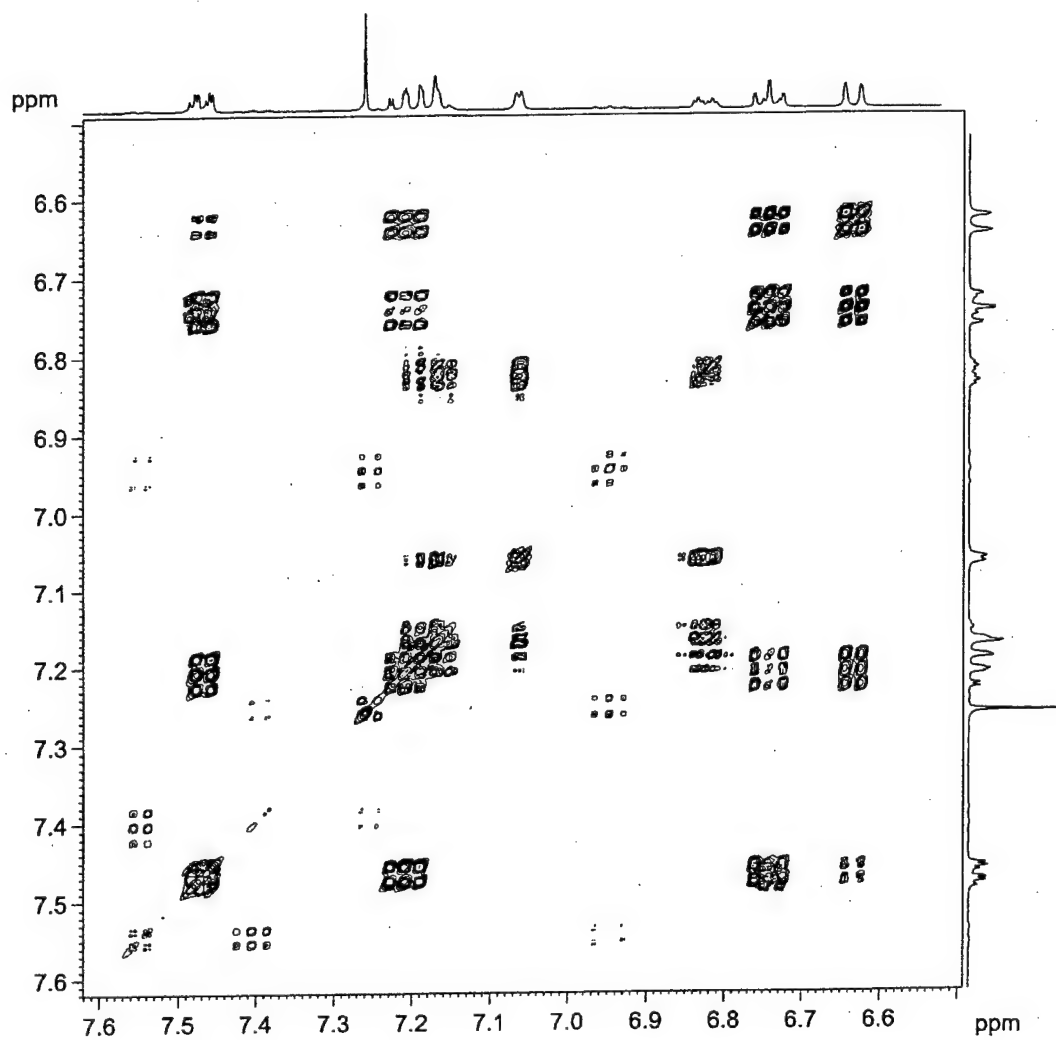


Figure 7-20. ^1H - ^1H NMR COSY of the aromatic region of Cp_7T_8 aniline.

Figure 7-20 shows the ^1H - ^1H NMR COSY of the aromatic region of 4. Analysis of this data and calculations based on the integral values of the ^1H NMR of the aromatic region reveal that 4 is a mixture of the para (5%), meta (38%) and ortho (57%) isomers.

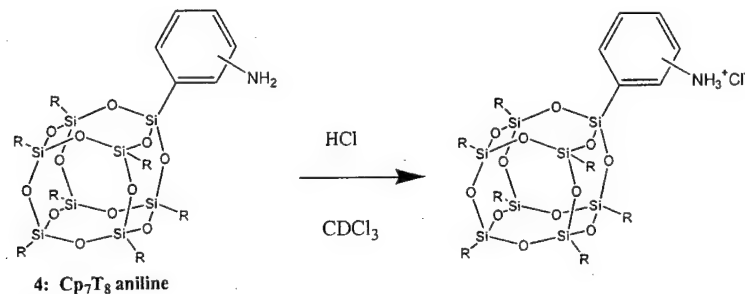


Figure 7-21. Reaction scheme for the synthesis of Cp_7T_8 aniline/HCl salt.

In order to ascertain that during synthesis of 4, the free base was indeed formed, a series of NMR tube reactions was conducted wherein 0.1 equivalents of HCl were added to Cp_7T_8 aniline to form the HCl salt while monitored intermittently with ^1H NMR.

Figure 7-21 depicts the reaction scheme. During these experiments the HCl salt indeed formed with the most basic of the isomers (meta) reacting first. Since the POSS cage is electron-withdrawing, the meta isomer would be the most basic, as shown in Figure 7-22, and would therefore be the first isomer to react to form the HCl salt as shown in Figure 7-23. This was further evidence that the correct isomer assignments had been given to the complex NMR spectra.

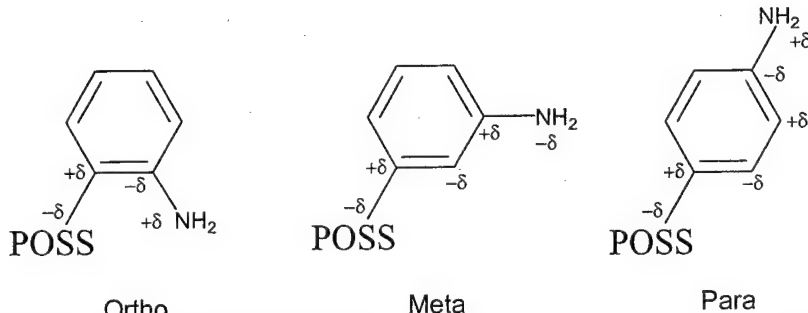


Figure 7-22. Basicity of isomers as affected by electron withdrawing POSS cage.

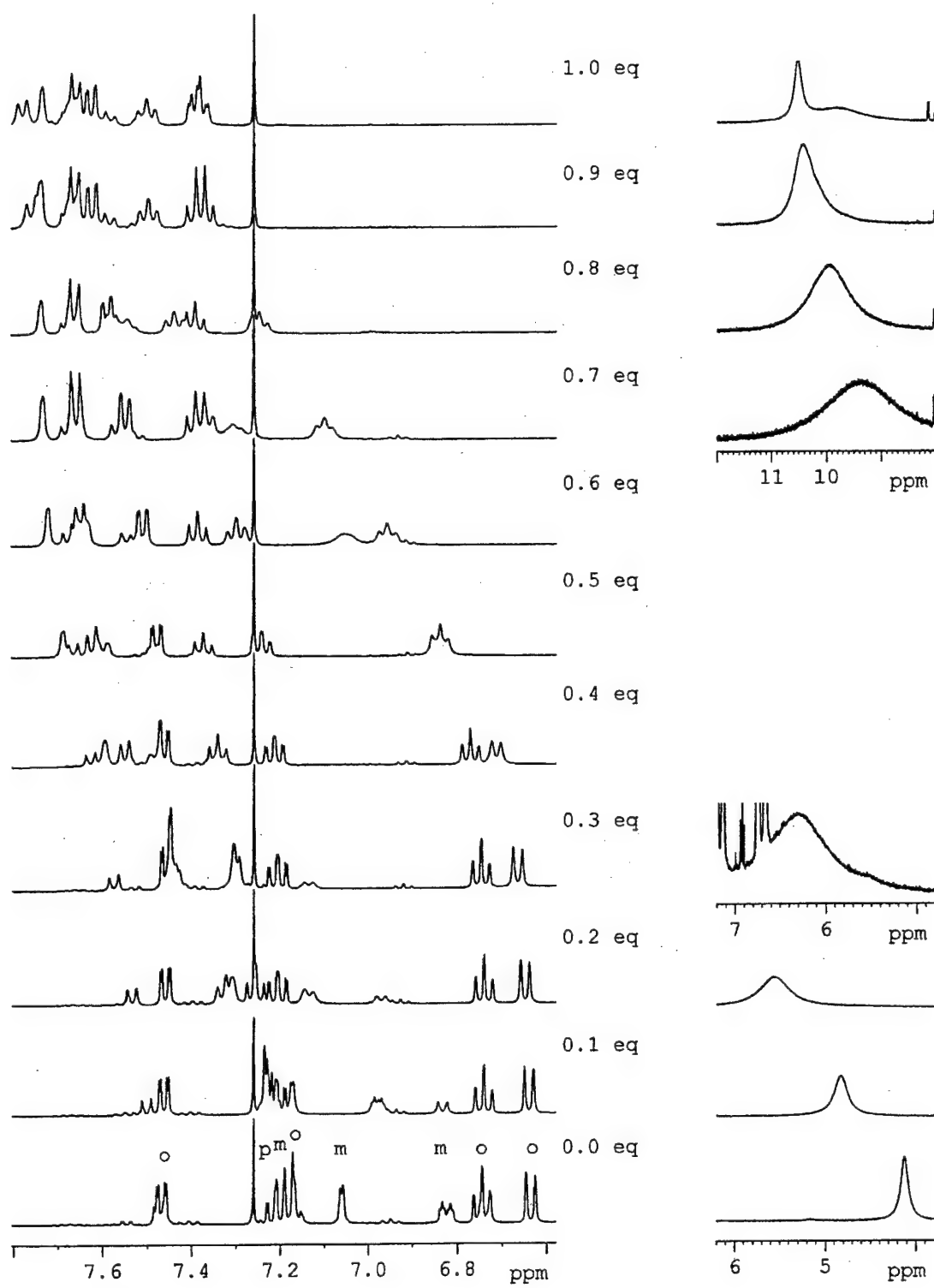


Figure 7-23. Formation of Cp_7T_8 aniline/HCl salt as monitored by ^1H NMR.

Since the majority (57%) of **4** was calculated to be the ortho isomer, there was concern that steric hindrance of the nitro group in relation with the POSS cage would impair its ability to react with an anhydride as would be the case to form a polyimide. In order to confirm that the molecule was indeed reactive, **4** was reacted with phthalic anhydride followed by chemical imidization with acetic anhydride as depicted in Figure 7-24. ^1H NMR of the reaction before chemical imidization is shown in Figure 7-25. Comparing this spectra with the spectra for **4** (Figure 7-19) it is evident that the monomer indeed reacted. In addition, the NH group of **9** is visible at 8.57 ppm. Upon chemical imidization with acetic anhydride the NH peak is no longer visible and instead a broader acid peak corresponding to acetic acid emerges at 11 ppm as seen in Figure 7-26.

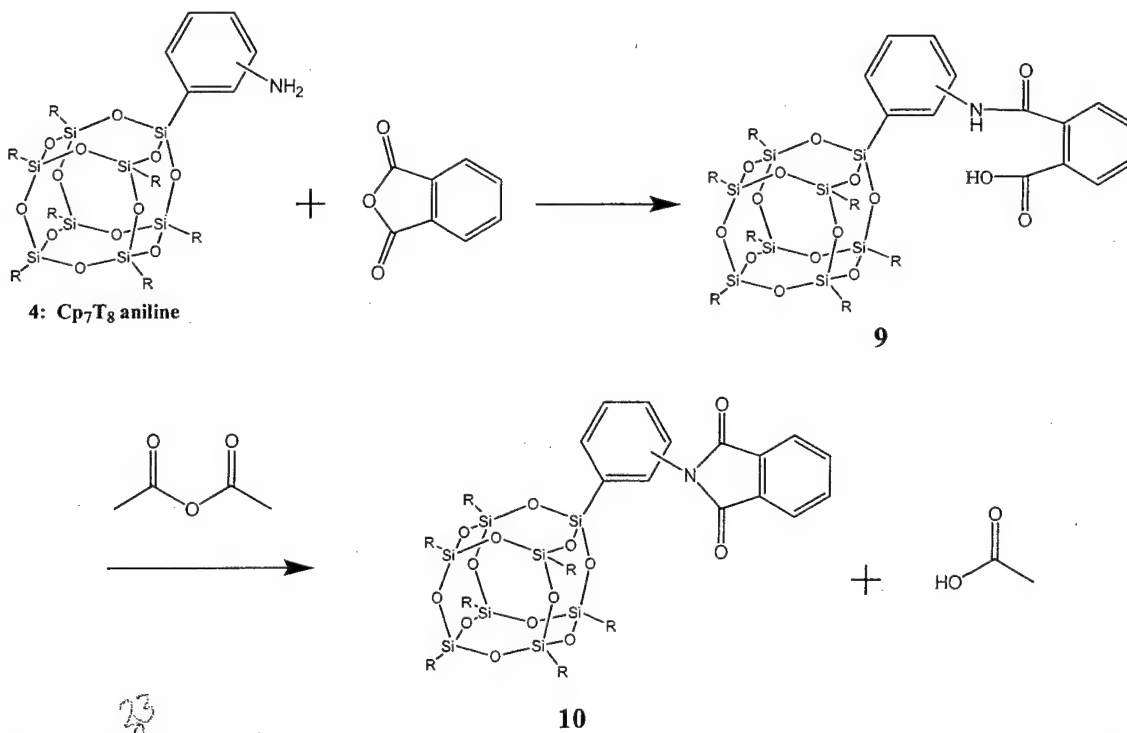


Figure 7-24. Reaction of Cp_7T_8 aniline with phthalic anhydride and subsequent chemical imidization with acetice anhydride.

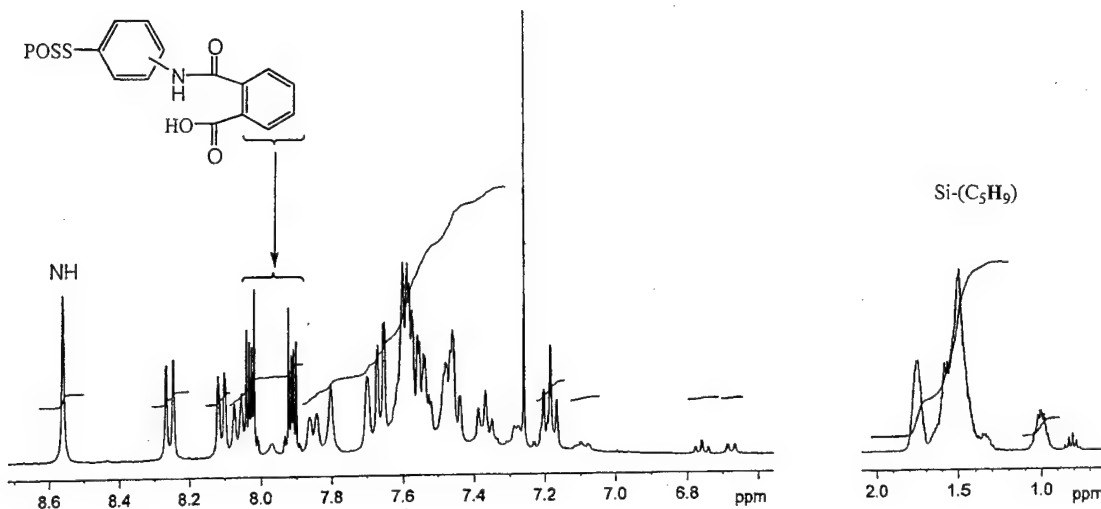


Figure 7-25. ^1H NMR of the reaction of Cp_7T_8 aniline with phthalic anhydride.

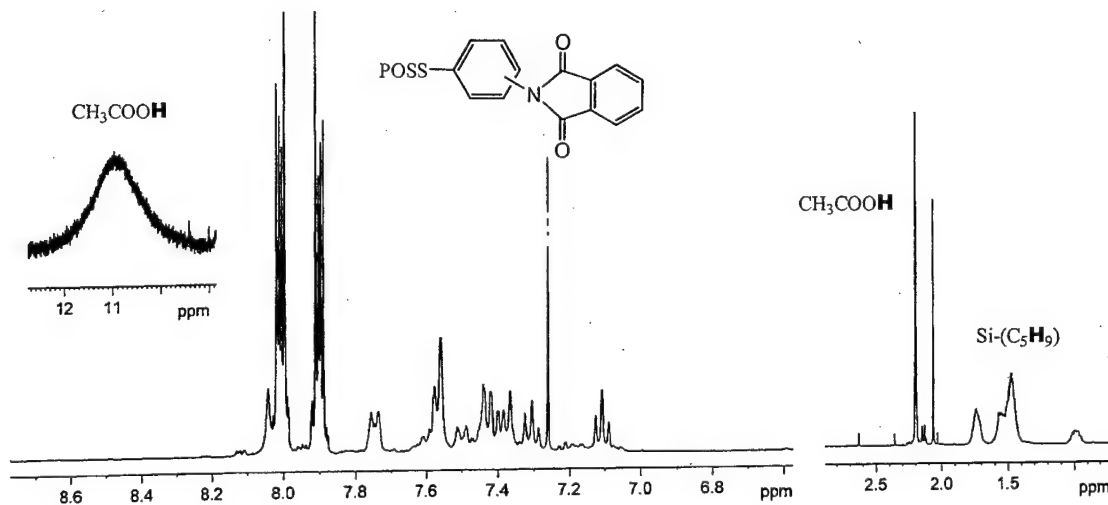


Figure 7-26. ^1H NMR of the reaction of Cp_7T_8 aniline with phthalic anhydride after chemical imidization with acetic anhydride.

In order to further address the issue of steric hindrance of the ortho isomer impairing these new POSS anilines from reacting to form polyimides, some very simple three dimensional modeling was carried out using the Chem3D program. Three dimensional space filling and ball and stick models of otrho- $\text{Cp}_8\text{T}_8\text{D}_1$ dianiline were derived using crystal structure coordinates obtained from X-ray diffraction data of

$\text{Cp}_8\text{Si}_8\text{O}_9(\text{SiMe}_2)$ [136]. The SiMe_2 unit was replaced with a $\text{Si}(\text{o-C}_6\text{H}_5\text{NH}_2)_2$ unit to show that the amines are not too crowded to react. Figure 7-26 and 7-27 show stereoviews of these models.

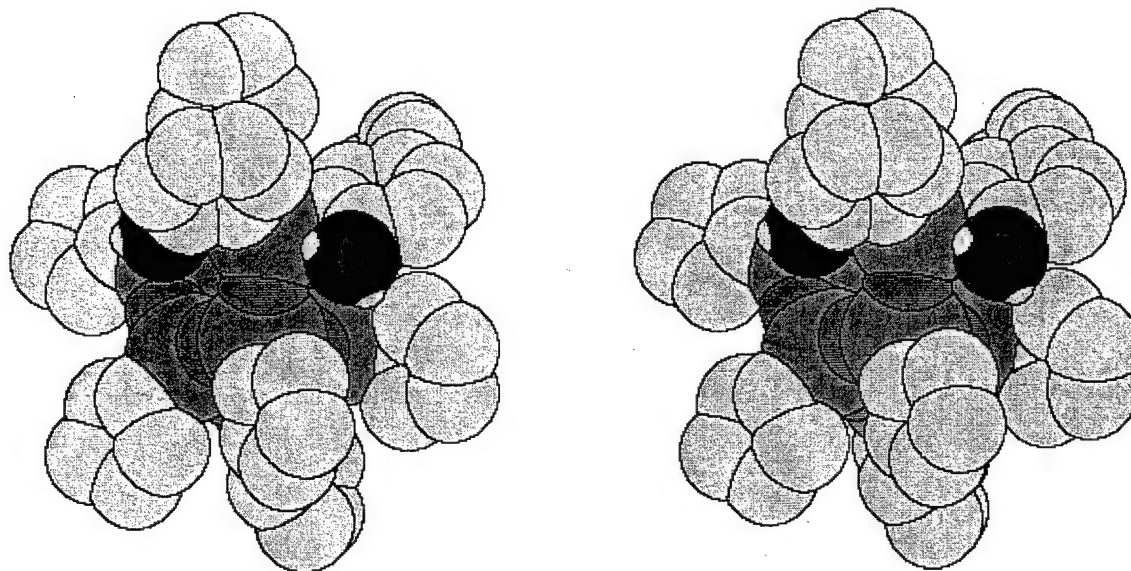


Figure 7-27. Stereoview of space filling model of otrtho- $\text{Cp}_8\text{T}_8\text{D}_1$ dianiline.

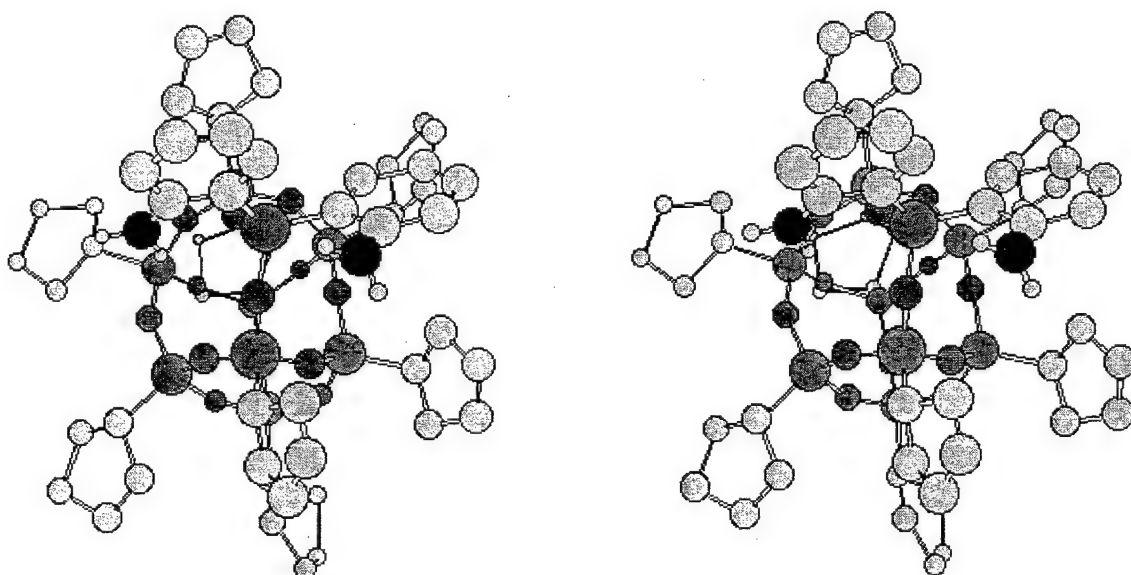


Figure 7-27. Stereoview of ball and stick model of otrtho- $\text{Cp}_8\text{T}_8\text{D}_1$ dianiline.

7.4 Summary

A new efficient route for synthesizing POSS aniline monomers was developed. The monomers formed are a mixture of the ortho, meta and para isomers, primarily ortho. The reactivity of the model monomer was verified by reacting with phthalic anhydride and simple 3 dimensional modeling using crystal structure coordinates obtained from X-ray diffraction measurements reveal that steric hindrance of the ortho isomer is not a concern.

CHAPTER 8

CONCLUSIONS AND SUGGESTIONS FOR FUTURE WORK

8.1 Atomic Oxygen Survivability of POSS-Polymers

The surfaces of a variety of polymers with and without polyhedral oligomeric silsesquioxanes were examined using XPS before and after exposure to atomic oxygen. We have shown that the addition of POSS to polymers results in improved resistance to degradation induced by AO exposure. This resistance is due to the rapid formation of a passivating silica layer which serves to protect the underlying virgin polymer from further erosion. In some cases, measurements have shown that a 1 mole % addition of POSS to the polymer matrix results in a full order of magnitude improvement in AO erosion resistance. In addition, several POSS polymers are currently orbiting the Earth while being exposed to the LEO environment on board the International Space Station. Upon retrieval, these polymers will be examined and the results compared to those contained herein. POSS incorporation into polymer systems is relatively simple and in most cases results in superior thermal and mechanical properties of the polymer. The Air Force is interested in using POSS to improve the survivability of polymers used in space related applications. Further investigations are currently underway to determine how POSS imparts this superior performance to these polymers.

8.2 Atomic Oxygen Source Characterization

8.2.1 Flux Characterization

The design of the ESD atomic oxygen source described in Chapter 2 has evolved over the years. Because of this it is essential to perform a series of experiments which fully characterize the magnitude and composition of the flux produced by the latest prototype. After using a large number of flux measurement methods, we believe that the most reliable is the growth of metal oxide films in which the metal deposition rate is known and stoichiometric oxides are formed [88, 101]. The standard flux measurement is currently based on the weight loss of Kapton. We plan to determine a flux based on stoichiometric metal oxide growth rate and then use the same AO source operating conditions to perform a Kapton erosion study. When an AO-eroded Kapton surface is exposed to air, it rapidly gains weight thereby making the weight-loss experimental results dubious. The standard procedure also may be incorrect because it is based on sources which introduce artifacts into the measurements as described above. We are in the process of attaching a glove box onto our sample entry point, and we will place a microbalance accurate to 6 places in the glove box. Using our source and this microbalance, we will be able to avoid all of the difficulties encountered in AO-induced Kapton weight-loss measurements.

Recently, several studies have been published which indicate that the electrical behavior of semiconducting oxides can be used to monitor flux [137-139]. We plan to carry out similar tests and calibrate the results with our AO source and known fluxes.

The latest prototype of the AO source produces fluxes just about 10^{15} O atoms/cm²-s. It is limited by the fact that the membrane material contains Ag. In order to produce higher AO fluxes, higher membrane operating temperatures are required to

increase the permeation rate. This results in evaporation of Ag and Ag deposition on the sample surface which is unacceptable. We are testing a new alloy material which will avoid this problem, and we anticipate that we will be able to attain AO fluxes of 10^{17} O atoms/cm²-s. This is about 100 times the actual AO flux encountered in space and will allow for accelerated testing of spacecraft materials.

8.2.2 Determination of AO Energy Distribution

Thus far, we have determined that most of the AO produced by the ESD source has an energy greater than 2 eV and that the O⁺ energy distribution forms an upper bound on the neutral energy distribution. We plan to determine the AO energy distribution by carrying a time-of-flight experiment. Knowing the flux at given source operating conditions, we also propose to determine the average energy of the flux using a bolometer.

8.3 Characterization Of Polymer Surfaces

Thus far, XPS has been used to characterize the surface of these polymers before and after AO exposure. However, a variety of other techniques are available to conduct further investigations as to how these surfaces react with AO.

8.3.1 Mass Spectrometry

A high sensitivity quadrupole mass spectrometer is installed in the UHV system which could be used to monitor species that are emitted from the polymer during erosion. This is the counterpart to what remains on the surface and therefore provides useful information about the erosion process. It also provides useful technological information because the emitted species in space often collect on other surfaces where they cause problems such as fogging lenses or windows. The species which are emitted by ion

irradiation are quite different for the different polymers and both the types of species and distribution changes with time as the polymer chains are broken during erosion. Therefore, it would be possible to monitor this species distribution as a function of time and correlate this information with that obtained from the XPS data.

8.3.2 Infrared Spectroscopy (IR)

Initially, the polymer is quite well defined, but the erosion process is violent both with respect to chemical effects and sputtering effects which produce a highly fragmented surface. XPS is useful in identifying a number of the species formed, but the peak position of many species are quite close so that they cannot be resolved. IR data can assist in interpretation of the XPS data. The usefulness of this technique has been demonstrated in studies of high-energy ion irradiation of PMMA [140]. As in the case of the XPS and MS data, the IR data will change with time so we will take IR spectra after the same erosion exposures that we take XPS data. The changes in the IR data will also provide detailed information about the mechanism of the erosion process.

8.3.3 Atomic Force Microscopy/ Secondary Electron Microscopy

During the AO erosion process, the surface morphology of Kapton has been shown to change. It is initially quite smooth and becomes very rough with AO exposure. SEM and AFM could be used to monitor the surface morphology as a function of erosion exposure. It will be interesting to determine if UV exposure as well as AO exposure alters surface morphology.

8.3.4 Mechanical and Tribological Experiments

As the chemical nature and morphology of a polymer change during AO erosion, its mechanical properties such as hardness and wear properties can also change. In some space applications of polymer surfaces, these properties are of importance. Hardness

testing and tribological testing on a few POSS-containing copolymer could be done to determine how these properties change as an SiO_2 layer is formed during AO erosion. In the case that all of the POSS copolymers form similar SiO_2 overlayers after AO erosion, then they should have similar mechanical and tribological properties. However, since the SiO_2 layer formed is very thin, the hardness and wear properties may also depend upon the nature of the deeper layers. A nano-indenter could be used to measure hardness on the as-prepared and AO-exposed POSS copolymers by varying the load which varies the surface sensitivity. In this way, it would be possible to determine if the near-surface hardness of the AO-exposed POSS copolymers are similar and if the hardness varies with depth sensitivity. Pin and disk wear studies could also be conducted on selected POSS copolymers to determine how AO erosion alters wear properties. Since the wear properties are strongly dependent upon surface chemical makeup and morphology, we anticipate that the changes in wear properties will be significant.

8.4 Exploring Synergistic Effects

8.4.1 Effects of UV Radiation

In addition to AO, the space environment also contains UV radiation. This is an important factor because UV radiation results in bond breakage and emission of surface species through photon stimulated desorption. Both vacuum UV (below 200 nm) and UV which reaches earth (200 to 400 nm) are encountered in the space environment. We are currently installing two lamps to the AO chamber so that we can carry out AO erosion studies with and without the presence of VUV and UV light. One lamp will be a deuterium lamp with a magnesium fluoride window. This system provides radiation between 118 and 200 nm. The other lamp will be a mercury-xenon short arc lamp with a

quartz window to provide UV radiation between 200 and 400 nm. The photon intensity at the polymer surface will be varied by changing the distance of the lamp to the sample and/or the lamp output power. Attempts will be made using calibration data to simulate the space environment as well as possible.

8.4.2 Effect of Temperature

In space the temperature of the polymer surfaces vary considerably depending upon the geometrical relationship of the surface with respect to the sun. To our knowledge, temperature effects have not been examined in AO erosion studies. We are currently incorporating the ability to heat and cool samples over the range of -100 to 500°C during AO exposure. We will select several POSS-containing copolymers and examine their AO-erosion properties as a function of temperature. It may be that the energetic collision of the AO with the polymer surface determines the reaction characteristics, but other processes such as diffusion of subsurface species to the surface may be quite temperature dependent. Therefore, these studies require consideration.

8.4.3 Effect of Total AO Fluence

Thus far we have carried out AO exposures for about 60 hrs at a flux equivalent to that in space while spacecraft are bombarded by AO for years so we do not know if further changes will occur. Even if further chemical changes are small, the morphological changes could be quite significant. Therefore, we propose carrying out longer exposures. This will be relatively easy if our new AO source prototype can attain fluxes of 10^{17} AO/cm²-s. A 7-day exposure in our system would be similar to a 2-year exposure in space. We will use the characterization methods described above to examine these samples.

8.4.4 Exposures to Different Gases

Previous studies [120, 121] demonstrated that both ion irradiation and AO bombardment of polymer surfaces results in highly chemically reactive surfaces. We attribute this as due to broken bonds which are unable to crosslink due to geometrical bonding constraints. The fact that this happens is beneficial for us because it gives us another way of characterizing the surface to obtain fundamental information about the mechanism of erosion. We could expose the AO-exposed surfaces to gases such as O₂, N₂, CH₄, H₂O and possibly others. We could also characterize the surfaces with XPS and IR to determine what chemisorbed on the surface and which species formed. This will provide information about the nature of the reactive species formed on the polymer surfaces during AO erosion. The gases exposures could be carried out in the preparation chamber which contain the recently installed IR instrumentation. With this setup, it would be possible to dose at high pressures (~ 1 atm) and simultaneously monitor the changes at the surface with IR.

8.4.5 Influence of Sputter Effects

Our previous studies [121] suggest that the 5 eV AO has enough kinetic energy to cause sputtering of atoms and ions off the surface. Since the AO is chemically reactive, it is not possible to isolate the influences of the chemical and sputtering effects. We propose to use 5 eV Ne atoms to study the effect of sputtering. The 5 eV Ne atoms will be produced by a fast-atom beam source (FABS) which we are currently building. The FABS will be located in the same chamber as the AO source so we will be able to determine the effects of the 5 eV Ne-exposed surface using XPS and IR without air exposure. We could also determine if reactive surfaces are formed using the gas chemisorption experiments described above. If sputtering occurs at a significant rate,

then both atoms and positive ions will be sputtered off the surface. We also have a secondary ion mass spectrometry (SIMS) system located in the atom source chamber. We could use the 5 eV Ne as the excitation to perform a SIMS experiment to monitor any positive ions emitted by sputtering.

BIOGRAPHICAL SKETCH



Rene I. Gonzalez Rodriguez was born on March 4, 1974, in Santurce, Puerto Rico, to Rene A. Gonzalez Freyre and Juanita F. Rodriguez Aleman. At the age of 4, his mother remarried to Francisco Rodriguez Rivera, and Rene and his family moved to Spain where he lived until the age of 15. Rene moved back to Puerto Rico where he resided with his uncle, Jose I. Gonzalez Freyre, while attending

high school at the Baldwin School of Puerto Rico, graduating in 1992. In May 1996,

Rene obtained a B.S. in chemical engineering from Rensselaer Polytechnic Institute in

Troy, New York, and was commissioned as a Second Lieutenant in the United States Air

Force. Sponsored by the Air Force, Rene entered graduate school at the University of

Florida at Gainesville, Florida, receiving an M.S. in chemical engineering in May 1998.

Rene was subsequently assigned to the Air Force Research Laboratory at Edwards Air

Force Base, California, where he conducted research on developing and testing high

performance plastics as spacecraft materials. During this time, Rene was promoted to

Captain and continued his collaboration with his research advisor, Professor Gar B.

Hoflund, at the University of Florida. Through this collaborative work between the Air

Force Research Laboratory and the University of Florida, he obtained a Ph.D. in May

2002. Rene is married to Monica C. Diaz-Gonzalez, who at the time of this writing was

expecting their first child.

I certify that I have read this study and that in my opinion it conforms to acceptable standards of scholarly presentation and is fully adequate, in scope and quality, as a thesis for the degree of Doctor of Philosophy.

Gar B. Hoflund, Chairman
Professor of Chemical Engineering

I certify that I have read this study and that in my opinion it conforms to acceptable standards of scholarly presentation and is fully adequate, in scope and quality, as a thesis for the degree of Doctor of Philosophy.

Oscar D. Crisalle
Associate Professor of Chemical
Engineering

I certify that I have read this study and that in my opinion it conforms to acceptable standards of scholarly presentation and is fully adequate, in scope and quality, as a thesis for the degree of Doctor of Philosophy.

Jason F. Weaver
Assistant Professor of Chemical
Engineering

I certify that I have read this study and that in my opinion it conforms to acceptable standards of scholarly presentation and is fully adequate, in scope and quality, as a thesis for the degree of Doctor of Philosophy.

Vaneica Y. Young
Associate Professor of Chemistry

This thesis was submitted to the Graduate Faculty of the College of Engineering and to the Graduate School and was accepted as partial fulfillment of the requirements for the degree of Doctor of Philosophy.

May 2002

Pramond P. Khargonekar
Dean, College of Engineering

Winfred M. Phillips
Dean, Graduate School

30 to ✓ →
Some editing
(highlighted)

LIST OF REFERENCES

1. Champion, K.S.W., Cole, A.E., and Kantor, A.J., *Standard and Reference Atmospheres*, in *Handbook of Geophysics and the Space Environment Chapter 14*, A.S. Jursa, Editor. 1985, Air Force Geophysics Laboratory, Air Force Systems Command, United States Air Force, National Technical Information Service: Springfield, VA, p. 14-1-14-43.
2. Hedin, A.E., "A Revised Thermospheric Model Based On Mass-Spectrometer and Incoherent-Scatter Data - Msis-83," *Journal of Geophysical Research-Space Physics*, 1983. **88**(A12): p. 170-188.
3. Koontz, S.L., Leger, L.J., Visentine, J.T., Hunton, D.E., Cross, J.B., and Hakes, C.L., "EOIM-III Mass-Spectrometry and Polymer Chemistry - STS-46, July-August 1992," *Journal of Spacecraft and Rockets*, 1995. **32**(3): p. 483-495.
4. Koontz, S.L., Leger, L. J., Rickman, S. L., Hakes, C. L., Bui, D. T., Hunton, D. E. and Cross, J.B., "Oxygen Interactions With Materials III- Mission and Induced Environments," *Journal of Spacecraft and Rockets*, 1995. **32**(3): p. 475-482.
5. Dever, J.A., "Low earth orbital atomic oxygen and ultraviolet radiation effects on polymers," *NASA Technical Memorandum-103711*, 1991.
6. Grobner, J. and Kerr, J.B., "Ground-Based Determination of the Spectral Ultraviolet Extraterrestrial Solar Irradiance: Providing a Link Between Space-Based and Ground-Based Solar UV Measurements," *Journal of Geophysical Research-Atmospheres*, 2001. **106**(D7): p. 7211-7217.
7. Thekaekal, M. P., "Extraterrestrial Solar Spectrum, 3000-6100 Å At 1-Å Intervals," *Applied Optics*, 1974. **13**(3): p. 518-522.
8. Whitaker, A.F., *LEO Atomic Oxygen Effects on Spacecraft Materials: STS-5 Results*. 1984, Marshall Space Flight Center, Springfield, VA, National Aeronautics and Space Administration, George C. Marshall Space Flight Center.
9. Connell, J.W., "The Effect of Low Earth Orbit Atomic Oxygen Exposure on Phenylphosphine Oxide-Containing Polymers," *High Performance Polymers*, 2000. **12**(1): p. 43-52.

10. Gilman, J.W., Schlitzer, D.S., and Lichtenhan, J.D., "Low Earth Orbit Resistant Siloxane Copolymers," *Journal of Applied Polymer Science*, 1996. **60**(4): p. 591-596.
11. Whitaker, A.F. and Gregory, J.C., *LDEF Materials Results for Spacecraft Applications*. 1994, Washington, DC, National Aeronautics and Space Administration, Office of Management, Scientific and Technical Information Program.
12. Banks, B.A., Rutledge, S. K., DeGroh, K.K., Mirtich, M.J. Gebauer, L., Olle, R., and Hill, C.M., "The Implication of the LDEF Results on Space Freedom Power System Materials," in *5th International Symposium on Materials in a Space Environment*. 1991. Cannes-Madelieu, France.
13. DeGroh, K.K. and Banks, B.A., "Atomic-Oxygen Undercutting of Long-Duration Exposure Facility Aluminized-Kapton Multilayer Insulation," *Journal of Spacecraft and Rockets*, 1994. **31**(4): p. 656-664.
14. DeGroh, K.K., Gaier, J.R., Espe, M.P., Cato, D.R., Sutter, J.K., and Scheiman, D.A. "Insights into the Damage Mechanism of Teflon/ FEP from the Hubble Space Telescope," *High Performance Polymers*, 2000. **12**(1): p. 83-104.
15. Liang, R. and Gupta, A., "Mechanistic Studies of Kapton Degradation in Shuttle Environments," in *AIAA Shuttle Environment and Operations Meeting*. 1983. Washington D.C.
16. DeGroh, K.K., Terlep, J.A., and Dever, T.M., "Atomic Oxygen Durability of Solar Concentrator Materials for Space Station Freedom," *NASA Technical Memorandum-105378*, 1990.
17. Cazaubon, B., Paillous, A., Siffre, J., and Thomas, R., "Five-Electron-Volt Atomic Oxygen Pulsed-Beam Characterization by Quadrupolar Mass Spectrometry," *Journal of Spacecraft and Rockets*, 1996. **33**(6): p. 870-876.
18. Golub, M.A., Wydeven, T., and Cormia, R.D., "ESCA Study of Kapton Exposed to Atomic Oxygen in Low Earth Orbit or Downstream From a Radio-Frequency Oxygen Plasma," *Polymer Communications*, 1988. **29**(10): p. 285-288.
19. Golub, M.A., Wydeven, T., and Cormia, R.D., "ESCA Study of Several Fluorocarbon Polymers Exposed to Atomic Oxygen in Low Earth Orbit or Within or Downstream From a Radio- Frequency Oxygen Plasma," *Polymer*, 1989. **30**(9): p. 1571-1575.
20. Golub, M.A. and Cormia, R.D., "ESCA Study of Poly(Vinylidene Fluoride), Tetrafluoroethylene Ethylene Copolymer and Polyethylene Exposed to Atomic Oxygen," *Polymer*, 1989. **30**(9): p. 1576-1581.

21. Golub, M.A., "Reactions of Atomic Oxygen [O(P-3)] With Polymer-Films," *Makromolekulare Chemie-Macromolecular Symposia*, 1992. **53**: p. 379-391.
22. Tennyson, R.C., "Atomic Oxygen Effects On Polymer-Based Materials," *Canadian Journal of Physics*, 1991. **69**(8-9): p. 1190-1208.
23. Vered, R., Matlis, S., Nahor, G., Lempert, G.D., Grossman, E., Marom, G., and Lifshitz, Y., "Degradation of Polymers By Hyperthermal Atomic Oxygen," *Surface and Interface Analysis*, 1994. **22**(1-12): p. 532-537.
24. Reddy, M.R., Srinivasamurthy, N., and Agrawal, B.L., "Atomic Oxygen Protective Coatings For Kapton Film -- a Review," *Surface & Coatings Technology*, 1993. **58**(1): p. 1-17.
25. Leger, L.J., "Oxygen Atom Reaction with Shuttle Materials at Orbital Altitudes," *NASA Technical Memorandum-58246*, 1982.
26. Eck, T.G. and Hoffman, R.W., *A Study of Kapton Degradation Under Simulated Shuttle Environment : NASA grant NAG 3-426: annual report for period May 1, 1984 to April 30, 1985*. NASA-CR-176003. 1985, Cleveland, Ohio; Washington, DC; Springfield, VA, Dept. of Physics, Case Western Reserve University; National Aeronautics and Space Administration; National Technical Information Service.
27. Arnold, G.S., Peplinski, D.R., and Cascarano, F.M., "Translational Energy-Dependence of the Reaction of Atomic Oxygen With Polyimide Films," *Journal of Spacecraft and Rockets*, 1987. **24**(5): p. 454-458.
28. Koontz, S.L., Albyn, K., and Leger, L., "Materials Selection For Long Life in Low Earth Orbit - a Critical-Evaluation of Atomic Oxygen Testing With Thermal Atom Systems," *Journal of the IES*, 1990. **33**(2): p. 50-59.
29. Ritchie, I. and Gjerde, H.B., "Atomic Oxygen Resistant Coatings On Kapton," *Surface & Coatings Technology*, 1989. **39**(1-3): p. 599-605.
30. Rutledge, S.K. and Mihelcic, J.A., "Undercutting of Defects in Thin-Film Protective Coatings On Polymer Surfaces Exposed to Atomic Oxygen," *Surface & Coatings Technology*, 1989. **39**(1-3): p. 607-615.
31. Wertheimer, M.R., Klembergsapieha, J.E., and Schreiber, H.P., "Advances in Basic and Applied Aspects of Microwave Plasma Polymerization," *Thin Solid Films*, 1984. **115**(2): p. 109-124.
32. Lee, L.H., *Adhesives, Sealants, and Coatings for Space and Harsh Environments*. Polymer Science and Technology; v. 37. 1988, New York, Plenum Press.

33. Banks, B.A., "Consequences of Atomic Oxygen Interaction with Silicone and Silicone Contamination on Surfaces in Low Earth Orbit," *NASA Technical Memorandum-209179*, 1999.

34. Thorne, J.A., Whipple, C. L., *Silicones in Outer Space*, in *The Effects of the Space Environment on Materials, 11th National Symposium and Exhibit, Society of Aerospace Material and Process Engineers*. 1967: North Hollywood, California. p. 243-253.

35. Koontz, S., Leger, L., Albyn, K. and Cross, J., "Vacuum Ultraviolet-Radiation/Atomic Oxygen Synergism in Materials Reactivity," *Journal of Spacecraft and Rockets*, 1990. **27**(3): p. 346-348.

36. Golub, M.A., Lerner, N. R., Wydeven, T, *Reactions of Atomic Oxygen (O(P-3)) with Polybutadienes and Related Polymers*, in *NASA Technical Report*, 1987, Jet Propulsion Laboratory, Proceedings of the NASA Workshop on Atomic Oxygen Effects. p. 161.

37. Dever, J.A., Bruckner, E.J., and Rodriguez, E., "Synergistic Effects of Ultraviolet Radiation, Thermal Cycling and Atomic Oxygen on Altered Coated Kapton Surfaces," *AIAA Paper 92-0774, 30th Aerospace Sciences Meeting and Exhibit, Reno, Nevada*, 1992.

38. Rutledge, S.K., "Materials Degradation in Low Earth Orbit," in *119th TMS Minerals Metals and Materials Annual Meeting and Exhibit*. 1990. Anaheim, CA.

39. Mutikainen, R., "Multiple Layer Coating Scheme to Protect Polymer-Films From Atomic Oxygen Erosion," *Thin Solid Films*, 1994. **238**(2): p. 248-257.

40. Rasoul, F.A., Hill, D.J.T., Forsythe, J.S., O'Donnell, J.H., George, G.A., Pomery, P.J., Young, P.R., and Connell, J.W., "Surface Properties of Fluorinated Polyimides Exposed to VUV and Atomic Oxygen," *Journal of Applied Polymer Science*, 1995. **58**: p. 1857-1864.

41. Cross, J.B., Koontz, S.L., and Hunton, D.E., "Flight Mass-Spectrometer Calibration in a High-Velocity Atomic- Oxygen Beam," *Journal of Spacecraft and Rockets*, 1995. **32**(3): p. 496-501.

42. Connell, J.W., Crivello, J.V., and Bi, D., "Effect of Low-Earth-Orbit Atomic Oxygen Exposure On Epoxy Functionalized Siloxanes," *Journal of Applied Polymer Science*, 1995. **57**(10): p. 1251-1259.

43. Packirisamy, S., Schwam, D., and Litt, M.H., "Atomic Oxygen Resistant Coatings For Low-Earth-Orbit Space Structures," *Journal of Materials Science*, 1995. **30**(2): p. 308-320.

44. Olsson, K., "An Improved Method to Prepare Octa-(alkylsilsesquioxanes) (RSi_8O_{12})," *Arkiv För Kemi*, 1958. **13**(37): p. 367-378.

45. Feher, F.J., Nguyen, F., Soulivong, D., and Ziller, J.W., "A New Route to Incompletely Condensed Silsesquioxanes: Acid- Mediated Cleavage and Rearrangement of $(c-C_6H_{11})(6)Si_6O_9$ to $C-2-[(c-C_6H_{11})(6)Si_6O_8X_2]$," *Chemical Communications*, 1999. (17): p. 1705-1706.

46. Feher, F.J., Terroba, R., and Ziller, J.W., "A New Route to Incompletely- Condensed Silsesquioxanes: Base- Mediated Cleavage of Polyhedral Oligosilsesquioxanes," *Chemical Communications*, 1999. (22): p. 2309-2310.

47. Feher, F.J., Soulivong, D., and Eklund, A.G., "Controlled Cleavage of $R_8Si_8O_{12}$ Frameworks: A Revolutionary New Method for Manufacturing Precursors to Hybrid Inorganic-Organic Materials," *Chemical Communications*, 1998. (3): p. 399-400.

48. Shockley, E.G., Bolf, A. G., Jones, P. F., Schwab, J. J., Chaffee, K. P., Haddad, T.S., and Lichtenhan, J.D., "Functionalized polyhedral oligosilsesquioxane (POSS) macromers: New graftable POSS hydride, POSS alpha-olefin, POSS epoxy, and POSS chlorosilane macromers and POSS-siloxane triblocks," *Applied Organometallic Chemistry*, 1999. **13**(4): p. 311-327.

49. Lichtenhan, J.D., Vu, N. Q., Carter, J. A., Gilman, J.W., and Feher, F.J., "Silsesquioxane Siloxane Copolymers From Polyhedral Silsesquioxanes," *Macromolecules*, 1993. **26**(8): p. 2141-2142.

50. Lichtenhan, J.D., Mantz, R.A., Jones, P.F., and Carr, M.J., "Structure-Property Relationships For Polyhedral Oligomeric Silsesquioxane (POSS)-Siloxane Copolymers," *Abstracts of Papers of the American Chemical Society*, 1994. **207**: p. 109.

51. Lichtenhan, J.D., Otonari, Y.A., and Carr, M.J., "Linear Hybrid Polymer Building-Blocks - Methacrylate- Functionalized Polyhedral Oligomeric Silsesquioxane Monomers and Polymers," *Macromolecules*, 1995. **28**(24): p. 8435-8437.

52. Lichtenhan, J.D., Mantz, R.A., Jones, P.A., Gilman, J.W., Chaffee, K.P., Ismail, I.M.K., and Burmiester, M.J., "Thermolysis of Polyhedral Oligomeric Silsesquioxane (POSS) Macromers and POSS-Siloxane Copolymers," *Abstracts of Papers of the American Chemical Society*, 1995. **210**: p. 140.

53. Lichtenhan, J.D., "Polyhedral Oligomeric Silsesquioxanes - Building-Blocks For Silsesquioxane-Based Polymers and Hybrid Materials," *Comments On Inorganic Chemistry*, 1995. **17**(2): p. 115-130.

54. Lichtenhan, J.D., Gilman, J.W., Feher, F.J., *Process For Preparation of Polyhedral Oligomeric Silsesquioxanes and Synthesis of Polymers Containing Polyhedral Oligomeric Silsesquioxane Group Segments*, Patent No. 5,484,867, 1996, The University of Dayton (Washington, DC); The Regents of the University of California (Washington, DC); The United States of America as represented by the Secretary of the Air Force (Washington, DC).

55. Lichtenhan, J.D., Haddad, T.S., Schwab, J.J., Carr, M.J., Chaffee, K.P., and Mather, P.T., "The Next Generation of Silicon-Based Plastics: Polyhedral Oligomeric Silsesquioxane (POSS) Nanocomposites," *Abstracts of Papers of the American Chemical Society*, 1998. **215**: p. 218-POLY.

56. Lichtenhan, J.D., Schwab J. J., Feher, F. J., Soulivong, D., *Method of Functionalizing Polycyclic Silicones and the Resulting Compounds*, Patent No. 5,942,638, 1999, The United States of America as represented by the Secretary of the Air Force (Washington, DC).

57. Haddad, T.S. and Lichtenhan, J.D., "Hybrid Organic-Inorganic Thermoplastics: Styryl-Based Polyhedral Oligomeric Silsesquioxane Polymers," *Macromolecules*, 1996. **29**(22): p. 7302-7304.

58. Lee, A. and Lichtenhan, J.D., "Viscoelastic Responses Of Polyhedral Oligosilsesquioxane Reinforced Epoxy Systems," *Macromolecules*, 1998. **31**(15): p. 4970-4974.

59. Mather, P.T., Chaffee, K.P., Haddad, T.S., and Lichtenhan, J.D., "Synthesis and Characterization of a Semiflexible Thermotropic LCP End-Capped With POSS-Macromers," *Abstracts of Papers of the American Chemical Society*, 1996. **211**: p. 284.

60. Mather, P.T., Jeon, H.G., Romo-Uribe, A., Haddad, T.S., and Lichtenhan, J.D., "Mechanical Relaxation and Microstructure of Poly(Norbornyl- POSS) Copolymers," *Macromolecules*, 1999. **32**(4): p. 1194-1203.

61. Haddad, T.S. and Lichtenhan, J.D., "Hybrid, Styryl-Based Polyhedral Oligosilsesquioxane Polymers and Copolymers," *Abstracts of Papers of the American Chemical Society*, 1995. **209**: p. 128.

62. Bharadwaj, R.K., Berry, R. J., and Farmer, B.L., "Molecular Dynamics Simulation Study of Norbornene-POSS Polymers," *Polymer*, 2000. **41**: p. 7209-7221.

63. Blanski, R.L., Phillips, S. H., Chaffee, K., Lichtenhan, J. D., Lee, A., and Geng, H.P., "The Preparation and Properties of Organic/Inorganic Hybrid Materials by Blending Polyhedral Oligosilsesquioxanes into Organic Polymers," *Polymer Preprints*, 2000. **41**(1): p. 585.

64. Siegbahn, K., *ESCA; Atomic, Molecular and Solid State Structure Studied by Means of Electron Spectroscopy*. Nova acta regiae societatis scientiarum Upsaliensis, ser. 4, v. 20. 1967, Uppsala, Almqvist & Wiksells.

65. Siegbahn, K., *ESCA Applied to Free Molecules*. 1970, Amsterdam, North-Holland Pub. Co.

66. Hoflund, G.B., *Spectroscopic Techniques: X-ray Photoelectron Spectroscopy (XPS), Auger Electron Spectroscopy (AES) and Ion Scattering Spectroscopy (ISS)*, in *Handbook of Surface and Interface Analysis: Methods for Problem-Solving*, J.C. Riviere and S. Myhra, eds., 1998, Marcel Dekker Inc., New York. p. 57-158.

67. Wagner, C.D., Riggs, W.M., Davis, L.E., and Moulder, J.F., *Handbook of X-ray Photoelectron Spectroscopy*, G.E. Muilenberg, ed., 1979, Eden Prairie, Minn., Perkin-Elmer Corp.

68. Ertl, G. and Kuppers, J., *Low Energy Electrons and Surface Chemistry*. Monographs in modern chemistry ; v. 4. 1974, Weinheim, Verlag Chemie.

69. Palmberg, P.W., "Combined ESCA-Auger System Based On Double Pass Cylindrical Mirror Analyzer," *Journal of Electron Spectroscopy and Related Phenomena*, 1974. **5**(V-D): p. 691-703.

70. Palmberg, P.W., "Combined ESCA and Auger Spectrometer," *Journal of Vacuum Science & Technology*, 1975. **12**(1): p. 379-384.

71. Gilbert, R.E., Hoflund, G.B., Asbury, D.A., and Davidson, M.R., "A Method For Rapid Collection of High-Energy-Resolution Auger- Electron Spectroscopy Data - the Digital-Derivative-Generation Technique," *Journal of Vacuum Science & Technology a-Vacuum Surfaces and Films*, 1988. **6**(4): p. 2280-2286.

72. Helmer, J.C. and Weichert, N.H., "Enhancement of Sensitivity in ESCA Spectrometers," *Applied Physics Letters*, 1968. **13**(8): p. 266.

73. Gilbert, R.E., Cox, D.F., and Hoflund, G.B., "Computer-Interfaced Digital Pulse Counting-Circuit," *Review of Scientific Instruments*, 1982. **53**(8): p. 1281-1284.

74. Savitzky, A. and Golay, M.J.E., "Smoothing + Differentiation of Data By Simplified Least Squares Procedures," *Analytical Chemistry*, 1964. **36**(8): p. 1627-&.

75. Hoflund, G.B., Davidson, M.R., and Outlaw, R.A., "Development of a Hyperthermal Oxygen-Atom Generator," *Surface and Interface Analysis*, 1992. 19(1-12): p. 325-330.

76. Hoflund, G.B. and Weaver, J.F., "Performance-Characteristics of a Hyperthermal Oxygen-Atom Generator," *Measurement Science & Technology*, 1994. 5(3): p. 201-204.

77. Outlaw, R.A., Sankaran, S. N., Hoflund, G. B. and Davidson, M. R., "Oxygen-Transport Through High-Purity, Large-Grain Ag," *Journal of Materials Research*, 1988. 3(6): p. 1378-1384.

78. Outlaw, R.A., Hoflund, G.B., and Davidson, M.R., "Continuous Electron-Stimulated Desorption Using a ZrO_2/Ag Permeation Membrane," *Journal of Vacuum Science & Technology a-Vacuum Surfaces and Films*, 1989. 7(3): p. 2087-2089.

79. Outlaw, R.A., Wu, D., Davidson, M.R., and Hoflund, G.B., "Study of the Oxygen-Transport Through Ag(110), Ag(Poly), and Ag 2.0 Zr," *Journal of Vacuum Science & Technology a-Vacuum Surfaces and Films*, 1992. 10(4): p. 1497-1502.

80. Davidson, M.R., Hoflund, G.B., and Outlaw, R.A., "Electron-Stimulated Desorption of Oxygen-Atoms and Ions From an Oxidized Ag-Zr Alloy Surface," *Surface Science*, 1993. 281(1-2): p. 111-119.

81. Davidson, M.R., Hoflund, G.B., and Outlaw, R.A., "Flux Measurement of a Hyperthermal Atomic Oxygen Beam," *Journal of Vacuum Science & Technology a-Vacuum Surfaces and Films*, 1993. 11(1): p. 264-266.

82. Hoflund, G.B. and Wolan, J.T., "Application of Novel O- and H-atom Sources in Molecular Beam Epitaxy," *Journal of Vacuum Science & Technology B*, 1998. 16(3): p. 1446-1450.

83. Weaver, J.F., Campbell, T.J., Hoflund, G.B., and Salaita, G.N., "Oxidation of Polycrystalline Tin by Hyperthermal Atomic Oxygen: An Investigation Using Electron Energy-Loss Spectroscopy," *Journal of Electron Spectroscopy and Related Phenomena*, 2000. 106(1): p. 81-91.

84. Wolan, J.T., Mount, C.K., and Hoflund, G.B., "Room-Temperature Oxidation of A GaAs(001) Surface Induced by the Interaction of Hyperthermal Atomic Oxygen and Studied by X- ray Photoelectron Spectroscopy And Ion Scattering Spectroscopy," *Applied Physics Letters*, 1998. 72(12): p. 1469-1471.

85. Wolan, J.T. and Hoflund, G.B., "Chemical Alteration of the Native Oxide Layer On InP(111) by Exposure to Hyperthermal Atomic Hydrogen," *Journal of Vacuum Science & Technology a-Vacuum Surfaces and Films*, 1998. **16**(4): p. 2546-2552.

86. Wolan, J.T. and Hoflund, G.B., "Chemical Alteration of the Native Oxide Layer on LiGaO₂(001) by Exposure to Hyperthermal Atomic Hydrogen," *Journal of Vacuum Science & Technology a-Vacuum Surfaces and Films*, 1998. **16**(6): p. 3414-3419.

87. Wolan, J.T., Mount, C.K., and Hoflund, G.B., "Chemical Reactions Induced by the Room Temperature Interaction of Hyperthermal Atomic Hydrogen with the Native Oxide Layer on GaAs(001) Surfaces Studied by Ion Scattering Spectroscopy and X-ray Photoelectron Spectroscopy," *Journal of Vacuum Science & Technology a-Vacuum Surfaces and Films*, 1997. **15**(5): p. 2502-2507.

88. Wisotzki, E., Balogh, A.G., Hahn, H., Wolan, J.T., and Hoflund, G.B., "Room-Temperature Growth of ZrO₂ Thin Films Using a Novel Hyperthermal Oxygen-Atom Source," *Journal of Vacuum Science & Technology a-Vacuum Surfaces and Films*, 1999. **17**(1): p. 14-18.

89. Terrill, H.M. and Ulrey, C.T., *X-ray Technology; The Production, Measurement and Applications of X-rays*. 1930, New York, D. Van Nostrand company, Inc.

90. Campbell, C.T., "Atomic and Molecular-Oxygen Adsorption On Ag(111)," *Surface Science*, 1985. **157**(1): p. 43-60.

91. Menzel, D. and Gomer, R., "Desorption from Metal Surfaces by Low-Energy Electrons," *Journal of Chemical Physics*, 1964. **41**(11): p. 3311.

92. Menzel, D. and Gomer, R., "Desorption from Surfaces by Slow-Electron Impact," *Journal of Chemical Physics*, 1964. **40**(4): p. 1164.

93. Menzel, D., "Electron Stimulated Desorption - Principles and Recent Developments," *Surface Science*, 1975. **47**(1): p. 370-383.

94. Menzel, D., "30 Years of Mgr - How It Came About, and What Came of It," *Nuclear Instruments & Methods in Physics Research Section B- Beam Interactions With Materials and Atoms*, 1995. **101**(1-2): p. 1-10.

95. Redhead, P.A., "Interaction of Slow Electrons with Chemisorbed Oxygen," *Canadian Journal of Physics*, 1964. **42**(5): p. 886-&.

96. Antoniewicz, P.R., "Model for Electron-Stimulated and Photon-Stimulated Desorption," *Physical Review B*, 1980. **21**(9): p. 3811-3815.

97. Pauling, L., *The Nature Of The Chemical Bond And The Structure Of Molecules And Crystals; An Introduction To Modern Structural Chemistry*. 3rd ed., 1960, Ithaca, N. Y., Cornell University Press.

98. Hoflund, G.B., "A Review of Electron-Stimulated Desorption (ESD) Phenomena - Energy Analysis of Desorbing Ions," *Scanning Electron Microscopy Part IV*, 1985: p. 1391-1420.

99. Corallo, G.R., Hoflund, G.B., and Outlaw, R.A., "An Energy-Resolved Electron-Stimulated Desorption (ESD) Study of Oxygen-Exposed Ag(110)," *Surface and Interface Analysis*, 1988. **12**(1-12): p. 185-190.

100. Outlaw, R.A., Hoflund, G.B., and Corallo, G.R., "Electron-Stimulated Desorption of Atomic Oxygen from Polycrystalline Ag," *Applied Surface Science*, 1987. **28**(3): p. 235-246.

101. Wisotzki, E., Hahn, H., and Hoflund, G., B, in *Trends and New Applications of Thin Films*, H. Hoffman, ed., 1998, Trans Tech Publications LTD: Zurich, Switzerland, p. 277-278, 181.

102. Koontz, S.L., Albyn, K., and Leger, L.J., "Atomic Oxygen Testing with Thermal Atom Systems - a Critical- Evaluation," *Journal of Spacecraft and Rockets*, 1991. **28**(3): p. 315-323.

103. Imai, F., Kunimori, K., and Nozoye, H., "Performance-Characteristics of an Oxygen Radical Beam Radiofrequency Source," *Journal of Vacuum Science & Technology a-Vacuum Surfaces and Films*, 1995. **13**(5): p. 2508-2512.

104. Kearns, D.M., Gillen, D. R., Voulot, D., McCullough, R. W., Thompson, W. R., Cosimini, G. J., Nelson, E., Chow, P.P., and Klaassen, J., "Study of the Emission Characteristics of a RF Plasma Source for Atomic Oxygen: Measurements of Atom, Ion, and Electron fluxes," *Journal of Vacuum Science & Technology a-Vacuum Surfaces and Films*, 2001. **19**(3): p. 993-997.

105. Yoshida, Y., Okazaki, Y., Ito, K., and Mizuguchi, S.I., "Production of an Atomic Oxygen Beam By a Nozzle-Beam-Type Microwave Radical Source," *Review of Scientific Instruments*, 1995. **66**(8): p. 4166-4169.

106. Giapis, K.P., Moore, T.A., and Minton, T.K., "Hyperthermal Neutral Beam Etching," *Journal of Vacuum Science & Technology a-Vacuum Surfaces and Films*, 1995. **13**(3): p. 959-965.

107. Hybrid Plastics LLC: company websight: www.hybridplastics.com.

108. Strong, A.B. and Ploskonka, C.A., *Fundamentals of Composites Manufacturing : Materials, Methods, and Applications*. 1989, Dearborn, Mich., Society of Manufacturing Engineers, Publications Development Dept., Reference Publications Division.

109. Taylor, G.N. and Wolf, T.M., "Oxygen Plasma Removal of Thin Polymer-Films," *Polymer Engineering and Science*, 1980. **20**(16): p. 1087-1092.

110. Beamson, G. and Briggs, D., *High Resolution XPS of Organic Polymers: The Scienta ESCA300 Database*. 1992, New York, Wiley.

111. Hoflund, G.B., Gonzalez, R.I., and Phillips, S.H., "In-situ Oxygen Atom Erosion Study of a Polyhedral Oligomeric Silsesquioxane-Polyurethane Copolymer," *Journal of Adhesion Science and Technology*, 2001. **15**(10): p. 1199-1211.

112. Phillips, S.H., Gonzalez, R. I., Chaffee, K. P., Haddad, T. S., Hoflund, G. B., Hsiao, B.S., and Fu, B.X., "Remarkable AO Resistance of POSS Inorganic/Organic Polymers," *Proc. 45th International SAMPE Symposium*, 2000. **45**(2): p. 1921-1931.

113. Reddy, M.R., "Effect of Low-Earth-Orbit Atomic Oxygen on Spacecraft Materials," *Journal of Materials Science*, 1995. **30**(2): p. 281-307.

114. Bonart, R., "X-ray Investigations Concerning the Physical Structure of Cross-linking Segmented Urethane Elastomers," *Journal of Macromolecular Science B*, 1968. **2**(1): p. 115-138.

115. Fu, B.X., Zhang, W., Hsiao, B. S. , Rafailovich, M., Sokolov, J., Johansson, G., Sauer, B. B., Phillips, S.H., and Blanski, R.L., "Synthesis and characterization of segmented polyurethanes containing polyhedral oligomeric silsesquioxanes nanostructured molecules," *High Performance Polymers*, 2000. **12**(4): p. 565-571.

116. Fu, B.X., Hsiao, B.S. , Pagola, S., Stephens, P., White, H., Rafailovich, M., Sokolov, J., Mather, P.T., Jeon, H.G., Phillips, S. H., Lichtenhan, J. D. and Schwab, J.J., "Structural development during deformation of polyurethane containing polyhedral oligomeric silsesquioxanes (POSS) molecules," *Polymer*, 2001. **42**(2): p. 599-611.

117. Shockley, E.G., Bolf, A.G., Jones, P.F., Schwab, J.J., Chaffee, K.P., Haddad, T.S., and Lichtenhan, J.D., "Functionalized Polyhedral Oligosilsesquioxane (POSS) Macromers: New Graftable POSS Hydride, POSS Alpha-Olefin, POSS Epoxy, and POSS Chlorosilane Macromers and POSS-Siloxane Triblocks," *Applied Organometallic Chemistry*, 1999. **13**(4): p. 311-327.

118. Gay, F.P. and Berr, C.E., "Polypyromellitimides: Details of Pyrolysis," *Journal of Polymer Science A*, 1968. **6**: p. 1935-1943.

119. Ojeda, J.R. and Martin, D.C., "High Resolution Microscopy of PMDA-ODA Poly(imide) Single Crystals," *Macromolecules*, 1993. **26**(24): p. 6557-6565.

120. Grossman, E., Lifshitz, Y., Wolan, J. T., Mount, C.K., and Hoflund, G.B., "In Situ Erosion Study of Kapton Using Novel Hyperthermal Oxygen Atom Source," *Journal of Spacecraft and Rockets*, 1999. **36**(1): p. 75-78.

121. Wolan, J.T. and Hoflund, G.B., "Chemical and Structural Alterations Induced at Kapton Surfaces by Air Exposures Following Atomic Oxygen or 1 keV Ar⁺ Treatments," *Journal of Vacuum Science & Technology A-Vacuum Surfaces and Films*, 1999. **17**(2): p. 662-664.

122. Beardmore, K. and Smith, R., "Ion Bombardment of Polyethylene," *Nuclear Instruments and Methods in Physics Research B*, 1995. **102**: p. 223-227.

123. Feher, F.J. and Wyndham, K.D., "Amine and Ester-Substituted Silsesquioxanes: Synthesis, Characterization and Use as a Core for Starburst Dendrimers," *Chemical Communications*, 1998(3): p. 323-324.

124. Feher, F.J., Terroba, R., and Ziller, J.W., "Base-Catalyzed Cleavage and Homologation of Polyhedral Oligosilsesquioxanes," *Chemical Communications*, 1999(21): p. 2153-2154.

125. Svejda, S.A., Lee, A., Feher, F. J., Jin, Z. R, Chaffee, K.P., and Phillips, S.H., "Preparation and Mechanical Properties of Polyimides Incorporating Polyhedral Oligomeric Silsesquioxanes," *Unpublished work*, Air Force Research Laboratory, Edwards AFB, CA, University of California, Irvine, 2001.

126. Dever, J.A., *et al.*, "Environmental Exposure Conditions for Teflon (R) Fluorinated Ethylene Propylene on the Hubble Space Telescope," *High Performance Polymers*, 2000. **12**(1): p. 125-139.

127. Minton, T.K., Zhang, J., Garton, D.J., and Seale, J.W., "Collision-Assisted Erosion of Hydrocarbon Polymers in Atomic-Oxygen Environments," *High Performance Polymers*, 2000. **12**(1): p. 27-42.

128. Zhang, J. and Minton, T.K., "Production of Volatile CO and CO₂ from Oxidized Polyethylene and Graphite Surfaces by Hyperthermal Atom-Surface Collisions," *High Performance Polymers*, 2001. **13**(3): p. S467-S481.

129. Pangborn, A.B., Giardello, M.A., Grubbs, R.H., Rosen, R.K., and Timmers, F.J., "Safe and Convenient Procedure for Solvent purification," *Organometallics*, 1996. **15**(5): p. 1518-1520.

130. Ruffieux, V., Schmid, G., Braunstein, P., and Rose, J., "T-8-OSS-Ethyldiphenylphosphine: A New Functional Oligosilsesquioxane Ligand," *Chemistry-A European Journal*, 1997. **3**(6): p. 900-903.

131. Feher, F.J., Budzichowski, T.A., Blanski, R.L., Weller, K.J., and Ziller, J.W., "Facile Syntheses of New Incompletely Condensed Polyhedral Oligosilsesquioxanes - [(cyclo-C₅H₉)₇Si₇O₉(OH)₃], [(Cyclo-C₇H₁₃)₇Si₇O₉(OH)₃], and [(Cyclo-C₇H₁₃)₆Si₆O₇(OH)₄]," *Organometallics*, 1991. **10**(7): p. 2526-2528.

132. Feher, F.J. and Budzichowski, T.A., "New Polyhedral Oligosilsesquioxanes Via the Catalytic- Hydrogenation of Aryl-Containing Silsesquioxanes," *Journal of Organometallic Chemistry*, 1989. **373**(2): p. 153-163.

133. Feher, F.J., Newman, D.A., and Walzer, J.F., "Silsesquioxanes as Models for Silica Surfaces," *Journal of the American Chemical Society*, 1989. **111**(5): p. 1741-1748.

134. Brown, J.F. and Vogt, L.H., "Polycondensation of Cyclohexylsilanetriol," *Journal of the American Chemical Society*, 1965. **87**(19): p. 4313-&.

135. Aue, W.P., Bartholdi, E., and Ernst, R.R., "2-Dimensional Spectroscopy - Application to Nuclear Magnetic- Resonance," *Journal of Chemical Physics*, 1976. **64**(5): p. 2229-2246.

136. Nguyen, F., *Functionalization of Silsesquioxanes and Synthesis of POSS-MMA and POSS-PDMS Copolymers*, Ph.D. Dissertation, Chemistry Department, University of California, Irvine, 2001.

137. Osborne, J.J., Roberts, G.T., Chambers, A.R., and Gabriel, S.B., "Thin-Film Semiconductor Sensors for Hyperthermal Oxygen Atoms," *Sensors and Actuators B-Chemical*, 2000. **63**(1-2): p. 55-62.

138. Osborne, J.J., Roberts, G.T., Chambers, A.R., and Gabriel, S.B., "Initial Results from Ground-Based Testing of an Atomic Oxygen Sensor Designed for Use in Earth Orbit," *Review of Scientific Instruments*, 1999. **70**(5): p. 2500-2506.

139. Gabriel, S.B., Osborne, J.J., Roberts, G.T., and Chambers, A.R., "Development of a Renewable Atomic Oxygen Sensor for Low Earth Orbit," *Journal of Spacecraft and Rockets*, 1998. **35**(3): p. 413-415.

140

Hoflund, G.B., Rex, S. L., Young, V. Y., Rück, D. M., Jürgen, E., Trautmann, C., Wagner, D., and Angert, N., "Modification of Polyethylene by Ar⁺ Irradiation: Analysis of Reaction Products and Chemical Bonding Alterations," in *Proceedings of the 9th International Conference on Ion Beam Modification of Materials (IBMM '95)*, Williams, J. S., Elliman, R. G., and Ridgway, M. C., eds., Elsevier, Amsterdam, 1996.